Integrating PET-MR data for a multiparametric approach of tumour heterogeneity in non-small-cell lung cancer (NSCLC)

Florent Besson

université
PARIS-SACLAY

Dynamic PET-MRI Integration for a new Multiparametric Approach of Tumor Heterogeneity in Non-Small Cell Lung Cancer (NSCLC)

Thèse de doctorat de l'université Paris-Saclay

École doctorale n°575 : Physique et ingénierie : Electrons Photons, Sciences du vivant (EOBE)
Spécialité de doctorat : imagerie et physique médicale
Unité de recherche : Université Paris-Saclay, CEA, CNRS, Inserm, Laboratoire d'Imagerie Biomédicale Multimodale Paris Saclay, 91401, Orsay, France
Référent : Faculté des sciences d'Orsay

Thèse présentée et soutenue en visioconférence totale le 04/06/2020 par

Florent L. BESSON

Composition du Jury

David MONTANI PU-PH, Inserm, université Paris-Saclay	Président
Ludovic DE ROCHEFORT CR, CNRS, université de Marseille	Rapporteur & Examinateur
Riemer SLART PU-PH, université de Groningen, Pays-Bas	Rapporteur & Examinateur
Alexandre COCHET PU-PH, université de Bourgogne	Examinateur
Jacques FELBLINGER PU-PH, Inserm, université de Lorraine	Examinateur
Mathieu HATT DR, Inserm, université de Bretagne	Examinateur
Pierre VERA PU-PH, université de Normandie	Examinateur
Emmanuel DURAND PU-PH, université Paris-Saclay	Directeur

Thèse de doctorat

NNT : 2020UPASS081

TABLE OF CONTENTS

PREFACE

Symbols and Abbreviations

AC	Attenuation Correction
ADC	Apparent Diffusion Coefficient
ADK	Adenocarcinoma
AFI	Actual Flip-angle Imaging
AIC	Akaike Information Criterion
AIF	Arterial Input Function
ANTs	Advanced Normalization Tools
AUC	Area Under the Curve
BIC	Bayesian Information Criterion
BSA	Body Surface Area
BW	Body weight
^{11}C	Carbone-11 isotope
^{13}C	Carbone-13 isotope
C_2H_3CN	Acetonitrile molecule
CPMG	Carr-Purcell-Meiboom-Gill
CT	Computed Tomography
DAM	Double Angle Method
DCE	Dynamic Contrast Enhanced
DGP	Diffusion Gradient Pulse
DREAM	Double Refocused Echo Acquisition Mode
DWI	Diffusion Weighted Imaging
EES	Extravascular Extracellular Space

EPI	Echo Planar Imaging
ETL	Echo Train Length
ETM	Extended Tofts Model
^{18}F	Fluor-18 isotope
^{19}F	Fluor-19 isotope
FDG	Fluoro-Deoxy-Glucose
FID	Free Induction Decay
FOV	Field Of View
FT	discrete Fourier Transform
FWHM	Full Width at Half Maximum
^{68}Ga	Gallium-68 isotope
Gd	Gadolinium
GFR	Glomerular Filtration Rate
GMM	Gaussian Mixture Model
GRE	GRadient Echo pulse sequence
^{1}H	Hydrogen-1 isotope
H_2O	Water molecule
Hct	Hematocrit
HySCO	HYperelastic Susceptibility Artifact COrrection
ICC	Intraclass Correlation Coefficient
ICS	IntraCellular Space
IDIF	Image Derived Input Function
IQR	InterQuartile Range

IR	Inversion Recovery
LASSO	Least Absolute Shrinkage and Selection Operator
LBM	Lean Body Mass
LC	Lumped Constant
LOR	Line Of Response
ME	Maximum Enhancement
MEFSE	Multi-Echo Fast Spin-Echo
MI	Mutual Information
MOLLI	Modified Look-Locker
MRGlu	regional Metabolic Rate of Glucose
MRI	Magnetic Resonance Imaging
MSE	Mean Squared Error
^{13}N	Azote-13 isotope
^{14}N	Azote-14 isotope
^{23}Na	Sodium-23 isotope
NEX	Number of EXcitations
NIfTI	Neuroimaging Informatics Technology Initiative
NMR	Nuclear Magnetic Resonance
N_{PE}	Number of Phase-Encode steps
NSA	Number of Signal Averages
NSCLC	Non-Small-Cell Lung Cancer
^{15}O	Oxygen-15 isotope
OSEM	Ordered Subset Expectation Maximization

^{31}P	Phosphore-31 isotope
PET	Positron Emission Tomography
PSF	Point Spread Function
pSNR	peak Signal-to-Noise Ratio
^{82}Rb	Rubidium-82 isotope
RF	Radio Frequency
RMSE	Root-Mean-Square Error
r_s	Spearman correlation coefficient
SAR	Specific Absorption Rate
SASHA	SAturation-recovery single-SHot Acquisition
SAT-TFL	pre-SATuration Turbo FLash
SCC	Squamous Cell Carcinoma
SCLC	Small-Cell Lung Cancer
SE	Spin Echo
SiPMs	Silicon PhotoMultipliers
SMART1	Saturation Method using Adaptive Recovery times for cardiac T_1 mapping
SNR	Signal-to-Noise Ratio
SPGR	Spoiled GRadient Echo
SR	Saturation Recovery
SUV	Standardized Uptake Value
Syn	SYmmetric diffeomorphic Non-linear transformations
TAC	Time Activity Curve
TCC	Time Concentration Curve

TE	Echo Time
TI	Inversion Time
TM	Tofts Model
ToF	Time of Flight
TR	Repetition Time
TTP	Time To Peak
VFA	Variable Flip Angle
VOI	Volume Of Interest
XGBoost	eXtreme Gradient Boosting
b	weighting level of diffusion gradient
B_0	Static magnetic field
B_1^+	Positively rotating RF field: transmit field
B_1^-	Negatively rotating RF field: receive field
h	Planck's constant
K_1	Inflow rate of glucose across the transcapillary membrane (PET)
k_2	Outflow rate of glucose across the transcapillary membrane (PET)
k_3	Rate of intracellular glucose phosphorylation (PET)
k_4	Outflow rate of intracellular phosphorylated glucose (PET)
K_{ep}	Outflow transfer constant through the capillary membranes (DCE)
Ki	Net influx constant (PET)
K_{trans}	Inflow transfer constant through the capillary membranes (DCE)
R_{Gd}	Gadolinium relaxivity (DCE)
v_e	Extravascular extracellular volume fraction (DCE)

ν_b	Blood volume fraction
ν_p	Plasma volume fraction
α	Flip angle
β^+	Positron
γ	Gyromagnetic ratio
μ	Linear attenuation coefficient
χ	Magnetic susceptibility measurement
ω	Larmor frequency

Acknowledgements

First and foremost, I want to thank my supervisor Emmanuel Durand. It has been an honor to be his Ph.D. student. His knowledge in medical physics, his kindness and his unwavering support during all these years were highly stimulating for me and greatly contributed to the success of this project. Emmanuel, thank a lot for your support during all these years. We designed this ambitious project together, and I will never forget that you have always supported me, from the beginning to the end, even in the most complicated times.

Second, this work could not have reached this level of technicity without the major help of two people:

- Brice Fernandez from GE Healthcare, who performed all the parametrization and optimization of the MR pulse sequences. Brice, it was a great adventure and a real pleasure to work with you all these years. Thank a lot for your support and disponibility.
- Sylvain Faure, from Laboratoire de Mathématiques d'Orsay, who optimized the curve fitting procedures of the compartmental models and was of great help for the semi automatization of all the maps computation. Sylvain, I could not have reached this level of voxel-wise kinetic analyses without your help and your disponibility. Thank a lot, I am honored and delighted that our roads have crossed.

Third, this project could not have been performed without the continuous support and kindness of Vincent Lebon. Vincent, it is an honor and a pleasure for me to do my research work in the unique ecosystem of the BioMaps team.

Fourth, because this work was also a great human adventure, I would like to thank all the people who contributed to make this project a reality:

- GE Healthcare, in particular Henri Souchay and Isabelle Dufour, for their help at the starting time of this project.

- The medical, technical and support team at SHFJ, Orsay: Elise, Ahmed, Fahd, Ghislaine, Martine, Philippe, Yoann, Kevin, Vincent, Thierry, Claude, Christine & Christine, Bérangère, Véronique, Stéphanie, Marion, Charlotte: your respective supports were essential for my research work.
- The team from the Department of Respiratory Medicine at Hôpitaux Universitaires Paris-Saclay, site Bicêtre: Andrei, my faithful colleague of every Fridays, Florence, Sophie, Xavier, Laurent, Athenais, Xavier, Mitja, Olivier, and Prof Marc Humbert: you substantially boosted my clinical recruitment!
- The teams from the Department of Surgery and Pathology at Hôpital Marie Lannelongue, le Plessis-Robinson: Prof Elie Fadel, Olaf, Sacha, Delphine and Maria Rosa: you substantially boosted my clinical recruitment too!
- The Thorax committee from Gustave Roussy, for their help in the recruitment of the IMAHTEP clinical trial: Caroline, Cécile, Angela, Frank, Antonin, Pernelle, Charles, David, Benjamin, Céline.

Fifth, many thanks to my two thesis reporters, Ludovic de Rochefort and Riemer Slart, and all the members of my PhD committee, Mathieu Hatt, Jacques Felblinger, Alexandre Cochet, Pierre Vera: It was an honor and a pleasure for me to be judged by researchers of your quality; and to David Montani, my president: we have worked together since my beginnings at Bicêtre; It is a real pleasure to work with you and a team of such medical level!

Sixth, in these difficult times related to COVID-19 around the world, I would like to thank all my colleagues and friends who supported me and who were present behind their personal computers at my PhD defense "version 2.0". I was very touched by this recognition. Many thanks to Jacques Bittoun, a precursor of MRI in France, who made me the honor to be part of this great support.

Seventh, many thanks to the colleagues from BioMaps who trained me for my PhD defense:

Emmanuel, Vincent, Claude, Sebastien, Jean-Luc, Charles, and Geneviève. Your advices were of great support!

Finally, I would like to thank my family, who believes in me,

And dedicate this work to my wife, Elodie, my engine in life, and my children Louis & Victoire, by far my greatest achievements!

RESUME DE THESE

Le concept d'hétérogénéité tumorale définit la tumeur comme une mosaïque de phénotypes régionaux spatialement et régionalement adaptatifs sous-tendus par la flexibilité génétique de ses sous-populations cellulaires. Actuellement, l'hétérogénéité tumorale est considérée comme un facteur important de progression et de résistance au traitement. Le cancer bronchique non à petites cellules (CBNPC), modèle tumoral naturellement hautement hétérogène, est la principale cause de décès oncologique dans le monde. L'imagerie oncologique, essentielle pour le diagnostic, la stadification pré-thérapeutique et le suivi des patients atteints de CBNPC, est principalement basée sur des critères morphologiques et/ou fonctionnels semi quantitatifs, qui, par nature limités, ne peuvent représenter la complexité des processus biologiques intra-tumoraux. À l'ère de la médecine de précision et de l'émergence des thérapies personnalisées, le développement de biomarqueurs d'imagerie plus « holistiques » est nécessaire pour mieux caractériser cette hétérogénéité tumorale. L'approche type Radiomique – l'extraction et l'analyse de grandes quantités de caractéristiques définies à partir d'images médicales TEP, TDM ou IRM – semble certes prometteuse, mais en aucun cas ne permet de caractériser les mécanismes biologiques fondamentaux incriminés dans la prolifération tumorale. En ce sens, l'imagerie multiparamétrique quantitative offre des opportunités uniques de caractérisation biologique cellulaire à l'échelle régionale intratumorale, et l'émergence de dispositifs TEP-IRM intégrés promet une évolution disruptive de nos capacités d'analyse multimodale quantitatives. Néanmoins, l'utilisation clinique actuelle des dispositifs TEP-IRM commercialisés reste très basique, et la plus-value diagnostique ou pronostique de cette technologie révolutionnaire reste à démontrer en imagerie oncologique, ceci dans un écosystème déjà très concurrentiel. De ce fait, les protocoles d'acquisition et les traitements d'images nécessaires à l'extraction de biomarqueurs pertinents en imagerie oncologique restent à définir, de manière à opérer un changement de paradigme pour que la TEP-IRM ne soit pas qu'une simple juxtaposition d'une TEP et d'une IRM.

Dans ce contexte, l'objectif de ce projet était donc d'évaluer la faisabilité d'une approche multiparamétrique dynamique simultanée TEP-IRM complète appliquée au CBNPC, pour mieux en caractériser l'hétérogénéité biologique régionale. Pour cela, nous avons exploité le temps d'acquisition IRM intrinsèquement long pour intégrer de manière simultanée des méthodes permettant d'obtenir l'ensemble des biomarqueurs TEP (^{18}F-FDG) et IRM cliniquement disponibles en imagerie : structure tissulaire (imagerie de diffusion, relaxométrie T_1/T_2), méta-

bolisme glucidique (modélisation compartimentale dynamique complète), et perfusion tissulaire (IRM dynamique avec produit de contraste).

Après une introduction des enjeux actuels TEP-IRM dans le CBNPC, trois chapitres abordent les concepts généraux bien établis en imagerie TEP et IRM, les obstacles méthodologiques et solutions proposées pour la réalisation de ce projet, ainsi que les résultats de nos travaux expérimentaux TEP-IRM multimodaux effectués de manière simultanée sur des patients atteints de CBNPC.

Le chapitre 1 détaille les bases physiques de l'imagerie TEP quantitative, et expose la démarche expérimentale qui a été suivie pour implémenter le modèle compartimental de référence du métabolisme glucidique (modèle de Sokoloff), de manière à pouvoir générer des cartes multiparamétriques de métabolisme glucidique régional tumoral indépendamment de tout logiciel de post-traitement. Pour cela, les paramètres cinétiques du métabolisme glucidique (K_1, k_2, k_3) et la fraction de volume sanguin (v_p), formalisés sous forme d'un système d'équations différentielles de premier ordre, ont été approximés en ajustant les données TEP mesurées au système d'équations différentielles, par méthode analytique itérative de Runge-Kutta d'ordre 2, avec optimisation de la fonction de coût (méthode des moindres carrés non linéaires de Levenberg-Marquardt). Plusieurs tests d'optimisation réalisés sur un patient (débruitage des données TEP, ajustement pondéré de la fonction de coût tenant compte de la variabilité du bruit dans les images TEP dynamiques, et ajustement adaptatif de la fonction de coût par différents niveaux d'échantillonnage du signal TEP mesuré) nous ont permis de valider la démarche pour la suite du projet (Figure 1).

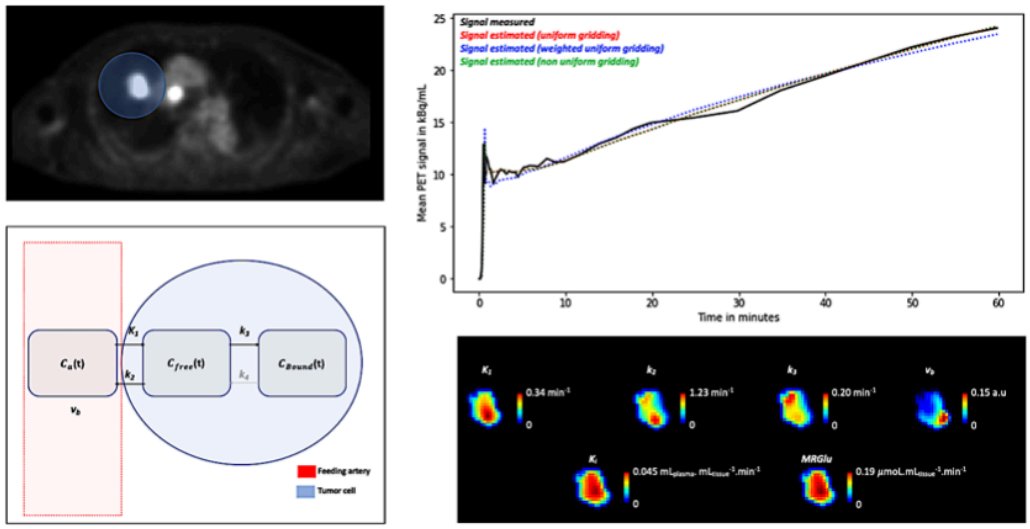

Figure 1 : Résultats de l'implémentation du modèle compartimental de Sokoloff dans l'environnement de programmation Python.

Le chapitre 2 rappelle les bases physiques de l'IRM et les principaux concepts en imagerie quantitative qui permettent d'appréhender plusieurs obstacles méthodologiques que nous avons dû tenter de résoudre.

L'imagerie de diffusion est largement utilisée en imagerie oncologique. Les distorsions géométriques en imagerie pondérée de diffusion, liées aux variations spatiales de susceptibilité de champ magnétique, restent néanmoins un frein aux analyses multimodales à l'échelle régionale intra-tumorale. L'importance des distorsions observées sur nos tumeurs nous a incité à proposer une méthode de correction, jamais évaluée au niveau thoracique, basée sur une approche dite d'encodage de phase inversée. La méthode a été validée sur fantôme, puis cliniquement évaluée sur 12 patients. Le fantôme, spécialement conçu pour cette problématique, consistait en deux tubes remplis respectivement d'acétonitrile pur et d'eau pure, dont les propriétés magnétiques et de diffusion, très différentes, étaient préalablement connues et parfaitement calibrées. Les deux tubes étaient immergés dans de l'eau standard. Les résultats de notre procédure expérimentale, réalisée sur le dispositif TEP-IRM 3T, montrent une nette amélioration des phénomènes de distorsion géométriques observés dans le sens d'encodage de phase à l'interface acétonitrile-eau, avec un recouvrement partiel des valeurs d'ADC mesurées. L'évaluation clinique réalisée sur patients montre que cette méthode de correction in-

duit une très nette amélioration du recalage des images de diffusions des tumeurs pulmonaires sur les images morphologiques et TEP correspondantes (Figure 2, panel droit), avec un impact significatif des valeurs d'ADC régional sur les cartographies générées. La résolution de cette problématique nous a donc permis de générer par la suite, pour les tumeurs pulmonaires, des cartes paramétriques de coefficient de diffusion apparent corrigées des distorsions géométriques, et de les intégrer dans nos analyses volumiques multiparamétriques régionales.

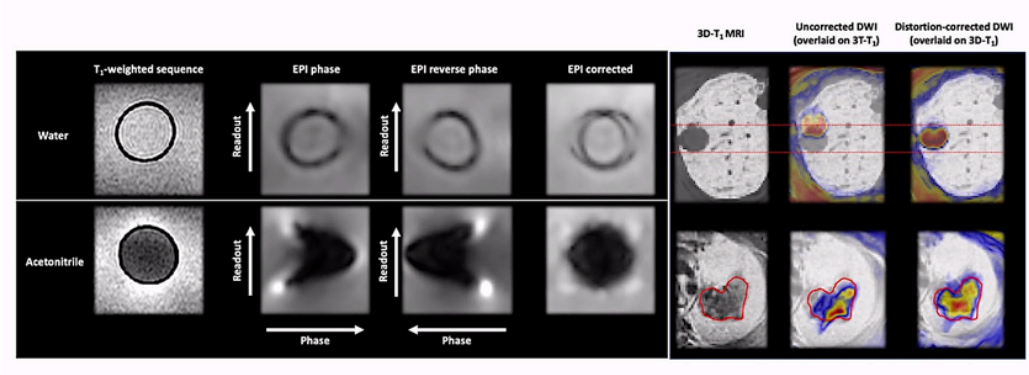

Figure 2 : Effets de la correction par inversion du codage de phase sur les distorsions géométriques en imagerie de diffusion sur fantôme et sur tumeurs pulmonaires.

L'IRM quantitative T_1/T_2 (cartographie T_1/T_2), largement utilisée en imagerie cardiaque, commence à être exploitée en imagerie oncologique clinique. Les différentes approches de routine clinique sont d'abord présentées. Les résultats des mesures expérimentales des méthodes dont nous disposions pour ce projet, réalisées sur le dispositif TEP-IRM 3T, sont ensuite exposées. Deux approches de cartographie T_1 (méthodes d'angles de bascule variables et de saturation récupération) et une approche de cartographie T_2 (écho de spin rapide multi échos) ont été évaluées par deux sessions d'acquisitions identiques, réalisées à 1 semaine d'intervalle sur le même fantôme commercial. Parmi les deux approches de cartographie T_1 évaluées, nos résultats montrent que, pour les valeurs de T_1 de plus de 500ms, la méthode de saturation-récupération présente une plus grande exactitude que l'approche angles de bascule variables (sans et avec correction des inhomogénéités de champ B_1^+ par méthode AFI), avec une bien meilleure reproductibilité (Figure 3). Pour la cartographie T_2, nos résultats expérimentaux montrent une exactitude et une reproductibilité excellentes de la séquence tes-

tée (Figure 3). D'autre part, deux méthodes d'amélioration des courbes d'ajustement T_2 basées sur le rejet du premier écho et le débruitage du signal s'avérèrent non concluantes. Compte tenu de ces résultats expérimentaux, nous avons testé cliniquement la séquence saturation-récupération de cartographie T_1 et la séquence de cartographie T_2, et avons pu générer, pour la première fois sur dispositif TEP-IRM 3T, des cartes paramétriques T_1/T_2 de tumeurs bronchiques (Figure 3).

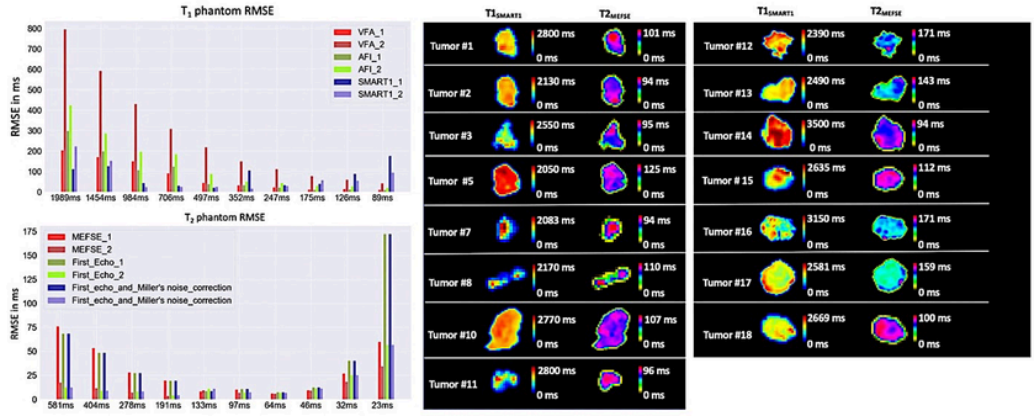

Figure 3 : Relaxométrie T_1/T_2 sur dispositif TEP-IRM 3T. Panel droit : erreur quadratique moyenne des mesures de relaxométrie T_1/T_2 sur fantôme. Panel gauche : cartes paramétriques T_1/T_2 de tumeurs bronchiques.

L'IRM dynamique de perfusion (DCE-IRM) est largement utilisée en imagerie oncologique. Ses grands principes, différents modèles, limitations et multiples considérations méthodologiques sont exposés, ainsi que les résultats expérimentaux de notre implémentation du modèle actuel de référence (modèle de Tofts, dans sa version étendue) dans l'environnement de programmation Python, effectués sur 1 patient. Pour cela, les paramètres cinétiques de perfusion/vascularisation (K_{trans}, ve, K_{ep} et v_p), formalisés sous forme d'un système d'équations différentielles de premier ordre, ont été approximés par la méthode d'ajustement décrite dans le chapitre 1, en y ajoutant les considérations méthodologiques spécifiques au prétraitement des images de DCE (estimation du temps de relaxation T_{10}, compensation du mouvement respiratoire compte tenu de la résolution temporelle de l'ordre de 3 ms des images, tests de débruitage, et conversion du signal mesuré en concentration plasmatique de gadolinium). Cette démarche nous a permis de pouvoir générer des cartes multiparamétriques de

perfusion/vascularisation en DCE, indépendamment de tout logiciel de post-traitement, comme l'illustre la Figure 4.

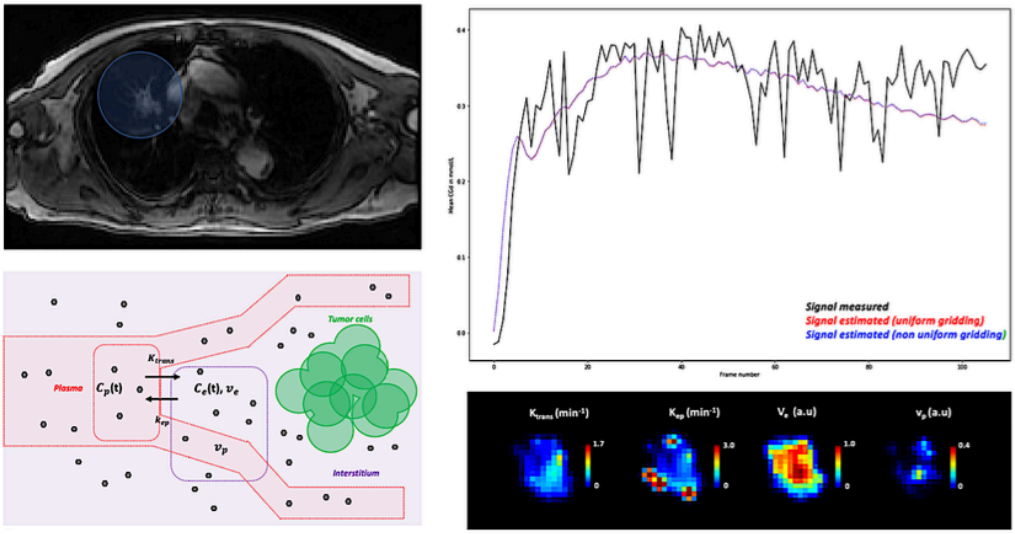

Figure 4 : Résultats de l'implémentation du modèle compartimental de Tofts (version étendue) dans l'environnement de programmation Python.

Le chapitre 3 aborde finalement le cœur de ce projet multiparamétrique dynamique simultané TEP-IRM appliqué au CBNPC : la combinaison de biomarqueurs structuraux (ADC, relaxométrie T_1/T_2), de métabolisme glucidique (^{18}F-FDG) et de perfusion/vascularisation tissulaire (DCE), ainsi que son analyse à l'échelle régionale intratumorale. Les caractéristiques complètes du protocole d'imagerie sont d'abord exposées, incluant notamment le recrutement des patients, les séquences et paramètres d'acquisition utilisées, tenant compte des défis méthodologiques abordés dans les chapitres précédents. Les démarches de post-traitement multimodal spécialement conçues pour ce projet sont ensuite exposées : la standardisation des données TEP et IRM dans un espace de référence ; la correction des artéfacts (distorsions géométriques en imagerie de diffusion et mouvements respiratoires durant les acquisitions DCE par méthodes de recalage non-linéaires) ; et la segmentation semi-automatique des lésions tumorales pulmonaires basée sur un modèle de contour actif.

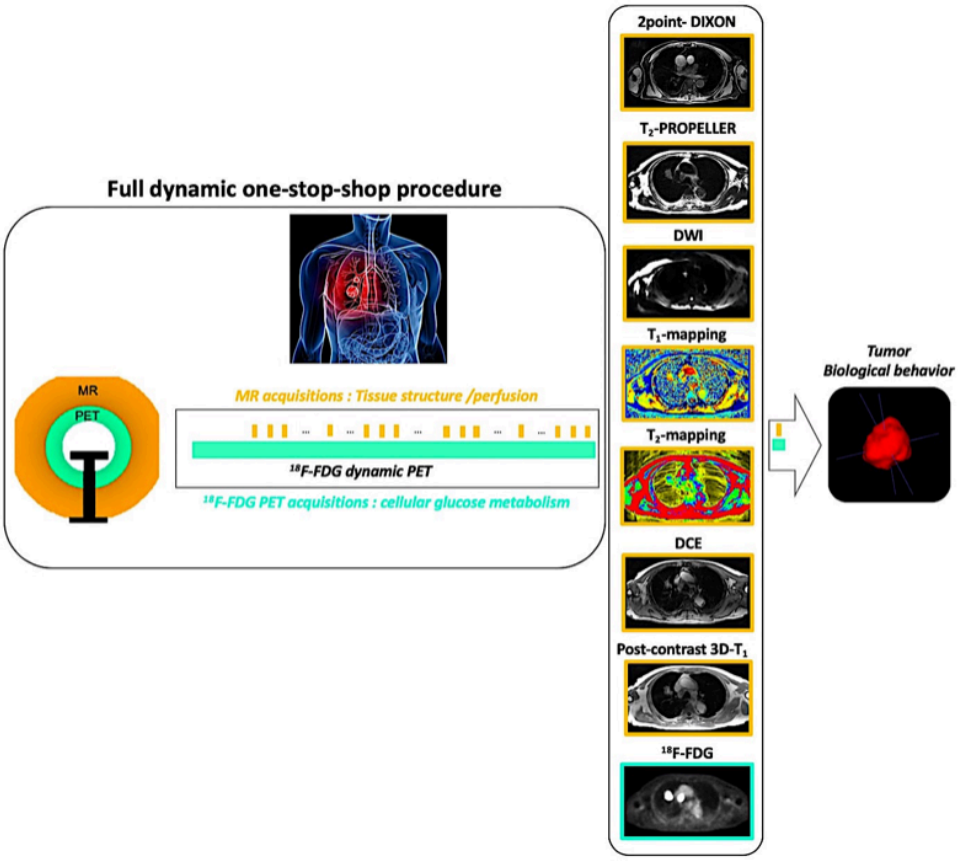

Figure 5 : Protocole TEP-IRM dynamique multiparamétrique appliqué au cancer du poumon.

Les résultats de nos travaux expérimentaux TEP-IRM multimodaux effectués de manière simultanée sont finalement exposés :

Réalisés sur 14 patients, où sont confrontés pour la première fois des biomarqueurs de métabolisme et de perfusion/ vascularisation dans le CBNPC à l'échelle régionale intra-tumorale. Nos résultats illustrent d'une part l'hétérogénéité spatiale inter et intra individuelle des rapports entre métabolisme glucidique et vascularisation, deux caractéristiques biologiques fondamentales de progression tumorale, et d'autre part confirment la complémentarité des paramètres cinétiques TEP et IRM estimés, dont les significations biologiques, complexes, ne sont pas interchangeables entre ces deux modalités d'imagerie (Figure 6).

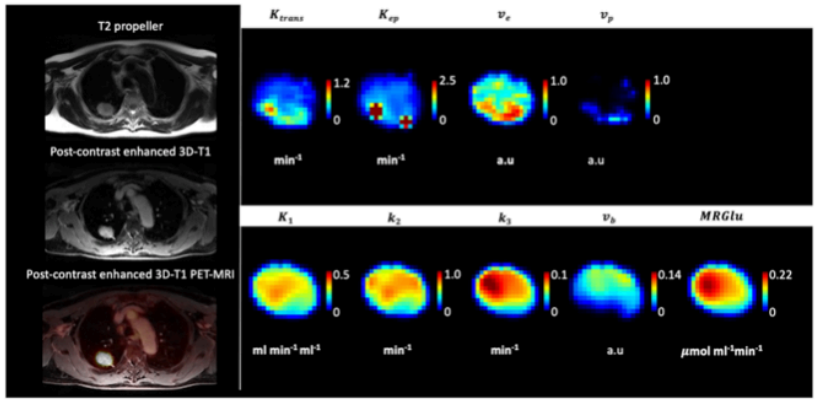

DCE parameters	$MRGlu$	v_b	K_1	k_2	k_3
K_{trans}	0.05 [0.04; 0.07]	0.09 [0.07; 0.1]	0.21 [0.20; 0.22]	0.03 [0.02; 0.05]	-0.08 [-0.09; -0.06]
v_e	-0.09 [-0.1; -0.07]	0.05 [0.04; 0.07]	0.16 [0.15; 0.18]	-0.07 [-0.08; -0.05]	-0.21 [-0.23; -0.20]
K_{ep}	0.12 [0.11; 0.14]	0.11 [0.09; 0.12]	0.15 [0.13; 0.16]	0.11 [0.09; 0.12]	0.06 [0.05; 0.08]
v_p	0.06 [0.05; 0.08]	-0.00063 [-0.02; 0.01]	0.14 [0.13; 0.15]	0.023 [0.009; 0.037]	-0.04 [-0.06; -0.03]

^{18}F-FDG PET parameters

Figure 6 : Corrélations multimodales des paramètres TEP/DCE à l'échelle du voxel. Le panel du haut illustre les cartes paramétriques TEP et DCE d'une tumeur bronchique. Le panel du bas montre les liens entre paramètres TEP et DCE à l'échelle du voxel chez 14 patients testés.

Réalisés sur 11 patients, où nous tentons d'identifier, par réduction dimensionnelle, des profils biologiques TEP-IRM multidimensionnels à l'échelle du supervoxel. Nos résultats montrent qu'un partitionnement tumoral non supervisé par modèle de mélange gaussien, réalisé sur l'ensemble des 11 tumeurs et intégrant l'ensemble des 12 biomarqueurs TEP-IRM structurels et fonctionnels estimés au cours de ce projet, individualise finalement 3 supervoxels génériques pour toutes les tumeurs (Figure 7).

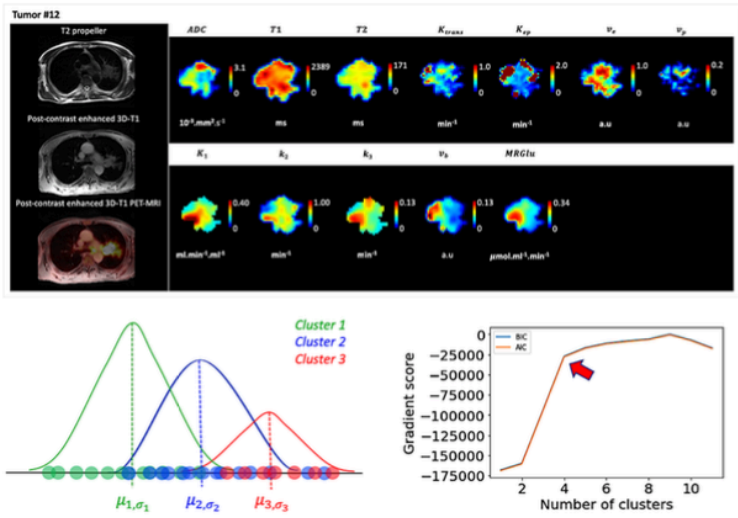

Figure 7 : Partitionnement tumoral non supervisé par modèle de mélange Gaussien. Le panel du haut illustre les cartes multiparamétriques TEP et IRM complètes d'une tumeur bronchique. Le panel du bas montre les résultats du partitionnement tumoral non supervisé réalisé à l'échelle des 11 patients testés.

En utilisant plusieurs approches métaheuristiques d'apprentissage machine, nous identifions finalement une signature multiparamétrique TEP-IRM de ces trois supervoxels, qui peut être définie, avec une exactitude de 97%, par seulement quatre des 12 biomarqueurs étudiés (Figure 8).

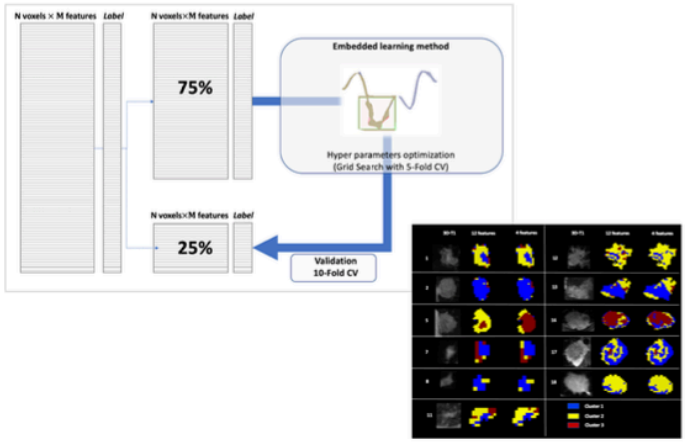

Figure 8 : Prédiction d'une signature multiparamétrique TEP-IRM (3 supervoxels) par approches méta-heuristiques d'apprentissage machine. Une signature biologique TEP-IRM a pu être prédite avec une exactitude de 97% par 4 des 12 biomarqueurs TEP-IRM évalués.

Cette démarche expérimentale TEP-IRM multimodale appliquée au cancer du poumon nous a permis :

- D'une part de démontrer la faisabilité clinique d'un protocole TEP-IRM dynamique multidimensionnel appliqué au CBNPC.
- D'autre part explorer au niveau régional intra-tumoral une signature fonctionnelle TEP-IRM multiparamétrique du CBNPC, dominée par quatre biomarqueurs dynamiques TEP et IRM d'intérêt.

À l'ère de la médecine de précision, la TEP-IRM multiparamétrique pourrait ouvrir la voie vers une évaluation diagnostique et thérapeutique hautement personnalisée. Ce travail méthodologique pourrait ainsi servir de base à la validation de cette signature TEP-IRM sur de plus grandes cohortes prospectives, ainsi qu'à son évaluation comme facteur pronostique de la réponse aux traitements innovants. L'optimisation de certaines problématiques d'instrumentation récurrentes (correction du mouvement et IRM quantitative notamment) est néanmoins requise pour espérer une standardisation future de ce type d'approches, et passe nécessairement par un renforcement des partenariats entre constructeurs et équipes de recherche TEP-IRM.

INTRODUCTION

Combining Positron Emission Tomography (PET) with Magnetic Resonance Imaging (MRI) was first considered in the 1990's, even before Computed Tomography (CT) (1–3). Numerous physical challenges—among which the inherent sensitivity of PET detectors for magnetic fields, the influence of PET electronics on MR signal and spatial technical constraints — delayed its commercial availability (4). Finally, first integrated PET-MRI systems emerged a decade ago (5,6) in a highly competitive medical imaging environment. Theoretically, integrated PET-MRI offers high powerful capabilities in terms of quantification and tissue characterization. However, the initial enthusiasm within the medical imaging community has partially eclipsed deeper reflection about its multimodal capabilities and mainly focused on its cosmetic aspect. The last ten years of PET-MRI clinical transfer were thus dominated by numerous comparative studies with other well-established imaging modalities in a wide variety of cancers, but failed to show substantial gain of PET-MRI in diagnosis or disease staging compared to PET/CT (7–11), with the cost of 4 to 5-fold scan duration. While the question "what are we expecting from PET-MRI" rises (12), there is growing rational of moving towards more functional and molecular PET-MRI multimodal capabilities for tumor characterization (13). Tumor heterogeneity — defining the tumor as a mosaic of spatially and regionally adaptive regional phenotypes underpinned by the genetic flexibility of its cellular subpopulations — is currently considered an important factor in progression and resistance to treatment (14–16).

Non-small cell lung cancer (NSCLC), the leading cause of cancer death worldwide, is naturally highly heterogeneous. Imaging, essential for diagnosis, pre-therapeutic staging or monitoring of patients with NSCLC, is mainly based on morphology assessed with CT and glucose metabolic visual positivity, assessed with PET. Although being the actual reference standards (17), these imaging biomarkers are currently of limited value to assess the complexity of intra-tumor biological processes, especially for the assessment of new targeted or immunotherapy treatments (18,19). In the era of precision medicine and the emergence of personalized therapies, the development of more holistic imaging biomarkers is necessary to better characterize tumor heterogeneity. Integrated PET-MRI approach applied to NSCLC is emerging (8,20–23) but full comprehensive multiparametric assessment of NSCLC has never been performed at the regional intra-tumor level. In this work, we propose a new multiparametric approach to characterize the heterogeneity of NSCLC at the regional level, taking advantage of the unique multimodal capabilities of recent integrated PET-MRI system. We exploited the

inherent long acquisition procedures of multiparametric MRI to combine in a one stop shop procedure all of the ^{18}F-FDG PET and MRI oncological imaging biomarkers clinically available: tissue structure (ADC, T_1/T_2 mapping), metabolism (dynamic 18F-FDG PET kinetic modeling) and perfusion (dynamic contrast-enhanced MRI). Three chapters are thus developed to detail the overall concepts based on well-grounded foundations and the methodological challenges encountered to reach our goal.

The first chapter is devoted to PET imaging and presents the experimental approach followed for the implementation of the Sokoloff's full compartmental model, the gold standard for ^{18}F-FDG PET kinetics in solid tissues (24–27).

The second chapter is devoted to MRI challenges encountered and the related experiments we performed. Lung MRI is currently not well-established in clinical practice, and we transferred some existing methods from other body parts to apply them on lung tumors. In Diffusion weighted imaging (DWI), geometric distortions limit the evaluation of voxel-wise multimodal analyses. We implemented the reverse phase-encoding correction method (28,29) on 3T PET-MRI. The method was validated in dedicated phantom and patients. T_1/T_2 relaxometry is well-established in clinical cardiac imaging (30,31), but its potential in clinical oncology has been very little exploited. Combining T_1/T_2 relaxometry to other quantitative imaging parameters could be of interest to characterize the tumors. We implemented T_1/T_2 relaxometry on 3T PET-MRI and validated the approach in phantom experiments and lung tumor patients. Finally, the chapter ends with the experimental approach followed for the implementation of the extended Tofts model, a widely used DCE model of perfusion in clinical imaging oncology(32).

The third chapter concerns the heart of this multimodal PET-MRI project applied to NSCLC. Based on the methodological challenges exposed and resolved in the first two chapters, imaging biomarkers of structure (DWI and T_1/T_2 relaxometry derived from MRI), metabolism (^{18}F-FDG PET kinetic modeling) and perfusion/vascularization (DCE MRI) were combined together in a one-stop-shop PET-MRI imaging procedure and applied to treatment-naïve and biopsy proven NSCLC patients. Multimodal analyses were performed at the regional tumor level. Finally, metaheuristic approaches were used to reveal, at the supervoxel regional level, biological signatures of NSCLC tumors underlied by all the ^{18}F-FDG PET and MRI biomarkers we estimated.

PROJECT

1. PET imaging, from bases to our purpose challenge

^{18}F-FDG PET-CT has become a worldwide reference imaging standard for the management of lung cancer (17). Switching to ^{18}F-FDG PET-MRI is not a trivial task, mainly due to the limitations of standard MR imaging applied to lung parenchyma, which is characterized by low proton density and fast signal decay due to the many interfaces between air and tissue in the lungs. In this chapter, a brief recall of the physical bases of PET(-MRI) imaging is first presented. We will then explore the essence of PET imaging – i.e. the absolute quantification - and in what the accomplishment of this task was challenging for this project.

1.1. Physical bases

PET was developed in the seventies at Washington University School of Medicine by Edward Hoffman, Michael M. Ter-Pogossian, and Michael E. Phelps (33–35). This functional imaging modality is based on the distribution analysis, in the body, of a β^+emitter radiotracer. Briefly, β^+ radioactivity is characterized by the conversion of a proton Z into a neutron, in the nucleus of an atom X, associated with the emission of a β^+ particle together with a neutrino ν_e

$$ {}^{A}_{Z}X \rightarrow {}_{Z-1}{}^{A}Y + \nu_e + {}^{0}_{1}\beta^+ \qquad (1.1) $$

As any radionuclide, β^+emitters are characterized by their own half-lives ($T_{1/2}$, in minutes in the case of β^+emitters), energies, which are expressed in kilo electron Volt – keV – in the case of β^+emitters) with their related free range in the matter, and their mode of production.

The main β^+radionuclides currently used for PET imaging are summarized in Table 1.1.

β^+ emitter	Half-life ($T_{1/2}$, in min)	Mean energy (keV)	Mean range (mm)	Production
^{11}C	20.3	252	1.27	Cyclotron
^{13}N	9.97	488	1.73	
^{15}O	2.03	730	2.97	
^{18}F	109.8	252	0.66	
^{68}Ga	67.8	844	3.56	Generator
^{82}Rb	1.27	1551	7.5	

Table 1.1 : Physical properties of the main β^+ emitters currently used in PET imaging.

Due to production and half-life characteristics, ^{18}F remains the most widely used β^+emitter for PET imaging in clinical practice.

In PET imaging, a β^+ and an electron collide to generate two high energy γ photons of 511 keV emitted at 180° approximatively from each other, named the annihilation process (Figure 1.1).

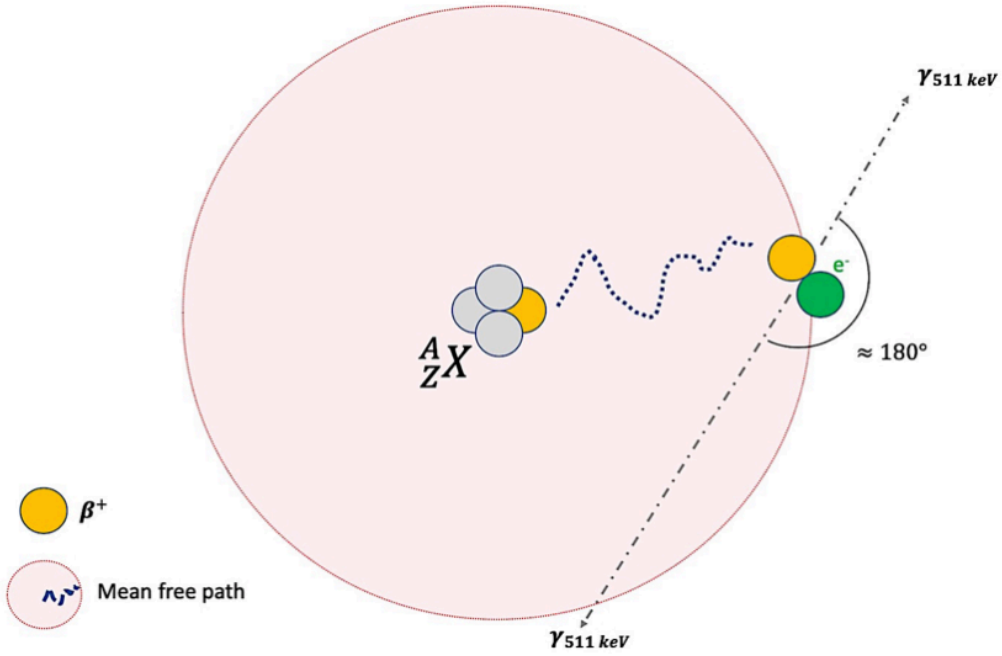

Figure 1.1 : Concept of electron-positron annihilation. The positron (in orange) interacts with an electron (green) to be converted into two photons of 511 keV. These two photons are emitted at approximatively 180°.

Also, each annihilation event defines a line of response (LOR) which is detected by the system in 3 dimensions (both direct and oblique planes) by coincidence. The events detected in coincidence during the acquisition are then integrated along all the LORs to be converted into projections along angles φ and re-organized into sinograms (Figure 1.2).

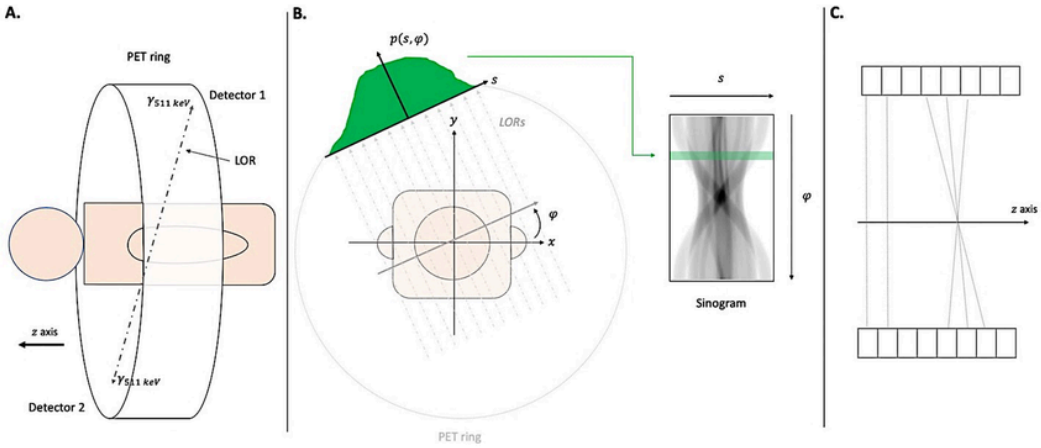

Figure 1.2 : PET signal detection (A) and storing into sinograms (B). For each projection along angle φ, all the LORs are integrated on a projection space and re-organized into sinograms. (C) direct and oblique planes.

Sinograms are then processed to be converted into 3D images. Today, iterative-based methods are the state-of-the art reconstruction methods in PET imaging.

Given a model for the volume (basically a discretized matrix of N distinct voxels), a probabilistic imaging system H (to define the probability that an emission from the voxel j is detected in projection i, and a statistical model for the distribution of the projection measurements, image reconstructions are mainly based on iterative Ordered Subsets Expectation Maximization algorithms (OSEM) (36), formalized by

$$\hat{f}_j^{(n+1)} = \frac{f_j^{(n)}}{\sum_{i' \epsilon S_b} H_{i'j}} \times \sum_{i \epsilon S_b} H_{ij} \times \frac{p_i}{\sum_k H_{ik} \hat{f}_k^{(n)}} \quad (1.2)$$

Where the volume estimate $\hat{\mathrm{f}}^{(\mathrm{n})}$ is forward-projected into a projection domain; all the projections $\sum_{\mathrm{k}} \mathrm{H_{ik}} \hat{\mathrm{f}}_{\mathrm{k}}^{(\mathrm{n})}$ are compared to the measured projections $\mathrm{p_i}$, to be corrected. Subsets of corrected projection data $\sum_{\mathrm{i} \epsilon \mathrm{S_b}} \mathrm{H_{ij}} \times \frac{\mathrm{p_i}}{\sum_{\mathrm{k}} \mathrm{H_{ik}} \hat{\mathrm{f}}_{\mathrm{k}}^{(\mathrm{n})}}$ are then back-projected into image domain and multiplied by the current volume estimate normalized by a weighting term $\frac{\hat{\mathrm{f}}_{\mathrm{j}}^{(\mathrm{n})}}{\sum_{\mathrm{i}' \epsilon \mathrm{S_b}} \mathrm{H_{i'j}}}$, to obtain an updated volume estimate $\hat{f}_j^{(n+1)}$. The process self-updates (iterations) while the volume estimate approaches the true volume. Random, dead time, scatter, decay, attenuation corrections are implemented into the model during the reconstruction procedure. A general overview of the iterative method is proposed in Figure 1.3.

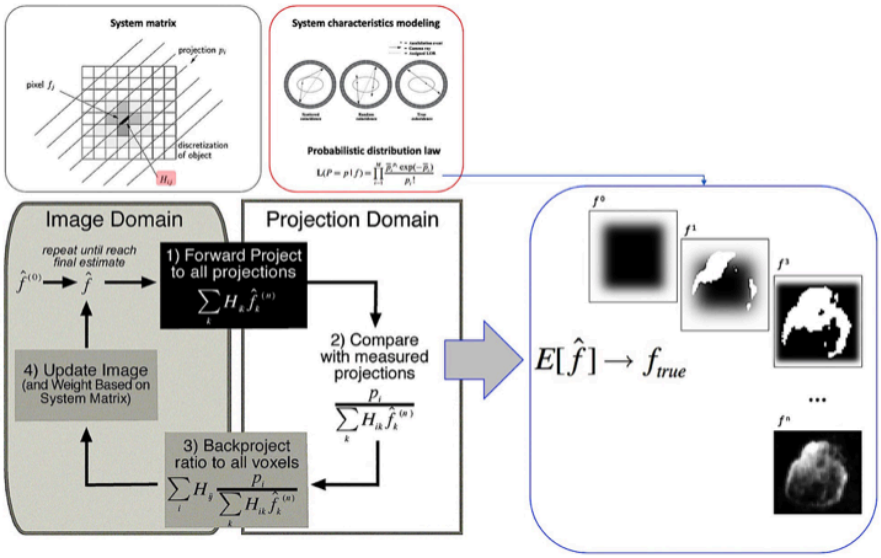

Figure 1.3 : Overview of PET image reconstruction by iterative method (adapted from (37)).

Importantly, Time of Flight (ToF) and Point Spread Function (PSF) modeling can also be implemented into the model (Figure 1.4), leading to a higher image quality and an increased in spatial resolution at the periphery of the PET gantry respectively.)

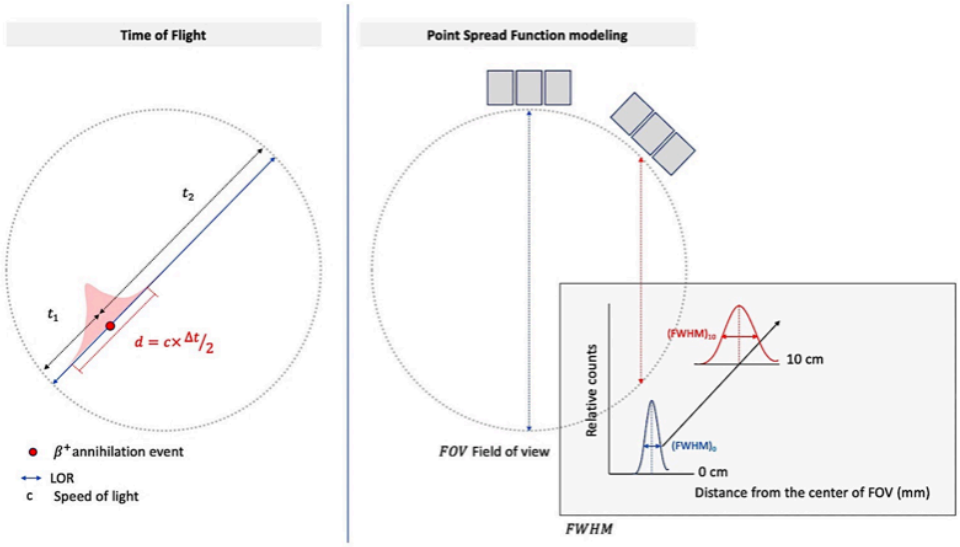

Figure 1.4: ToF and PSF. ToF provides an estimate of annihilation position along the LOR, resulting in higher signal-to-noise ratio, better image quality and faster iterative reconstruction. PSF gives the spatial resolution of the system, defined by the full width at half maximum (FWHM).

1.2. From PET to PET-MR integration

Serendipitously, the integration of PET and MRI in a single compact system has significantly improved PET performances in terms of sensitivity. Sensitivity here is the number of counts per time unit detected by the device per each activity unit, defined for a point source at the center of a single ring scanner by (38)

$$S = \frac{A}{4\pi r^2} \times \varepsilon^2 \times e^{-\mu t} \quad (1.3)$$

Where A is the detector area seen by the source point, ε is the detector's efficiency, μ is the linear attenuation coefficient of 511 keV photons in the detector, t is thickness of the detector, and r is detector ring radius (the sensitivity is highest at the center of the axial FOV and decreases gradually toward the periphery by a factor $\frac{w}{2r}$, where w is the axial width of the detector element.

Compared to standard PET/CT, the increased sensitivity can be explained by the fact that the inner diameter of the PET ring was reduced from 80cm to 60cm to fit in the MRI bore, and the axial field of view (FOV) was extended to 25 cm to reach the typical axial FOV of MRI, increasing the solid angle two- to threefold (6,39,40). The replacement of standard photo multiplicators by silicon photomultipliers (SiPMs), which are insensitive to magnetic fields, improved the coupling to the scintillator crystals, increasing ε. Considering the attenuation by MR coils and the decrease in PET during the MR acquisitions, the overall PET sensitivity is increased twofold (40).

However, the accuracy of attenuation correction (AC) has decreased. CT-based AC uses the proportional relationship between CT Hounsfield units and linear attenuation coefficients at 511 keV. In MRI, proton density is not proportional to the signal measured in MR images, not allowing direct conversion to linear attenuation coefficients. For thorax and lung, MR-AC is thus performed by segmenting Dixon MR images into 3 tissue classes (air, fat and soft tissues), which are finally assigned with predefined linear attenuation coefficients (Figure 1.5) that may lead to quantitative underestimations up to 30% (41–43).

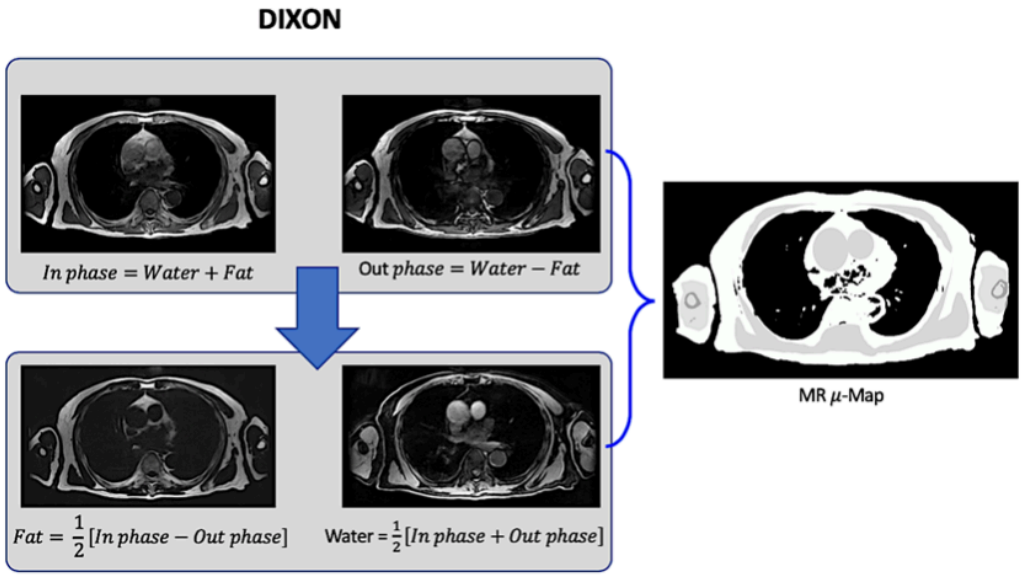

Figure 1.5 : principles of MR-AC. In phase and Out phase imaging data are acquired, and Fat and Water images are reconstructed and used to segment MR images into tissue classes.

Also, combining the PET and MRI underlying concepts is not a simple merging process, because two imaging cultures are facing:

- The MRI one is rather a pre-processing culture that requires numerous adaptive settings and parametrization before images acquisition.
- The PET one is rather a post-processing culture: the device is optimized to acquire and reconstruct images in a particular way that is fixed beforehand image acquisition. The list-mode acquisition of PET raw data allows any type of image reconstruction and processing.

Although whole-body MRI emerge in clinical routine, MRI is more organ-oriented, focusing on multiple acquisitions on a given organ of interest. Acquisition protocols are time consuming. Conversely, PET is intrinsically a whole-body mapping imaging that can be currently done in less than 10 minutes. Although several rule-out protocols have been promoted to speed up the PET-MRI imaging workflow, combining the two entities is not only a simple physical challenge, but also the conceptual task of merging two antagonistic cultures.

In this project, all PET images were acquired on the same Signa PET-MR system, (General Electric, Waukesha, WI, USA). The PET part is a 60 cm bore-diameter gantry composed by 28 modules of 20 solid-state detector blocks (light converters that are insensitive to magnetic fields) for MR compatibility reasons. Each block is made up of a 4 × 9 array of 4.0 × 5.3 × 25 mm^3 lutetium-based scintillator (LBS) readout by 1 × 3 arrays of Geiger mode silicon PMs (SiPMs for signal digitization and processing), resulting in transaxial/axial fields of view (FOV) of 62/25 cm. This PET system is characterized by an energy resolution of 10.3%, a time resolution of 400 ps, a sensitivity detection of 23.3 kcps/MBq and an intrinsic spatial resolution of 4.4 mm full width at half maximum (FWHM) at 1 cm offset the center of the FOV. The Signa PET-MRI system has ToF and PSF modeling capabilities (44).

1.3. Quantification: from visual analysis to full compartmental kinetic modeling

PET imaging is the modality of choice for the image-base quantification of biological functions. With a high degree of detection sensitivity (factor 10^9 compared to radiological-based contrast agents), its main advantage is its capability in inferring *in vivo* biological processes by exploiting the proportional relationship between the activity detected in the tissue of interest and the numerical signal measured in the imaging data, subject to several calibration procedure (45). Basically, two imaging frameworks may be used (Figure 1.6): a static acquisition mode, consisting in a single frame acquired after a predefined delay after radiotracer injection; or a dynamic acquisition mode, for which multiple frames are acquired over time, starting immediately after the radiotracer injection. The latter requires, in the vast majority of cases, a continuous acquisition of at least 60 minutes for state-of-the-art procedures (25).

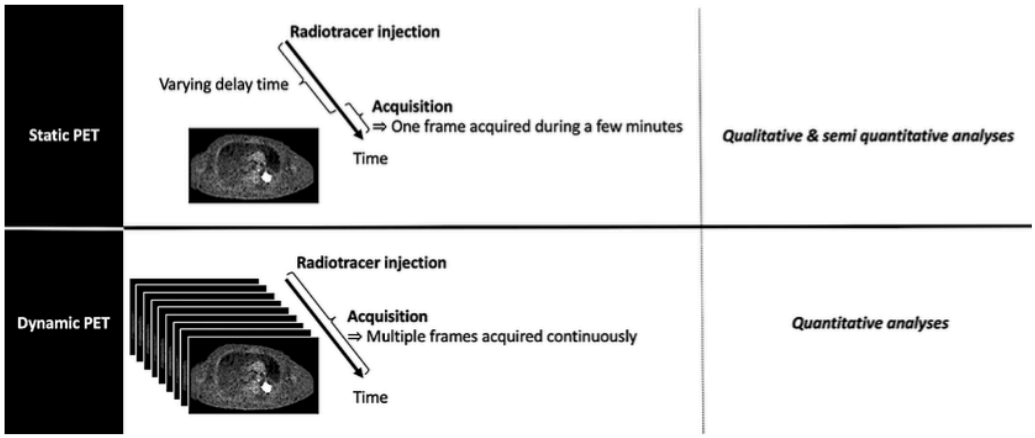

Figure 1.6 : Two different PET imaging frameworks. Static workflow (dominant in clinical practice) consists in acquiring one frame during a few minutes after a delay after radiotracer injection (typically 60 minutes for ^{18}F-FDG). Dynamic workflow consists in acquiring the signal continuously over time. Acquisition starts immediately after the radiotracer injection, and may vary from minutes to more than one hour.

Depending on PET imaging purpose, static or dynamic acquisitions are performed, motivated by the balance between their clinical feasibility and the level of complexity of the information

sought. Static imaging framework is the state-of-the-art procedure in clinical practice, and visual or semi quantitative analyses are usually performed. Visual approach remains the simplest method, but it has many drawbacks: its subjectivity, depending on the experience of the physician; and the lack of metrics to quantify the image abnormalities. Semi-quantitative approaches have been developed to partially overcome these limitations, the most widely used being the standardized uptake value (SUV) and its derivatives that represent the uptake in a targeted region normalized to the injected activity and body weight, lean body mass or body surface area (Figure 1.7) (46–49). Although imperfect but useful in clinical practice, semiquantitative approaches do not provide relevant information on the underlying pathophysiological processes. By using adapted predefined models, "absolute" quantitative methods make it possible. Two major limitations for their use in clinical practice are the requirement for dynamic PET acquisitions and much more computational complexity (Figure 1.8). Among these approaches, we can briefly individualize graphical analyses (Patlak plot for irreversible tracer compartments and Logan plots for reversible tracer compartments) which are simplified kinetic analyses, and the full compartmental analyses that remains the gold standard for absolute quantification in PET imaging.

$$SUV_{BW/LBM/BSA} = \frac{Radioactive\ concentration}{Activity\ injected \times \rho} \times (BW\ or\ LBM\ or\ BSA)$$

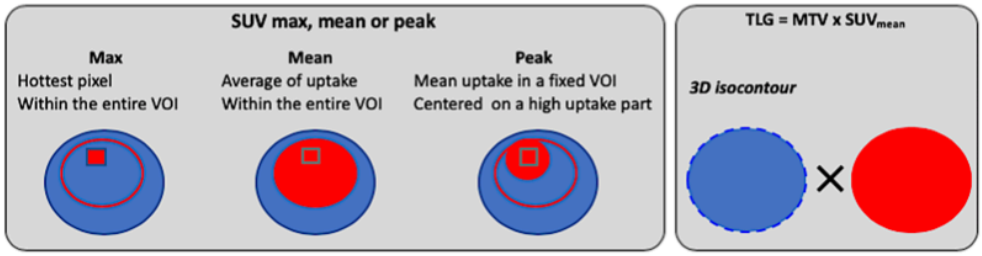

Figure 1.7 : SUV and its main derivatives. SUV_{BW} is the most widely use metric in PET imaging. SUV_{LBM} is increasingly used to limit the underestimation of ^{18}F-FDG uptake in obese patients. SUV_{max} is sensitive to noise in the images; SUV_{mean} is sensitive to the volume of interest; SUV_{Peak} is a compromise between SUV_{max} and SUV_{mean}. Total Lesion Glycolysis (TLG) is a surrogate of metabolic tumor volume (MTV) and SUV_{mean}.

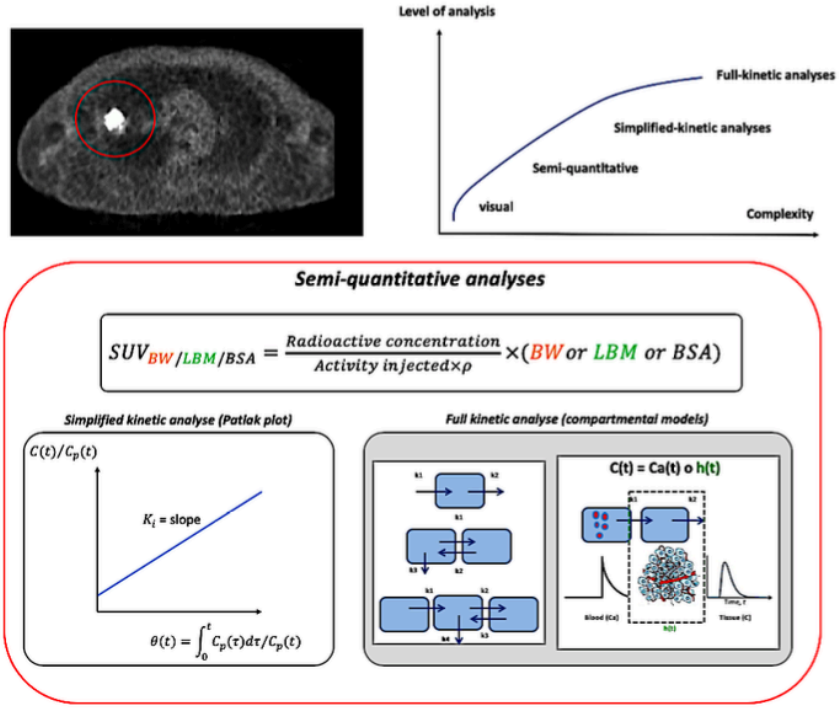

Figure 1.8 : Different levels for PET quantification. More the level of analysis is improved, more the complexity of implementation is increased.

Full kinetic analyze is the only method to fully capture the physiological processes underlying the tissue of interest. Based on differential equation systems that depends on the physiological task we want to measure (for example one-tissue two-parameters method for blood perfusion, two-tissues three parameters for metabolism, and two-tissue four-parameters method for receptor-ligand binding), the same general framework can be empirically defined:

a) Dynamic image acquisitions

First of all, a state-of-the-art dynamic PET acquisition requires a continuous imaging acquisition (Figure 1.9) adapted to the function that is targeted (from 2-3 minutes for perfusion analyses to 60 minutes for state-of-the art cellular metabolism as in our project) (25,50,51), centered on the region of interest (in our case the thorax), starting immediately after the intravenous injection of the radiotracer (^{18}F-FDG in our case). The respect of a suitable acquisition time is important to obtain unbiased measures.

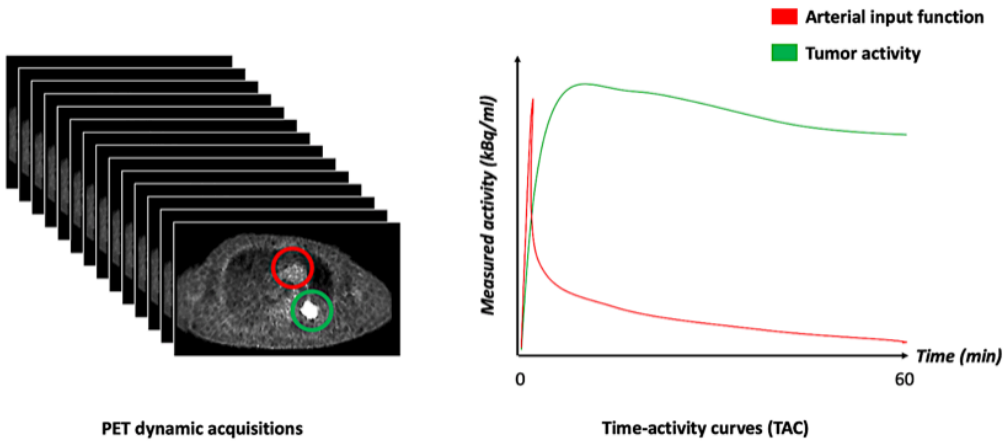

Figure 1.9 : Dynamic acquisition and TACs. By drawing VOIs in a large artery and the tissue of interest, the related time varying radioactivity concentrations may be measured.

b) compartment model selection

One, two, three compartments may be possible depending on the function we want to measure. For the model we will apply in this work (cellular glucose metabolism), the two-compartment three parameters model of Sokoloff is the reference (24,52) (Figure 1.10).

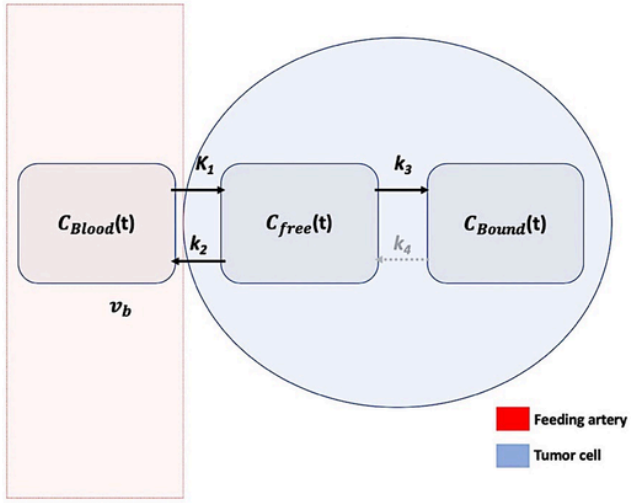

Figure 1.10: PET Sokoloff compartmental model. In this scheme, C_{Blood}(t) is the time-varying activity concentration of ^{18}F-FDG in the arterial blood. C_{free}(t) and C_{Bound}(t) are the two intracellular compartments representing ^{18}F-FDG in its non-phosphorylated and phosphorylated states respectively. K_1, k_2 and k_3 are the microparameters to estimate (the k_4 microparameter can be neglected in this case, as no phosphorylated glucose goes out from the cell).

Given $C_{Blood}(t)$ the time-varying activity concentrations of ^{18}F-FDG in the arterial blood; the intracellular time-varying activity concentrations of ^{18}F-FDG in its unphosphorylated ($C_{free}(t)$) and phosphorylated ($C_{Bound}(t)$) states are defined by

$$\frac{dC_{Free}(t)}{dt} = K_1 \times C_{Blood}(t) - (k_2 + k_3) \times C_{Free}(t) \quad (1.4)$$

$$\frac{dC_{Bound}(t)}{dt} = k_3 \times C_{Free}(t) \quad (1.5)$$

Where K_1 ($mL_{plasma}.mL_{tissue}^{-1}.min^{-1}$) represents the inflow rate of glucose across the transcapillary membrane, k_2 (min^{-1}) represents the outflow rate of glucose across the transcapillary membrane, and k_3 (min^{-1}) represents the rate of glucose phosphorylation.

From equations (1.4) and (1.5), the total time-varying activity concentration of ^{18}F-FDG in the tissue of interest $C_{PET}(t)$ is defined by the following equation

$$C_{PET}(t) = (1 - v_b) \times [C_{Free}(t) + C_{Bound}(t)] + v_b \times C_{Blood}(t) \quad (1.6)$$

Where v_b is the blood volume fraction (no dimension).

In this scheme, blood is not considered as a compartment, but as arterial input. The first and second compartments are the intracellular space with glucose molecule in non-phosphorylated and phosphorylated states respectively.

Based on this model assumption, we can estimate the kinetic microparameters K_1 ,k_2 and k_3. From the estimated parameters, we infer the influx constant Ki ($mL_{plasma}.\ min^{-1}.\ mL_{tissue}^{-1}$)

$$Ki = \frac{K1 \times k3}{k2 + k3} \quad (1.7)$$

And finally, the Glucose consumption $MRGlu$ ($\mu mol.min^{-1}.mL^{-1}$):

$$MRGlu = \frac{Ki}{LC} \times Glycaemia \quad (1.8)$$

Where LC is the "lumped constant" (no dimension) that follows the principles of competitive substrate kinetics.

Basically, because ^{18}F-FDG does not perfectly fulfill the transport and phosphorylation properties of glucose, LC is used to convert the ^{18}F-FDG uptake rate to glucose uptake rate. Several values have been proposed for brain, myocardium, skeletal muscle, adipose tissue or Liver ^{18}F-FDG studies (53–59). For oncological studies, it is often set to 1 because of unknown relevant value (60).

c) Arterial input function

The main methods for arterial input function measurement (AIF) are summarized in Figure 1.11. Typically, the reference standard remains the arterial blood sampling at several times over the image acquisition (61,62). This method is technically invasive, very difficult to implement, especially on PET-MR systems (the patient mobilization during each sampling induces magnetic perturbations, the access to the patient arm is not trivial if considering the surface coils). Non-invasive alternatives have been proposed, including population-based or Image based derived input function (IDIF). Population-based methods are simple to use but not well adapted for individual purpose, as any template-based approach. IDIF methods are increasingly used because of their simplicity. Two major challenges with IDIF are the identification of a large feeding vessel (to avoid partial volume effect) and the measurement of the arterial plasma activity. Concerning the first pre-requisite, it is less challenging at the thoracic level compared to other body levels in the presence of aorta, whose large size precludes major partial volume effect. Concerning the second prerequisite, the image-derived input function contains the whole-blood ^{18}F-FDG concentration, and not the arterial one. However, this approach has provided accurate results and was validated against the arterial ground truth in oncology studies (63). For this reason and for simplicity sake, we decided to use uncorrected IDIF method in our project.

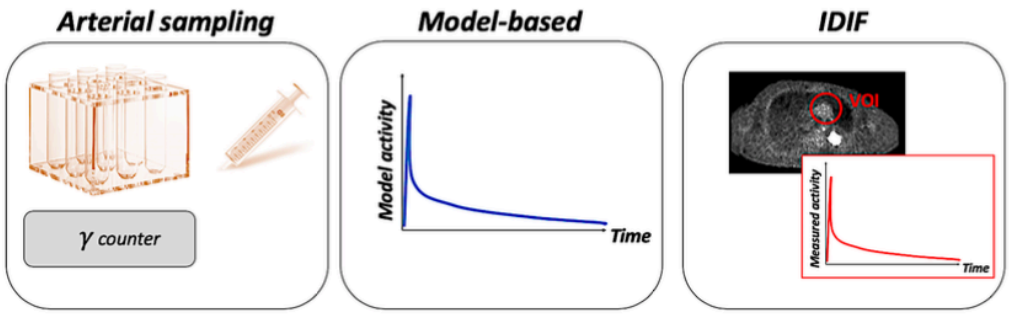

Figure 1.11: methods for AIF measurement. Arterial sampling with radioactivity counting remains the gold standard. However, this invasive procedure is rarely performed and model-based or image-derived input functions (IDIF) are preferred in practice.

1.4. Technical challenges for our purpose

1.4.1. Context

Several methodological PET challenges were faced to implement full compartmental dynamic approach for this project:

- First, the time between injection and acquisition start had to be carefully evaluated, to capture the first pass of radiotracer at the beginning of PET acquisitions.
- Second, in the case of static PET image acquisitions (duration of minutes), several motion compensation procedures are routinely available (PET gating using respiratory belts or multimodal registration procedures for example). However, these methods are less trivial for one-hour dynamic acquisition procedures. The variability of the radiotracer biodistribution over time, combined with low signal-to-noise ratio especially in the first frames, together with the lack of spatial references make motion compensation highly challenging in dynamic PET imaging. Currently there is no validated method to compensate motion for dynamic PET studies outside the brain.
- Finally, a major challenge was to implement "in-house" voxel-wise procedure for the full dynamic compartmental task. The few software that currently propose solutions to compute PET kinetic analyses with preprocessing pipelines are mainly dedicated for brain imaging and rarely implement full kinetic analyses. Furthermore, these software do not integrate unified PET and DCE multimodal computation tasks. Thus, we had to develop "in-house" computation procedures for two-tissue three parameters modeling. Although the main principle is well defined, programming is not trivial. The time activity curves are typically noisy at the voxel level, and the computation task is challenging because of i) the huge number of voxels to potentially estimate depending on the tumor size, ii) the sensitivity of the parameters to initial estimates. In this context, convergence of state-of-the art non-least square fitting procedure may be computationally expensive, and require several constraints for optimized fine-tuning.

1.4.2. Preliminary test for in-house implementation of the full compartmental PET metabolism kinetic modeling

To validate our implementation, we used the reconstructed PET data of patient 1 (for more details, please refer to sections 3.1.1 for patient's characteristics; and section 3.1.2 for PET reconstruction parameters).

1.4.2.1. Signal denoising analyses

Reconstructed PET raw data are inherently highly noisy. Because the signal may be approximated by a Gaussian distribution in reconstructed PET data, a typical denoising procedure consists in smoothing the data to regularize the TACs. Although several equations have been suggested (*64*), the level of smoothing is mainly empirical, depending on the local habit and imaging purpose. The objective being not to lose too much relevant information, several levels of 3D Gaussian filtering were tested to search for good compromise between TACs regularization, signal loss and visual image quality (smoothing degrades the spatial resolution and the details in the image). Considering the voxel size Δx, the Gaussian filter width σ may be defined as follows (*64*):

$$\sigma = 2b + 1 \quad (1.9)$$

$$b = \left[\frac{FWHM}{\Delta x}\right] + 1 \quad (1.10)$$

The PET detector on the Signa PET-MR system has an intrinsic resolution of 4mm. An appropriate Gaussian filtering would be of 7 mm, according to (64). To be exhaustive, six σ cut-off levels around this value were tested: 3, 4, 5, 6, 7, 8 and 10 mm. The main results of the different levels are illustrated in Figure 1.12.

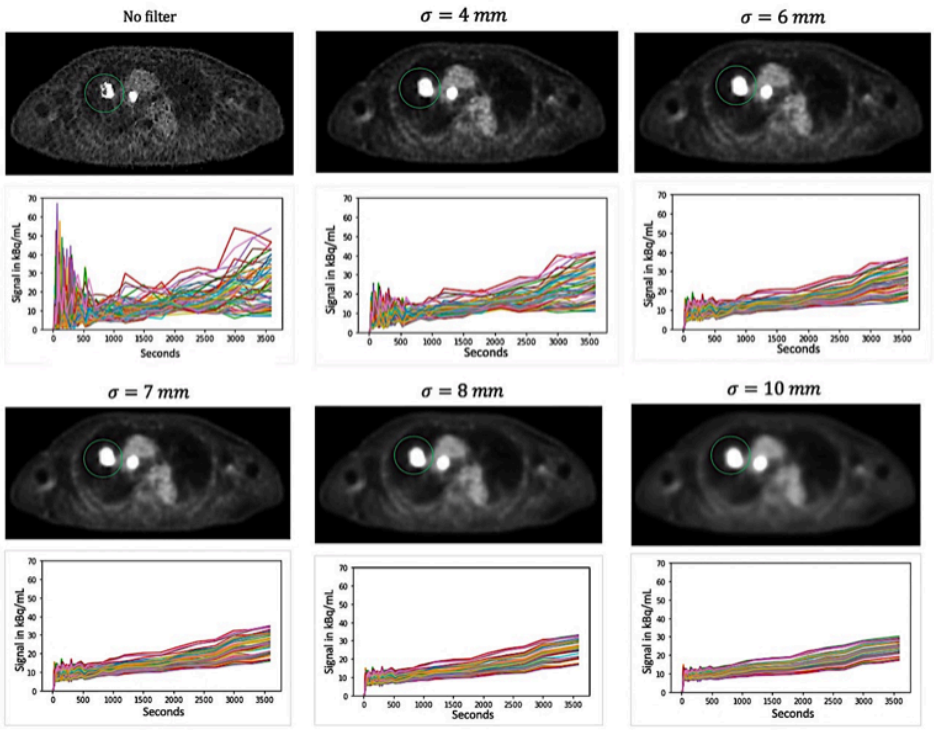

Figure 1.12: PET results with different levels of smoothing. A visual inspection of the post-filtered data (both the 3D volumes and the TACs of the tumors) shows that the voxel-wise TACs appear better regularized with higher levels of smoothing, especially above 7mm. Also, as expected, a loss of sharp details together with the increase level of smoothing is observed, especially in the contours of the lesion (green circle).

To quantify the signal loss induced by Gaussian filtering, the peak signal to noise ratios (pSNR) of the post-filtered images from a tumor subset (57 voxels) were computed. The pSNR, computed in Python with the compare_psnr module (scikit-image library), was defined as follows

$$pSNR = 10 \times Log\left(\frac{MAX_I^2}{MSE}\right) \quad (1.11)$$

Where MAX_I is the maximum pixel value of the image, and MSE is the mean squared error between the reference image I and the test image.

The pSNR results are provided in Table 1.2. The pSNR ranged from 32.2 (3 mm Gaussian filtering) to 25.1 (10 mm Gaussian filtering), with low variations above 5 mm Gaussian filter. Because the TAC appeared less erratic above 7 mm, and to ensure that the majority of the

voxels in the tumors would be correctly fitted (especially in the case of patient respiratory motion), a 8 mm Gaussian cut-off was finally considered to be a good compromise between TAC regularization over time and signal loss, and used for all the PET dynamic procedures of the project.

Gaussian filter (σ in mm)	pSNR
3	32.2
4	32.2
5	26.9
6	26.2
7	25.7
8	25.5
10	25.1

Table 1.2: pSNR of PET data according to the Gaussian filter.

1.4.2.2. Model implementation

We used the whole masked PET tumor data of the patient (41 frames, 562 voxels) previously smoothed with an 8 mm Gaussian filter to validate the PET kinetic modeling.

a) Model parametrization

A two-tissue three-parameter compartment model including the blood volume fraction (24,25,52,65) was implemented in Python environment (libraries numpy, nibabel, nilearn, pandas, math and scipy).

We used an iterative second order Runge-Kutta numerical method analysis to resolve the system(*66*) defined by the equations (1.4), (1.5), (1.6), (1.7), and (1.8). A Levenberg-Marquardt non-linear least square fitting algorithm was used to minimize the cost-function, which was defined by

$$S(\beta) \equiv argmin_{\beta}\ {}^{1}/_{2} \sum_{i=1}^{m} [y_i - f(x_i, \beta)]^2 \quad (1.12)$$

Where $S(\beta)$ is the minimum sum of squares deviations between the measured and estimated C_{PET} values (y_i and $f(x_i, \beta)$ respectively) at each time-point i, x_i is the measured C_{Blood} value at each time-point i, and $\beta = \{K_1, k_2, k_3, v_b\}$.

Several constraints were also implemented to optimize the fitting procedure:

- Empirical [0-10] numerical bounds were imposed to the K_1, k_2, k_3 kinetic parameters.
- [0-1] numerical bounds were imposed to the v_b expected values.

To validate the procedure, several experiments were performed by using 4000 sampled time-points, including:

- A uniform gridding of the sampled time-points.
- A uniform gridding of the sampled time-points with least square estimation weighted by a ponderation factor w_i to test the influence of noise variability over time:

$$w_i = \Delta t_i \times \frac{1-e^{(-\lambda \times \Delta t_i)}}{e^{\lambda \times T_i} \times \lambda \times \Delta t_i} \quad (1.13)$$

Where Δt_i is the delay time between two successive sampled time-points, $\lambda = \frac{ln2}{T}$ with T the period of the radionuclide, and T_i is the delay time between t_0 and the sampled time-point i.

- A nonuniform gridding (initial fine time sampling with progressive enlargement to prioritize the first part of the TAC) as illustrated in Figure 1.13. This choice was motivated to be sure to capture the very first data points of the AIF.

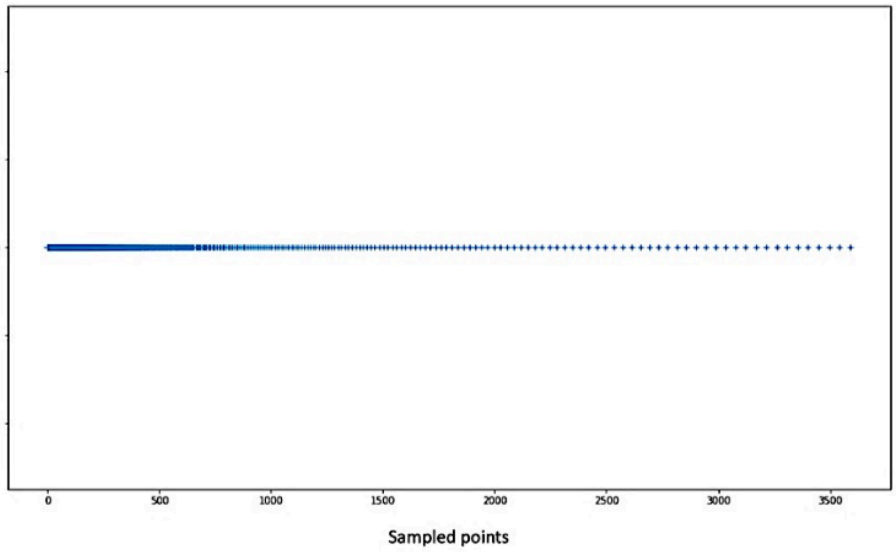

Figure 1.13: Nonuniform gridding for dynamic image sampling.

b) Computation efficiency

The number of iterations required to estimate the kinetic parameters is provided in Figure 1.14.

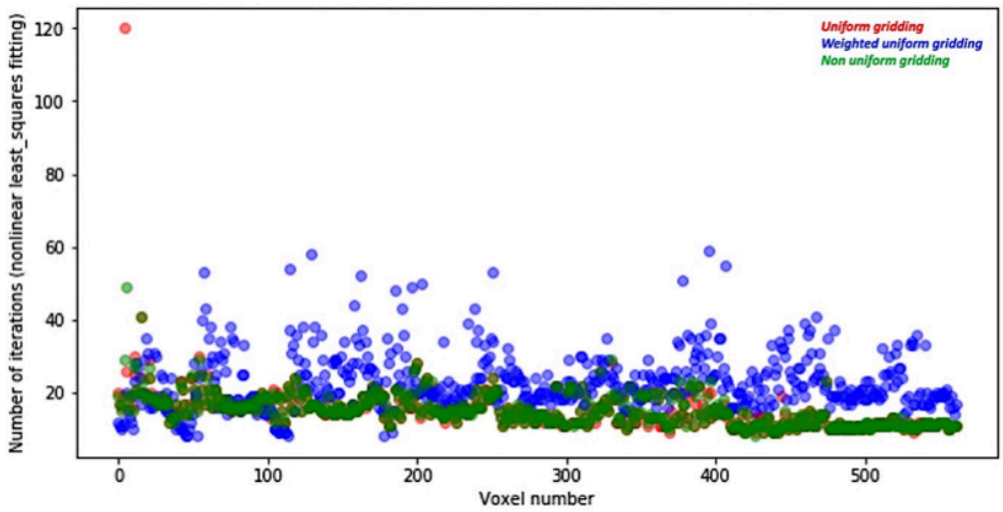

Figure 1.14: Number of iterations required per voxel to estimate the kinetic parameters. The x-axis represents the voxel identity number in the tumor. The y-axis represents the number of iterations required to reach the convergence of the Levenberg-Marquardt algorithm (max = 400 iterations).

To estimate the kinetics parameters of the 562 tumor voxels, the weighted least square estimation with uniform gridding required a mean number of 23.1 iterations (range = 8-59), versus 15.4 (range = 9-120) and 15.3 (8-49) for the uniform and non-uniform gridding respectively (the maximum number of iterations (400) was not reached for any of the methods).

The computation time, on a standalone personal computer, is proportional to the number of sampled points considered to resolve the differential equation system.

To give an order of magnitude in the case of uniform gridding, the computation time on a random voxel was 0.7 s for 100 sampled points, 4.74 s for 600 sampled points, 11.8 s for 1500 sampled points, 21.05 s for 3000 sampled points, 35.7 s for 5000 sampled points and 70.5 s for 10 000 sampled points.

Also, preliminary experiments (subset of 57 voxels) showed similar performance between nonuniform and uniform gridding when considering more than 2000 points (additional figures are provided in the Appendix section A.1: Figure A. 1 and Figure A. 2).

c) Accuracy of the procedure

Figure 1.15 shows the Root-Mean-Square Error ($RMSE$) per voxel for uniform, uniform weighted and nonuniform gridding approaches, defined by

$$RMSE = \frac{1}{\sqrt{N}} \times \|Measured\ C_{PET} - Estimated\ C_{PET}\|_2 \quad (1.14)$$

With N the number of frames. The median $RMSE$ (IQR) were 1.7 [1.2-2.3] kBq/mL, 1.8 [1.3-2.7] kBq/mL and 1.7 [1.2-2.4] kBq/mL for the uniform, uniform weighted and nonuniform gridding respectively.

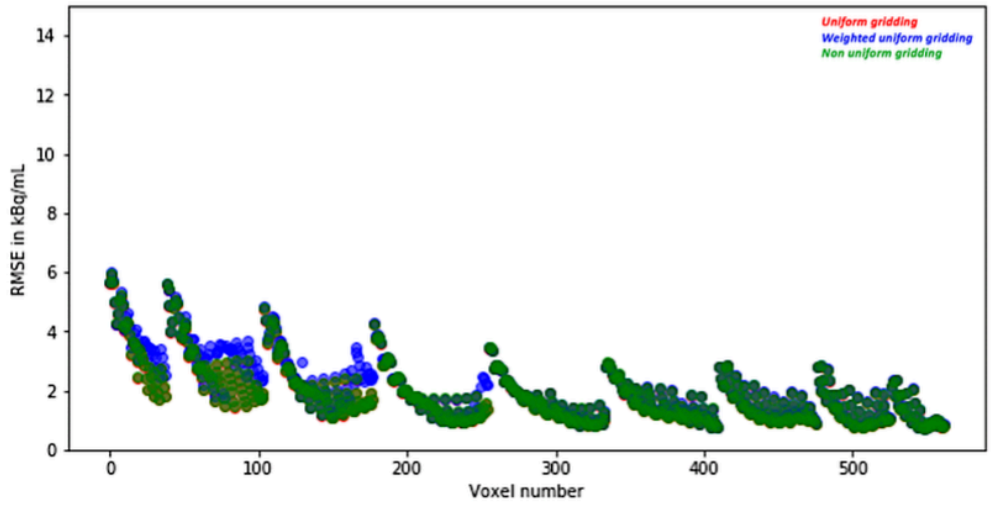

Figure 1.15: Per voxel RMSE of gridding fitting approaches. The x-axis represents the voxel identity number in the tumor. The y-axis represents the related RMSE in kBq/mL.

Figure 1.16 shows the $RMSE$ (equation (1.14) with N the number of voxels) per frame for uniform, uniform weighted and nonuniform gridding approaches. The median $RMSE$ (IQR) for the 41 frames were 0.5 [0.3-1.0] kBq/mL, 0.8 [0.4-1.4] kBq/mL and 0.8 [0.4-1.4] kBq/mL for the uniform, uniform weighted and nonuniform gridding respectively. For comparison, the corresponding results without PET smoothing are provided in the Appendix section A.2 (Figure A. 3).

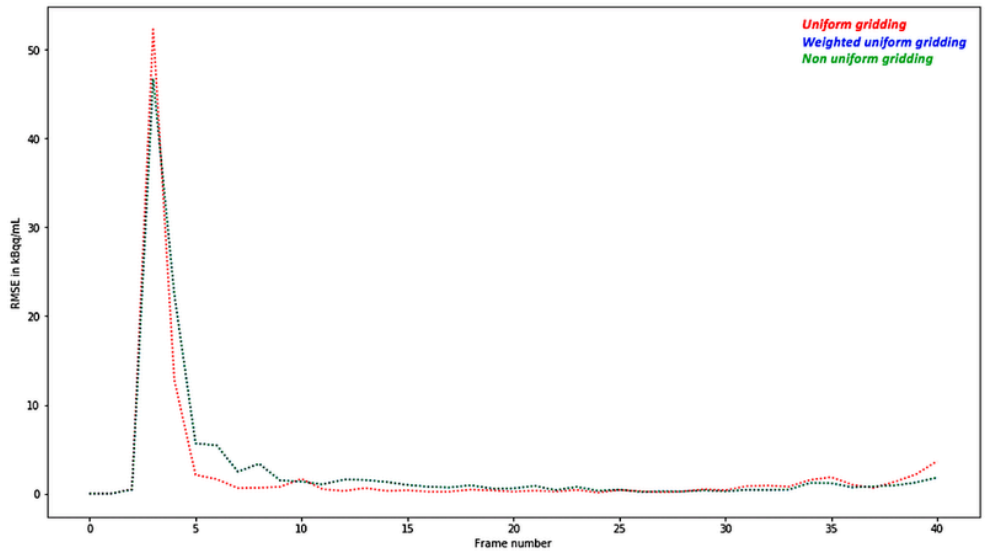

Figure 1.16: Per frame RMSE of gridding fitting approaches. The x-axis represents the identity number of the PET frames. The y-axis represents the related RMSE in kBq/mL.

d) PET kinetic modeling results

Figure 1.17 provides the results of the curve fitting procedure. Uniform and nonuniform gridding provided the same results (as expected with 4000 sampled points). For comparison, the corresponding results without PET smoothing are also provided in the appendix section A.2 (Figure A. 3).

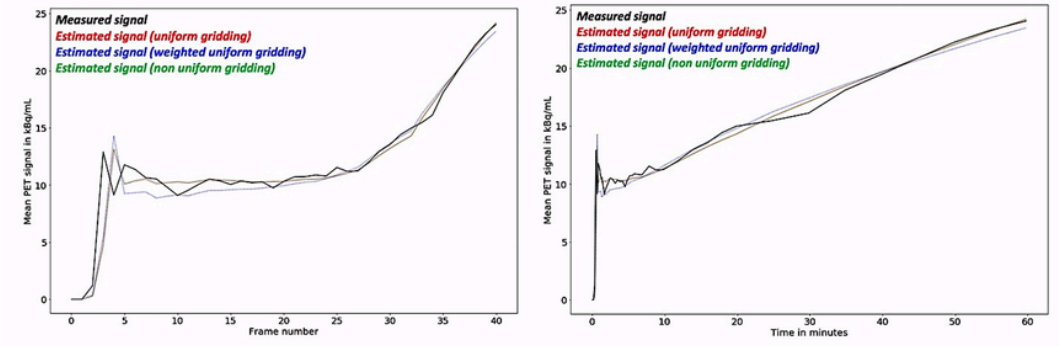

Figure 1.17: Curve fitting results of the PET kinetic modelling. The measured PET signal (in black) is compared to the estimated PET signal calculated with the estimated kinetic parameters (K_1, k_2, k_3, v_b). The results are provided per frame (top) and per minute (bottom).

Figure 1.18 shows the 3D maps for the test patient.

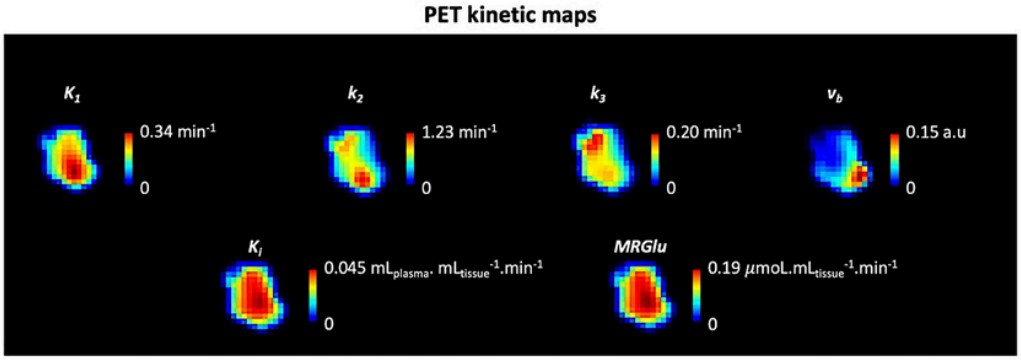

Figure 1.18 Dynamic PET maps (for better display, the 3D kinetic maps were smoothed at 3mm). The vascular (AIF) and tumor TACs were extracted from the denoised 4D PET data, and the K_1, k_2, k_3, and v_b PET kinetic parameters were estimated by fitting the Sokoloff full kinetic model to the measured TACs on a voxel-wise fashion. The estimated parameters were then used to compute K_i and MRGlu parameters, together with the corresponding 3D parametric maps.

Additional illustrations of voxel-wise fitting analyses for all the patients included in the PET kinetic analyses are provided in the Appendix section A.3 (Figure A. 4 and Table A. 1).

1.4.2.3. Conclusion

Our preliminary tests for the implementation of PET kinetic modeling showed that

- A denoising step was required to clean the time-varying activity curves: an 8 mm Gaussian filter was a good trade-off between signal loss and TAC regularization
- Uniform and nonuniform signal sampling provided the same accuracy with 4000 sampled points.
- The noise variability weighted factor did not improve the curve fitting procedure, but increased the computation time.
- The curve fitting procedure was accurate at the voxel level, with low RMSE values for the majority of the voxels.

Based on these experiments, all the PET data were smoothed with a 8 mm Gaussian filter before kinetic maps computation. Also, to be sure not to miss the arterial first pass in the very

early phase of the TACs, we choose to keep a nonuniform gridding approach. Future refinements may be of interest to speed up the procedure with less than 2000 sampled points. Finally, the pipeline was automated to allow the computation of multiple patient kinetic maps at once, and transferred to the parallel calculation platform at the Laboratoire de Mathématiques d'Orsay. To be launched, the automated procedure required for each patient the following input data:

- The 4D ^{18}F-FDG PET denoised data, in NIfTI format
- The tumor and AIF masks in NIfTI format, previously generated semi-automatically (67)
- The glycaemia in mmol/L.

The PET technical challenges were clarified, and we will now discuss the MRI foundations and methodological challenges we encountered.

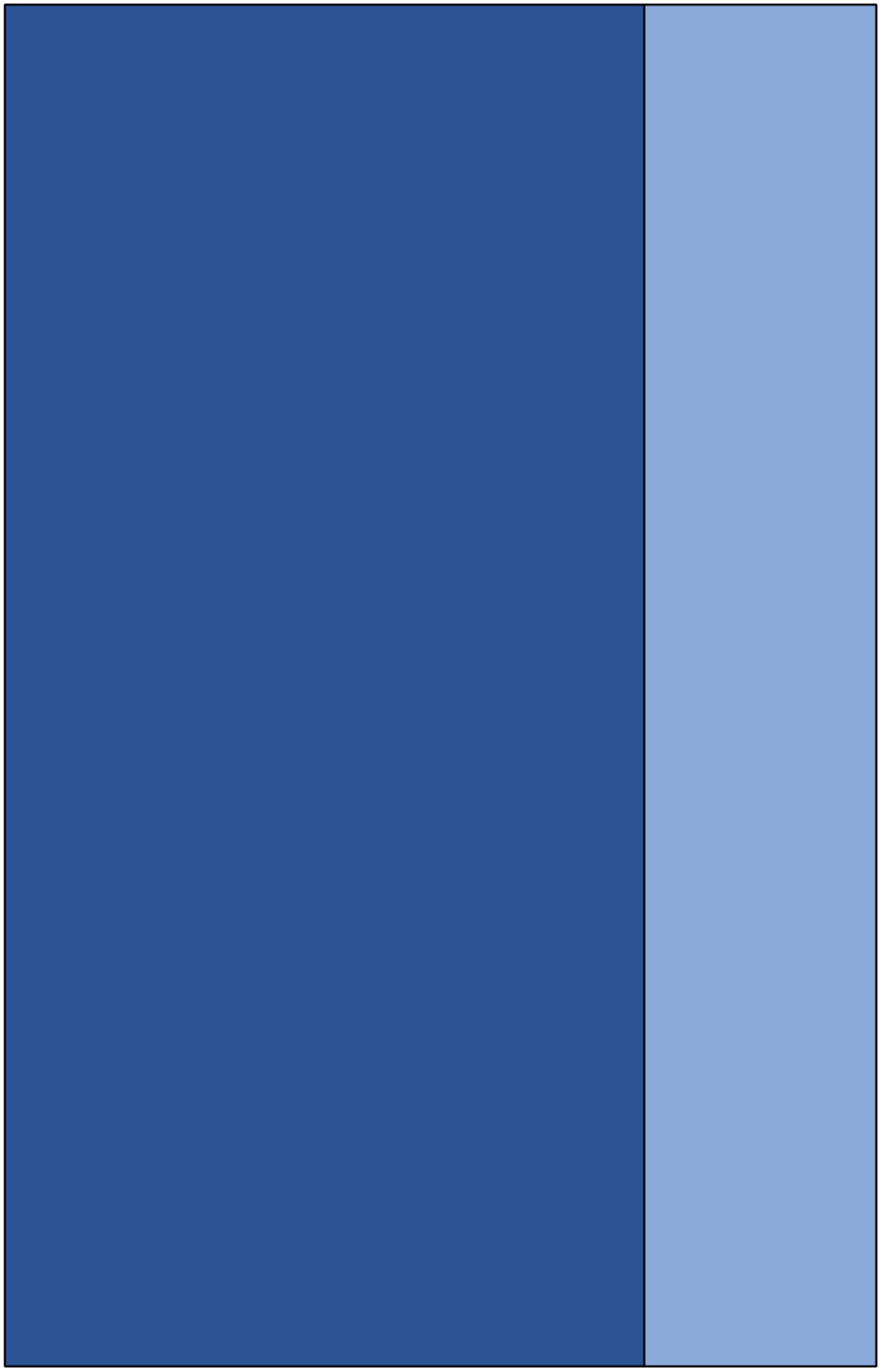

2. MRI imaging: from bases to our purpose challenge

2.1. Physical bases

The phenomenon of nuclear magnetic resonance (NMR) was discovered in 1938 by Isidor Isaac Rabi (Columbia University, New York, USA), who received for its work the Nobel Prize of Physics in 1944 (https://www.nobelprize.org/prizes/physics/1944/rabi/biographical). The first experimental NMR measurements were made by Felix Bloch (Stanford University, USA) and Edward Mills Purcell (Harvard, USA) in 1946, who shared the Nobel Prize for Physics in 1952 (https://www.nobelprize.org/prizes/physics/1952/purcell/biographical). In the 1970s, Paul Lauterbur (University of New York, USA) and Peter Mansfield (University of Nottingham, United Kingdom) applied the NMR principle to imaging and thus defined the beginnings of Magnetic Resonance Imaging (MRI). Their work led to the development of MRI in the 1980s-90s, which earned them the Nobel Prize in Physiology and Medicine in 2003 (https://www.nobelprize.org/prizes/medicine/2003/summary/). MRI could not have been developed without the fundamental scientific works of Joseph Fourier (Signal processing, École Normale, 19th century, Paris, France), Sir Joseph Larmor (Electrodynamics, Cambridge University, 19th century, United Kingdom), and Erwin Hahn (principles of spin echo, 1949, Stanford and UC Berkeley, California, USA).

2.1.1. The phenomenon of Nuclear Magnetic Resonance

Nuclei with unpaired proton/neutron or both have magnetic properties. Table 2.1 summarizes the atoms with magnetic properties occurring in the human body.

Nuclide	Annotation	Natural Abundance	Gyromagnetic ratio (MHz/T)	Relative sensitivity In NMR	I (spin)
Hydrogen-1	^{1}H	99.98%	42.6	1.0	$1/2$
Carbon-13	^{13}C	1.11%	10.7	0.016	$1/2$
Nitrogen-14	^{14}N	99.63%	3.1	0.001	$1/2$
Fluorine-19	^{19}F	100%	40.4	0.83	$1/2$
Sodium-23	^{23}Na	100%	11.3	0.093	$3/2$
Phosphorus-31	^{31}P	100%	17.2	0.066	$1/2$

Table 2.1: Nuclei with magnetic properties in the human body.

The magnetic moment $\vec{\mu}$ of a nuclide is a characteristic derived from quantum physics, which is related to the intrinsic angular momentum (or spin $\vec{I}$) of its moving electric particles by the following equation:

$$\vec{\mu}=\gamma.\vec{I} \quad (2.1)$$

Where γ is the Gyromagnetic ratio. Under natural conditions, the spins of an object have a random orientation, and the overall magnetic resultant of this object is zero. Submitted to an ideally homogeneous magnetic field B_0, the majority of spins will align in the direction $\overrightarrow{B_0}$ by experiencing a torque $\vec{T}$ (Figure 2.1), which is defined as follow

$$\vec{T} = \vec{\mu} \times \overrightarrow{B_0} = \gamma.\vec{I} \times \overrightarrow{B_0} \quad (2.2)$$

Where the angular momentum vector $\vec{I}$ (the spin) precesses around $\overrightarrow{B_0}$ at angular frequency $\omega = \gamma \times B_0$, named the Larmor frequency.

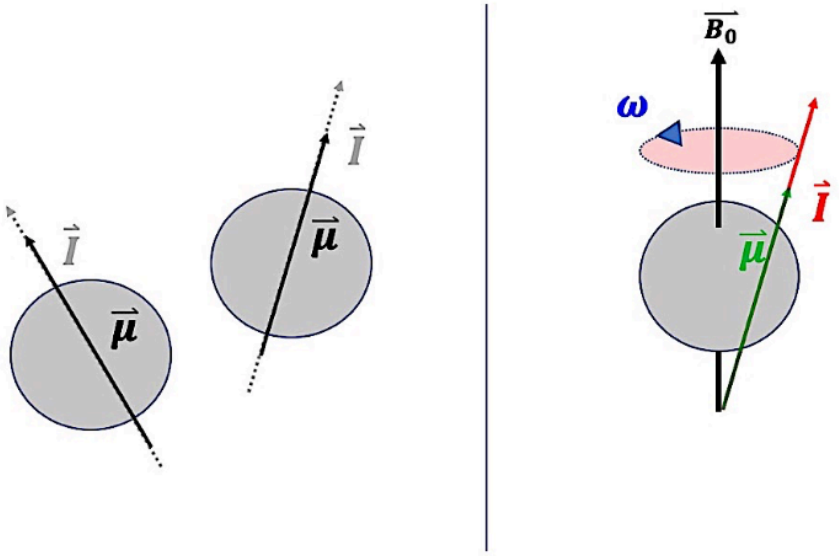

Figure 2.1: The torque principle. $\vec{I}$ is the angular momentum vector (the spin) and $\vec{\mu}$ the magnetic moment of the nuclide. Submitted to a magnetic field B0, the majority of spins align in the direction $\overrightarrow{B_0}$ by experiencing a torque $\vec{T}$, and precess around $\overrightarrow{B_0}$ at larmor frequency ω.

A rotating magnetic radiofrequency (RF) pulse (B_1^+) close to the Larmor frequency, perpendicularly applied to the spins aligned along B_0, tilts them into the transverse plane by energy transfer (NB: the principle of Heisenberg uncertainty does not allow to define individual spin trajectory, but only for a spin population). This interaction corresponds to the resonance phenomenon. The flip phenomenon (angle = α), referred to "excitation", is determined by the envelope, duration and the frequency width of B_1^+). The return to equilibrium, referred to "relaxation", generates an electromagnetic signal named free induction decay (FID) (Figure 2.2).

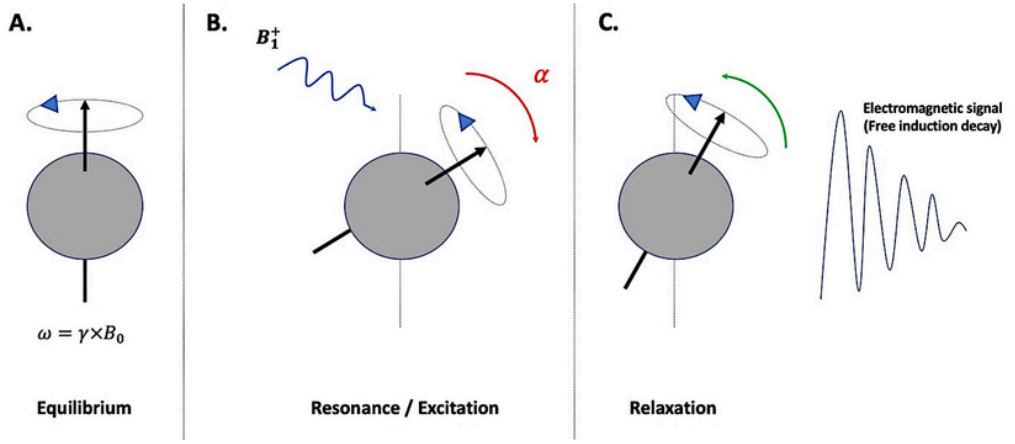

Figure 2.2: the phenomenon of Nuclear Magnetic Resonance (NMR). Under equilibrium, the spins are aligned along B_0. A rotating RF pulse applied to the spins at Larmor frequency tilts them by energy transfer (excitation). The spins return then to equilibrium (relaxation) and generate an electromagnetic signal named free induction decay (FID).

2.1.2. Principles of Nuclear Magnetic Resonance Imaging

MRI consists in applying the NMR principle to an object and spatially encoding the measured signal using magnetic field gradients to generate an image (2D or 3D image). A superconducting solenoidal electromagnet (coil cooled with liquid helium) generates a high intensity permanent static magnetic field (B_0) - typically a 60cm bore 3T on the Signa PET-MRI- which is 60,000 times stronger than the earth magnetic field. Active or passive shielding limits the extension of the magnetic field. In addition, a Faraday cage isolates the device from potential external electromagnetic interactions. In clinical practice, the targeted nucleus is ^{1}H hydrogen, naturally abundant in the human body (γ = 42.576 MHz/T). Submitted to B_0, the spins of the object of interest are aligned and precess at the Larmor frequency. Additional magnetic fields transiently generate gradients of low intensity in the 3 planes of the space (x, y, z) to allow slice selection and spatial encoding of the signal (Figure 2.3).

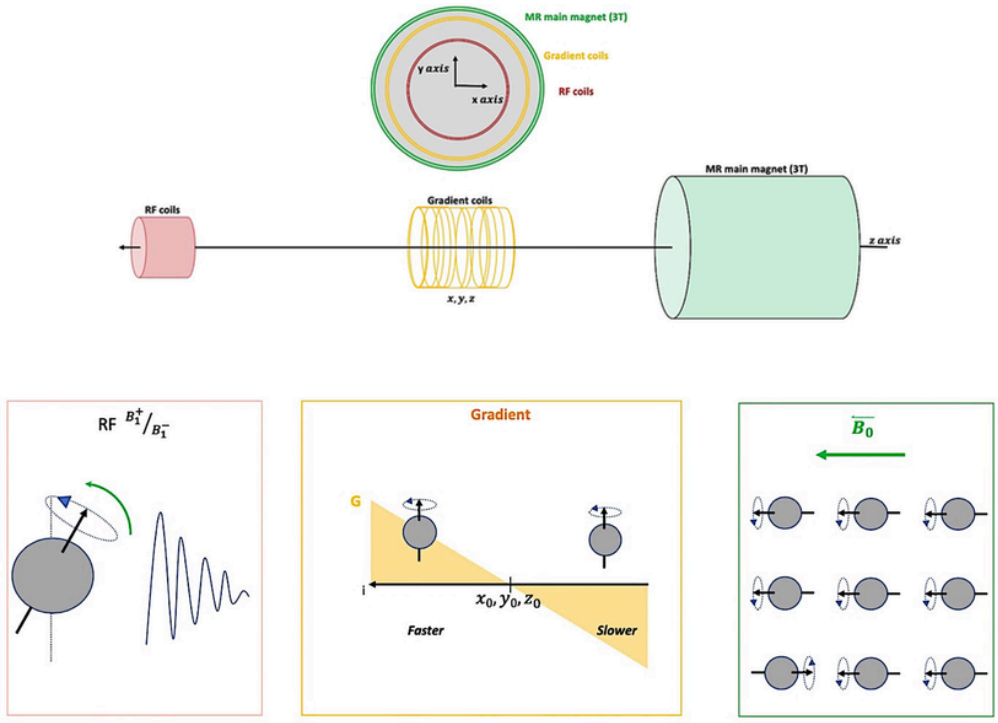

Figure 2.3: MR principles. The spins in the MR magnet are aligned to $\overrightarrow{B_0}$ (green); the RF chain (red) transmits a rotating RF pulse B_1^+ to the spins and receives the electromagnetic signal B_1^- generated by the spin relaxation. The received signal is spatially encoded by using transient magnetic gradient fields (orange).

2.1.2.1. Tissue excitation and signal measurement

Based on the NMR properties, a radiofrequency pulse that matches the Larmor frequency is applied to the object of interest (RF, magnetic field B_1^+) using RF transmitter coils (wire loops). For ^{1}H, and according to equations (2.1) and (2.2), the RF is typically centered at 42.6 MHz/T × 3T = 127.8 MHz on the 3T Signa PET-MRI system. The excited spins are tipped into the transverse plane, inducing transient longitudinal and transverse magnetization vector components that precess at the Larmor frequency. Based on the basic principles of electromagnetism (Faraday's law of induction (68), the transverse magnetization component generates an alternating electrical current in a receiver RF coils (B_1^-), which is frequency-encoded by applying gradient fields. The receiver coil's signal is proportional to the signal amplitude generated by the magnetization in the excited tissue sample. As the precessing ^{1}H nuclei are gradually dephased, the signal induced in the receiving coil decreases and constitute the

"free induction decay". The transmitter and receiver RF coils constitute the RF chain. A calibration of the system at the spin resonance frequency (typically 127.8 MHz at 3T for ^{1}H) is necessary to get an optimized signal. Two receiver RF coils can (ideally) be placed at right angles with a 90° phase difference to increase the signal to noise ratio (SNR) by a factor of $\sqrt{2}$. The signal detected from the net magnetization M, in quadrature, has a complex notation with two channels: a real part (in-phase, I) and an imaginary part (quadrature phase, Q), as illustrates Figure 2.4. To increase the SNR, several pulses-excitations can be performed to obtain several FIDs. The signal collected is therefore an average of the multiple FIDs obtained.

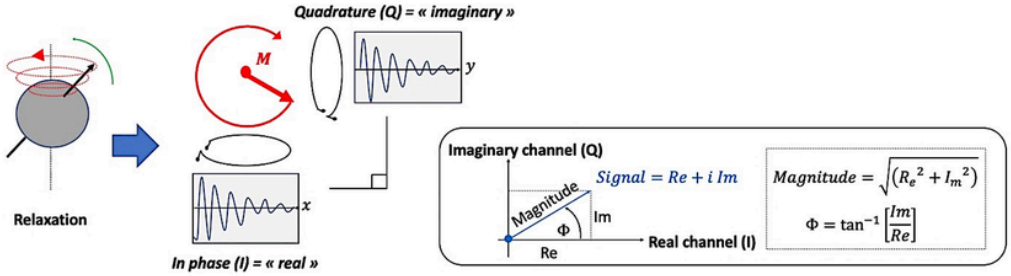

Figure 2.4: Detection in quadrature. The MR signal has real (Re) and imaginary (Im) components. Signal data may be reconstructed as a "real" image, an "imaginary" image, a phase image (Φ) or a Magnitude image (Magnitude). In clinical practice, Magnitude images are used for diagnosis. Phase-images may be used for velocimetry or susceptibility mapping purposes.

2.1.2.2. Magnetization relaxation: T_1 and T_2 relaxation times

After a B_1^+ excitation pulse, the net magnetization vector is flipped by an angle α, then progressively realigns with B_0 (relaxation state). This vector can be separated into two components: a longitudinal magnetization M_z (which is restored with a time constant T1: spin-lattice or T_1 relaxation), and a transverse magnetization M_{xy} (which vanishes with a time constant T2: spin-spin or T_2 relaxation), the latter generating the MR signal (free induction decay) based on the Faraday's law of induction (68). The return of magnetization to equilibrium (M_0) can be formalized by the Bloch equations (69)

$$\frac{dM_x(t)}{dt} = \gamma\left(M_y B_z - M_z B_y\right) - \frac{M_x}{T_2} \quad (2.3)$$

$$\frac{dM_y(t)}{dt} = \gamma\left(M_z B_x - M_x B_z\right) - \frac{M_y}{T_2} \quad (2.4)$$

$$\frac{dM_z(t)}{dt} = \gamma\left(M_x B_y - M_y B_x\right) - \frac{M_z - M_0}{T_1} \quad (2.5)$$

Where $M_{x,y,z}$ are the net magnetization along the x, y and z axis respectively, and $B_{x,y}$ are the B_1^+ magnetic field in the x and y directions. When B_1^+ is turned off ($B_1^+ = 0$), the net magnetization vector realigns with B_0. During this relaxation phase, the longitudinal magnetization M_z recovers as the spinning nuclei release energy, whereas the transverse magnetization M_{xy} decreases because of spinning nuclei dephasing. The Bloch equations are then rewritten as

$$\frac{dM_z(t)}{dt} = \frac{M_0 - M_z(t)}{T_1} \quad (2.6)$$

$$\frac{dM_{xy}(t)}{dt} = -\frac{M_{xy}(t)}{T_2} \quad (2.7)$$

Considering a B_1^+ RF pulse with $\alpha = 90°$, initial $M_{xy} = M_0$ and $M_z = 0$, equations (2.6) and (2.7) yield

$$M_z(t) = M_0\left(1 - e^{\left(-t/T_1\right)}\right) \quad (2.8)$$

$$M_{xy}(t) = M_0 \times e^{\left(-t/T_2\right)} \quad (2.9)$$

T_1 and T_2 relaxation times are the rates of longitudinal magnetization recovery (M_z) and transverse spin dephasing (M_{xy}) respectively. In fact, the spins also experience local field inhomogeneities that accelerate the spin-spin dephasing, defined as T_2^*. T_2 and T_2^* are linked by the following relationship:

$$\frac{1}{T_2^*} = \frac{1}{T_2} + \gamma \Delta B_0 \quad (2.10)$$

Where ΔB_0 is the difference in magnitude of the locally varying field. T_1 and T_2 concepts are summarized in Figure 2.5.

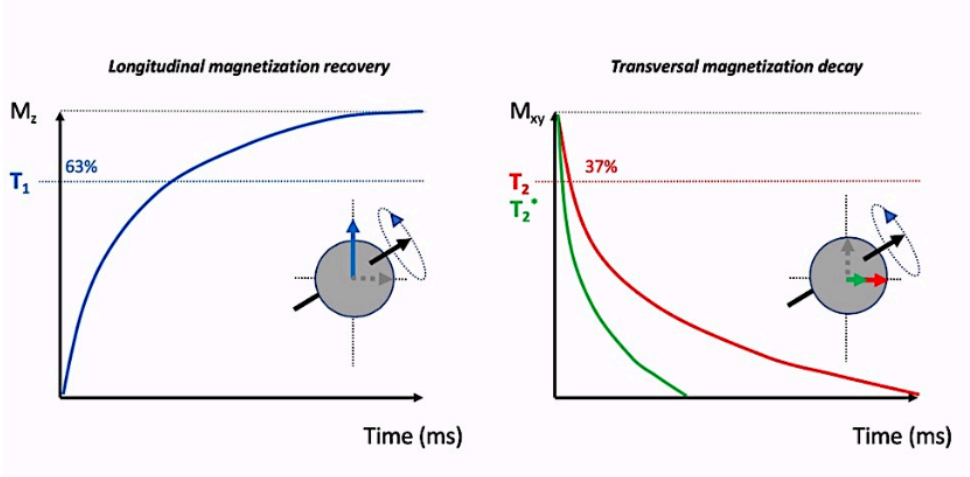

Figure 2.5: T_1 and T_2 magnetization components. At $t = T_1, M_z(t) = M_0\left(1 - \frac{1}{e}\right) \approx 0.63\, M_0$; *At* $t = T_2, M_{xy}(t) = M_0 \times \frac{1}{e} \approx 0.37\, M_0$.

T_1 and T_2 relaxation times are determined by the environment of the ^1H dipoles. Briefly, T_1 is strongly determined by the abundance of macromolecules, because of their energy transfer capabilities. On the other hand, T_2 is driven by the level of water fluidity in the vicinity of macromolecules, on which depends the degree of magnetic field homogeneity. Consequently, T_1 and T_2 relaxation times depend on tissues characteristics. As example, in pure fluids, T_1 and T_2 value are long because

- There a few macromolecules to allow energy transfer (T_1)
- The rapidly moving water molecules generate motional averaging with homogeneous magnetic environment that limits the dephasing of the spins (T_2).

Tissue	Mean T_1 range (ms)	Mean T_2 range (ms)
Gray matter	968-1815	83-109
White matter	750-1735	65-75
Fat	346-450	41-371
Muscle	898-1509	27-44
Myocardium	1116-1341	39-67
Prostate	1400-1700	74-80
Liver	745-809	31-34
Spleen	1232-1328	60-61
Bone marrow	106-586	40-160

Table 2.2: Ranges of T_1 and T_2 mean values in human tissues at 3T (adapted from (71)).

2.1.2.3. Contrast mechanisms

In MRI, differences in T_1 and T_2 weighting create tissue contrasts (T_1-weighted, T_2-weighted or proton density respectively). Those weights are fine-tuned by two key acquisition parameters: the repetition time (TR, in ms) and the echo time (TE, in ms), basically defined as follows: TR is the time between two consecutive B_1^+ excitation pulses, whereas TE is the time between a B_1^+excitation pulse and the signal measurement (72). Because the difference in T_1 relaxation time between two tissues is emphasized at short TRs, T_1-weighted imaging mainly relates to TR fine-tuning. In the same way, because the difference in T_2 relaxation time between two tissues is emphasized at long TEs, T_2-weighted imaging mainly relates to TE fine-tuning. And finally, because image contrast in MR is defined by the balance between both TR and TE parameters, MR images are thus more or less T_1 or T_2 weighted, as illustrated in Table 2.3.

Weighted contrast	TR	TE
T_1-weighted	Short	Short
T_2-weigthed	Long	Long
Proton density	Long	Short

Table 2.3: Image contrast in MRI. Tuning TR and TE parameters make the MR signal more T_1 or T_2-weighted.

2.1.2.4. MR pulse sequences, k-space and Fourier transform

The measured signal is spatially-encoded and converted to imaging data by repeating MR pulse sequences (series of RF pulses, time-varying gradients tuning, and signal-encoding steps). For this purpose, magnetic gradients are switched on and off rapidly along the x, y or z directions to generate transient additional magnetic field that vary linearly along the chosen direction. The precession frequency of ^{1}H dipoles changes linearly with position along the axis of interest, and can be then spatially located along the axis of interest (Figure 2.6).

Let consider the following equations

$$B = B_0 + \vec{G}.\vec{r} \quad (2.11)$$

$$\text{Where } \vec{G} = \begin{bmatrix} G_x \\ G_y \\ G_z \end{bmatrix} \text{ and } \vec{r} = \begin{bmatrix} x \\ y \\ z \end{bmatrix}$$

$$f = \frac{\gamma}{2\pi} \times B \quad (2.12)$$

Given an axis of interest i, combining equations (2.11) and (2.12) yields

$$\Delta fi = \frac{\gamma}{2\pi} \times B = \frac{\gamma}{2\pi} \times (\Delta i \times Gi) \quad (2.13)$$

Where Δi is the distance between two points of interest along i-axis.

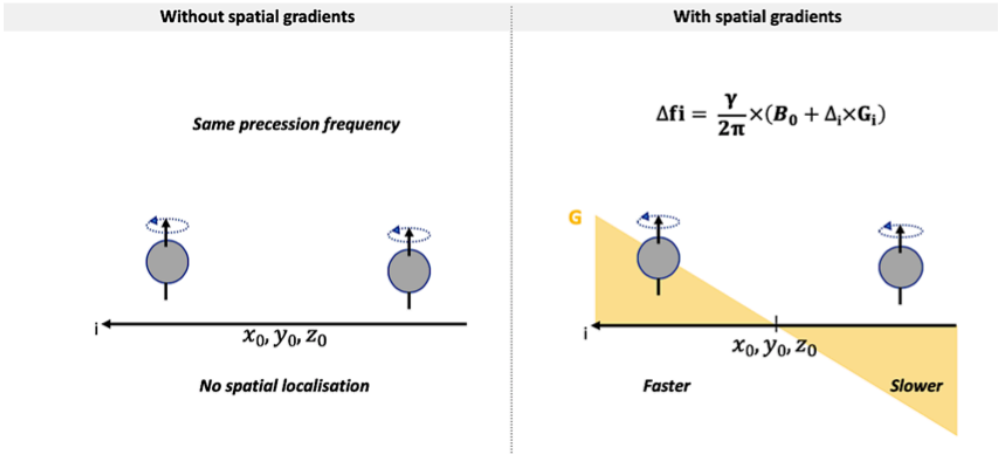

Figure 2.6: Spatial encoding with transient magnetic gradients. Transient magnetic field gradient applied along an axis of interest generates spatial variations in the precession frequency of nuclides.

A targeted slice of tissue is firstly excited by applying a narrow band RF excitation pulse (B_1^+) that matches the precession frequency of the desired location, along with a spatial gradient of interest (x, y or z direction). This selective excitation-thickness can be varied with the gradient amplitude and the bandwidth of B_1^+ as illustrated in Figure 2.7.

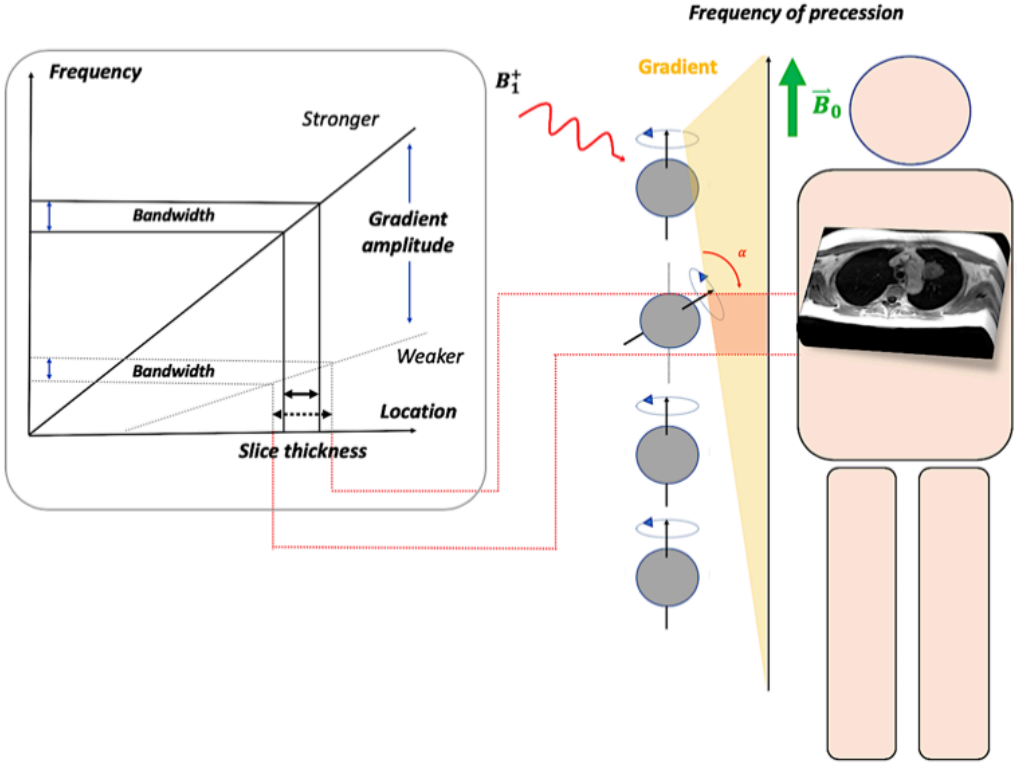

Figure 2.7: Slice selection. A transient spatial magnetic field gradient is applied along an axis of interest, together with an excitation RF pulse that matches the precession frequency of the desired location along the considered axis. Slice thickness may be adjusted by tuning the gradient amplitude or/and the bandwidth of B_1^+.

The complex signal measured in the selected slice is then encoded in a spatial-frequency domain named k-space (73). For this purpose, the two other gradients are turned on and off sequentially to fill the k-space grid along its x- and y- axes. By convention, the nominal echo time (TE) of an MR pulse sequence corresponds to the time at which the k space center (k_x = 0, k_y = 0) is sampled. A general overview of MR pulse sequence is provided in Figure 2.8 A,

and concept of k-space with its main general features are illustrated in Figure 2.8 B and C. Briefly, k-space presents several key properties:

- First, the coordinates of k-space are spatial frequencies that describe features variations into the MR image.
- Second, the MR signal is sampled discretely along the k_x and k_y axis, and the data sample coordinates along each axis are governed by the net strength and duration of the related gradients according to

$$\vec{k}(t) = \int_0^t \gamma . \vec{G}(t') . dt' \quad (2.14)$$

With γ is the gyromagnetic ratio, $\vec{G}$(t) the gradient of magnetic field as a function of time.

- Third, a 180° RF pulse switches the actual (k_x, k_y) coordinates to the opposite (k_x, k_y) coordinates symmetric to the k-space center.
- Fourth, frequencies are hierarchically ordered into k-space. Low spatial frequencies that encode the shape and contrast in the MR image are mapped to the center of k-space, whereas high spatial frequencies (edges and details) are mapped to the periphery of k-space (Figure 2.8 C).
- Fifth, dimensions of k-space and related MR image are interlinked. The extent of k-space coverage along the k_i ($i \in \{x, y, z\}$) axis is inversely proportional to the pixel size Δi along the i-axis in the image domain: $k_{i\ maximum} = {}^{1}/_{2\Delta i}$. Also, the distance between two sampled points along the k_i-axis of the k-space (Δki) is inversely proportional to the field of view (L_i) along the corresponding axis in the image domain: $\Delta ki = {}^{1}/_{L_i}$ (Figure 2.8 C). Because of those interlinks, the Nyquist frequency sampling must be respected to avoid aliasing artefacts in the MR image (74).
- Finally, because a basic MR pulse sequence typically encodes one line of the k-space, the same sequence needs to be repeated with a step-wise increment in the phase encoding gradient to acquire every new line of the k-space (Figure 2.8 A and B, purple, red and green lines).

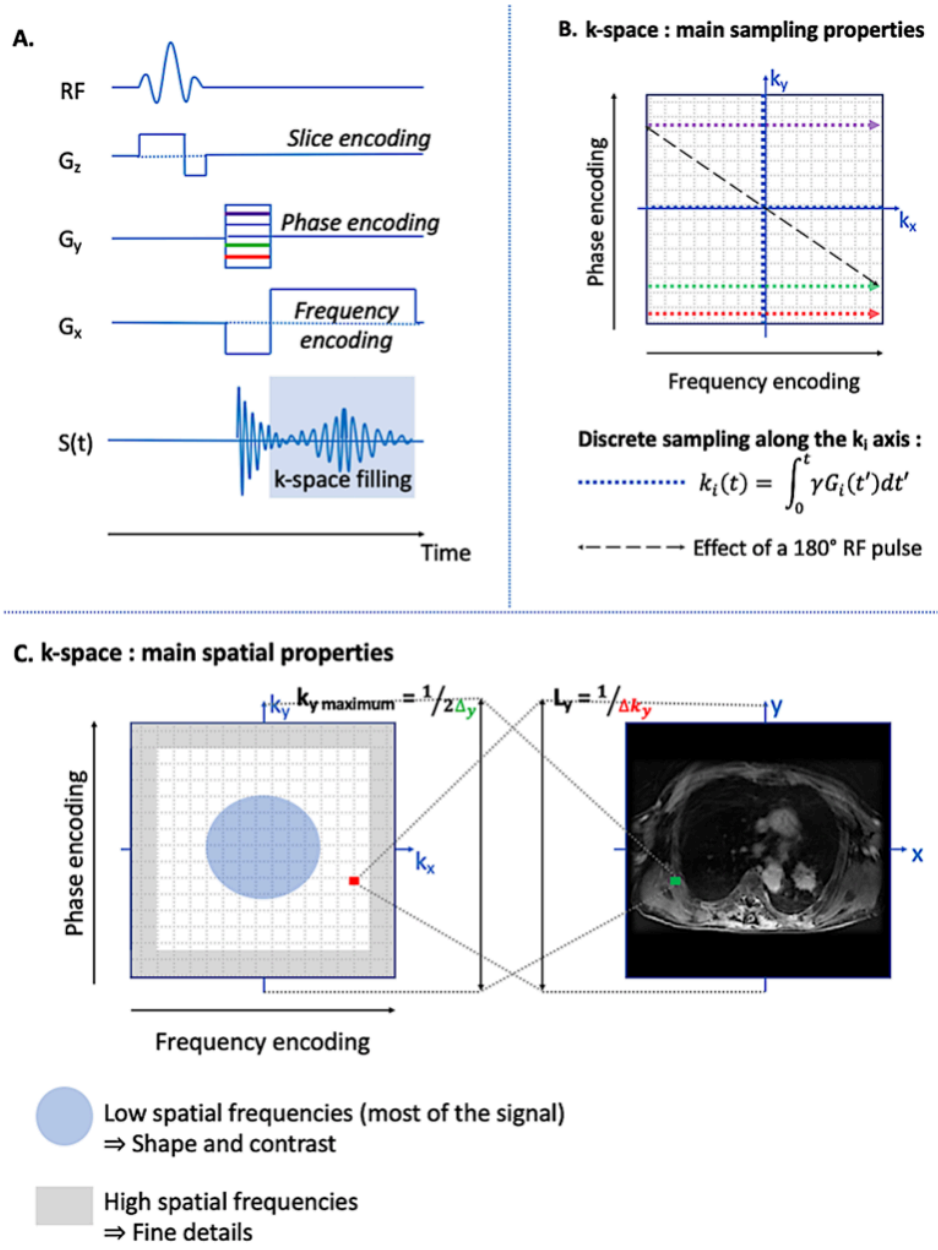

Figure 2.8: Basics of an MR pulse sequence and k-space. A. MR pulse sequence diagram. B. k-space filling properties. C. k-space spatial properties.

Therefore, the total number of MR pulse sequences required to acquire the full k-space is driven by the number of phase-encoding steps, and impact the scan time:

$$Scan\ Time = TR \times NSA \times N_{PE} \quad (2.15)$$

Where TR is the time between two successive RF excitation pulses, NSA is the number of signal averages (also named NEX for number of excitations), and N_{PE} is the number of phase-encode steps. Based on equation (2.15), several tricks can be used to potentially speed-up the scan time, with their respective flaws:

- Reducing the TR requires rapid gradient switching with potential electrical side effects (nerve stimulation) and less signal due to incomplete longitudinal relaxation.
- Reducing N_{PE} by using an accelerator factor R (sub-sampling of the k-space using parallel imaging technics) yields a reduced FOV in the PE direction. The risk of aliasing artefacts (Nyquist frequency is no longer respected) may be minimized by using parallel imaging.

Also, fast k-sampling methods can be used: Partial Fourier sampling exploits Hermitian symmetry property of the k-space, but yields reduced SNR; in echo planar imaging (EPI), all the k-space trajectories can be acquired in one (single shot) or several (multi-shot) acquisitions by using rapid iterative inverted frequency-encoding gradient combined with transient phase-encode steps.

Importantly, the way the frequency and phase encoding gradients are combined defines the pattern of k-space filling (73,75) (Figure 2.9). Cartesian k-space filling (rectangular grid) remains the most widely used in clinical routine, because of the fast and efficient image reconstruction-related algorithms. Non-cartesian k-space filling (radial or spiral) is more computationally intensive and classically requires initial rectilinear gridding before image reconstruction. However, its advantages are a better sampling of the center of the k-space with intrinsic motion correction, a better k-space coverage and higher gradient efficiency.

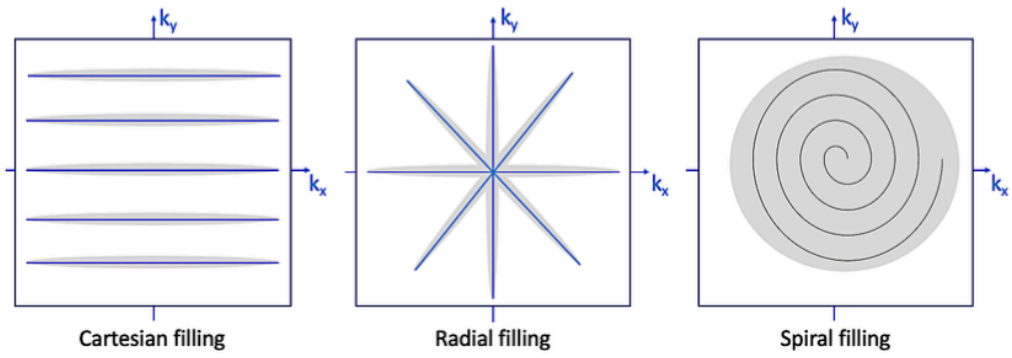

Figure 2.9: Main k-space filling patterns.

Finally, the data acquired in the k-space (frequency domain) are Fourier-transformed (Discrete Fourier Transform, FT) to be reconstructed in several ways: "real", "imaginary", "phase" or "magnitude" images (image domain). In practice, the optimized version of the Discrete Fourier Transform (the fast FT) requires 2^n points to be sampled, reason why k-space axes are typically power of 2 (64, 128, or 256) (*74*). Figure 2.10 illustrates the main principle of FT.

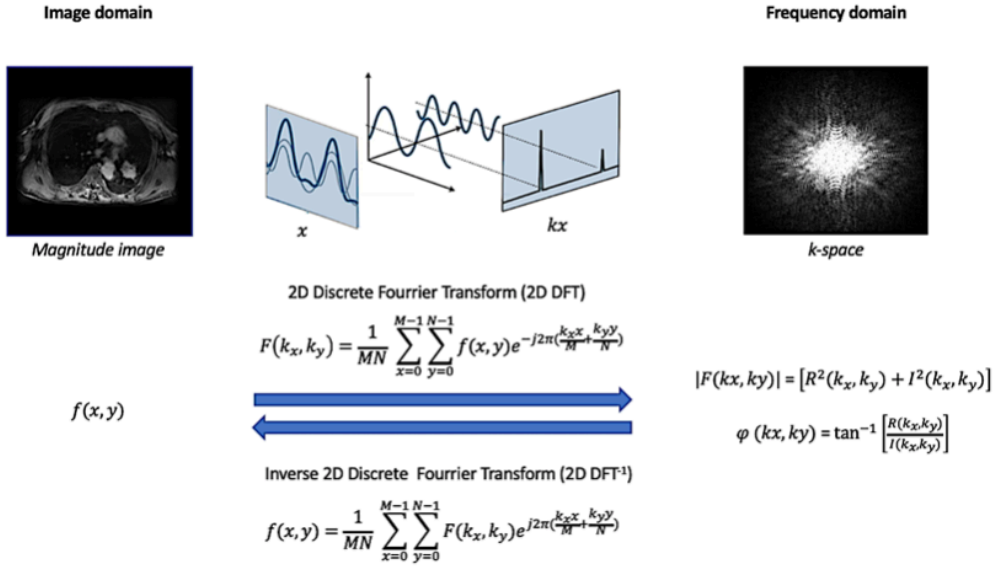

Figure 2.10: Principe of discrete FT. The variables (x,y) represents the imaging data, (k_x,k_y) the frequency data, f(x, y) the magnitude image, $|F(kx,\ ky)|$ the Fourier spectrum (real and imaginary parts), and $\varphi\ (kx,\ ky)$ the phase data.

2.1.2.5. Main MR pulse-sequences

To close this first part, we will just briefly review the two categories of MR pulse sequences (spin echo SE; and gradient echo GRE), from which almost all others are derivatives. As mentioned before, an MR pulse sequence is a combination of RF pulses, gradient variations, and signal-encoding steps. Two-dimensional MR pulse sequences consist in acquiring the signal in a slice, whereas 3D ones concern multiple slices in one acquisition.

A SE pulse sequence is based on the spin echo properties initially demonstrated by Hahn in the 1950s (76), by using RF pulse sequence to restore the transverse magnetization of the precessing ^{1}H nuclei that gradually dephase. The successive application of two RF pulses of any flip angle value α, separated by a delay time of TE/2 generates an echo at TE (the "spin echo"), corresponding to the rephasing of the spins inherently altered during the free induction decay. A classical SE pulse sequence includes a 90° RF pulse followed by a 180° rephasing pulse (Figure 2.11). To speed up the scan time, fast variants of SE have been proposed (fast or turbo SE), consisting in one 90° RF pulse followed by N 180° rephasing pulses (echo train length, ETL) that generate multiple echoes (the echo train) in a reduced acquisition time, proportional to 1/ETL.

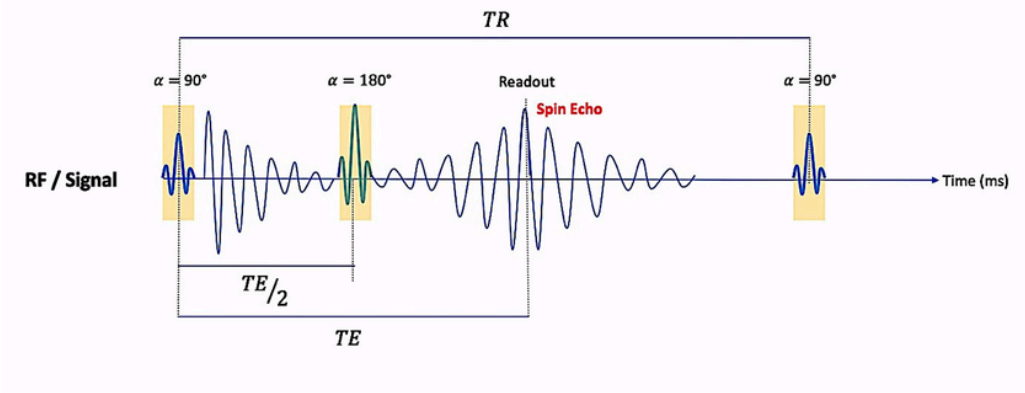

Figure 2.11: General concept of spin echo pulse sequence.

In a GRE pulse sequence, one RF pulse partially flip the spins (flip angle α), and the gradient are used to dephase (negative gradient) and rephase (positive gradient) the transverse magnetization of the precessing ^{1}H nuclei (Figure 2.12) (NB: because gradient pulses do not refo-

cus magnetic field inhomogeneities, GRE sequences are more sensitive to magnetic susceptibility illustrated by local signal loss).

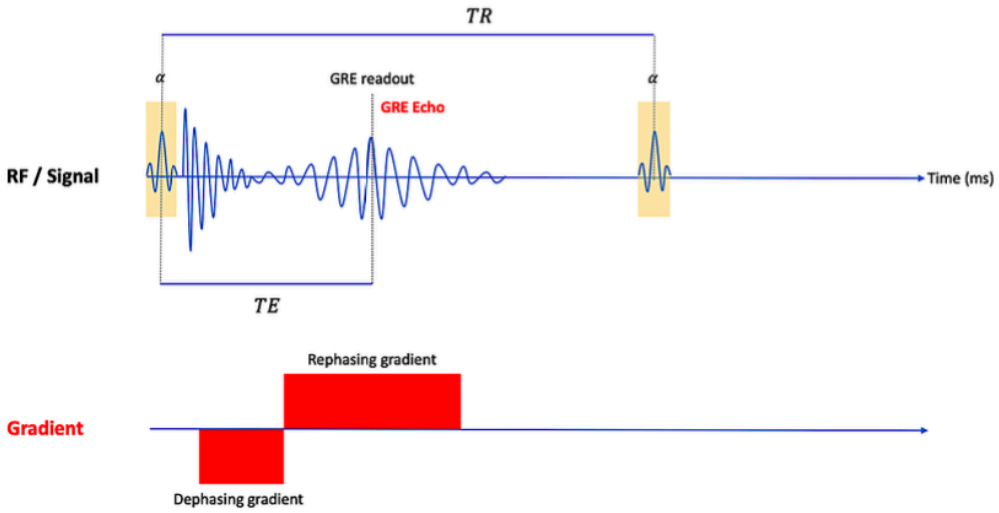

Figure 2.12: General concept of GRE pulse sequence.

Depending on the way to fine-tune the gradients (timing, amplitude and duration), numerous GRE sequences exist and may be classified based on:

- Which of the FID, echo or both is rephased (GRE with FID/Echo/combined FID and echo refocusing)
- Whether cycle-to-cycle transverse coherence is preserved or spoiled (coherent or spoiled GRE sequences).

GRE sequences are fast MRI imaging approaches mainly used for rapid 2D or 3D acquisitions.

2.2. An inherent functional multiparametric imaging

MRI allows a wide variety of imaging contrast, either for structural or functional purposes. In this project, we used diffusion weighted imaging (DWI), but also T_1/T_2 relaxometry and dynamic contrast-enhanced MRI (DCE-MRI) in the same imaging protocol. In this section, I will sum-up the main characteristics of these MRI approaches, and will expose in what the use of these sequences was challenging for this project, with several preliminary tests we performed.

2.2.1. Diffusion Weighted Imaging

2.2.1.1. Main concepts

Because the microscopic diffusion of water molecules is naturally restricted within biological tissues (membranes, organelles, macromolecules, compartments, etc.), its effective measurement is reduced compared to a Brownian free diffusion model. Diffusion-weighted imaging (DWI) consists in measuring the random motion of water molecules within voxels of a tissue of interest. For this purpose, an approach introduced by Stejskal and Tanner in the 1960's (77) consists in combining SE sequence with strong diffusion gradient pulses (DGP of weighting level *b*), symmetrical to the SE 180° rephasing pulse, in x, y, and z directions (isotropic DWI) (Figure 2.13).

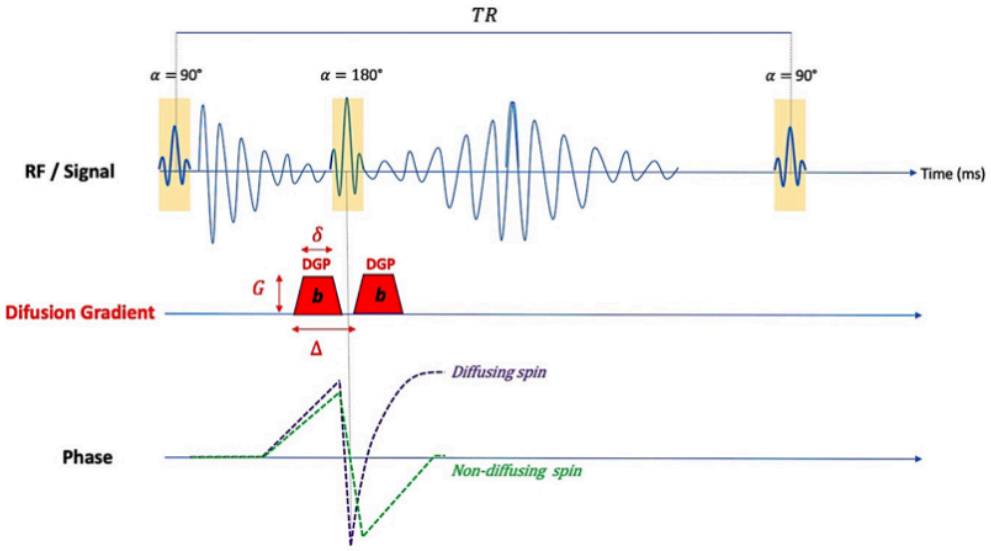

Figure 2.13: Diffusion-weighted pulse sequence. Diffusion gradient pulses (DGPs) are applied symmetrically to the SE 180° refocusing pulse. Non-diffusing molecules being dephased by the first DGP are rephrased by the second DGP. However, diffusing molecules are not perfectly rephased by the second DGP, inducing signal loss.

The value of b (in s/mm^2) depends on several parameters: the amplitude, the width (duration) and the interval of each pair of DGP, as given by

$$b = \gamma^2 G^2 \delta^2 (\Delta - \frac{\delta}{3}) \quad (2.16)$$

With γ the Gyromagnetic ratio, G the Amplitude of the diffusion gradient pulses, δ the duration of the diffusion gradient pulses, and Δ the time interval between the diffusion gradients pulses.

Between the applications of DGPs, water molecules are dephased by the first DGP and rephased by the second DGP. In case of non-diffusing water molecules, the spins are submitted in the same way to the two DGPs, being dephased by the first DGP then rephased by the second DGP. Whereas in case of diffusing water molecules, the spins are no longer submitted in the same way to the second DGP, and will not be rephased. The signal loss related to their imperfect rephasing is related to their degree of diffusivity. The diffusion-weighted images can then be generated from the geometric mean of the signal measured in each of the directions of the space as follows:

$$SI = \sqrt[3]{S_x S_y S_z} \quad (2.17)$$

DWI are purely qualitative images with mixed T_2-weighted / diffusion components. To quantify the diffusion component, the apparent diffusion coefficient (ADC) is calculated by adjusting the DWI signal SI at different b values (typically between 0 and 1500 s/mm^2 in clinical practice) to the Stejskal-Tanner formula (77)

$$S_b = S_0 \times e^{(-b \times ADC)} \quad (2.18)$$

Where S_b is the measured signal intensity on DWI with weighted b value, S_0 is the measured signal intensity on DWI with weighted b value = 0 s/mm^2 (No diffusion gradient), b is the weighted diffusion value, and ADC is the Apparent Diffusion Coefficient.

Conceptually, ADC represents the slope of a mono exponential graph of signal attenuation plotted against increasing b values (typically 2 or 3 in clinical practice), that are typically log-linearized for fitting as illustrated in Figure 2.14 (78). Other approaches out of the scope of this project are based on bi or multi-exponential decays are used for intra voxel incoherent motion (79), require more b values, show high degrees of variability and reproducibility, and are currently used for research purpose only.

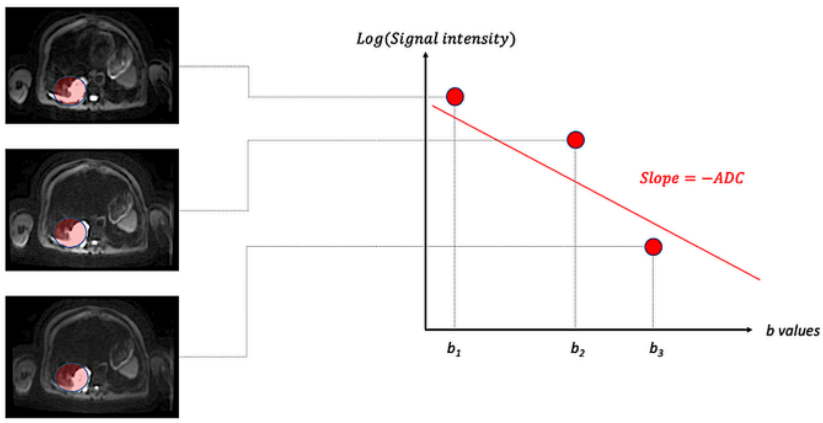

Figure 2.14: Apparent Diffusion Coefficient computation. For each voxel, signal intensity values for two or three b values are log linearized and fitted to an ordinary least squares fitting algorithm. ADC value corresponds to the opposite of the regression slope.

In this project, three b values were used to calculate all the ADC maps: b = 20 s/mm^2, b = 500 s/mm^2, and b = 800 s/mm^2.

2.2.1.2. DWI technical challenges

We had to face two main methodological challenges to implement DWI for the purpose of this project:

- Geometric distortions related to Echo Planar Imaging (EPI)
- ADC maps computation using unified multimodal pipeline.

First, DWI is mainly based on EPI (80), because of its fast k-space sampling properties (one acquisition of a 2D section lasts about 50-100 ms). Although being relatively robust to macroscopic motion, EPI is highly sensitive to B_0 field inhomogeneities due to its inherent k-space filling properties: in EPI, the filling of k-space trajectories relative to the signal evolution is almost instantaneous along the x-direction, but not along the y-direction. Because the occurrence of magnetic field susceptibility artefacts across the image space is related to the speed of filling the k-space, the accumulation of errors (and related geometric distortions) occurs along the phase-encoding direction (73). The phenomenon is illustrated in Figure 2.15.

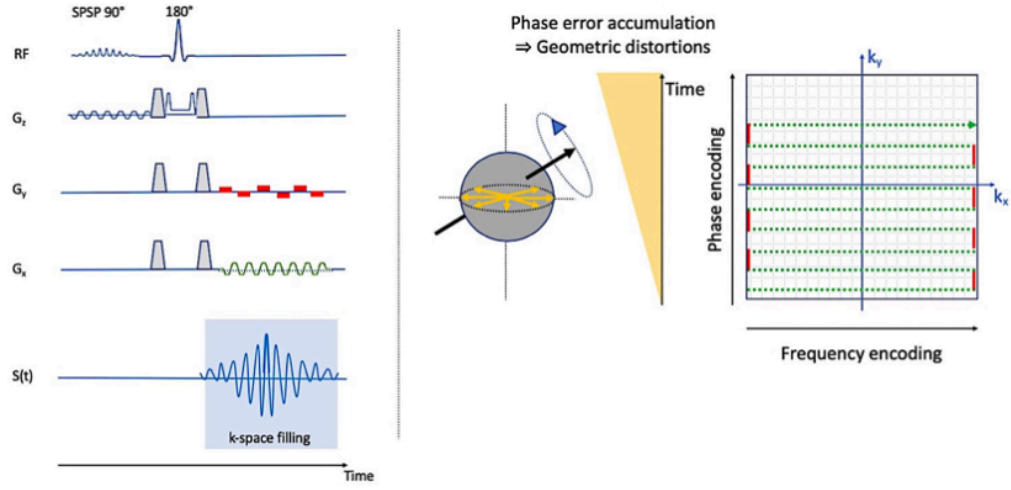

Figure 2.15: DW-SE-EPI and geometric distortions. The filling of k-space is almost instantaneous along the x-direction, but not along the y-direction. The accumulation of errors (and related geometric distortions) occurs along the phase-encoding direction.

In lungs, millions of air-tissue interfaces with different magnetic susceptibility properties (χ) generate local susceptibility gradients with B_0 field inhomogeneities. These off-resonance effects corrupt the local Larmor frequency of the spins along the y-axis of the k-space during EPI acquisitions. This signal mismapping along the y-direction results in spatial shifts/geometric distortions of the corresponding voxels in the reconstructed images after inverse Fourier Transform (Figure 2.16). The spatial shifts observed in DWI data makes any multimodal voxel-wise approach unrealistic. Surprisingly, we found only one study applied to head and neck cancer that addressed specifically this problematic in PET-MRI (81).

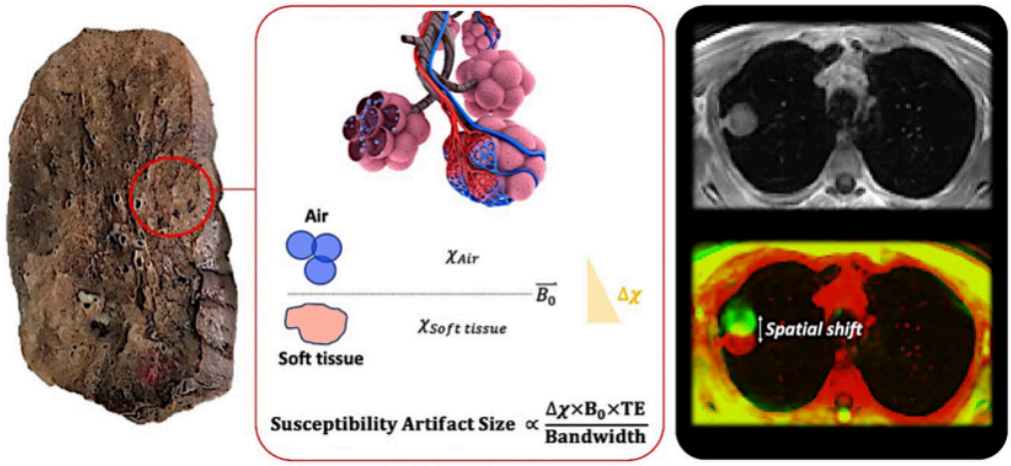

Figure 2.16 Spatial shift in DWI due to EPI sensitivity to B0 field inhomogeneities. The susceptibility gradient at the interface air-soft tissues induces local fields B0 inhomogeneities, corrupting the precession of the spins. For the same tumor, DWI data (green) are spatially shifted compared to the T1-weighted ones (red).

Second, the software that currently propose solutions do not integrate full PET and MRI multimodal computation tasks. As previously explained, I decided to program in-house pipelines to free myself from these constraints, by applying state-of-the-art computation procedures for the majority of the imaging parameters. As the software that currently propose solutions to compute ADC maps are proprietary, computation procedures are not available to users. Furthermore, standardized procedure is currently lacking (82). Therefore, because of its robustness and computational-effectiveness for our voxel-wise purpose, log-linear fitting procedure was used to adjust equation (2.18) to DWI signal data (b values of 20, 500 and

800 s/mm^2), by using Levenberg-Marquardt least-square fitting algorithm. The procedure was implemented in Python environment (libraries numpy, nilearn, nibabel and pandas).

2.2.1.3. Preliminary tests: correction of susceptibility-induced EPI-related distortions

A) Context

Many approaches have been proposed to minimize the distortion effects in EPI.

- Reducing the FOV matrix is a simple efficient method (83,84). However, on PET-MRI system, the MRI FOV is locked in superior/inferior direction by the PET FOV, and cannot be substantially adapted according to the MR acquisitions.
- Multi-shot EPI reduces the distortion by partitioning the filling of the k-space, but remains very sensitive to respiratory movements during the acquisition of the different shots (85).
- B_0 mapping by using the double TE approach (86,87) exploits the phase difference between two images acquired at different TE, which is proportional to the difference in echo times and field inhomogeneities B_0

$$\Delta\Phi = \gamma \Delta TE \times B_0 \quad (2.19)$$

The B_0 map is therefore obtained by dividing the difference of the two-phase images ($\Delta\Phi$) by the difference in TE (ΔTE). A major drawback remains the need of MRI raw data (real and imaginary parts of the signal), which requires to keep complex data.

- The reverse phase encoding method consists in acquiring two EPI acquisitions (weighting b = 0 s/mm^2) in direct and reverse phase encoding directions (*28*). The B_0 field map is thus estimated from the two magnitude images (in phase opposition) by symmetric non-linear registration along the phase-encode direction, and used to generate an undistorted image (29,88).

Because reverse phase encoding is easily implementable on any PET-MRI system, we assessed its feasibility and accuracy for 3T PET-MRI oncology purpose.

B) Phantom experiments

1) Phantom design

To reproduce susceptibility-induced geometric distortions in EPI and evaluate their impact on ADC maps, a dedicated phantom with susceptibility gradients was built (Figure 2.17), made up of:

• One compartment (rectangular plastic box of 2L) filled with water

• Two 50 mL polypropylene centrifugation tubes (Falcon® brand) each containing 50 mL of a pure liquid component with different magnetic susceptibilities (χ, dimensionless) and known diffusion coefficients (ADC):

- Water (H_20) for High Performance Liquid Chromatography, $\chi_{H20} = -9 \times 10^{-6}$, ADC = 2.32×10^{-3} mm^2/s at ambient temperature (HPLC, LC/MS, CAS: 7732-18-5, Manufacturer: J.T. Baker®);
- Acetonitrile (C_2H_3CN), solvent for chemical reactions, $\chi_{C2H3CN} = -28 \times 10^{-6}$, ADC = 3.18×10^{-3} mm^2/s (CAS: 75-05-8, Manufacturer: Carlo Erba®).

The tubes were kept at the bottom of the submerged compartment by means of polyethylene foam bases fixed beforehand (Pattex® gel 100% multi-use, 24h of drying before immersion).

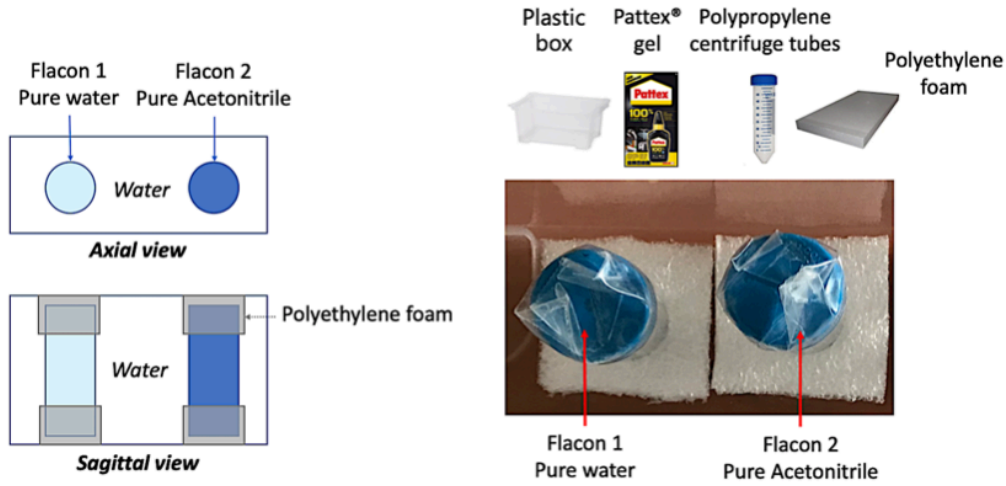

Figure 2.17: Home-made phantom for susceptibility-induced geometric distortions.

2) Phantom acquisitions

Three successive acquisitions were performed on the Signa PET-MR (GE Healthcare, Waukesha, WI, USA) at room temperature (21.8°C) and included the following sequences (thoracic surface coil, suite GEM Coil, GE Healthcare):

- A series of EPI-based SE DWI acquisitions (single echo, 2D axial) in the direct phase encoding direction (TR/TE = 4290/70.9 ms; flip angle = 90°, matrix = 256x256, cutting thickness = 5 mm, bandwidth = 1953.12 Hz, voxel size = 1.64 x 1.64 x 6 mm, values of b in $s.mm^2$ = [0, 20, 500, 800]] $s.mm^2$)
- Two SE acquisitions (b = 0 s/mm^2), in direct and reverse phase encoding directions, with the same acquisition parameters otherwise.
- A high-resolution 3D fast spoiled gradient echo T_1-weighted sequence with inversion recovery (3D IR-FSPGR BRAVO, TR/TE = 8.86/3.72 ms) for spatial image reference (3D-T_1).

Illustration of one phantom acquisition is provided in Figure 2.18.

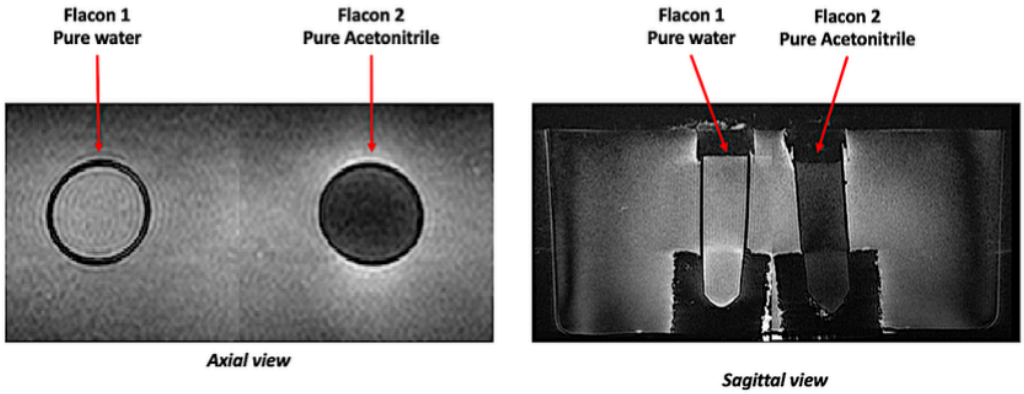

Figure 2.18 : Phantom acquisitions (3D IR-FSPGR BRAVO).

3) Correction of geometric distortions

We used the open access academic software HysCO (Hyperelastic Susceptibility Artifact Correction(89), developed by Lars Ruthotto (Department of Mathematics and Computer Science, Emory University, Atlanta), implemented in the ACID Toolbox for SPM12 (Statistical Parametric Mapping, www.spm.fil.ion.ucl.ac.uk). This software generates an estimate of the B_0 field inhomogeneities from the direct and reverse phase SE images, using nonlinear registration algorithm and fields deformation prior. The B_0 field map estimate is then applied to all the DWI data (b = 20, 500 and 800 s/mm^2) to obtain distortion-corrected DWI (Figure 2.19).

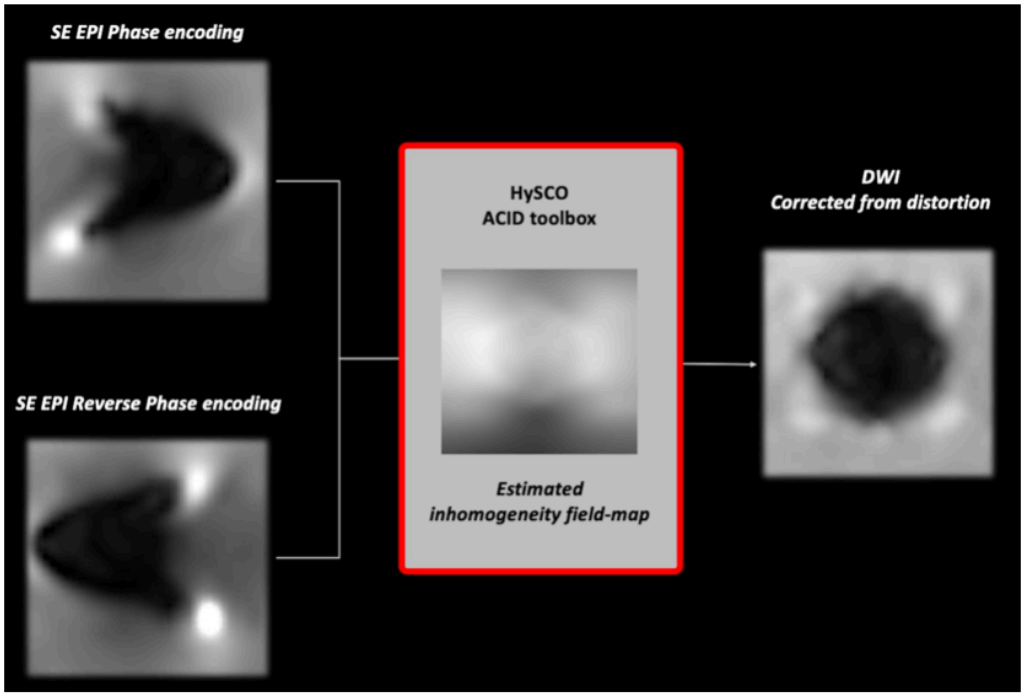

Figure 2.19 HysCO concept. The direct and reverse phase SE images are used to estimate the B_0 field inhomogeneities by using nonlinear registration algorithm and fields deformation prior. Then the B_0 field map estimate may be applied to correct DWI data from distortion.

4) Data processing

Data processing was performed off-line on a standalone personal computer (Intel Core i5, central processing units at 2.7 GHz; 8 GB of random-access memory) using Python (version 3.6; Python Software Foundation, www.python.org) and Matlab (version 2015a; MathWorks, Natick, Mass). First, all the SE data were resampled to the T1-weighted MRI isotropic reference space. For each tube, a morphological mask was semi-automatically generated from the 3D-T1 reference by using the segmentation tool ITK-SNAP (67,90). Then all the DWI data (uncorrected and corrected from distortion) were masked to compute the regional ADC maps within the whole tubes.

5) Statistical analyses

For each tube (H_20 and C_2H_3CN), the voxel-wise percent differences between uncorrected ADC maps (uADC) or distortion-corrected ADC maps (cADC) and the phantom ground truth (ADC_{H20} = 2.32×10^{-3} mm^2/s and ADC_{C2H3CN} = 3.18×10^{-3} mm^2/s) were computed. Two-tailed

paired t-tests were performed between the percent maps to test for significant difference at the voxel level. Also, the RMSE of the ADC measures within the whole tubes (H_20 and C_2H_3CN) were computed for each of the 3 phantom acquisitions as follows:

$$RMSE = \sqrt{\sum_{i=1}^{n} \frac{(\hat{y}_i - y_i)^2}{n}} \quad (2.20)$$

Where $\hat{y}_n$ are the measured values, y_n the ground truth values, n is the number of voxels within the tube (H_2O or C_2H_3CN). All the statistical analyses were performed using Python (version 3.6; Python Software Foundation, www.python.org). All p-values < .05 were considered significant).

6) Results

As illustrated in Figure 2.20, phantom experiments showed that magnetic susceptibility at the water-acetonitrile interface generated major EPI-related geometric distortions in the phase encoding directions: the shape of the tube containing acetonitrile successively showed strong distortion to the right for the left-to-right encoding direction (x-axis phase encoding), and to the left for the right-to-left encoding direction (x-axis reverse phase encoding). Also, the shape of the tube was restored by the reverse phase encoding method.

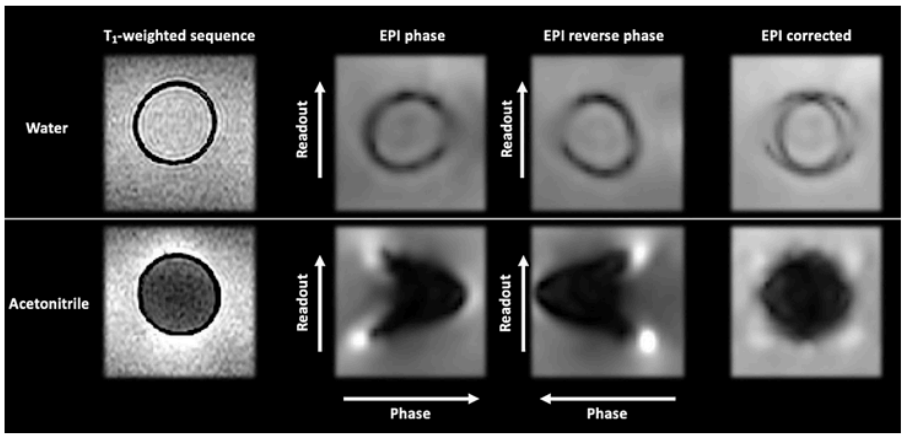

Figure 2.20 Distortions induced by susceptibility gradients in the phase encoding direction at the water/acetonitrile interface (Bottom).

Results of the curve fitting procedure for ADC maps computation are exposed in the Appendix section A.5 (Figure A. 5). Within the water tube, relative errors were 2.4% ± 8.1% for uADC

and 2.0% ± 8.3% for cADC (difference between the uADC and cADC maps = -0.32% ± 3.9%). Within the whole acetonitrile tube, relative errors were -25.4% ± 17.8% for uADC and -23.6% ± 17.6% for cADC (difference between the uADC and cADC maps = 7.2% ± 38.6%). Also, voxels exceeding 20% error threshold within the whole tube were reduced from 60.1% to 48.9% after correcting the distortion. The results are summarized in Figure 2.21.

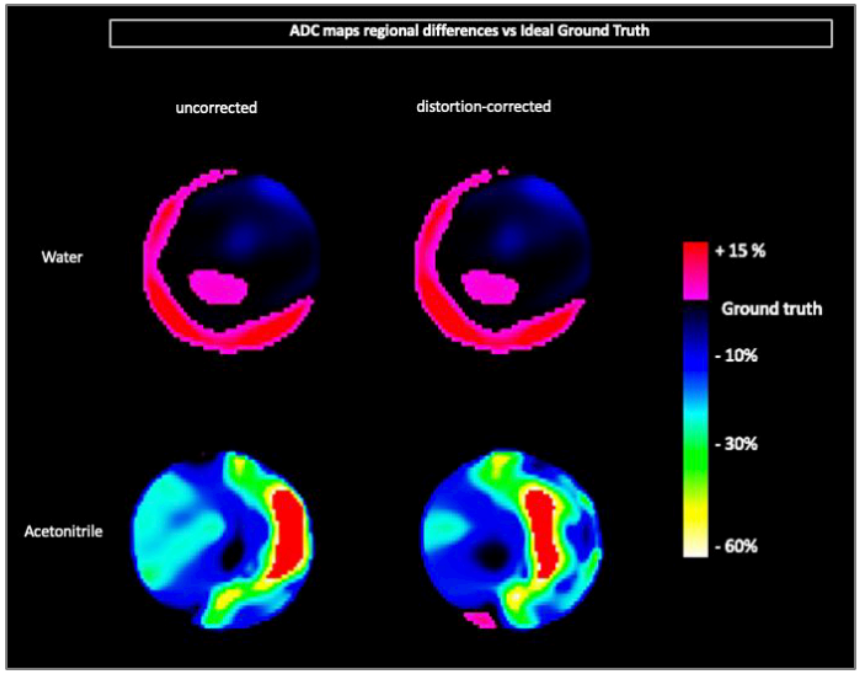

Figure 2.21: the ADC regional percent differences maps (mean of the 3 phantom experiments) against the related ideal ground truth (pure water: 2.3x10-3 mm2/s; pure acetonitrile: 3.18x10-3 mm2/s). For water, correcting the distortions did not modify the regional ADC values, whereas the extent of acetonitrile regional errors was consistently reduced in the distorted area.

When considering a targeted distorted region in the acetonitrile tube (Figure 2.22), the same spherical mask matched perfectly between the 3D-T1 and EPI-corrected images but appeared outside the uncorrected EPI data. Within this particular area, relative errors were -25% ± 10.6% for uADC and -18.4% ± 12.6% for cADC (difference between the uADC and cADC maps = 8.7% ± 9%). Voxels exceeding 20% error threshold were reduced from 85.3% to 31.4% after correcting the distortion. Also, cADC values within this area were statistically closer to the ground truth ($t = -114.64$, $p < .001$), and the RMSE of ADC values was reduced (Figure 2.23).

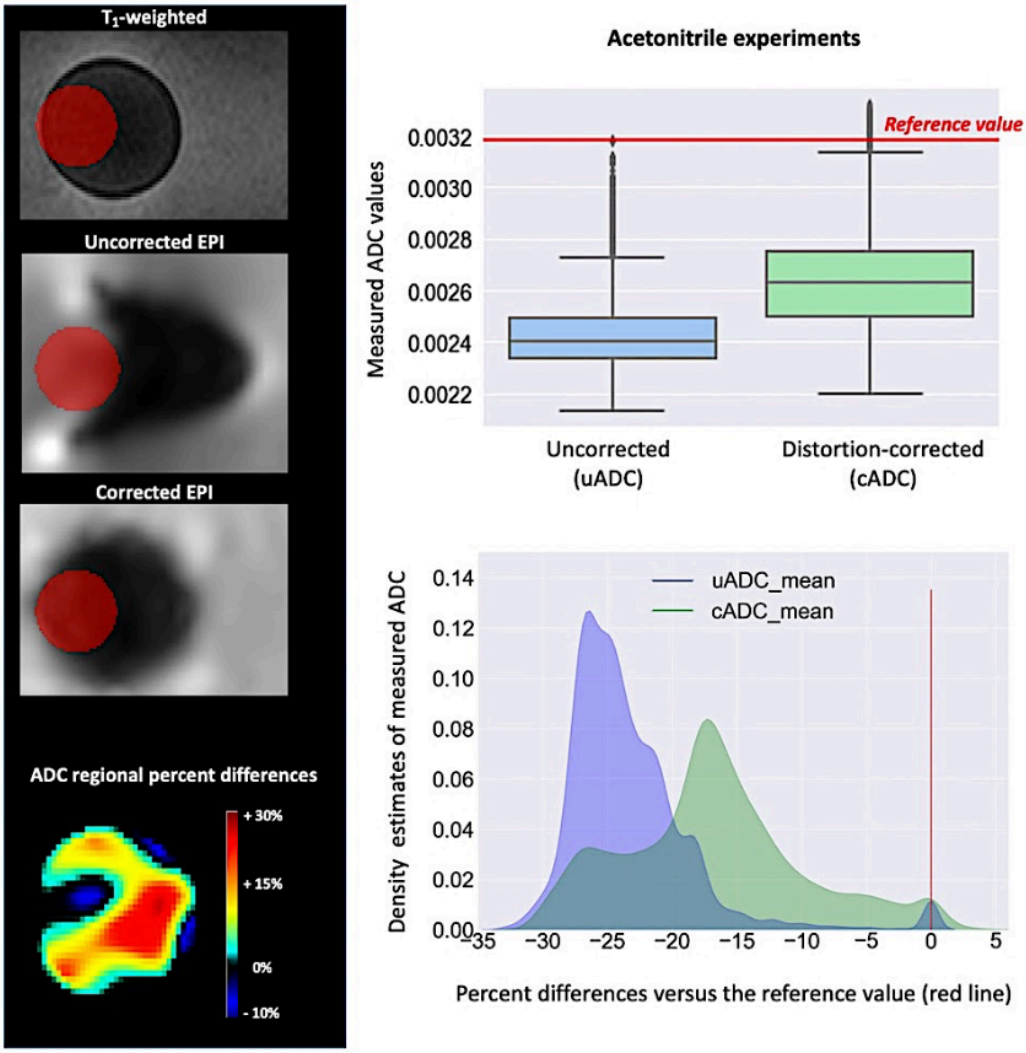

Figure 2.22: Left panel: The mask (red sphere) generated on the 3D-T1 reference image appears clearly outside the tube on the uncorrected EPI image, whereas its position perfectly matches the corrected EPI image. The corresponding ADC values are modified up to 30% when correcting the geometric distortions. Right panel: the ground truth is represented by a solid red line. The ADC corrected for distortions (cADC) were still biased but significantly closer to the ground truth both in terms of values (top) and distribution (bottom).

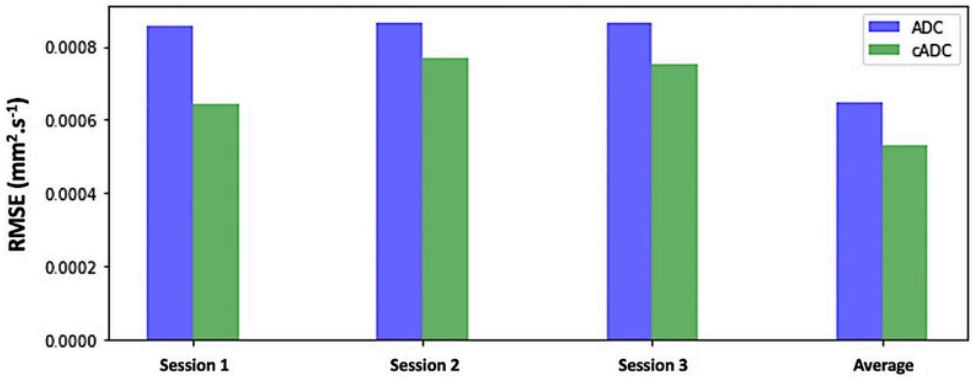

Figure 2.23: RMSE of acetonitrile ADC values uncorrected and corrected from distortion. The values of each phantom session and the session average are computed specifically in the distorted area.

7) Validation on real clinical data

✶ *Patients data and image post-processing*

The reverse phase encoding correction method was applied on 12 consecutive patients (the main lesions characteristics are provided in section 3.1.5, Table 3.2). The workflow dedicated to distortion correction is summarized in Figure 2.24. The DWI data were warped to the corresponding 3D T1-weighted MRI resampled to 2 mm^3 isotropic using the Advanced Normalization Tools (ANTs), a state-of-the-art medical image registration toolkit (91).

The quality of the coregistration between DWI (non-warped and warped) and 3D-T1 clinical data was assessed both visually and quantitatively by computing the normalized mutual information metric of the lesion data as follows (92):

$$I(X;Y) = \sum_{x\epsilon X, y\epsilon Y} p(x,y) log\left(\frac{p(x,y)}{p(x)p(y)}\right) \quad (2.21)$$

where X and Y are the two images of interest, x and y their related voxels intensity values, $p(x)$ and $p(y)$ are the marginal probabilities of x, y and $p(x,y)$ their joint probability. As for the Phantom study, the image post processing was performed off-line on a standalone personal computer (Intel Core i5, central processing units at 2.7 GHz; 8 GB of random-access memory) using Python (version 3.6; Python Software Foundation, www.python.org).

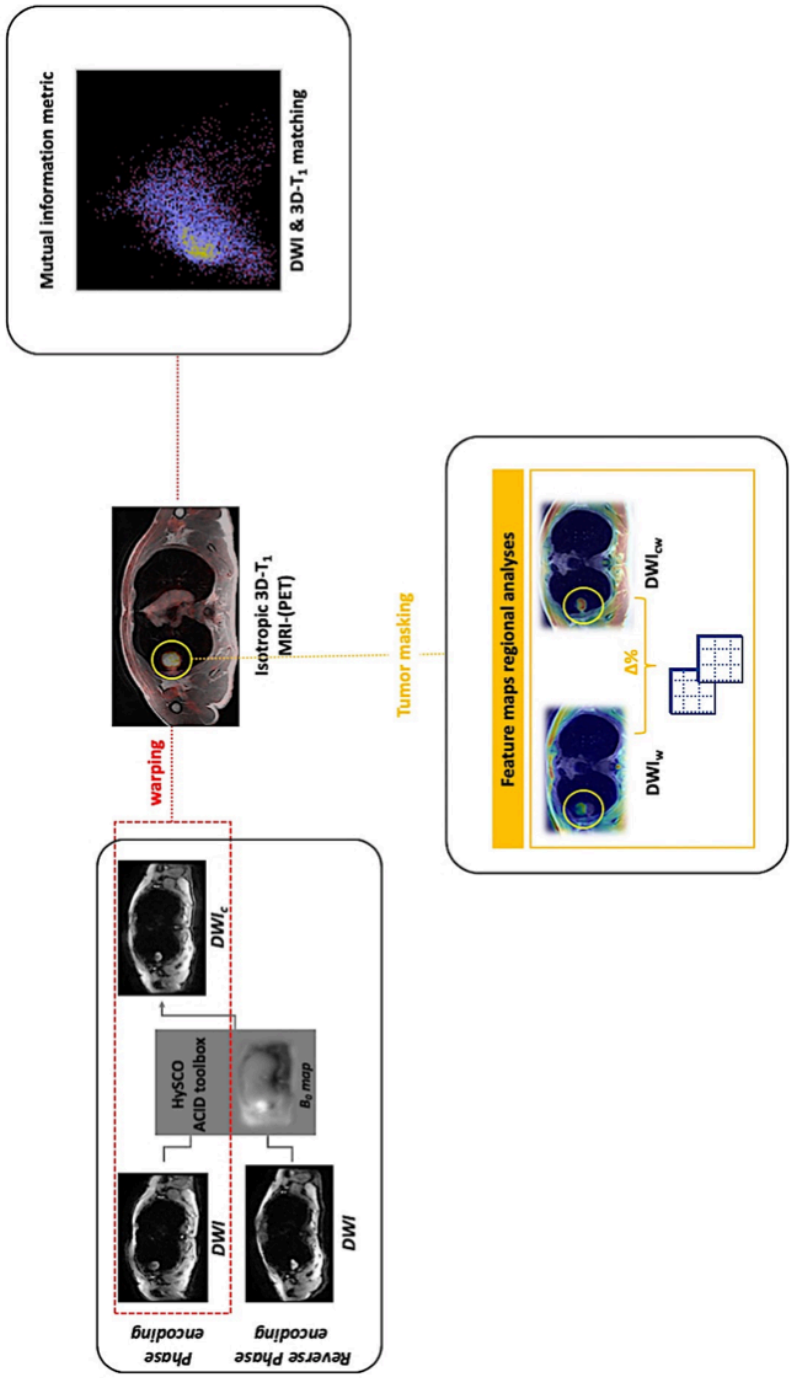

Figure 2.24: workflow dedicated to DWI distortion correction. DWI data were corrected for geometric distortions and warped to their corresponding isotropic 3D-T1 volume (2mm^3). The quality of the co-registration between the corrected DWI data and their 3D-T1 was assessed by mutual information. ADC maps were then computed from masked DWI data for voxel-wise tumor regional analyses.

✶ *Results*

As shown in Table 2.4, the warping procedure improved the mutual information metric between the EPI and the 3D-T1 images from 0.3 to 17% for 10 of the 12 lesions. Performing the distortion correction before warping further improved coregistration for all the data (relative gain = 0.4% to 44%).

Patient	Mutual information metric using 3D-T_1 image as the reference					
	Raw data	Warped data				
	EPI	EPI warped	Δ% (vs EPI)	EPI corrected for distortion and warped	Δ% (vs EPI)	Δ% (vs EPI warped)
1	0.618	0.470	-31.5	0.529	-16.8	+11.2
2	0.816	0.986	+17.2	0.99	+17.6	+0.4
5	0.414	0.426	+2.8	0.491	+15.7	+13.2
6	0.725	0.793	+8.6	0.827	+12.3	+4.1
7	0.289	0.290	+0.3	0.298	+3.1	+2.7
8	0.369	0.397	+7.1	0.423	+12.8	+6.2
9	0.342	0.414	+17.4	0.545	+37.3	+24
10	0.709	0.747	+5.1	0.829	+14.5	+9.9
11	0.498	0.424	-17.5	0.757	+34.2	+44
12	0.447	0.524	+14.7	0.490	+8.8	+7
13	0.382	0.445	+14.2	0.469	+18.6	+5.1
14	0.357	0.396	+9.9	0.428	+16.6	+7.5

Table 2.4: Mutual information metric values using 3D-T1 as the reference volume. DWI data were resampled to 2-mm3 isotropic voxel resolution for the metric computation.

Clinical illustrations of EPI-related distortion effects in the phase-encoding direction are provided in Figure 2.25 (A). The lesion of interest (right upper lobe) appears distorted in the phase-encoding direction from the reference red dotted line, which is centered on the lesion on the corrected image. The inhomogeneity field maps for all patients generated from the forward and reverse phase-encoding polarity EPI acquisitions are also provided (B). In all participants, the targeted lung lesions were impacted, as illustrated by the high magnitude of B_0 inhomogeneity in the lesion areas (red circle).

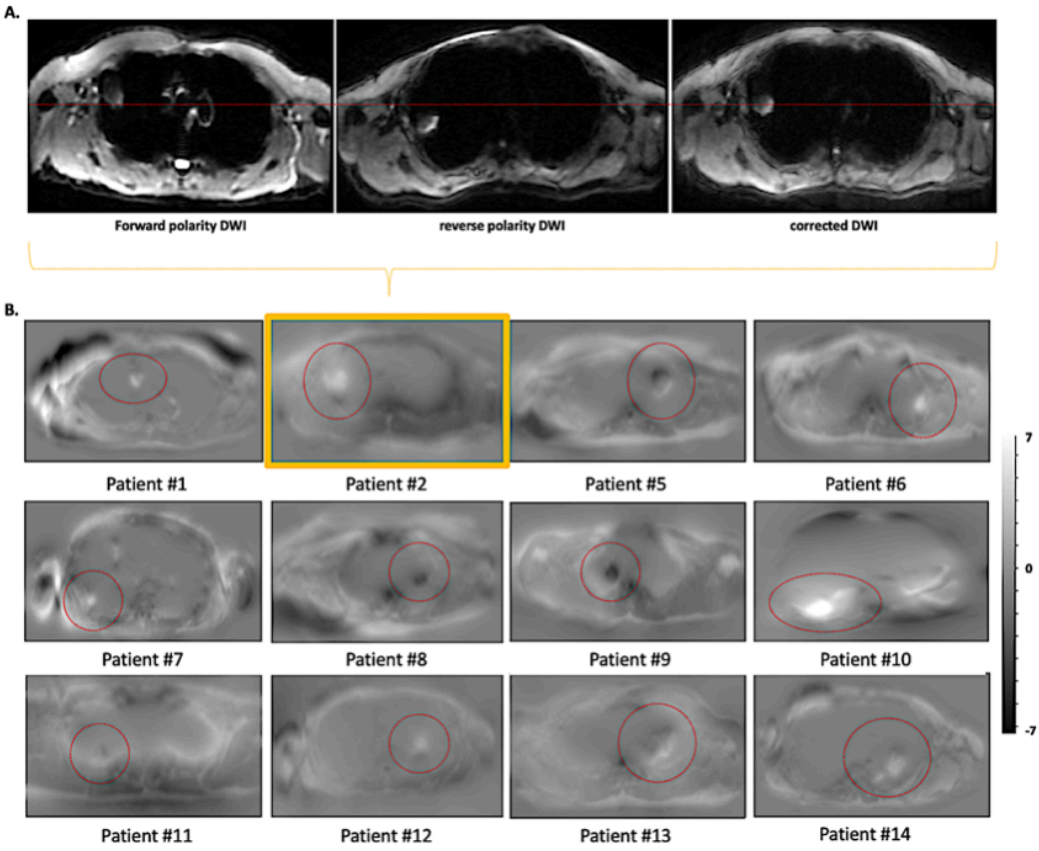

Figure 2.25: EPI-related distortion on 3T PET-MRI. A: example of forward- and reverse-polarity EPI acquisitions, with increased distortion in the phase-encoding y-axis direction (i.e., the vertical axis). The exact lesion position (centered by a red line) is provided on the corrected DWI. B: estimated inhomogeneity-field maps of all thoracic acquisitions (lesions are tagged with red circles). The maps were z-scored for standardization and the normalized grayscale coding for magnitude of inhomogeneities was set to ± 7 standard deviations from the mean.

As shown on Figure 2.26, substantial lesion mismatches between uncorrected EPI and 3D-T1 images were observed, whereas the corrected EPI images appeared less distorted and matched the 3D-T1 images correctly.

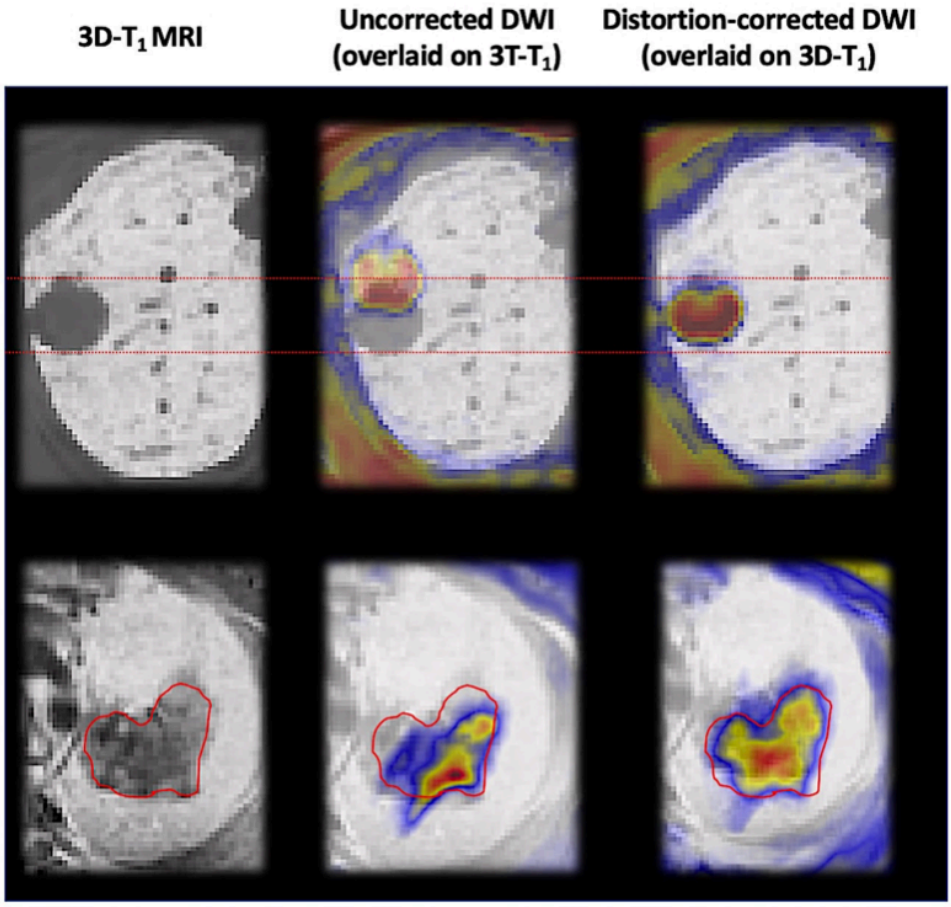

Figure 2.26: Two illustrative examples of matching improvement between DWI and 3D-T1 PET-MRI data after distortion correction (Top. Patient 2; Bottom. Patient 13). In the two cases, the data were not warped to clearly illustrate the specific distortion-correction effect.

The uncorrected and the distortion corrected DWI data were finally semi-automatically masked using ITK-SNAP (90) to compute ADC maps. As expected, the distortion correction impacted the ADC results generated from the DWI images, as illustrated in Figure 2.27. The mean ADC values computed from the uncorrected and corrected DWI data were different (t values ranged from -27.3 to 38.9, $p < .001$). At the voxel regional level, the percent-map differences ranged from -100% to more than +150% depending on the lesion.

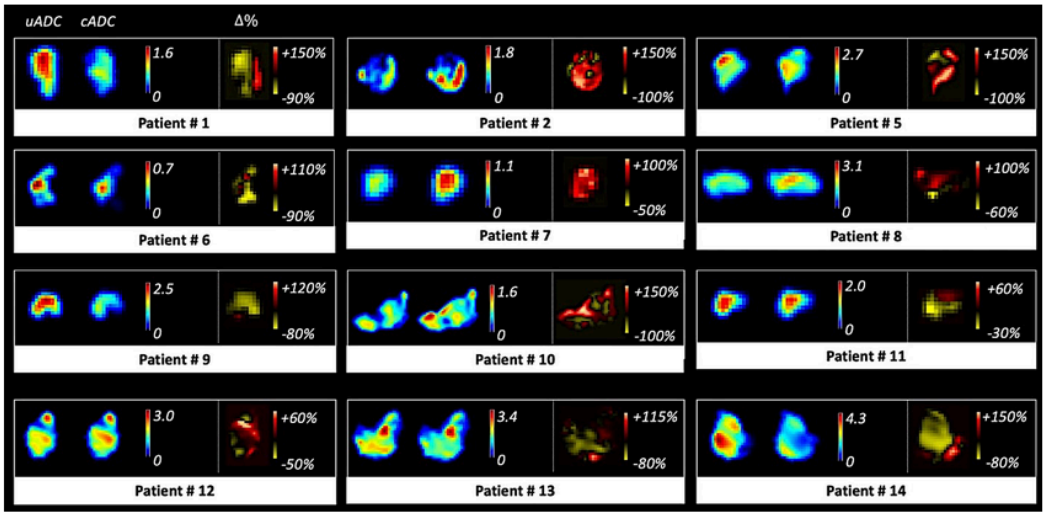

Figure 2.27: ADC maps computed from the uncorrected EPI data (first column, uncorrected ADC) and corrected EPI data (middle column, Distortion-corrected ADC), and the voxel-wise relative percent difference maps (last column). All the maps are provided in axial view, with 4-mm FWHM Gaussian smoothing. ADC are expressed in 10-3mm^2.s^{-1}.

2.2.1.4. Conclusion

To summarize this methodological subpart, we assessed the effectiveness of reverse phase encoding in correcting DWI geometric distortion for multimodal thoracic PET-MRI voxel-wise analyses. Basically, the signal lost in areas of B_0 inhomogeneities prevents the complete recovery of true ADC values. However, returning distorted signal to its proper location should partially improve the regional ADC values.

Based on our experiments,

- The correction of distortion by reverse-phase encoding on diffusion-weighted 3T PET-MRI showed that correcting the distortion improved the apparent diffusion coefficient (ADC) by reducing the mean error against the ground truth from -25% to -18.4%, ($p < .001$) and reducing the number of voxels with more than 20% error from 85% to 31%.
- The regional difference between corrected and uncorrected ADC maps of lung tumors ranged from -100% to more than +150%.

- For all lung tumors, the coregistration of multimodal PET-MRI data was improved from 0.4 to 44%, and voxel-wise r_s values between ADC and standardized uptake value revealed null or weak monotonic relationships (mean r_s of 0.016 ± 0.24). This work was recently published and validate the use of reverse-phase encoding to correct distortions in diffusion-weighted imaging of lung tumors in 3T PET-MRI (93).

2.2.2. Relaxometry

Unlike conventional MRI, which remains qualitative (images are more or less T_1- or T_2-weighted), relaxometry is a quantitative imaging method based on tissue nuclear magnetic resonance properties. MR relaxometry consists in measuring the T_1, T_2 or T_2* relaxation times (in ms) of tissues using adapted MR sequences. Current fields of application in medicine are dominated by neurology (inflammatory diseases such as multiple sclerosis, neuro-oncology), cardiology (tissue characterization of myocardiopathies, amyloidosis) and osteo-articular (study of cartilage). In oncology, Damadian firstly proposed in 1974 the use of NMR relaxometry to characterize tumors (94). Fifty years later, only few tumors subtypes have been explored by MR relaxometry (95–99). The wide variability in imaging protocols and T_1/T_2 relaxation values makes this MR quantitative method still highly challenging in clinical routine, and only range of magnitude in T_1/T_2 relaxation times of several tissue structures are currently defined (70,71), with significant overlaps.

Anyway, combining T_1/T_2 relaxometry to other quantitative imaging parameters could be of interest to characterize the tumors, reason why we decided to implement this approach in our multimodal PET-MRI research work applied to lung cancer.

2.2.2.1. T_1 relaxometry

T_1 relaxometry may be based on inversion/saturation recovery (IR/SR) or variable flip angle (VFA) approaches. All these methods have been extensively studied and have their own specificities. However, it is important to mention that IR/SR methods have been mainly used and optimized for cardiac imaging purpose, whereas VFA approaches remain more generalist approaches. I will briefly summarize the underlying concepts of these methods in the following paragraphs.

A. Inversion and saturation recovery methods

The reference method for measuring T_1 longitudinal relaxation times is the single-point inversion recovery approach (IR T_1-mapping) (100,101) which consists of inverting the longitudinal magnetization M_z by a 180° pulse (inversion) and acquiring a series of independent meas-

urements (single points) of the T_1 signal recovery at different inversion times (Figure 2.28). The pulse sequence can be either a SE or GRE.

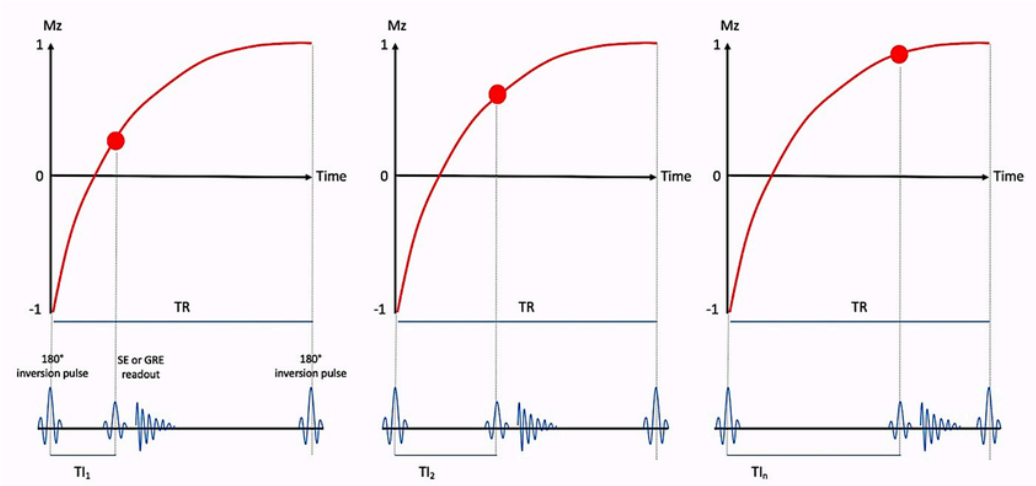

Figure: 2.28 Inversion recovery pulse sequence. Independent signal measurements are performed at different inversion times (TI) after the 180° inversion pulse.

According to the Bloch equations, signal recovery along the M_z axis can be formalized as follows:

$$S(TI) = C(1 - 2e^{-TI/T_1} + e^{-TR/T_1}) \quad (2.22)$$

Where C is the constant to optimize, and TI the inversion time of the IR acquisition. Also, if TR >> T_1 (typically TR ≥ $5T_1$), the equation can be simplified as follows:

$$S(TI) = C \times (1 - 2e^{-TI/T_1}) \quad (2.23)$$

The major disadvantage of standard IR is that extremely long TRs are necessary to achieve complete recovery of the T_1 signal along the M_z axis. Given its prohibitive acquisition time, several alternatives have been developed to be feasible in clinical routine.

The Look-Locker approach (*102*,*103*) is a modified version of standard IR that includes a unique inversion pulse, followed by a rapid sequence of N "α" pulses (separated by a time interval τ) with GRE readout. In this case, the residual transverse magnetization between each consecutive α pulse has to be controlled (by respecting a delay time τ of $5\times T_2$ between each α pulse, or by using gradient spoiling). Also, the T_1 value obtained is underestimated due to

continuous perturbation of the magnetization, and represents an "apparent" T_1 or T_1^* (Figure 2.29).

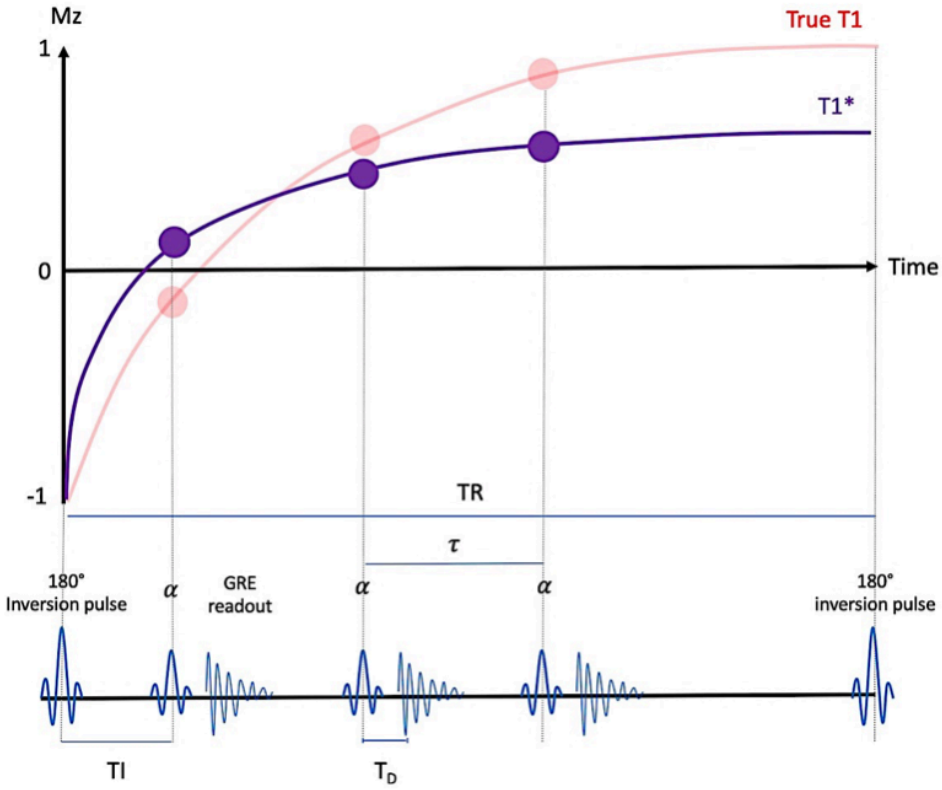

Figure 2.29: Look-Locker pulse sequence. One inversion pulse is followed by several signal measurements. Compared to the reference IR method (red), the T_1 value obtained is underestimated due to continuous perturbation of the magnetization, and represents an "apparent" T_1 or T_1^* (purple).

T_1^* measured after the nth sampling (n = 1, …, N) is formalized as follows:

$$Sn = \beta \times (1 - T_D e^{-n\tau/T_1^*}) \quad (2.24)$$

With $\beta = \frac{M_0(1-e^{-\tau/T_1^*})}{\left(1-\cos\alpha\, e^{\left(-\frac{\tau}{T_1^*}\right)}\right)\sin\alpha}$, $T_D = -\left(\frac{\cos\alpha(1-[\cos\alpha\, e^{-\tau/T_1^*}]N-1)}{1+\cos\alpha[\cos\alpha\, e^{-\tau/T_1^*}]N-1} + 1\right)$.

And finally, the true T_1 is obtained given the following relationship:

$$T_1^* = \frac{\tau}{\frac{\tau}{T1} - Ln\,(cos\,\alpha)} \quad (2.25)$$

The Modified Look-Locker Imaging (MOLLI) approach (*104*) has been specifically conceptualized for rapid cardiac imaging and allows the acquisition of images in apnea (about 20 seconds). The principle is to use only two to three 180° pulses followed by balanced steady state-free precession single-shot acquisitions to different TIs. Between each 180° pulse, short periods of rest are observed in order to restore the longitudinal magnetization between each cycle (Figure 2.30).

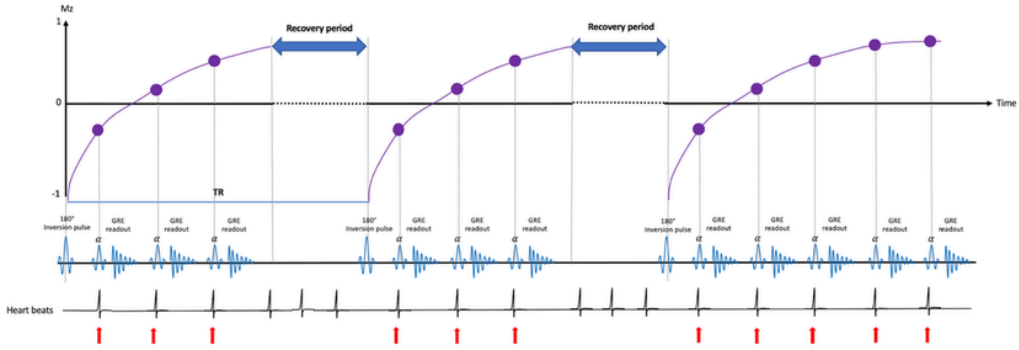

Figure 2.30: MOLLI pulse sequence. Two to three IR pulse are performed. For each IR, three to five signal measurements are performed at the same period of the cardiac cycle.

The images are acquired at the same time of the cardiac cycle, the 180° pulses being synchronized to the heart rate (typically 5 (3) 3 or 5-1-1). The signal is obtained according to

$$SI(TI) = \left|(A - B \times e^{(-TI/T_1^*)})\right| \quad (2.26)$$

From equation (2.26), the true T_1 is given by

$$T_1 = T_1^* \times (\frac{B}{A-1}) \quad (2.27)$$

Finally, the saturation recovery methods (SR) use saturation pulses instead of inversion pulses. For example, SASHA (saturation-recovery single-shot acquisition) approach, also designed for cardiac T_1-mapping, uses a 90° magnetization preparation instead of the 180° inversion pulse (Figure 2.31), with two advantages: the 90° pulse eliminates half the residual magnetization of previous cycles. An estimate of the true T_1 value is therefore directly obtained (*105*).

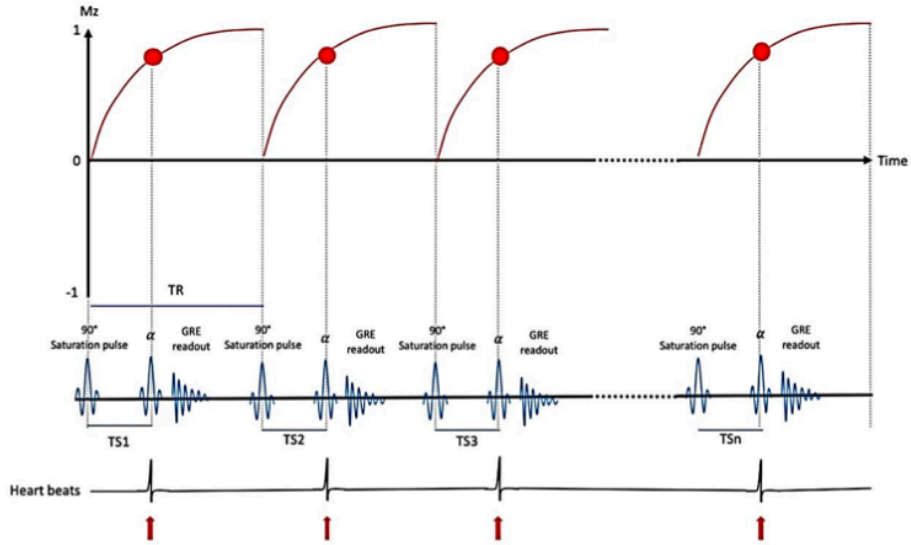

Figure 2.31: SASHA pulse sequence. IR pulse is replaced by a 90° saturation pulse (SR). Independent signal measurements are performed at the same period of the cardiac cycle after the 90° inversion pulse.

The signal is obtained according to

$$SI(TS) = A - (1 - e^{(-TS/T_1)}) \quad (2.28) \text{ for the 2-parameters model}$$

$$SI(TS) = A - B \times e^{(-TS/T_1)}) \quad (2.29) \text{ for the 3-parameters model}$$

B. *Variable flip angle method*

Signal intensity in a Spoiled GRE pulse sequence (SPGR) is a function of T_1, TR, and flip angle α. Assuming TR > T_2^* and a perfect free equilibrium-precession state of the SPGR sequence, the signal S at a particular angle α is given by the following non-linear function:

$$S = \frac{M0\left(1-e^{-\frac{TR}{T_1}}\right) sin\,\alpha}{1-cos\,\alpha\, e^{-\frac{TR}{T_1}}} \quad (2.30)$$

S is the signal of an SPGR sequence (absolute value), α the flip angle, TR the repetition time.

The variable flip angle (VFA) method consists of estimating the T_1 value by fitting, at constant TR and with variable flip angles ($\alpha = 1, \ldots, n$) the signal S from equation (2.30) (Figure 2.32).

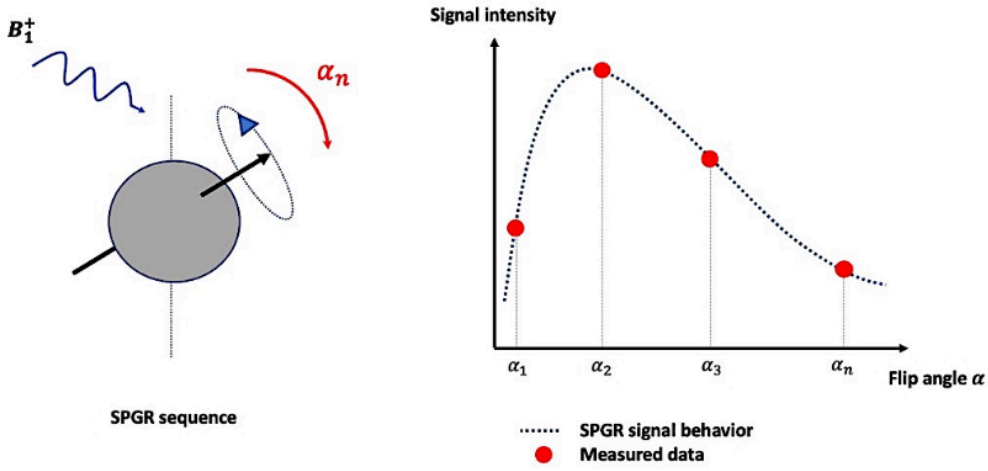

Figure 2.32: VFA concept. The signal intensity of an SPGR pulse sequence is acquired at different flip angles α_n. The signal behavior at different flip angles is then linearized and fitted, the T_1 value being proportional to the inverse of the regression slope

For this purpose, equation (2.30) can be rearranged as y = mx + b (*106*,*107*)

$$\frac{Sn}{\sin \alpha_n} = e^{-\frac{TR}{T_1}} \frac{Sn}{\tan \alpha_n} + C \quad (2.31)$$

Where S_n is the signal measured at a flip angle α_n. Finally, the T_1 value is estimated from the linear regression slope calculated from (2.31)

$$T_1 = {}^{-TR}/_{Ln(slope)} \quad (2.32)$$

With TR the repetition time. The main advantages of VFA are the acquisition speed, the large spatial coverage together with high anatomical resolution, allowing highly resolute 3D-T_1 maps. However, this approach is extremely sensitive to B_1^+ field inhomogeneities, especially in high fields (see below).

C. Technical considerations concerning B_1^+ field inhomogeneities for flip angle sensitive T1-mapping methods (Look locker and VFA)

At the Larmor resonance, the value of flip angle α depends on B_1^+

$$\alpha = \gamma \int_0^t B_1^+(t)\, dt \quad (2.33)$$

Where α is the flip angle, γ the gyromagnetic ratio, and B_1^+ the transmit RF field. From equation (2.33) we can directly deduce that local inhomogeneities of B_1^+induce variations in flip angle and corrupt the estimated T1 values. This issue increases with the MR field strength and cannot be neglected at 3T. For this reason, T1-mapping methods that are sensitive to flip angle all require the acquisition of a B_1^+regional map to calibrate the nominal flip angle (i.e the value of α which is set at the console) to its actual value (i.e the true flip angle experienced by the spins).

For this purpose, several methods for correcting B_1^+ field inhomogeneities have been proposed:

1) Amplitude-based methods

Double-angle method (DAM) (*108*,*109*): by assuming a complete recovery of the signal after the TR, the signal measured is proportional to sin α. Two successive pulse sequences are made with flip angles α (S_1) and 2α (S_2) respectively, corresponding to the following relations:

$$S1 = A \times sin\,(\alpha) (2.34)$$

$$S2 = A \times sin(2\alpha) = 2A \times cos(\alpha) sin(\alpha)\ (2.35)$$

From (2.34) and (2.35), we can deduce the true α_{actual}

$$\alpha_{actual} = cos^{-1}\left(\frac{S_2}{S_1}\right) (2.36)$$

Because the complete regrowth of the signal between two acquisitions is required, and because TR >> T_1, this method is slow. Furthermore, this method works especially for high flip angles (S_2 / S_1 ≈1 for flip angles < 20 °; S_2 / S_1 < 0.5 for flip angles > 60°).

Double-echo method (double SE)(*110*,*111*) exploits the stimulated echo properties of SE sequences. Using an EPI pulse sequence, the signal S_1 is measured after a first pulse of flip an-

gle 2α (spin echo), and the signal S_2 after the second pulse of flip angle α (stimulated echo, at time T_D). The true α_{actual} is then deduced from the relation:

$$\alpha_{actual} = cos^{-1}\left(\frac{S_2}{S_1}\right) \times e^{TD/T_1} \approx cos^{-1}\left(\frac{S_2}{S_1}\right) \text{ if TD << T1 (2.37)}$$

Although much faster and requiring only one sequence, this 2D approach is intrinsically subject to the artifacts of the EPI methods, in particular the geometric distortions induced by the inhomogeneities of B_0 fields.

Actual flip angle imaging method (AFI)(*112*) allows rapid acquisitions of large 3D volumes. A double TR GRE pulse sequence with one RF B_1^+ pulse is used. After the RF B_1^+pulse of flip angle α, two successive signals S_1 and S_2 are measured at TR_1 and TR_2 respectively, with $TR_2 > TR_1$. Assuming the main assumption $TR = TR_1 + TR_2 \ll T_1$:

$$n = \frac{TR_2}{TR_1} \text{ (2.38)}$$

$$r = \frac{S_2}{S_1} \text{ (2.39)}$$

The true α_{actual} is then deduced from (2.38) and (2.39) as follows:

$$\alpha_{actual} = cos^{-1}\left(\frac{nr-1}{n-r}\right) \text{ (2.40)}$$

Pre saturation method Turbo FLASH (SAT-TFL)(*113–115*) consist of two 2D acquisitions of the same flip angle β, one without preparation of the magnetization (S_1), the other with preparation of the magnetization by applying a nominal angle α (S_2). Assuming a complete recovery of the transverse magnetization between S_1 and S_2, and a measurement of S_2 immediately after $\alpha_{nominal}$, the true α_{actual} is deduced by

$$\alpha_{actual} = cos^{-1}\left(\frac{S_2}{S_1}\right) \text{ (2.41)}$$

Double refocused echo (DREAM)(*116*) is based on the same principle as the previous one: preparation of the magnetization before recording the signal. On the other hand, two successive nominal pulses α are carried out for the preparation of the magnetization, followed by a flip angle β to generate two successive echoes S_1 (stimulated echo) and S_2 (free induction decay signal) during the same acquisition. The effective angle α is deduced by

$$\alpha_{actual} = tan^{-1}\sqrt{\left(\frac{2S_1}{S_2}\right)} \text{ (2.42)}$$

2) Phase-based methods

Phase sensitive method (*117,118*) consists in measuring the signal of a GRE sequence including two successive 90° phase-shifted excitation pulses (2α and α) twice (S_1 for the first acquisition and S_2 for the second acquisition), the two 2α RF pulse being 180° phase-shifted. The effective angle α may be deducted from the linear relationship between the phase of $\frac{S_2}{S_1}$ and the flip angle α. This approach is nevertheless sensitive to B_0 fields inhomogeneities.

Bloch-Siegert shift method (*119*) consists in inducing a phase-shift of the signal (ωBS) using an off-resonance pulse (RF) applied after the excitation pulse. Since this phase shift is proportional to B_1^+, the value of the field B_1^+ is deduced from the formula:

$$\omega BS = \frac{(\gamma B_1^+)^2}{2\omega RF} \quad (2.43)$$

This approach is fast and robust to T_1 values and B_0 inhomogeneities. However, it induces a significant increase of the specific absorption ratio (SAR) with tissue warming.

3) Pros and Cons for B_1^+ mapping methods

Among these different B_1^+ mapping methods, the double-SE, DREAM, Phase sensitive and Bloch-Siegert methods are specific absorption-rate (SAR) expensive, limiting their use for long multimodal imaging protocol in clinical routine. Of the remaining methods, DAM is very slow, sensitive to T1 value, and is efficient only for high flip angles. AFI and SAT-TFL are finally robust against T1 or B_0 parameters, and relatively SAR-sparing. AFI is slower than SAT-TFL, but allows 3D acquisition, with good accuracy for a wide range of flip angle values, making it a good generalist candidate for B_1^+ mapping.

2.2.2.2. T2 RELAXOMETRY

A. Main concept

T_2 relaxometry consists of measuring the phase shift of the spins (transverse magnetization M_{xy}) after the application of an RF pulse. All the sequences used are based on the spin echo properties initially demonstrated by Hahn in the 1950s (*76,101*). After a SE pulse sequence, the signal measured follows the equation

$$S = M0\left[1 - e^{\left(-\frac{TR}{T_1}\right)}\right] \times e^{-\frac{TE}{T_2}} \quad (2.44)$$

If $TR \gg T_1$, the T_1 component can be removed and (2.44) yields

$$S = M_0 \times e^{-\frac{TE}{T_2}} \quad (2.45)$$

To estimate T_2 relaxation time (T_2-mapping), the signal is sampled at different TE (Figure 2.33) and adjusted by least squares method (Levenberg-Marquardt) to an exponential decay model

$$Si = M_0 \times e^{-\frac{TE_i}{T_2}} \quad (2.46)$$

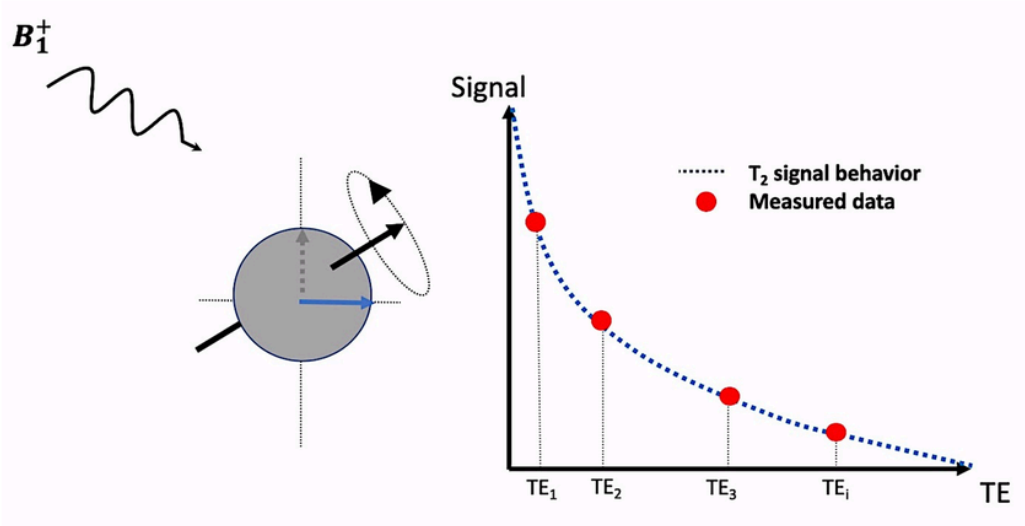

Figure 2.33: T_2-mapping concept. The T2 signal decay is sampled at different TE and fitted to an exponential model.

B. Technical considerations concerning T_2-mapping pulse sequences

The reference standard remains the single-echo SE pulse sequence (Figure 2.34). However, its very long implementation (one acquisition per TE) remains a major drawback that strongly limits its use in clinical practice. The faster version proposed by Meiboom and Gill (*120*,*121*), multi-echo SE (several TE per acquisition), consists in a 90° RF pulse followed by N successive 180° rephasing pulses performed at regular intervals (Figure 2.34). Alternating phase-shift (90°) pulse can be implemented to reduce the accumulated phase errors (Carr-Purcell-Meiboom-Gill, CPMG). Accelerated CPMG-based methods (multi echo turbo or fast spin echo, ME-FSE) combine multi echo SE with ordered phase encoding (Figure 2.34). Multiple lines of k-space are thus filled within one TR, and acquisition time is significantly reduced.

However, because the lines of k-space are filled at different TEs, actual image contrast is reduced. Also, the nominal (effective) TE and ETL have to be adapted to minimize image blurring effects. Finally, modified CPMG approaches using GRE sequences inherently reduce the SAR, but lower flip angles are in turn more sensitive to B_1^+ inhomogeneities.

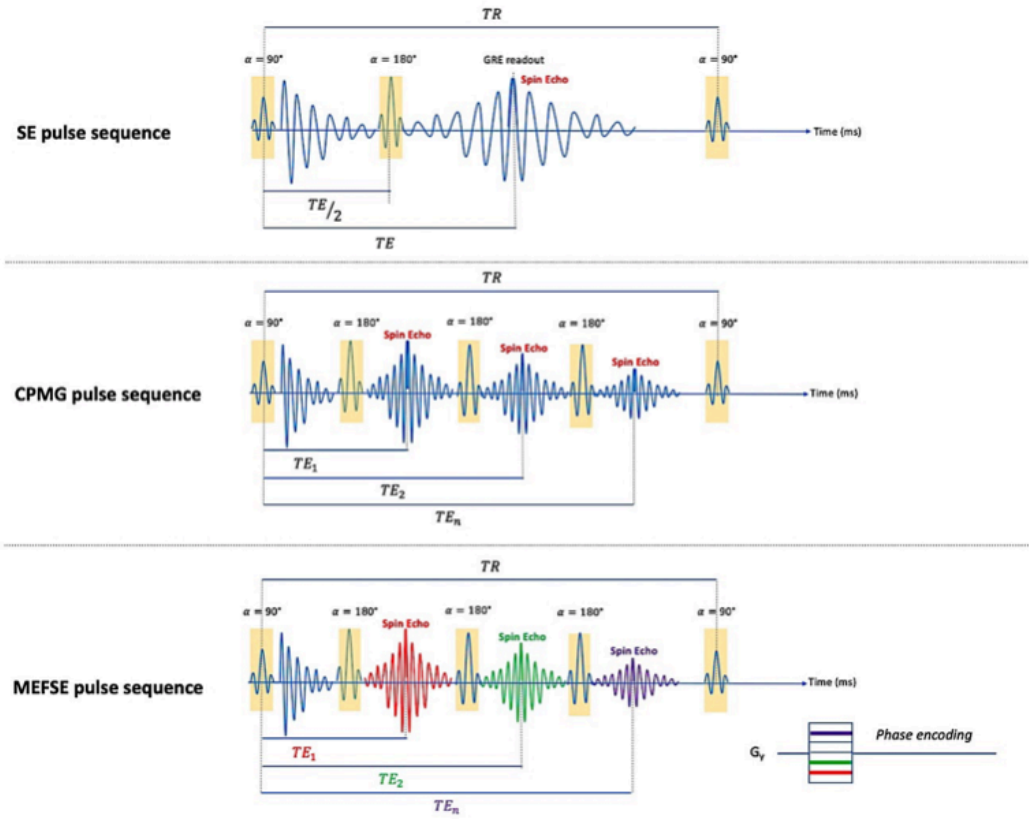

Figure 2.34: single-shot SE pulse sequence and its accelerated versions (CPMG and MEFSE). SE method consists in performing one acquisition per TE. CPMG method consist in generating a train of multiple echos by performing N successive 180° refocusing pulses. The signal is measured at each TE following the initial 90° RF pulse. In MEFSE, the CPMG concept is applied with ordered phase encoding to speed up the filling of k-space.

Importantly, the mono-exponential decay is rarely verified in clinical practice especially because

- The tissue structures are inherently heterogeneous
- RF pulse imperfections generate stimulated or secondary echoes, leading to signal decay corruption and T_2 values over estimation (*122*).

Also, background noise originating from the system or/and from the imaging data may alter the signal fitting procedure, in particular for TE sampling of long T_2 components (*123*). Denoising approaches before adjustment may be used (*124*), or a noise floor offset parameter may be added to the equation (2.46) to minimize the T_2 over estimation (*125*,*126*).

2.2.2.3. Preliminary test for implementation of T1/T2 mapping

A. Context

We had to face a double challenge to implement T_1/T_2 mapping on the Signa PET/MRI system for our purpose specifically: first, T_1/T_2 mapping pulse sequences are not routinely available on PET-MRI systems, limiting the choice of methods we could use. Second, this project focused on lung tumors specifically. This implied to choose pulse sequences that were feasible in clinical routine and robust to thoracic motion (i.e. fast acquisitions allowing breath hold-condition or motion-compensable pulse sequences).

B. Phantom experiments

1) Material

We used a quantitative MRI System Phantom (qMRI, High Precision Devices, Inc., Boulder, Colorado, USA). The qMRI phantom consists of a plastic sphere of 20 cm diameter encapsulating 3 arrays, each array containing 2 cm diameter spheres of known T_1, T_2 and proton density values (Figure 2.35).

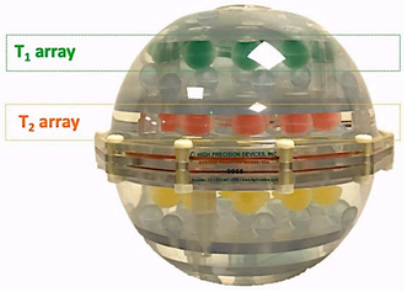

Sphere	T_1 ground truth		T_2 ground truth	
	$NiCl_2$ (± 5%, mM)	T_1 (ms) ± SD	$MnCl_2$ (± 5%, mM)	T_2 (ms) ± SD
1	0.299	1989 ± 1.0	0.013	581.3 ± 0.39
2	0.623	1454 ± 2.5	0.021	403.5 ± 0.55
3	1.072	984.1 ± 0.33	0.031	278.1 ± 0.28
4	1.720	706 ± 1.5	0.047	190.94 ± 0.011
5	2.617	496.7 ± 0.4	0.069	133.27 ± 0.073
6	3.912	351.5 ± 0.9	0.101	96.89 ± 0.049
7	5.731	247.1 ± 0.01	0.145	64.07 ± 0.034
8	8.297	175.3 ± 0.1	0.207	46.42 ± 0.014
9	11.936	125.9 ± 0.3	0.296	31.97 ± 0.083
10	17.07	89.0 ± 0.17	0.421	22.56 ± 0.012

Figure 2.35 : MRI System Phantom (qMRI, High Precision Devices, Inc., Boulder, Colorado, USA). Each sphere of the T_1 and T_2 arrays have calibrated T_1 and T_2 values.

2) Methods

Based on the considerations exposed in section 2.2.2.1, we tested two T_1-mapping methods: one saturation-recovery method (SMART1) highly robust to magnetic field inhomogeneities, designed for cardiac imaging purpose (*31,127*); and VFA method which remains the most widely use method in clinical practice. Because of its inherent high sensitivity to magnetic field inhomogeneities, we tested the AFI B_1^+ mapping procedure to correct the flip angle in-accuracies (*112*).

For T_2-mapping, we used a MEFSE pulse sequence, which is the most widely used T_2-mapping method in cardiac imaging (*30*). To prevent for potential T_2 overestimation, two previously published fitting procedures were tested:

- First echo discarding to compensate potential signal oscillations in the early echoes (*126,128–131*).
- Miller's noise correction (*124*) that corrects the signal of the surrounding background noise (signal offset) by considering the high square images according to

$$I_{Denoised}(TE)^2 = I_{Signal}(TE)^2 - I_{Noise}(TE)^2 \quad (2.47)$$

$$S(TE_i)^2 = (M_0)^2\, e^{-2TE_i/T_2'} \quad (2.48)$$

$$T_2' = \frac{T2_{True}}{2} \quad (2.49)$$

Also, and for the same reasons previously exposed, the image post-processing was implemented in Python environment (libraries numpy, SciPy, nilearn, nibabel and pandas) to allow multimodal unified post-processing pipelines.

3) Phantom acquisitions

Two identical phantom experiments were performed at 1-week intervals on the same Signa PET/MR (GE Healthcare, Waukesha, WI, USA) by using a thoracic phased array from the GEM Coil Suite (GE Healthcare, Waukesha, WI, USA). Acquisition parameters were:

- SMART1: TR/TE = 3.051/1.336 ms; flip angle = 45°; pixel bandwidth = 781.25 Hz; slice thickness = 5 mm, matrix size of 128 x 128, 10 slices.
- VFA: a set of nine independent 3D spoiled gradient echo pulse sequences with variable flip angles; TR/TE = 5.636/1.54 ms, nominal flip angles α = [2°, 4°, 6°, 8°, 10°, 15°, 20°, 30°, 40°]; pixel bandwidth = 976.562 Hz; slice thickness = 5 mm, matrix = 192 x 128, 12 slices.
- AFI pulse sequence to correct T_1 from B_1^+ field map inhomogeneities: flip angle = 50°; TR_1/TR_2= 40 / 200 ms; pixel bandwidth = 976.562 Hz; slice thickness = 5 mm; matrix = 192 x 128, 12 slices).
- 2D MEFSE pulse sequence: TR/TE = 4976 ms / [14, 42, 70, 98, 126, 154, 182, 210] ms; slice thickness = 5 mm; matrix 128x128, interpolated at 256x256, six slices.

4) Data processing

The spheres of T_1/T_2 imaging data were semi-automatically masked using ITK-SNAP (*90*). $T1_{SMART1}$, $T1_{VFA}$, and $T2_{MEFSE}$ relaxation times were estimated from the masked data as follows:

- T1-mapping*:* $T1_{SMART1}$ (directly generated on the vendor workstation) followed the saturation recovery fitting equation (2.28). $T1_{VFA}$ values were estimated from the equations (2.31) and (2.32). $T1_{VFA}$ values with B_1^+ mapping ($T1_{AFI}$) were obtained from the same equations by replacing the nominal flip angles α by the actual flip angles α_{True} computed from the equations (2.38), (2.39) and (2.40). Results of the curve fitting procedures are available in Appendix section A.6 (Figure A. 6, Table A. 3 and Table A. 4).

- T_2-mapping: assuming a theoretical mono-exponential signal decay, $T2_{MEFSE}$ values were estimated by linear fitting of the log-linear values of voxel intensities (S_i) along echo times (TE_i):

$$Log\ (S_i) = Log(M_0) - TE_i/T_2 \quad (2.50)$$

The log-linear decay model was chosen because of better fitting results in the case of signal decay corrupted curves, and for higher fitting precision using the SciPy library (although multi-exponential approach has no relevance in pure fluids, it is less robust and requires larger TE sampling, typically 40 to 100 points that are difficult to apply in clinical routine (*132*). Results of the curve fitting procedures are available in Appendix section A.7 (Figure A. 7, and Tables A. 5, A. 6 and A. 7).

5) Statistical analyses

For each T_1/T_2 sphere, the accuracy of phantom measurements was assessed by calculating the RMSE of the two phantom sessions (for more details, please refer to equation (2.20)). Reliabilities between the two phantom sessions were assessed by computing the intra class correlation coefficient estimates of the measured T_1 or T_2 relaxation times (ICC) and their 95% confidence intervals (mixed effect model, absolute agreement) (*133*). All statistical analyses were performed with Python (version 3.6; Python Software Foundation, www.python.org) and R studio (version 3.4.0; R Project for Statistical Computing, www.r-project.org).

6) Phantom results

- T_1-mapping

Accuracy of T_1-mapping depended both on the method used and the target value in the two sessions, as illustrated in Figure 2.36 and Table 2.5.

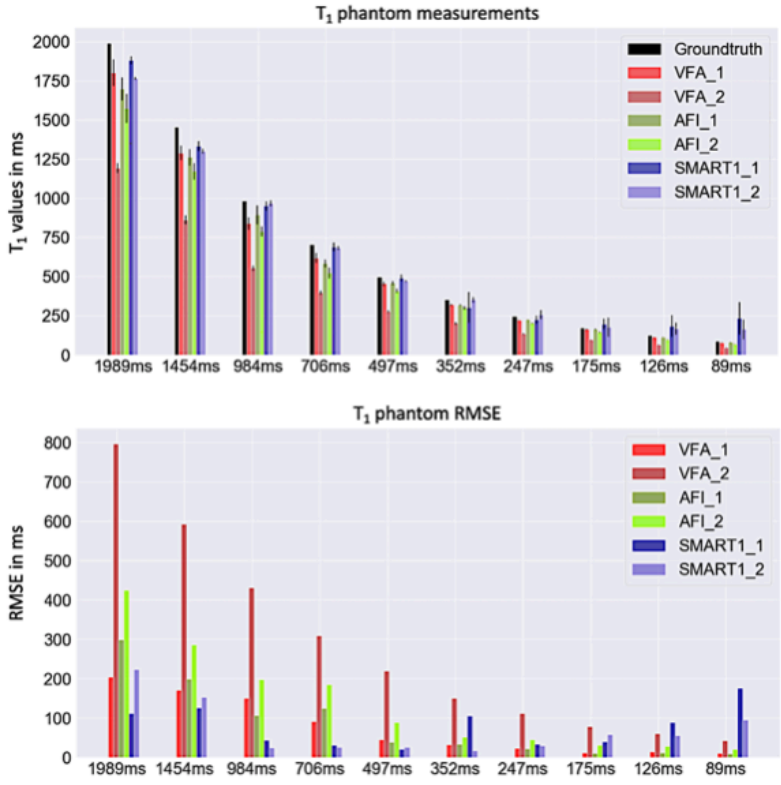

Figure 2.36: Results of the T_1-mapping experiments. For each sphere, (x-axis), the corresponding measured T_1 values (y-axis, top, the vertical black lines corresponding to SD) and RMSE (y-axis, bottom) are provided.

		Sphere 1	Sphere 2	Sphere 3	Sphere 4	Sphere 5	Sphere 6	Sphere 7	Sphere 8	Sphere 9	Sphere 10
Ground truth in ms		1989	1454	984	706	497	352	247	175	126	89
RMSE in ms (%)	VFA session 1	205 (10.3)	171 (11.8)	150 (15.2)	92 (13)	45 (9)	32 (9)	24 (9.7)	12 (6.9)	14 (11.1)	11 (12.4)
	VFA session 2	797 (40)	593 (40.8)	431 (43.8)	309 (43.8)	220 (44.3)	150 (42.6)	112 (45.3)	78 (44.6)	60 (47.6)	42 (47.2)
	AFI session 1	300 (15)	199 (13.6)	106 (10.8)	125 (17.7)	39 (7.8)	33 (9.4)	22 (8.9)	11 (6.3)	13 (10.3)	9 (10.1)
	AFI session 2	425 (21.4)	287 (19.7)	198 (20.1)	185 (26.2)	89 (17.9)	52 (14.8)	45 (18.2)	31 (17.7)	28 (22.2)	21 (23.6)
	SMART1 session 1	112 (5.6)	126 (8.7)	44 (4.5)	32 (4.5)	22 (4.4)	106 (30)	34 (13.8)	40 (22.9)	88 (69.8)	176 (198)
	SMART1 session 2	224 (11.3)	153 (10.5)	25 (2.5)	26 (3.7)	26 (5.2)	17 (4.8)	30 (12.1)	58 (33.1)	56 (44.4)	96 (108)

Table 2.5: RMSE values for the two T_1-mapping experiments. For T_1 values above 500ms, $T1_{SMART1}$ was the most accurate for the two sessions.

B_1^+ mapping ($T1_{AFI}$) partially improved the accuracy of the VFA method. In particular, $T1_{AFI}$ was not optimal for high T_1 values, that may be explained by the following considerations:

- We used short TRs for the AFI pulse sequence to verify the main AFI assumption (equations 2.32 and 2.33), which is driven by the T_1 expected values. Higher the TR to

T_1 ratio will be (the optimal ratio depends on the flip angle considered), better will be the accuracy of flip angle measurements (flip-angle weighted signal) (*134*,*135*).

- As shown in Figure 2.32, signal intensity of an SPGR pulse sequence depends on the flip angle considered (the signal intensity is maximized at the Ernst angle $\alpha_E = arcos(e^{-\frac{TR}{T_1}})$).

These problematics are largely beyond the scope of our project. For information, the trade-off between optimal TR, AFI assumption, optimal flip angles and expected T_1 values may be optimized by simultaneously combining VFA and AFI acquisitions (*136*).

Finally, $T1_{SMART1}$ was the most reliable, as illustrated in Table 2.6.

Method	ICC	95% confidence interval
VFA	0.996	[0.986-0.999]
AFI	0.854	[0.166-0.968]
SMART1	0.992	[0.843-0.999]

Table 2.6: ICC of the T_1-mapping phantom experiments.

- T_2-mapping

Accuracy of T_2-mapping is provided in Figure 2.37 and Table 2.7.

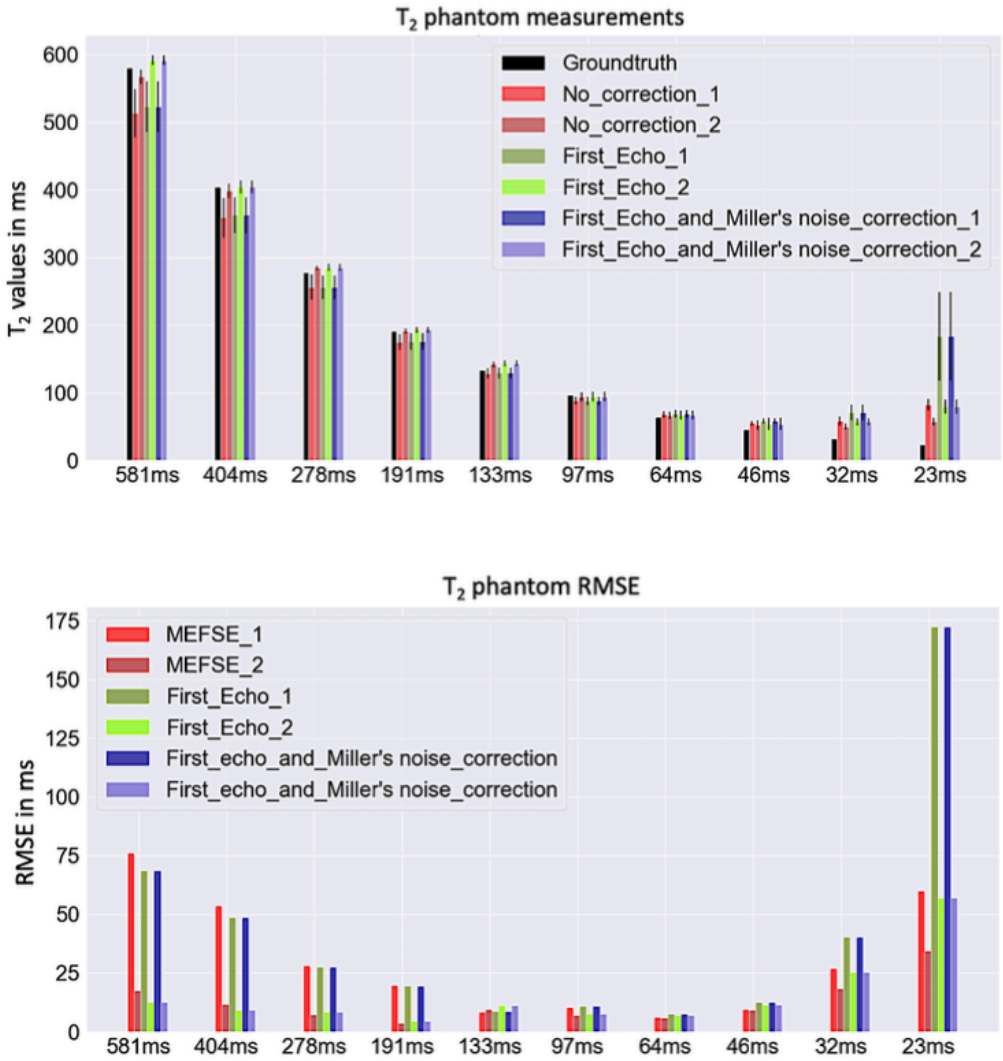

Figure 2. 2.37 results of the T_2-mapping experiments. For each sphere, (x-axis), the corresponding measured T2 values (y-axis, top, the vertical black lines corresponding to SD) and RMSE (y-axis, bottom) are provided.

		Sphere 1	Sphere 2	Sphere 3	Sphere 4	Sphere 5	Sphere 6	Sphere 7	Sphere 8	Sphere 9	Sphere 10
Ground truth in ms		581	404	278	191	133	97	64	46	32	23
RMSE in ms (%)	MEFSE 1	76 (13)	54 (13.4)	28 (10)	20 (10.5)	8 (6)	10 (10.3)	6 (9.4)	9 (19.6)	27 (84.4)	60 (260)
	MEFSE 2	17 (2.9)	12 (3.0)	7 (2.5)	4 (2.1)	10 (7.5)	7 (7.2)	6 (9.4)	9 (19.6)	18 (56.3)	35 (152)
	MEFSE_First echo_1	69 (11.9)	49 (12.1)	28 (10.1)	19 (10)	9 (6.8)	11 (11.3)	8 (12.5)	13 (28.3)	40 (125)	172 (748)
	MEFSE_First echo_2	13 (2.2)	9 (2.2)	9 (3.2)	5 (2.6)	11 (8.3)	8 (8.3)	7 (10.9)	11 (23.9)	25 (78.1)	57 (248)
	MEFSE_First echo_Miller_1	69 (11.9)	49 (12.1)	28 (10.1)	19 (10)	9 (6.8)	11 (11.3)	8 (12.5)	13 (28.3)	40 (125)	172 (748)
	MEFSE_First echo_Miller_2	13 (2.2)	9 (2.2)	9 (3.2)	5 (2.6)	11 (8.3)	8 (8.3)	7 (10.9)	11 (23.9)	25 (78.1)	57 (248)

Table 2.7: RMSE values in ms (%) for the T2-mapping experiments.

First echo discarding (*126*,*128*–*131*) without or with Miller's noise correction (*124*) did not improved the accuracy of the method. Miller's noise correction had no impact on the T_2 accuracy in our experiments. Also, the measurement errors dramatically increased for very low T_2 values when using these correction methods. These results may be explained by the fact that:

- The eight TE values we chose to sample the T_2 signal decay were adapted to T_2 expected values in biological tissues (T_2 in the range 50-150ms (*70*,*71*), reason why only two TE values were in the range 10-50ms.
- Discarding the first echo penalized our fitting procedure from early TE. The remaining seven TE values were thus non-optimized for low T_2 values sampling.

Finally, in all the cases, $T2_{MEFSE}$ provided high reliability between the two sessions (ICC = 0.989, 95CI = 0.923-0.995).

C. Experiments on real clinical data

1) Patients data and image processing

Based on our phantom experiments, saturation recovery pulse sequence (SMART1) for T_1-mapping and MEFSE for T_2 mapping were tested clinically on 15 patients (main characteristics are provided in Table 3.2, page 162).

The T_1/T_2-mapping sub-study workflow is illustrated in Figure 2.38.

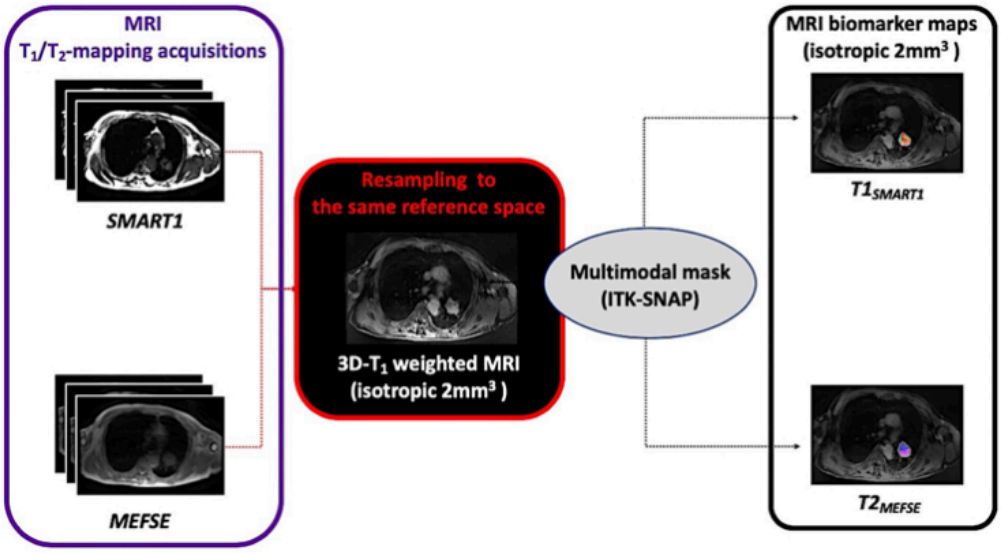

Figure 2.38: T_1/T_2-mapping sub-study workflow. For each patient, whole volume T_1 map and MEFSE imaging data were resampled to the 3D-T_1 weighted volume (previously resampled to 2mm^3). T_1 map of the tumor was then generated by masking the resampled whole volume $T1_{SMART1}$ map; and $T2_{MEFSE}$ map was computed off-line from the resampled masked MEFSE data.

For each patient, the T_1/T_2 MRI data were resampled into the same isotropic reference space (i.e. the 3D T_1-weighted MRI resampled to 2mm isotropic resolution, 3D-T1). Then, T_1/T_2 and 3D-T_1 tumors data were masked semi-automatically with ITK-SNAP (*90*) to be intersected into one multimodal tumors mask (for details please refer to Figure 3.3, in section 3.1.4). T_1/T_2 parametric tumors maps were finally computed from the masked data. $T1_{SMART1}$ tumor maps were obtained by masking the SMART1 whole volume maps. $T2_{MEFSE}$ tumor maps were computed off-line according to equation (2.50).

2) *Statistical analyses*

The relationships between T_1 and T_2 relaxation times of the tumors were finally assessed at the regional voxel level. Spearman correlation coefficients (r_s) between the measured T_1 and T_2 relaxation times were computed along with their respective bootstrapped 95% confidence intervals (n = 1000 iterations). The statistical analyses, performed with R studio (version 3.4.0; R project for Statistical Computing, www.r-project.org),

3) *Results*

Results of the T_1 and T_2 maps of the 15 lung tumors are provided in Figure 2.39.

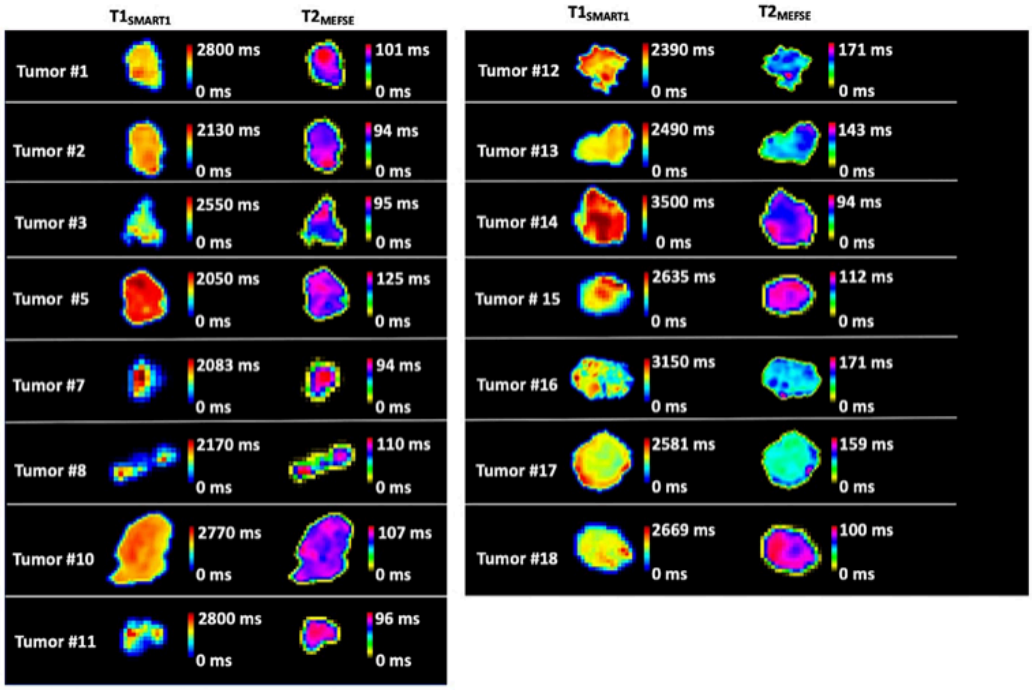

Figure 2.39: T_1 and T_2 maps of the 15 lung tumors. For display, all the maps were smoothed by using a 3 mm Gaussian filter.

The measured T_1 and T_2 relaxation times and density estimates of the tumors are provided in Figure 2.40 and Figure 2.41.

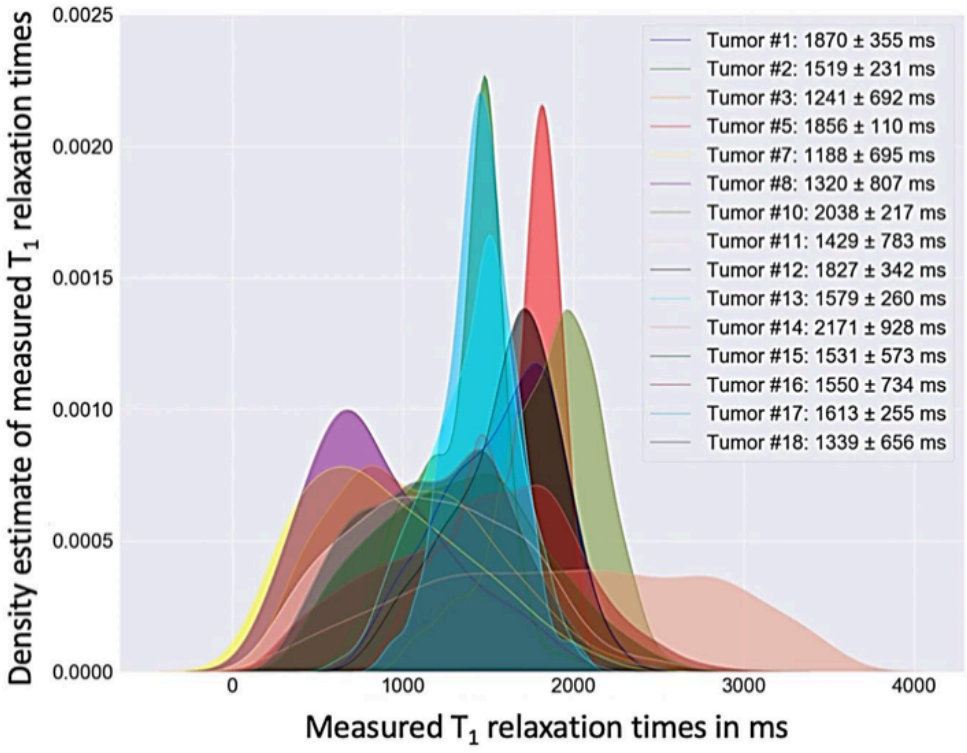

Figure 2.40: Measured T_1 relaxation times (x-axis) and the corresponding density estimates (y-axis). For each tumor, the mean T_1 value and standard deviation is also provided in the legend. Mean $T1_{SMART1}$ ranged from 1 188 ms to 2 171 ms.

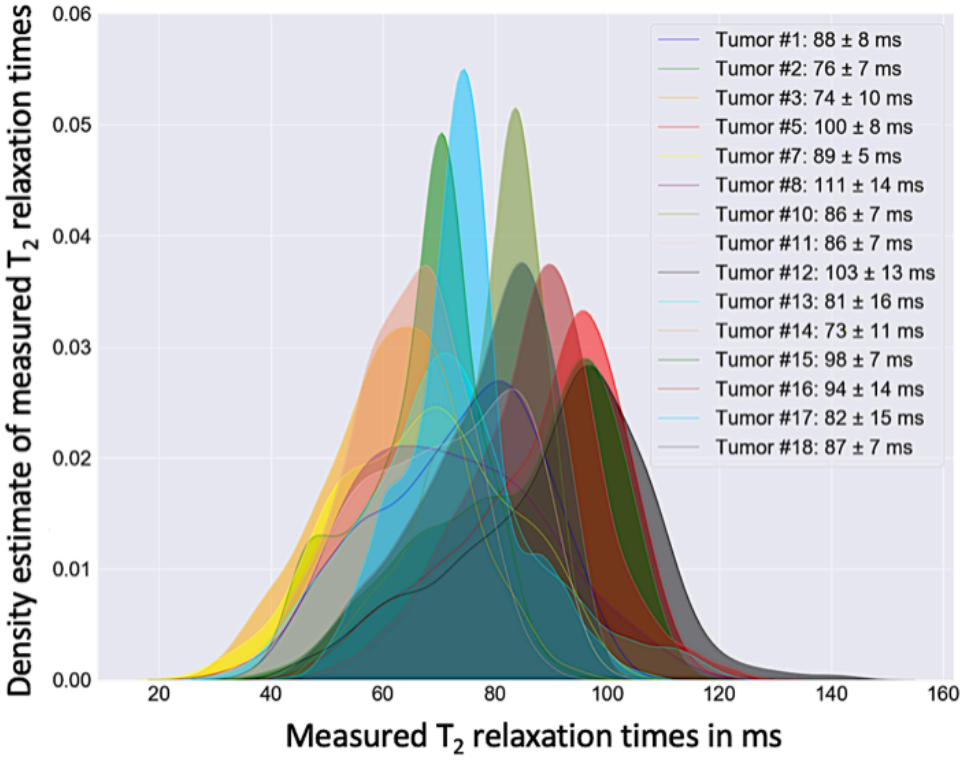

Figure 2.41: Measured T_2 values (x-axis) and the corresponding density estimates (y-axis). For each tumor, the mean T_2 value and standard deviation is also provided in the legend. Mean $T2_{MEFSE}$ were in the range 73-111 ms.

The relationships between T_1 and T_2 relaxation times of the tumors are shown in Table 2.8.

Tumor n°	r_s	95% confidence interval
1	-0.16	[-0.24; -0.09]
2	*0.04*	*[-0.02; 0.1]*
3	*-0.008*	*[-0.08; 0.06]*
5	0.24	[0.19; 0.29]
7	-0.71	[-0.81; -0.58]
8	0.19	[0.01; 0.35]
10	0.30	[0.26; 0.32]
11	-0.14	[-0.23; -0.04]
12	0.24	[0.20; 0.28]
13	0.47	[0.43; 0.50]
14	0.14	[0.09; 0.18]
15	*0.04*	*[-0.03; 0.1]*
16	*-0.02*	*[-0.04; 0.005]*
17	0.46	[0.43; 0.48]
18	-0.09	[-0.14; -0.04]

Table 2.8 voxel-wise correlations between measured T_1 and T_2 relaxation times. No strong relationships between the two biomarkers were observed at the regional voxel level. All the biomarker pairs showed absolute r_s values ($|r_s|$) less than 0.5, except for the T_1/T_2 pair for one tumor (tumor 7, which was the smallest lesion: 107 voxels, 1.6cm of maximum axial diameter). The majority of the biomarker pairs showed absolute r_s values less than 0.2 (9 tumors), and moderate correlations ($0.2 < |r_s| < 0.5$) were observed for 5 tumors. Furthermore, for 4 tumors, the correlation was not significant (confidence intervals in italic).

2.2.2.4. Conclusion

In this methodological subpart, we implemented two T_1-mapping strategies (SMART1 and VFA without and with B_1^+ correction with AFI) and one T_2-mapping approach (MEFSE) on a 3T signa PET-MRI device. Based on our phantom experiments, we then clinically applied T_1/T_2-mapping on 15 lung tumors.

Our phantom experiments showed that:

- SMART1 outperformed VFA for T_1-mapping both in terms of accuracy and reliability (even when considering AFI B_1^+ correction) to estimate the expected T_1 relaxation times of biological tissues at 3T (*70,71*).
- MEFSE was an accurate T_2-mapping procedure to estimate the expected T_2 relaxation times of biological tissues at 3T (*70,71*). First echo discarding (*126,128–131*) and Miller's noise correction (*124*) did not improve the accuracy of the measured T_2 relaxation times.

Quantitative T_1/T_2 maps of 15 lung tumors, respectively generated with SMART1/MEFSE robust pulse sequences, showed:

- A wide variability in the regional distribution of T_1 and T_2 relaxation times among the tumors
- No strong relationship between T_1 and T_2 relaxation times at the voxel level for 14 of the 15 tumors (93.3 % of the tumors).

2.2.3. Dynamic contrast-enhanced MRI

2.2.3.1. Main concepts

Dynamic contrast-enhanced (DCE-MRI) is a quantitative imaging technique developed during the 1990s that uses a bolus injection of paramagnetic gadolinium contrast agent to measure the exchanges between blood and the extravascular space at the microcirculatory level, based on the signal enhancement kinetics (T_1 shortening) normalized per mass or volume of tissue.

The net tissue enhancement depends on the contrast agent leakage capability through the capillary wall. In the case of gadolinium, it represents a combination between perfusion and interstitium accumulation/release. In the tissue of interest, the signal measured thus reflects a mix between perfusion, vascular permeability and the fractional volume of interstitial space (Figure 2.42).

The main microcirculatory parameters are (*137*):

- Tissue blood flow (F_T).
- Tissue blood volume fraction (v_b), which corresponds to the volume of capillary blood per tissue volume.
- Permeability or surface-area product ($P \times S$) that corresponds to the leakage rate of molecules through the capillary membranes per volume unit.
- Transfer constant (K_{trans}) which is a surrogate of ($P \times S$) and F_T.
- Interstitial volume or extravascular extra cellular volume fraction (v_e).

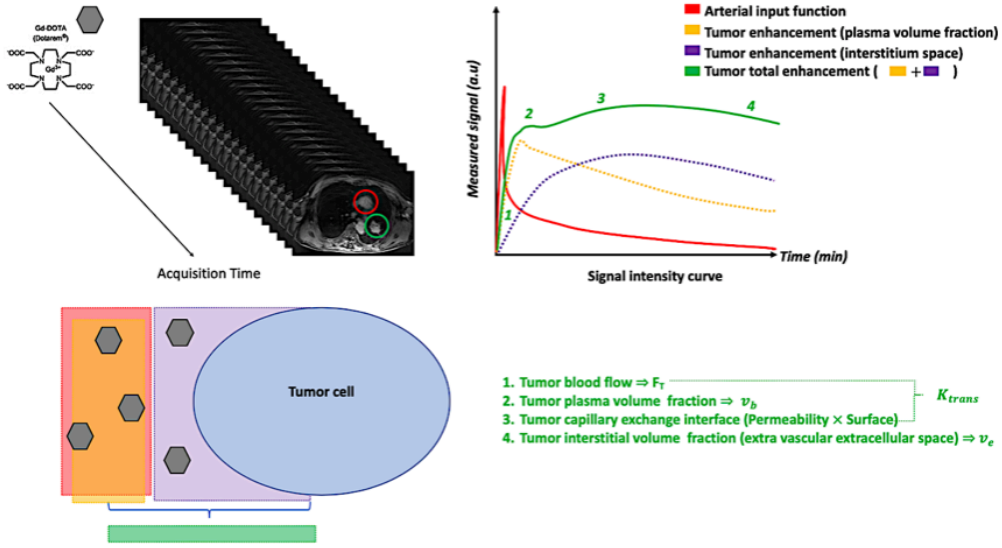

Figure 2.42: DCE principles and microcirculatory parameters.

DCE-MRI have shown promising result in the field of oncology (for review please refer to (*138–140*), and several levels of analysis of increasing complexity have been proposed:

The simple visual approach is the most common method in clinical routine, which consists in subjectively characterizing the shape of the signal intensity curves (Figure 2.43 A).

Semi-quantitative approach consists in calculating empirical indexes by integrating the different parts of the signal intensity curves: the time to peak time (TTP), the wash-in, the wash-out, the area under the curve (AUC), the maximum enhancement (ME) and the percentage of maximum enhancement (% ME) compared to the pre-contrast reference signal (Figure 2.43 B).

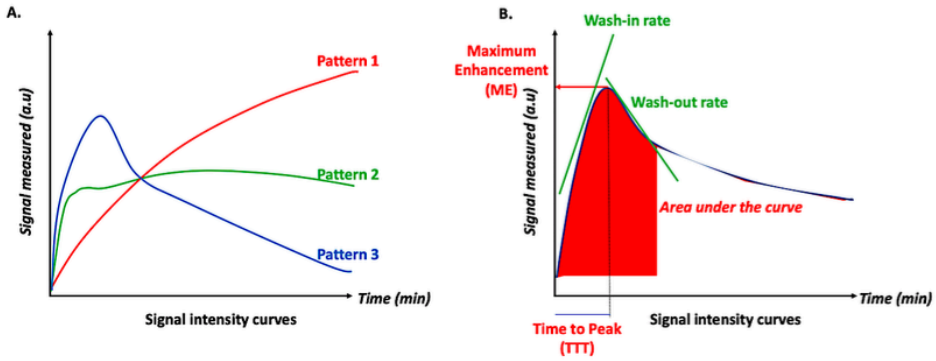

Figure 2.43: Visual and semi-quantitative analyses in DCE. Visual analysis consists in qualitatively describing the shape of the signal intensity curves. Semi-quantitative analysis consists in calculating empirical indexes by integrating the different parts of the signal intensity curves

Finally, the absolute quantitative approach relies, as for dynamic quantitative PET imaging, on pharmacokinetic modeling, and provides insight into the underlying tumor vascularization through the microcirculatory parameters of perfusion and capillary permeability defined above. Numerous compartmental or spatially distributed kinetic models have been developed over the past 30 years with their respective strengths and weaknesses (for review cf (*140*, *141*). Because of the lack of standardization in DCE-MRI (*32*), standard 2-compartment Tofts model (TM) (*142*) remains the most widely used for DCE-MRI clinical studies, defined by

$$C_t(t) = K_{trans} \int_0^t C_p(\tau) e^{-(K_{trans}/v_e)(t-\tau)} \, d\tau \quad (2.51)$$

$$k_{ep} = \frac{K_{trans}}{v_e} \quad (2.52)$$

Where $C_t(t)$ is the measured tissue concentration of contrast agent, $C_p(t)$the measured plasma concentration of contrast agent, K_{trans} a surrogate of blood flow (F_T) and the surface-area product ($P \times S$), and v_e the extravascular extra cellular volume fraction.

Importantly, the original TM does not consider the fraction of tissue vascularization v_p, which cannot be neglected in highly vascular tissues such malignant tumors. This is why a revised version of the Tofts model, or extended Tofts model (ETM), introduces the intravascular contribution $v_p C_p(t)$ to the tissue concentration (*143*):

$$C_t(t) = v_p C_p(t) + K_{trans} \int_0^t C_p(\tau) e^{-(K_{trans}/v_e)(t-\tau)} \, d\tau \quad (2.53)$$

Figure 2.44 illustrates the TM approaches, which have been extensively used in many tumor subtypes, including NSCLC (*144–147*).

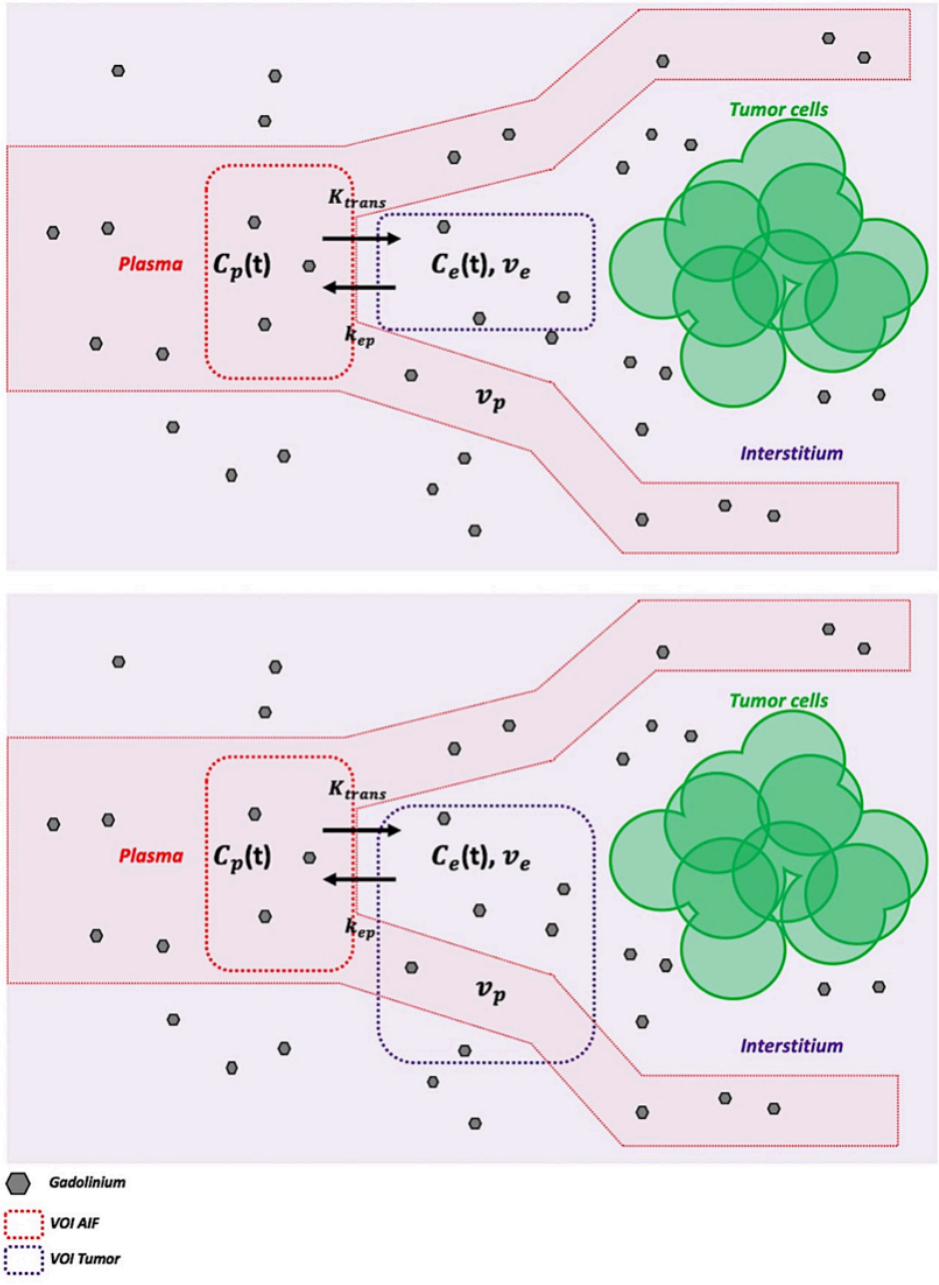

Figure 2.44: Tofts models (top: standard Tofts; bottom: extended Tofts).

2.2.3.2. Technical considerations for DCE kinetic modeling implementation

A. Pre-contrast T_1-mapping

Accurate DCE analyses require an estimate of the pre-contrast enhanced T_1 relaxation times. Approaches using pre-defined fixed values of T_1 have a double disadvantage. T_1 measurements depend on numerous parameters as explained in section 2.2.2.1: magnetic field inhomogeneities, sequences and acquisition parameters, magnetic field strength, which explain the great range of T_1 values in human tissues in the literature (70,71).

Also, the choice of a fixed T1 value implies that the tissue of interest is homogeneous, which is not the case in tumors. Therefore, it seems relevant to have true estimates of regional T1 relaxation times for accurate voxel-wise DCE analyses of the tumors.

B. Motion correction

Physiological movements during DCE-MRI acquisition degrade the DCE analyses. Motion correction of the dynamic DCE frames is therefore mandatory before analyses, including rigid or non-rigid standard registration procedures (148–151) or more advanced motion compensation techniques (152,153).

C. Noise filtering

Noise filtering: multiple MR-based denoising methods have been proposed (spatial, transformed or statistical domains (*154–156*). In any case, the goal is to reduce the noise without altering anatomical details of images nor temporal resolution.

D. Arterial input function

DCE-MRI analysis requires an arterial input function. Several input function measurement approaches can be used (for extended review please refer to (140)):

- Population-based methods are input function models generated from samples of given populations. This approach is nevertheless approximate because of its standardized nature.
- Image-based measurement approaches (IDIF) are currently the most used, consisting of setting a region or volume of interest on a feeding vessel and measuring its signal

over time. It is also sometimes necessary to correct the delay of arrival of the contrast agent due to the distance with the feeding vessel. Nevertheless, in practice, the estimation of this delay time is difficult to correct, and therefore rarely performed (137).

E. Signal conversion to gadolinium concentration

The signal measured over time must be converted into gadolinium concentration [Gd], using the following equation

$$C(t) = \left(\frac{1}{T_1(t)} - \frac{1}{T_{10}}\right)/R_{Gd} \quad (2.54)$$

With T_{10} being the pre-contrast T_1 relaxation time (estimated or fixed), R_{Gd} the contrast agent relaxivity, and $T_1(t)$ the measured T_1 signal over time, which is obtained according to the formulas

$$\frac{1}{T_1(t)} = \frac{-1}{TR} \times ln\left[\frac{1-A}{1-cos\,\alpha \times A}\right] \quad (2.55)$$

$$A = B \times \frac{SI(t)}{SI(0)} \quad (2.56)$$

$$B = \frac{1-E_{10}}{1-cos\,\alpha \times E_{10}} \quad (2.57)$$

$$E_{10} = e^{\left(-\frac{TR}{T_{10}}\right)} \quad (2.58)$$

Where α is the flip angle of the 3D SPGR pulse sequence, TR is the repetition time of the 3D SPGR pulse sequence, SI *(t)* and SI *(0)* are the signal strengths at time t and time 0. The alternative method called "Look up table" based on a phantom calibration of different T1 values, allows to estimate the relaxation times T1 without passing through a T1 baseline mapping. Nevertheless, this method assumes a great signal uniformity.

Finally, because gadolinated contrast agents have an exclusive plasma distribution, $[Gd]_{Blood}$ must be converted into $[Gd]_{Plasma}$, by considering the relationship:

$$[Gd]_{Blood} = [Gd]_{Plasma} \times (1 - Hct) \quad (2.59)$$

Where Hct is the Hematocrit.

2.2.3.3. Preliminary test for DCE maps computation

As previously mentioned, the vendor workstations currently do not allow full dynamic PET and MRI voxel-wise quantitative analyses. Hence, all the post-processing steps of DCE-MRI were recomputed using in-house procedures in Python environment. For this section, we used the DCE data of patient 1 (for more details, please refer to sections 3.1.1, page 148 for patient's characteristics; and section 3.1.2, page 150 for MRI acquisition procedure).

A. Pre-contrast T_1-mapping

We used the SR pulse sequence validated in our phantom experiments (section 2.2.2.3). The corresponding T_1 map is provided in Figure 2.45.

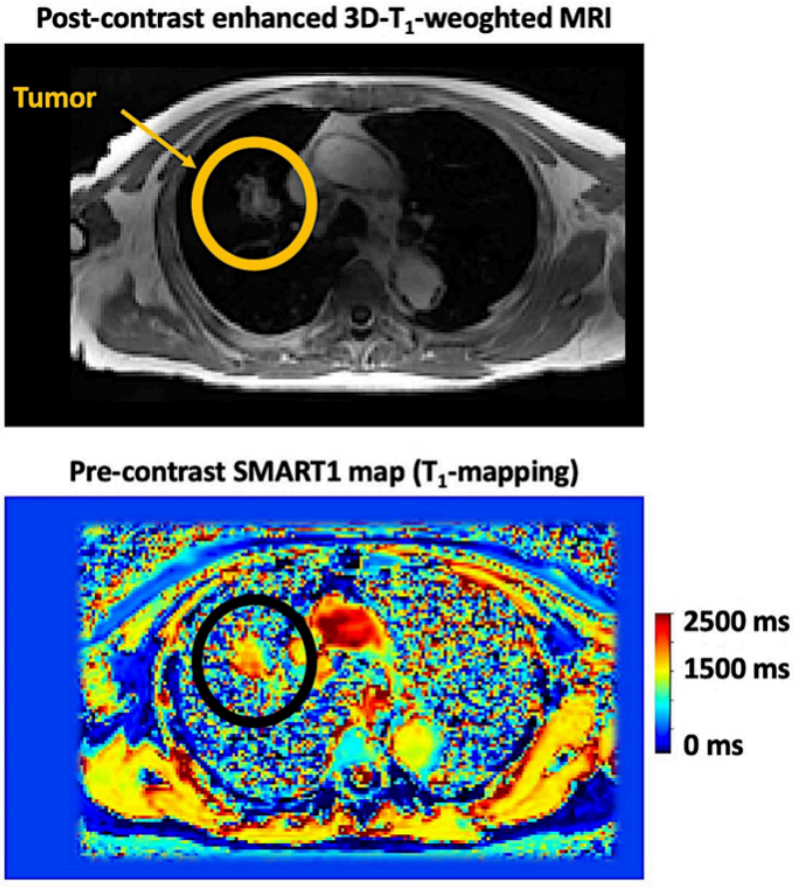

Figure 2.45: Pre-contrast T1-mapping using the SMART1 pulse sequence.

B. Motion correction

Patient physiological motion (cardiac or respiratory motion, voluntary motion) may significantly alter the quality of the signal intensity curves and corrupt the DCE kinetic analyses. The total DCE scan duration (7 minutes) precluded breath-hold acquisitions. Furthermore, the 3D fast SPGR pulse sequence used to gain sufficient volume recovery and temporal resolution ruled-out respiratory triggering for motion compensation. Although advanced DCE motion compensation methods have been studied (152,153), no advanced MR-based motion compensation procedure was available locally for this project. Therefore, we applied a standard frame-to-reference non-linear coregistration procedure illustrated in Figure 2.46. For this purpose, we used the SynQuick normalization procedure implemented in ANTs (91). Briefly, rigid plus affine plus symmetric diffeomorphic non-linear transformations (Syn) are applied sequentially to maximize a mutual information-cost metric between the moving image and the fixed image.

The method was automated but computationally intensive (around 2 to 5 minutes per frame) on a standalone personal computer (Intel Core i5, CPU 2.7 GHz; 8 GB of RAM). For convenience sake, this computation task was performed at the computing cluster of Laboratoire de Mathématiques de Paris-Saclay.

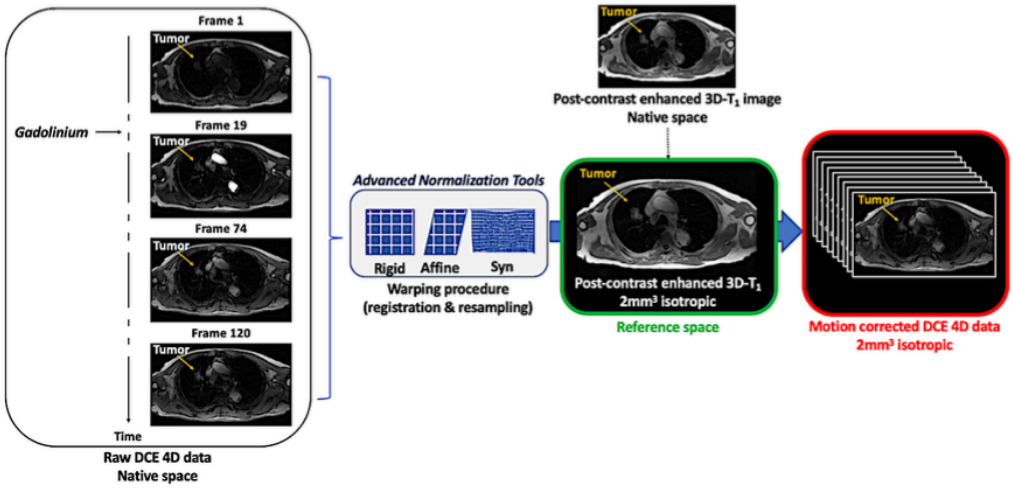

Figure 2.46: DCE motion correction. For each patient, all the DCE frames (120 frames of 3.4 second each) were warped to a reference morphological space (i.e. the post contrast-enhanced 3D-T_1 volume resampled to 2mm^3 isotropic).

Figure 2.47 provides the AIF, voxel-wise (voxels n°351 and 501 are displayed here) and mean tumor (540 voxels) signal intensity curves of the patient test, without and with motion compensation *(NB: For the signal extraction, aorta and tumor were masked semi automatically using ITK-SNAP* (*90*).

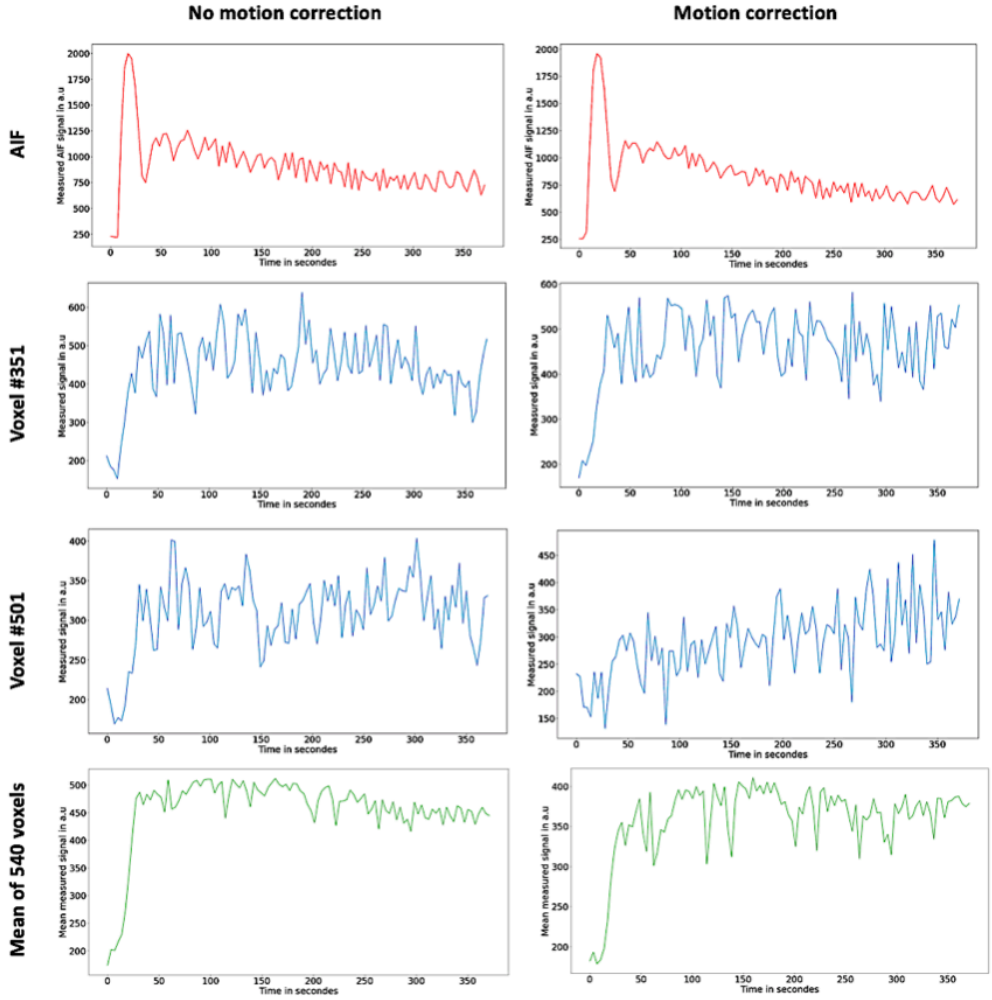

Figure 2.47 results of the motion correction procedure. AIF (red), voxel-wise (in blue) and mean (in green) tumor signal time curves, without and with motion correction, are exposed. Signal irregularities and shapes along time were only slightly impacted.

C. Noise filtering

In MRI, noise from real and imaginary components of the signal measured in quadrature (cf Figure 2.4) has Gaussian distribution. In final magnitude images, noise is additive and follows a Rician distribution. As mentioned in section Technical consideration for DCE kinetic modeling implementation (page 132), numerous MR-based denoising methods have been proposed. Also, parallel imaging induces spatial noise inhomogeneities, that precludes the use of basic denoising post-filtering methods. Therefore, to evaluate the influence of noise on the DCE signal intensity curves, we assessed on the same patient test the effect of an advanced MR denoising algorithm with spatial adaptation of the Rician distribution of the signal (NLM algorithm) implemented in ANTs (*157*).

Signal-to-noise ratio (SNR) is basically defined by

$$SNR = \frac{Signal}{SD} \quad (2.60)$$

Where SD is the standard deviation of signal over many measurements under the same conditions. As a surrogate, the standard deviation within a region of interest void of signal is often used. Considering equation (2.60), the last DCE frame of the patient test was semi-automatically masked with ITK-SNAP (*90*) and SNR was computed by following the procedure illustrated in Figure 2.48:

- A semi-automated tumor VOI was generated (Signal VOI).
- A semi-automated rectangular VOI was set out of the body, in a signal free-region. To be sure no signal artefact would corrupt the chosen VOI, the image was scaled at its maximum before the region definition.

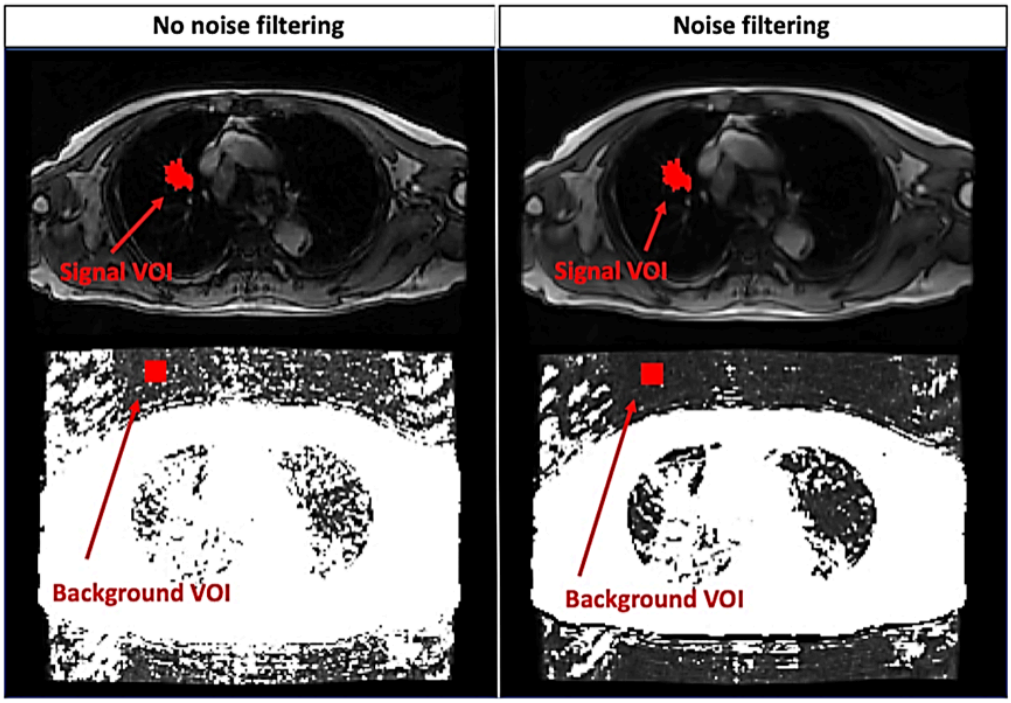

Figure 2.48: SNR computation procedure before and after denoising.

Table 2.9 provides the results of SNR calculation.

		No noise filtering	Noise filtering
Signal VOI	Voxel count	837	
	Mean signal	364.7	346.8
Background VOI	Voxel count	900	
	Standard Deviation	4.62	3.48
SNR		78.95	99.72

Table 2.9 Extracted parameters from the tumor and background VOIs before and after denoising, and corresponding SNR. SNR increased from 78.95 before noise filtering to 99.72 after noise filtering, that corresponds to a relative SNR of + 1.26.

Figure 2.49 provides the results of denoising on the signal intensity curves.

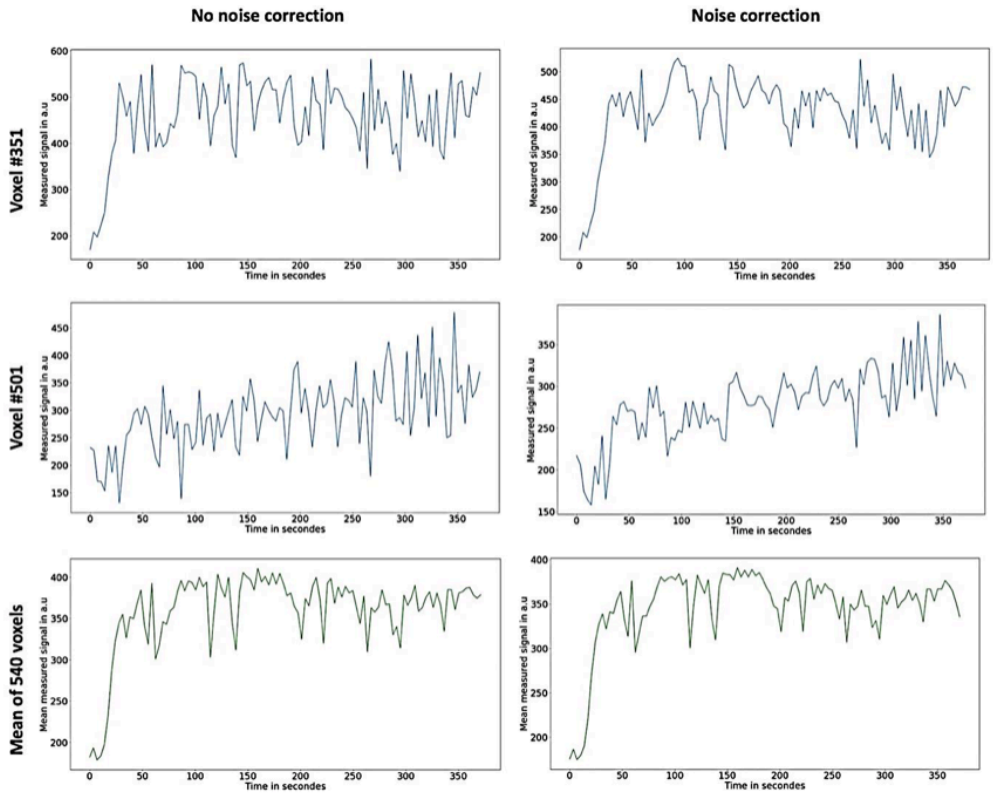

Figure 2.49: Results of the noise filtering. Voxel-wise and mean signal activity curves (motion corrected data), without and with noise filtering, are exposed. In both cases, the signal irregularities were not substantially improved.

The denoising results appeared modest. Also, denoising process required 13 GB of RAM and 23 hours of calculations on this individual DCE dataset.

We thus conclude that, despite motion compensation, the residual disturbances we observed in the signal activity curves were mainly due to patient motion, and that noise filtering had only modest influence on the quality of the DCE data. Based on those results, and considering the huge computational task of the denoising procedure we tested, we thus decided not to correct for the noise for the rest of the project.

D. Arterial input function

As performed in section 1.4.2, we used IDIF method to extract the arterial input function. A small standardized VOI was manually placed in the center of the thoracic aorta.

E. Conversion of Signal intensity to contrast agent concentration

For each voxel, the measured signal measured was converted to [Gd] according to equations (2.54) to (2.59), where T_{10} values were estimated for each voxel by using the SR method described in section 2.2.2.3, page116; R_{Gd} was set to 3.4 $s^{-1}.mM^{-1}$ (158); and $[Gd]_{Blood}$ was corrected into $[Gd]_{Plasma}$ by fixing Hct to 0.45 (159).

2.2.3.4. DCE kinetic modeling implementation

A. Methods

As previously exposed, the extended Tofts Model (ETM) (Figure 2.44) was retained for the DCE pharmacokinetic modeling of the lung tumors. The ETM was implemented in Python environment (libraries numpy, nilearn, nibabel, pandas, math and scipy) as a differential equation system, which is defined as follows (160)

$$\frac{dC_e(t)}{dt} = \left(\frac{K_{trans}}{ve}\right) \times \left(C_p(t) - C_e(t)\right)$$

(2.61)

$$C_{Gd}(t) = v_p C_p(t) + v_e C_e(t)$$

Where $\frac{K_{trans}}{ve} = K_{ep}$

As for the PET dynamic pharmacokinetic modeling exposed before, we used an iterative second order Runge-Kutta numerical method analysis to resolve the system. A Levenberg-Marquardt non-linear least square fitting algorithm was used to minimize the cost function (1.12), where $S(\beta)$ is the minimum sum of squares deviations between the measured and estimated C_{Gd} values (y_i and $f(x_i, \beta)$ respectively) at each time-point i, x_i is the measured C_p value at each time-point i, and $\beta = \{K_{trans}, v_e, v_p\}$.

Several constraints were also implemented to optimize the fitting procedure:

- Empirical [0-10 min^{-1}] numerical bounds were imposed to the K_{trans} kinetic parameters
- [0-1] numerical bounds were imposed to v_e and v_p expected values.

B. Results of the implementation of DCE kinetic modeling

Figure 2.50 shows the $RMSE$ per voxel for uniform and nonuniform gridding approaches, defined by:

$$RMSE = \frac{1}{\sqrt{N}} \times \|Measured\ C_{Gd} - Estimated\ C_{Gd}\|_2 \quad (2.62)$$

With N the number of frames.

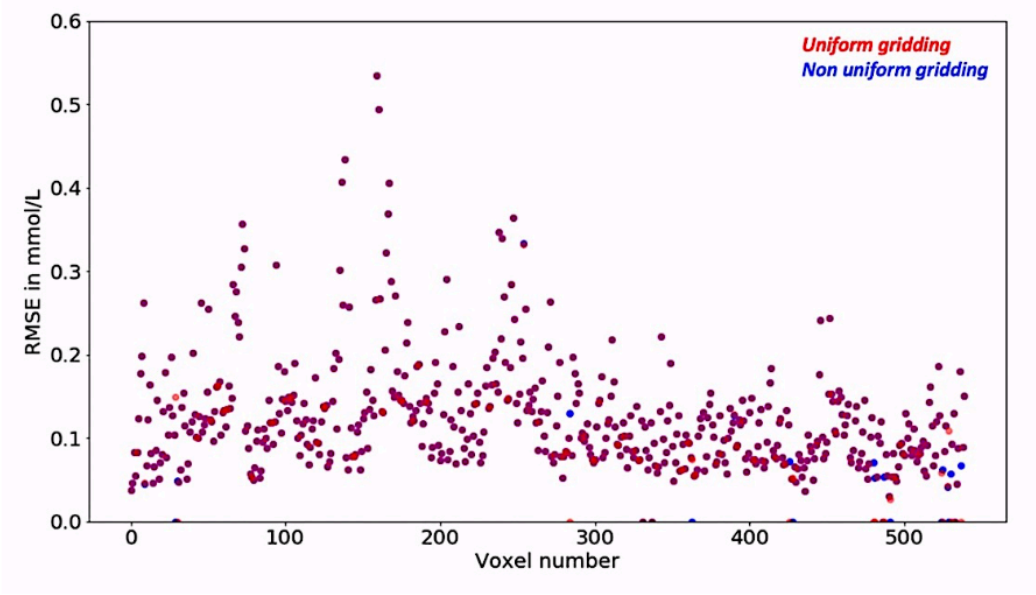

Figure 2.50: Per voxel RMSE of gridding approaches for curve-fitting. The x-axis represents the voxel identity numbers in the tumor, and the y-axis the corresponding RMSE in mmol/L. The median RMSE (IQR) were 0.11 mmol/L (0.08-0.15) both for the uniform and nonuniform gridding.

Figure 2.51 shows the $RMSE$ (equation (2.62) with N the number of voxels) per frame for the uniform and nonuniform gridding approaches.

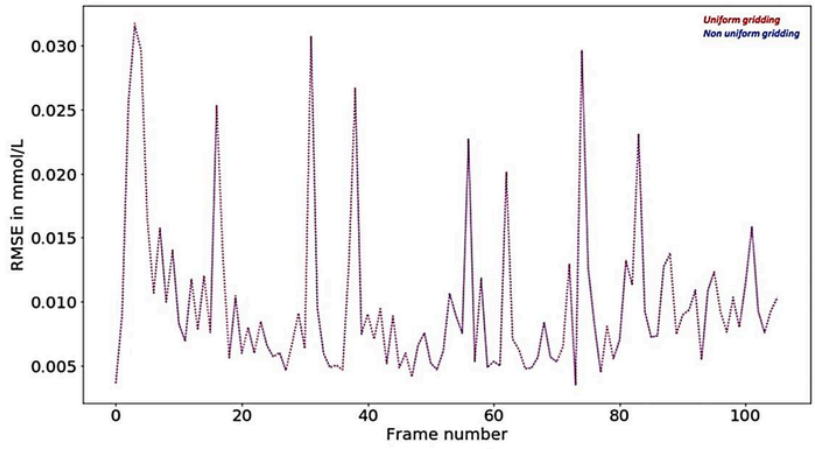

Figure 2.51: Per frame RMSE of gridding approaches for curve-fitting. The x-axis represents the frame identity numbers, and the y-axis the corresponding RMSE in mmol/L. The median $RMSE$ (IQR) for the 106 frames were 0.008 mmol/L (0.006-0.01) both for the uniform and nonuniform gridding.

Figure 2.52 provides the estimated [Gd] from the curve fitting procedure.

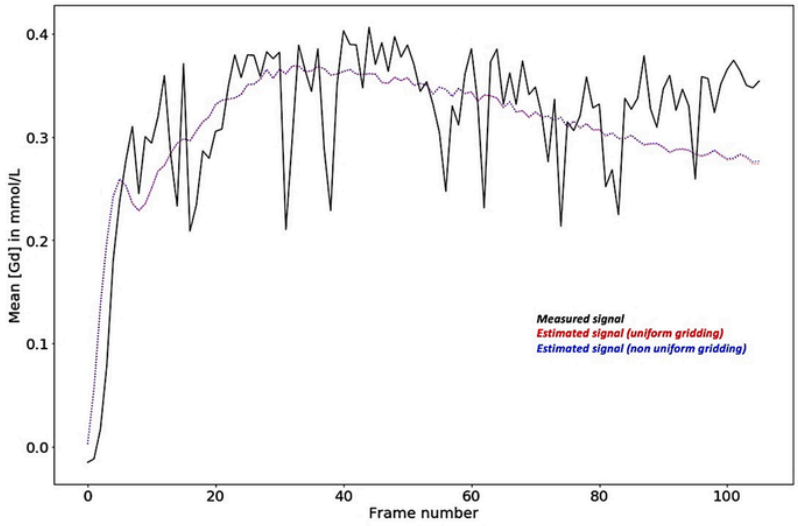

Figure 2.52: Result of the curve fitting procedure for the DCE of the patient test. The measured [Gd] (in black) is compared to the estimated [Gd] computed from the estimated kinetic parameters (K_{trans}, ve, v_p). Uniform and nonuniform gridding provided the same results strictly.

And finally, Figure 2.53 provides the related DCE 3D maps.

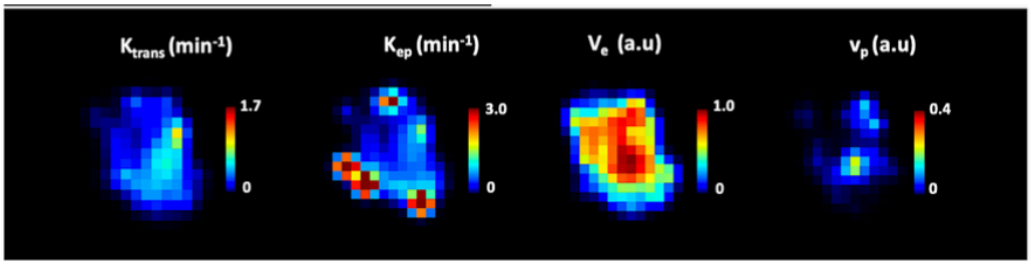

Figure 2.53: 3D maps of DCE kinetic parameters K_{trans}, k_{ep}, v_e and v_p for the tumor test (540 voxels of 2mm3). For better visual rendering, all the maps were smoothed with a 3 mm Gaussian filter.

For patients details, the curve fitting results of all patients are illustrated in the Appendix section A.8 (Figure A. 8 and Table A. 8).

2.2.3.5. Conclusion

Our preliminary tests for the implementation of DCE kinetic modeling showed that

- Our motion correction method was not very effective
- A denoising step based on an advanced MR denoising algorithm with spatial adaptation of the Rician distribution of the signal did not improve the signal intensity curves.
- Uniform and nonuniform signal sampling provided the same accuracy with 4000 sampled points.
- Considering the high degree of motion corruption in the signal intensity curves, the curve fitting procedure was acceptable at the voxel level, with low to moderate RMSE values for the majority of the voxels.

Based on these results, we decided to keep the same nonuniform gridding used for PET kinetic modeling for the rest of the project. Despite low performance, and because no advanced methods were available for this project, we systematically applied our motion correction method to the DCE data before kinetic maps computation. As for PET kinetic modeling, the pipeline was automated, transferred to the parallel calculation platform at Laboratoire de Mathématiques d'Orsay, and required the following input patient data to be launched:

- 4D DCE imaging data, standardized to 2 mm^3, into NIfTI format.
- Pre-contrast enhanced T_1-maps, also resampled to 2 mm^3.
- Tumor and AIF masks (previously generated by using ITK-SNAP (90).
- Gadolinium relaxivity R_{Gd} at 3T
- Hct
- DCE frame duration
- Frame number of the first-past aortic enhancement, defined visually
- Flip angle α of the 3D fast SPGR pulse sequence
- TR value of the 3D fast SPGR pulse sequence

Additional illustrations of voxel-wise fitting analyses for all the patients included in the DCE kinetic analyses are provided in Appendix section A.8 (Figure A. 8 and Table A. 8).

3. ^{18}F-FDG PET-MRI in Lung Cancer: towards of a full dynamic protocol

Based on the methodological challenges exposed and resolved in the first two chapters, we were able:

- To implement the full ^{18}F-FDG PET kinetic model to generate voxel-wise kinetic maps of K_1, k_2, k_3, v_b and $MRGlu$ in lung tumors.
- To correct the geometric distortions in DWI and improve the PET-MRI multimodal image matching of lung tumors, allowing DWI-related voxel-wise multimodal analyses of lung tumors.
- To generate reliable voxel-wise T_1/T_2 maps of lung tumors.
- To implement the extended Tofts model to generate acceptable kinetic maps of K_{trans}, v_e, k_{ep}, and v_p at the regional lung tumor level.

In this last chapter, we will now extract all these ^{18}F-FDG PET and MRI imaging biomarkers from treatment-naïve and biopsy proven NSCLC patients, combine them together and go further insight the characterization of biological heterogeneity of NSCLC.

3.1. Protocol design for clinical dynamic PET-MRI thoracic imaging

Currently, the duration of PET-MRI procedures for clinical oncology may be considered a strong limitation compared to what is done with last generation of PET/CT systems. However, the simultaneous PET-MRI acquisitions has brought up to date kinetic modeling approaches: because a PET-MRI acquisition is inherently long (35 to 50 minutes for a standard whole-body PET-MRI with basic morphological MR pulse sequences), we chose to use this long duration to perform state-of-the-art dynamic PET acquisitions. Therefore, we got around the issue of the one-hour post-injection delay requirement in clinical ^{18}F-FDG PET imaging, by immediately starting the dynamic thoracic PET acquisition after the intravenous injection of ^{18}F-FDG, and exploited this one-hour duration to perform numerous thoracic MRI acquisitions. For routine, because the ^{18}F-FDG PET-MRI replaced the standard ^{18}F-FDG PET-CT plus brain MRI, a whole-body post contrast-enhanced PET-MRI acquisition including the brain was added to the course, lengthening the protocol by about 30 minutes.

3.1.1. Patients recruitment

Patients with NSCLC were prospectively recruited in several medical centers from Île de France:

- Institut Gustave Roussy (clinical trial)
- Hôpitaux Universitaires Paris-Saclay (routine)
- Hôpital Marie Lannelongue, le Plessis Robinson (routine)
- Hôpital de Melun, Melun (routine)

A. Clinical research trial

I designed an interventional clinical research trial promoted by Gustave Roussy, in partnership with GE Healthcare and CEA, entitled "Multiparametric PET-MRI Integration for a New Approach to Tumor Heterogeneity in Non-Small Cell Lung Cancer (NSCLC): Pilot Study

(IMAHTEP, ClinicialTrials.gov identifier: NCT03606070). A total of 20 participants with locally advanced NSCLC (stages IIB, IIIA/IIIB of the TNM classification 7th edition) or trace metastatic stage IV (oligometastatic patients with up to 5 metastases in up to 3 organs) were planned to be recruited by Dr Caramella (radiologist, MD, MSc, appointed Principal Investigator by Gustave Roussy) between November 2017 and May 2019 (total duration of the clinical trial: 30 months, November 2017-March 2020). The participants were planned to undergo two thoracic ^{18}F-FDG PET-MRI dedicated examinations in addition to their standard imaging workup, performed before the chemoradiotherapy treatment (the baseline PET-MRI scan) and at mid-treatment (33±4 Gy, second PET-MRI scan). All details of the draft and agreements (in French) are available in Appendix (5.3).

Inclusion criteria were defined as follows:

- Patients with locally advanced NSCLC or oligometastatic disease with up to 5 metastases in up to 3 organs
- Exclusive therapeutic management by concomitant radio-chemotherapy
- Signed consent
- Patients affiliated with the social security scheme or beneficiary of a similar scheme

Exclusion criteria were defined as follows:

- Patients under 18-year old
- Pregnant or lactating women
- Persons deprived of liberty by judicial or administrative decision, adults who were subject of a legal protection measure or unable to give consent
- Previous cancer in the 2 years prior to registration
- Previous radiotherapy or thoracic surgery
- Patients under experimental treatment or for whom the administration of an experimental treatment is planned
- Contraindications for MRI (including contrast agent ones): claustrophobia; severe renal insufficiency (eGFR MDRD or Cockcroft < 30 mL/min); patients with metallic implants not compatible with MRI, electronic medical devices)

- Contraindications for ^{18}F-FDG PET imaging: Uncontrolled diabetes mellitus, hyperglycemia > 1.8 g/L.

B. Clinical routine

During 6 months (between November 2018 and April 2019), 29 consecutive patients with suspected NSCLC (highly suspicious lung nodule or mass on routine CT scan) who required a baseline ^{18}FDG PET imaging underwent a whole body ^{18}FDG PET-MRI including a one hour dedicated dynamic PET-MRI thoracic acquisition. The exclusion criteria were claustrophobia, metal implants, renal failure (eGFR MDRD or Cockcroft < 30 mL/min), and uncontrolled diabetes mellitus. The protocol complied with the Declaration of Helsinki principles, and it was approved by the local institutional review board. A written informed consent was obtained from all patients to use their anonymized medical data for research purpose.

3.1.2. Dynamic thoracic PET-MRI protocol

All images were acquired on the same hybrid 3T PET-MRI scanner (Signa PET/MR, GE Healthcare, Waukesha, WI, USA) by using a thoracic phased array from the GEM Coil Suite (GE Healthcare, Waukesha, WI, USA). All patients were positioned in supine position into the PET-MRI, with a respiratory belt positioned around the abdomen and a finger-type heart rate sensor positioned to the right index. A peripheral catheter was placed on the left arm and connected to the contrast agent automated power injector. The thoracic PET bed position was centered onto the lung tumor. Importantly, the MRI FOV position was locked in superior/inferior directions by the PET FOV, limiting the possibilities of FOV modifications during simultaneous PET-MRI acquisitions.

In all cases, the dynamic PET acquisition was started 10 seconds before the manual intravenous injection (left arm) of 3-4 MBq of ^{18}F-FDG per kilogram body weight not to miss the first-pass radiotracer. Then, the following MR pulse sequences were performed:

- Two-point Dixon pulse sequence for MR-AC
- T2 PROPELLER pulse sequence with respiratory triggering (expiration phase)

- SE-single-shot EPI acquisitions with both direct (anterior-posterior) and reversed phase-encoding polarity (posterior-anterior direction) for distortion correction (cf section 2.2.1.3) (93).
- EPI DWI for ADC map computation
- SMART1 pulse sequence (127) for pre-contrast T_1-mapping and MEFSE pulse sequence for T_2-mapping (for more details, please refer to section 2.2.2.3).
- Pre-contrast 3D T1-FSPGR pulse sequence (LAVA-FLEX)
- DCE acquisition (3D T1-FSPGR) performed before, during and after bolus injection of gadolinium (0.2 mmol/kg body weight, Dotarem, Guerbet GmbH; injecting rate of 2 ml/s by power injector) using under free breathing).
- Post-contrast 3D T1-FSPGR pulse sequence (LAVA-FLEX) in breath-hold position (expiration phase).

According to the local expertise, the dynamic PET data were histogrammed into multiframe sinograms as follows: 41 frames of 12 x 10 s, 12 x 20s, 4 x 60 s, 5 x 120 s, 8 x 300 s respectively. The multiframe sinograms were reconstructed using an iterative algorithm (3D ToF-OSEM, 6 iterations and 28 subsets with ToF and PSF modeling, and with random, dead time, scatter, decay, and attenuation corrections, matrix size = 256 x 256; voxel size = 2 x 2 x 2.78 mm), without post-filtering.

A summary of the ^{18}F-FDG PET-MRI imaging workflow is provided in Figure 3.1, and the corresponding main MRI acquisitions parameters are provided in Table 3.1.

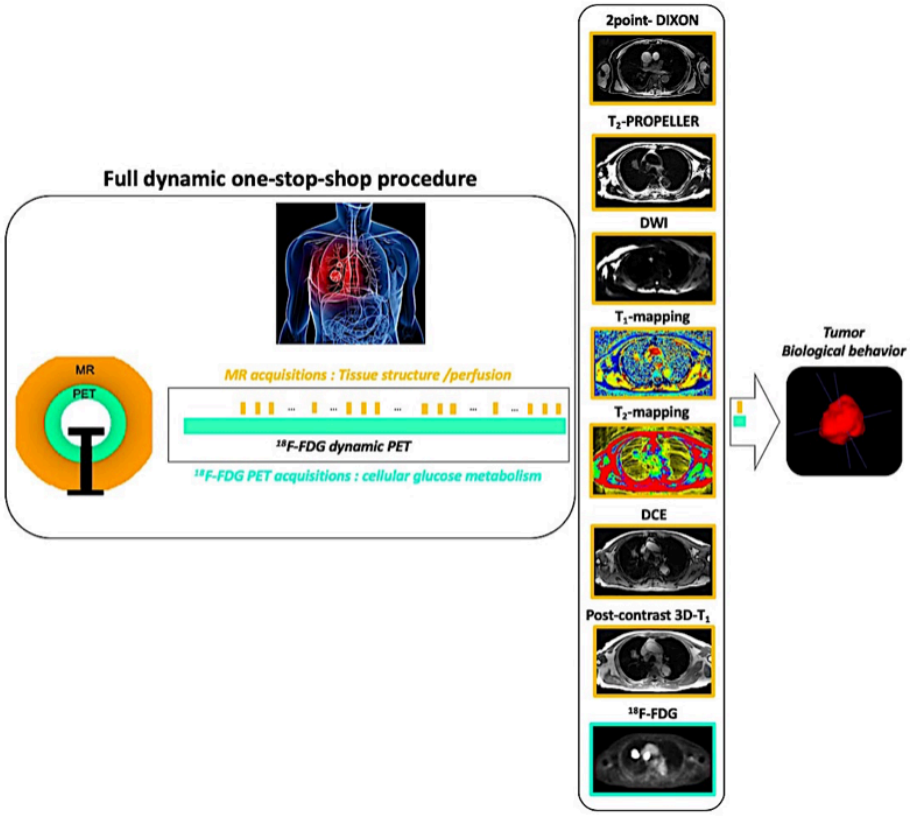

Figure 3.1: Full dynamic ^{18}F-FDG PET-MRI protocol applied to NSCLC. The patients underwent a one-hour thoracic ^{18}F-FDG PET-MRI acquisition, including: a dynamic ^{18}F-FDG PET acquisition, and the following MR pulse sequences performed simultaneously: a DIXON pulse sequence for MR-AC; a T_2-PROPELLER pulse sequence for anatomy; DWI pulse sequence with reverse phase-encoding acquisitions to compute ADC maps without geometric distortions; SR pulse sequences for T_1 mapping; MEFSE pulse sequences for T_2 mapping; DCE acquisitions performed before, during and after the intravenous injection of gadolinium; and a post-contrast T_1-weighted 3D SPGR pulse sequence for contrast-enhanced anatomy.

Université Paris-Saclay
Espace Technologique / Immeuble Discovery
Route de l'Orme aux Merisiers RD 128 / 91190 Saint-Aubin, France

Table 3.1: MR pulse sequences of the full dynamic PET-MRI protocol.

	MRAC (LAVA Flex)	T2-weighted (PROPELLER)	EPI / DWI	T1-mapping (SMART1)	T2-mapping (MEFSE)	3D-T1 (LAVA Flex)	DCE (FSPGR)
2D/3D	3D	2D	2D	2D	2D	3D	3D
Pulse sequence	GRE-Dixon	Fast recovery FSE	Stejskal-Tanner (single SE) single-shot	GRE - SR	MEFSE	GRE-Dixon	GRE
k space sampling	Cartesian	Radial	Cartesian	Cartesian	Cartesian	Cartesian	Cartesian
Scan Plane	Axial	Axial	Axial	Axial	Axial	Axial	Axial
Acquisition matrix*	256/128/64	320/308/15	90/128/15	128/128/6	128/128/6	256/224/56	192/128/24
ETL / Blades / echoes	n.a./n.a./n.a.	32/11/n.a.	n.a./n.a./n.a.	n.a./n.a./n.a.	16/n.a./8	n.a./n.a./n.a.	n.a./n.a./n.a.
Slice Thickness (mm)	5.2	5.0	5	5	5	3.2	5.0
Slice Gap (mm)	0	1	1	0	0	0	0
Acquisition FOV X/Y/Z (mm)	500/375/332.8	400/400/90	420/420/90	420/420/30	420/420/30	440/352/179.2	400/320/120
Respiratory trigger	No	Yes	Yes	No / Trigger cardiac (PPG)	No	No (Breath hold)	No
Flip angle (degrees)	5	90 (flip)/142(refocus)	90	45	90(flip)/180(refocus)	15	15
TR (ms)	4	8000 (For respiration rate of 15 cyc/min - every 2 cycles)	4000 (For respiration rate of 15 cyc/min)	2.9	5242 (RR interval=6 for 70 bpm)	4.48	3.456
TE (ms)	1.1/2.2	117	Minimum (~70ms)	1.1	11/23/35/46/58/70/81/93	1.2/2.4	1.104
TI (ms)	n.a.	n.a.	n.a.	~136/136/136/136/818/1583/2109/2808/20000	n.a	n.a	n.a
Bandwidht/2 (kHz)	166.67	41.67	250	100	62.5	142.86	125
Nex	0.7	2	2/2/2/2/4/5/6	1	1	0.7	0.69
b-values	n.a	n.a	20/40/80/100/300/500/800/1000	n.a.	n.a.	n.a.	n.a
Partial Fourier sampling	Yes	No	Yes	No	No	Yes	Yes
Acceleration Factor $x/y/z$	None/None/None	None/3/None	None/2/None	None/2/None	None/2/None	None/2/None	None/2/1
Parallel imaging algorithm	None	GRAPPA (ARC)	SENSE (ASSET)	SENSE (ASSET)	GRAPPA (ARC)	GRAPPA (ARC)	GRAPPA (ARC)
Reconstructed matrix $x/y/z$	256/256/128	400/400/15 ($kx/ky/kz$)	256/256/15 ($x/y/z$)	256/256/6 ($x/y/z$)	256/256/6 ($kx/ky/kz$)	256/256/224 ($kx/ky/kz$)	256/256/48 ($kx/ky/kz$)
Reconstructed voxel size (mm)	1.95/1.95/2.6	1.00/1.00/6.00	1.64/1.64/6.00	1.64/1.64/5.0	1.64/1.64/5.00	1.72/1.72/0.8	1.56/1.25/2.5
Duration (min:sec)	00:18	02:40	05:12	02:48	02:50	00:21	06:04 (3.03 s per frame)

3.1.3. Workflow for processing multimodal ^{18}F-FDG PET-MRI data

As explained through the manuscript, no vendor-workstation currently allows full multimodal PET-MRI post-processing workflows. Also, because acquisition matrices are adapted to each modality/pulse sequence, the reconstructed matrices and voxel sizes varied across the imaging modalities and MR pulse sequences. Therefore, the simultaneity of PET and MRI acquisitions on hybrid PET-MRI devices does not exempt from image post-processing to allow multimodal analyzes at the voxel level. For this reason, in-house voxel-wise post-processing multimodal imaging workflows were developed using the freely available Python programming environment, which has become very popular for its broad collection of image post-processing tools. Because Python libraries expect image files to be in the NIfTI format, all the PET and MRI imaging data were first converted from DICOM to NIfTI format, by using the open source software dcm2niix (161).

To allow multimodal comparisons at the tumor voxel level, the PET and MRI imaging data of each patient were standardized to their corresponding post-contrast-enhanced 3D-T1 weighted MRI before in-house maps computation (Figure 3.3):

- The denoised 4D PET, T1-map and MEFSE data were resampled to their corresponding 3D-T1 isotropic space.
- DWI raw data were corrected from geometric distortions by using the reverse phase encoding method described in section 2.2.1.2 and recently published (93).
- DCE data were motion corrected and co-registered to the reference space as described in section 2.2.3.3.

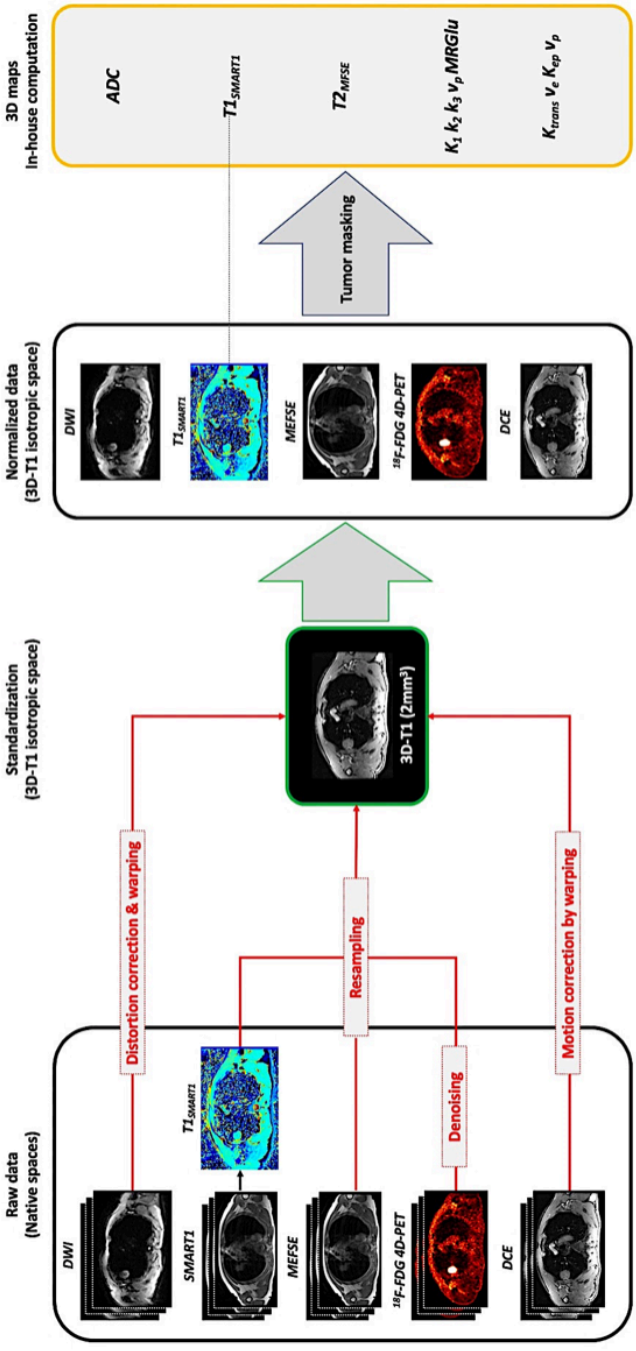

Figure 3.2: Image processing workflow for multimodal voxel-wise analyses. Imaging data were acquired, and standardized in the same isotropic reference space. Parametric maps were then computed from masked tumor data. For T_1-mapping, whole volume parametric map were directly generated by the vendor workstation. These maps were resampled to the reference space, and masked with the tumor masks to obtain the tumor parametric maps without off-line computation.

3.1.4. Tumor Segmentation task for PET-MRI voxel-wise multimodal analyses

To date, threshold-based methods are the most widely used to segment PET tumor data because of the inherent PET image properties and their facility to use (162). However, its accuracy and robustness were validated on optimized phantom experiments with idealistic conditions (especially homogeneity and sphericity) that are not frequently verified in clinical practice (162–164). To overcome this limitation, and based on the results of our previous PET validation study (67), the freely available semi-automatic active-contour algorithm ITK-SNAP (90) was used for all the PET and MRI segmentation tasks.

Briefly, the SNAP algorithm consists in modelling a closed surface that iteratively evolves to fit the lesion boundaries, driven by regularity constraints and image intensity properties. The lesion boundaries are defined either by converting the input image into gradient magnitude, either by thresholding the intensities of the input image into background and foreground. One or several spherical seeds are then positioned on the lesion of interest to initialize the segmentation task. For each tumor, because the number of slices were not homogeneous among the imaging modalities/MR pulse sequences, the tumor was first segmented on isotropic ^{18}F-FDG PET, $T1_{SMART1}$, MEFSE, DWI and post-contrast 3D-T_1 weighted MRI independently, and then combined the masks of interest into multimodal tumor masks.

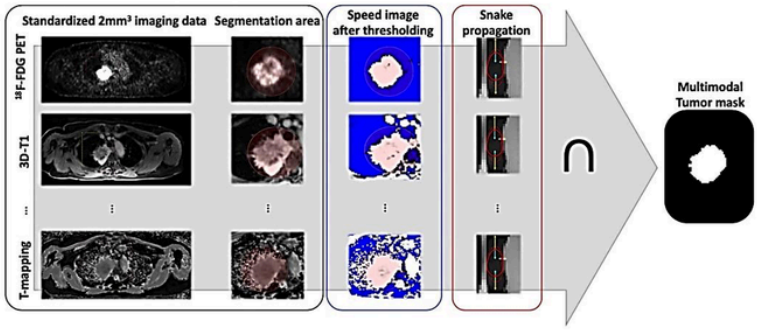

Figure 3.3: Semi-automated segmentation procedure for multimodal mask generation. For each patient, a region of interest was roughly defined on the standardized imaging data. For each modality, a thresholding speed image was automatically generated and manually tuned to emphasize the lesion boundaries. A close surface (the snake) was initialized around the tumor and automatically evolved to fit the lesion boundaries. Finally, the generated masks of the different modalities were intersected into one multimodal tumor mask.

3.1.5. Usable PET-MRI data

At the final step of this work, a total of 38 patients underwent a thoracic ^{18}F-FDG PET-MRI, which 29 came from clinical routine and 9 from the IMAHTEP research trial. Among them, only 18 patients could be exploited. Pie chart of the usability of the ^{18}F-FDG PET-MRI data is provided in Figure 3.4.

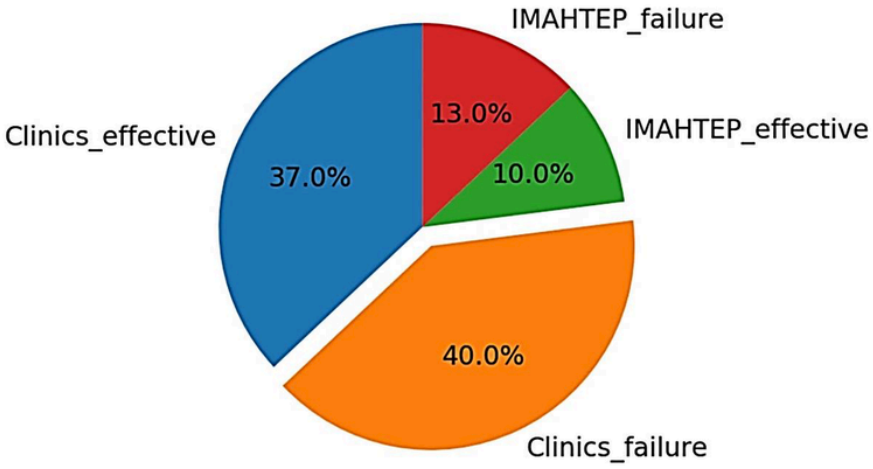

Figure 3.4: Pie chart of the patients' data (total = 38 patients).

Also, a general flowchart of the clinical PET-MRI experiments is available in Figure 3.5, and the main characteristics of the effective patients are available in Table 3.2

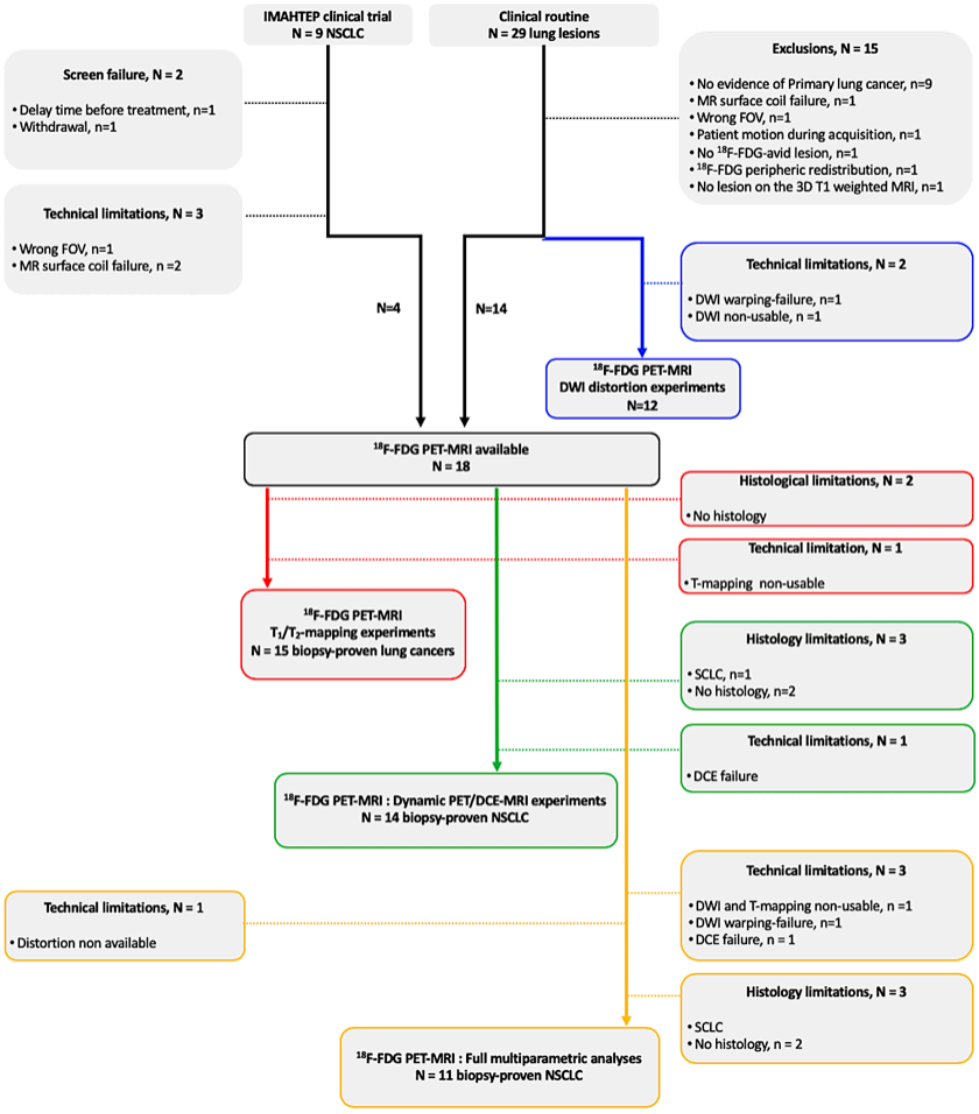

Figure 3.5: Flowchart of the PET-MRI clinical experiments. The blue boxes concern the DWI clinical experiments, the red boxes the T_1/T_2-mapping experiments, the green boxes the PET/DCE experiments, and the yellow boxes the full dynamic multiparametric experiments.

Patient	Age	Gender	Tumor		Experiments			
			Topography	Histology	DWI distortion	T1/T2-mapping	PET / DCE interlinks	Full multiparametric
1	82	Male	Right upper lobe	NSCLC (Poorly differentiated carcinoma)				
2	47	Male	Right upper lobe	NSCLC (unknown)				
3	71	Female	Right lower lobe	Undifferentiated carcinoma				
4	67	Female	Left upper lobe	NSCLC (ADK)				
5	80	Female	Left upper lobe	NSCLC (SCC)				
6	69	Male	Left upper lobe	Unknown				
7	53	Male	Right medial lobe	NSCLC (ADK)				
8	78	Female	Left upper lobe	NSCLC (ADK)				
9	54	Male	Right upper lobe	Unknown				
10	74	Female	Right lower lobe	SCLC				
11	55	Male	Right upper lobe	NSCLC (ADK)				
12	63	Male	Left upper lobe	NSCLC (Poorly differentiated SCC)				
13	57	Male	Left upper lobe	NSCLC (ADK)				
14	83	Male	Left upper lobe	NSCLC (SCC)				
15	62	Male	Right peri-hilar	NSCLC (ADK)				
16	61	Male	Right upper lobe	NSCLC (SCC)				
17	71	Female	Right upper lobe	NSCLC (ADK)				
18	71	Male	Right upper lobe	NSCLC (ADK)				

Included

Not included

Table 3.2: Patients' characteristics.

3.2. Toward a dynamic ^{18}F-FDG PET-MRI voxel-wise regional characterization of NSCLC

In the last section of this project, and based on the whole methodology exposed in the previous parts, we propose to go further insight the characterization of NSCLC by exploring the potential interlinks between the PET and MRI image-based biomarkers computed from the multimodal PET-MRI imaging protocol.

3.2.1. Deciphering metabolic and perfusion/vascularization biomarkers interlinks

3.2.1.1. Context

In the era of precision medicine, multiparametric imaging offers many opportunities to better characterize the biological process of tumors. In lung cancer, previous ^{18}F-FDG PET/MRI imaging studies have been performed mainly for disease clinical staging (8,20,21,23,165), SUV-ADC correlation analyses (166–169) and prognostic value (170).

Although metabolism and vascularization are two fundamental hallmarks of cancer (171),

- Only few multimodal imaging studies compared them in primary NSCLC (144,172–175),
- Of which only two combined dedicated ^{18}F-FDG PET and DCE-MRI imaging data (144,175).

So far, full dynamic ^{18}F-FDG PET and DCE-MRI analyses have never been performed simultaneously at the regional tumor level, and may be of particular interest to better characterize the spatial heterogeneity of these two cancer hallmarks in NSCLC (176,177)

3.2.1.2. Methods

In this part, we thus assessed the metabolism/vascularization regional interlinks in 14 patients of this project, representing a total of 21 571 voxels of 2 mm^3 (88 to 5 356 voxels). Main char-

acteristics of the patients are provided in Table 3.2. After the general image processing described on Figure 3.3, two level of dedicated analyses were performed.

A. At the whole dataset level

A correlation matrix (spearman, r_s) of all the PET and DCE kinetic parameters was computed at (14 patients, 21 571 voxels) after data z-scaling (zero mean and unit variance) and cleaning-up from outliers (z-score > 3). The PET/DCE r_s coefficients were estimated along with their respective bootstrapped 95% confidence intervals (n = 1000 iterations).

B. At the tumor regional level

The PET/PET, DCE/DCE and PET/DCE voxel-wise interlinks were estimated for each of the 14 tumors. Absolute r_s estimated values ($|r_s|$) were considered low under 0.4, moderate between 0.4 and 0.7, and high above 0.7 (*178*).

3.2.1.3. Results

A. At the whole dataset level

The full characteristics of ^{18}F-FDG PET/DCE kinetic parameters are provided in Appendix section A.11 (Table A. 9). The main characteristics of ^{18}F-FDG PET/DCE kinetic parameters are summarized in Figures 3.6 and 3.7.

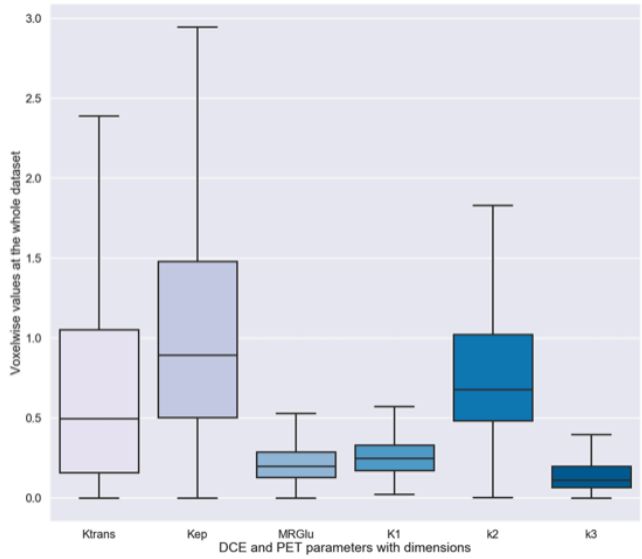

Figure 3.6: Boxplots of dynamic DCE and ^{18}F-FDG PET parameters with dimensions (median with IQR). $Ktrans$ and Kep values were 0.44 min^{-1} (0.14-0.92) and 0.79 min^{-1} (0.44-1.3) respectively. $K1, k2, k3,$ and $MRGlu$ values were 0.25 $mL.min^{-1}.mL^{-1}$ (0.17-0.33), 0.68 min^{-1} (0.48-1.02), 0.11 min^{-1} (0.07-0.2), 0.20 $\mu mol.mL^{-1}.min^{-1}$ (0.13-0.29) respectively.

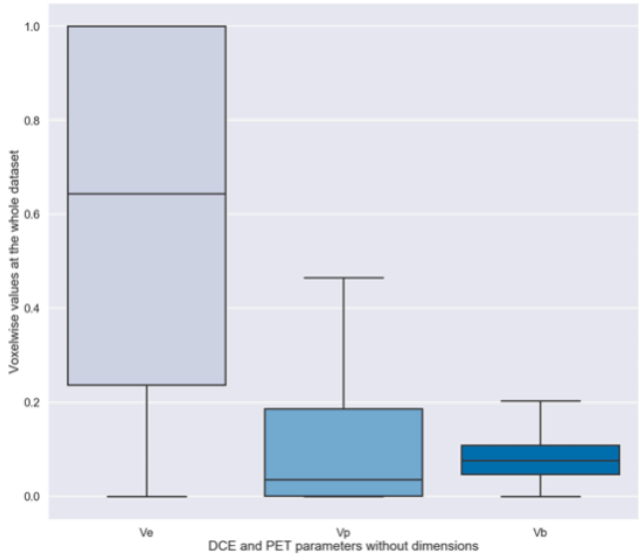

Figure 3.7: Boxplots of dynamic DCE and ^{18}F-FDG PET parameters without dimensions (arbitrary units, median with IQR). v_e, v_p and v_b values were 0.08 (0.05-0.10), 0.64 (0.24-1.0) and 0.04 (0.0007-0.19) respectively.

The correlation matrix of the ^{18}F-FDG PET and DCE kinetic parameters is provided in Figure 3.8.

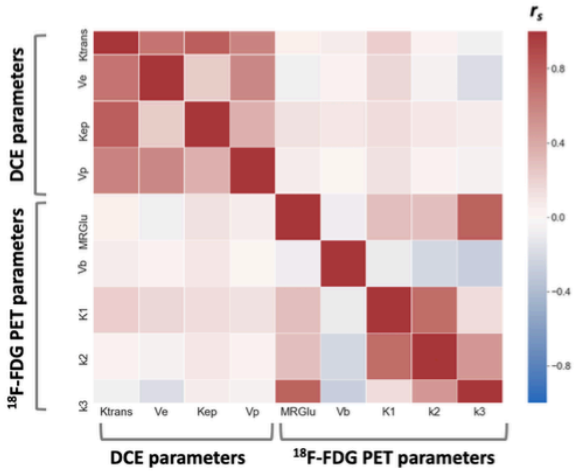

Figure 3.8: Spearman correlation matrix of the PET and DCE dynamic parameters. monotonic relationships varied function of the kinetic parameters considered.

The PET/DCE r_s coefficients are provided in Table 3.3 along with their respective bootstrapped 95% confidence intervals (n = 1000 iterations).

DCE parameters \ ^{18}F-FDG PET parameters	$MRGlu$	v_b	K_1	k_2	k_3
K_{trans}	0.05 [0.04; 0.07]	0.08 [0.06; 0.09]	0.22 [0.20; 0.23]	0.05 [0.03; 0.06]	-0.06 [-0.08; -0.05]
v_e	-0.09 [-0.1; -0.08]	0.04 [0.02; 0.05]	0.18 [0.16; 0.19]	-0.05 [-0.07; -0.03]	-0.20 [-0.21; -0.18]
K_{ep}	0.13 [0.11; 0.14]	0.11 [0.09; 0.12]	0.15 [0.13; 0.16]	0.10 [0.09; 0.12]	0.06 [0.05; 0.08]
v_p	0.06 [0.05; 0.07]	0.001 [-0.01; 0.02]	0.13 [0.12; 0.15]	0.02 [0.006; 0.03]	-0.05 [-0.06; -0.03]

Table 3.3: PET/DCE interlinks. Estimated rs values and their 95% confidence intervals are provided. All PET/DCE interlinks were weak at the whole dataset level.

B. At the tumor regional level

Figure 3.9 provides the results of the PET/PET, DCE/DCE and PET/DCE regional interlinks.

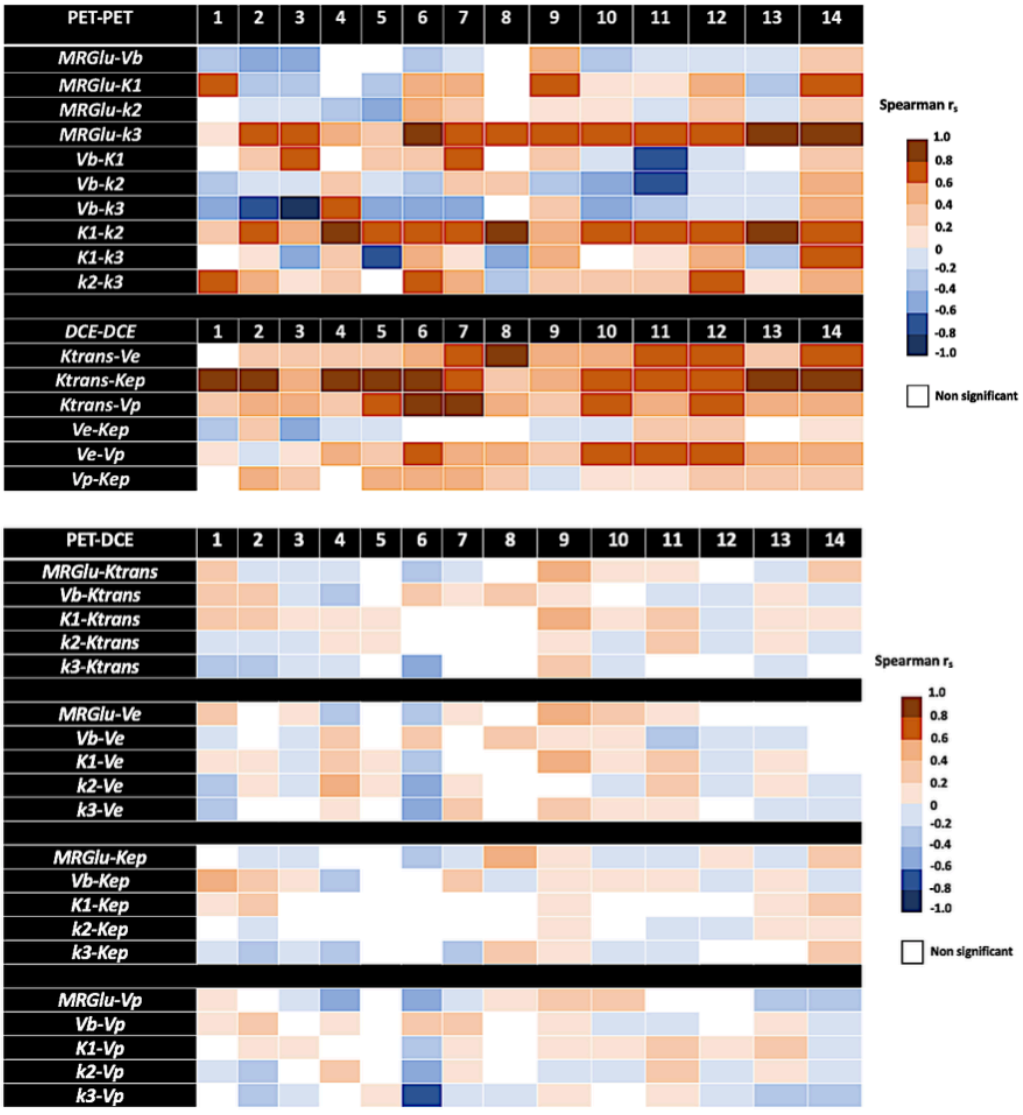

Figure: 3.9 PET/PET, DCE/DCE and PET/DCE regional interlinks at the tumor level.

Figures 3.10 and 3.11 illustrate two interesting tumor cases (n°5 and 18) with a majority of moderate to high PET/PET and DCE/DCE interlinks, but with poor PET/DCE interlinks profiles. Interestingly, K_{trans} and k_3 regional kinetic parameters showed high inverse relationship. This

multimodal pattern of poorly perfused/vascularized area together with high cellular density and metabolic activity suggested an aggressive hypoxic tumor area. PET/DCE maps of all patients are available in the Appendix section A.11 (Figure A. 9).

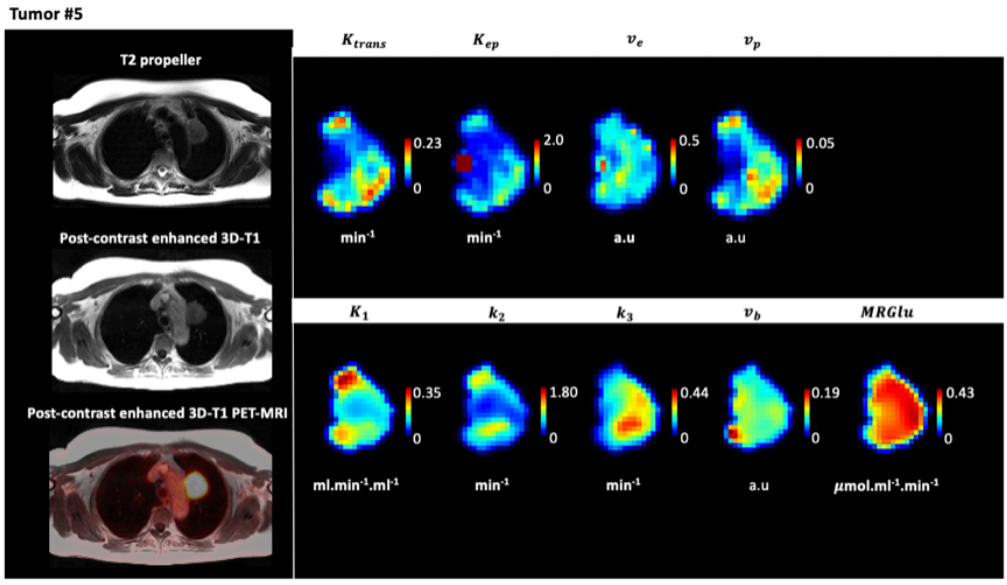

Figure 3.10: DCE and ^{18}F-FDG PET multiparametric maps of the left upper lobe tumor (patient 5). For illustration, all parametric maps were smoothed with a 3mm Gaussian filter.

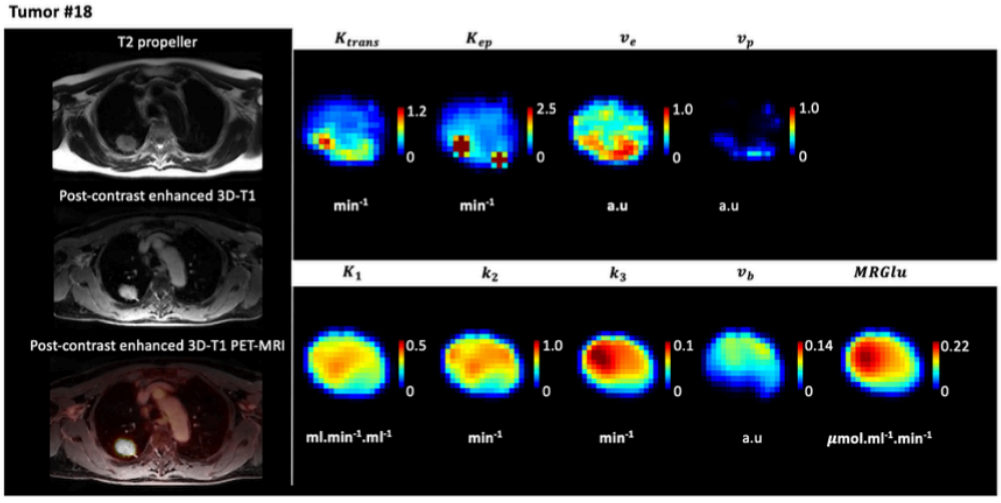

Figure 3.11: DCE and ^{18}F-FDG PET multiparametric maps of the right posterior upper lobe tumor (patient 18). For illustration, all parametric maps were smoothed with a 3mm Gaussian filter.

3.2.1.4. Conclusion

In this part, we could assess the metabolism/vascularization regional interlinks in 14 NSCLC, both at the whole dataset (21 571 pooled voxels of 2 mm^3) and at the individual tumor regional level (tumors of 88 to 5 356 voxels of 2 mm^3).

At the whole dataset level,

- DCE/DCE interlinks were moderate to high mainly. Only K_{ep}/v_e and K_{ep}/v_p showed weak correlations (r_s = 0.23 and 0.37 respectively).
- PET/PET interlinks were more heterogeneous: K_1/k_2 and $k_3/MRGlu$ interlinks were high (r_s = 0.72 and 0.77 respectively), k_2 and k_3 were moderately correlated (r_s=0.49) and K_1 and k_3 were weakly correlated (r_s =0.15). Also, PET interlinks with v_b parameter were weak in all the cases.
- PET/DCE interlinks were also weak in all the cases.

At the tumor regional levels, a wide variability in PET/PET, DCE/DCE and PET/DCE regional interlinks was observed. Interestingly, $K_1 - K_{trans}$ regional interlinks were mainly weak. Although being in line with previous Head and Neck ^{18}F-FMISO (179) and preclinical VX-2 ^{13}N-NH_3 (180) PET / DCE-MRI studies, this trend is not surprising considering the three following key concepts:

- First, "Perfusion" reflects a weighted mixture of blood flow and Permeability-Surface area product (137,181,182) that depends, in the case of fixed flow and microvascular characteristics, on the tracers exchange properties (^{18}F-FDG is actively transported across the cellular membrane, whereas Gd is a purely extra cellular diffusive contrast agent).
- Second, DCE Tofts models do not consider the intra-cellular space (ICS) (143,183), whereas standard compartmental PET models (*24*) do not distinguish the extravascular extracellular space (EES) from the ICS, assuming steady state between EES and ICS at the injection time.
- Consequently, K_1 depends on a mixed perfusion-extraction weighting of ^{18}F-FDG that may, in the case of high metabolic rate conditions, overestimate the perfusion component (181).

In 7 of the 14 tumors, k_3 and K_{trans} showed area of low to moderate inverse relationship. In all the case, the regional profile was a high k_3 to low K_{trans} uncoupling ratio, a well-known hallmark of tumor hypoxia/aggressiveness (184). Also, v_b and v_p parameters were low to moderately positively correlated for 7 tumors, inversely correlated for tumors, and non-significant for 2 tumors. We explain these heterogeneous interlinks by the same tracer exchanges considerations exposed above. The inverse relationship observed for the last tumor (tumor n°18) may be explained by the EES/ICS consideration exposed above: because this tumor presented a large area of high metabolic activity (k_3) with poor perfusion/vascularization in DCE (K_{trans} and v_p), the vascular/perfusion parameters assessed with PET probably reflected the high extraction rate of the tumor cells rather than the true regional vascular profile.

Anyway, these dynamic PET/DCE-MRI voxel-wise analyses showed that individual metabolism/vascularization regional interlinks appear highly heterogeneous, and emphasize the wide heterogeneity of NSCLC tumor being.

3.2.2. Intra Tumor partioning – What are we measuring?

3.2.2.1. The supervoxel opportunity

In this last part, to go further insight the regional characterization of NSCLC tumor being based on PET-MRI dynamic imaging, our aim was to explore the overall meaning of the voxel-wise regional interlinks between the biomarkers of structure (ADC, T_1 and T_2 relaxation times), glucose metabolism (K_1, k_2, k_3, v_p and $MRGlu$), and perfusion/vascularization ($K_{trans}, v_e, K_{ep}, v_b$) by exploring their spatial relationship at the supervoxel level, defined here as a group of voxels with similar ^{18}F-FDG PET-MRI multimodal properties.

In other words, based on our exhaustive combination of ^{18}F-FDG PET and MRI biomarkers extracted from biopsy-proven and treatment naïve NSCLC,

- Can we partition any NSCLC tumor into fewer relevant super voxels of biological significance?

- If the answer is yes, what are we measuring mainly at the supervoxel level?

For this purpose, we could exploit the data of 11 tumors (17 316 pooled voxels, Figure 3.5). The characteristics of patients are available in Table 3.2. Also, for all patients, the corresponding parametric maps with the overall 12 features are available in Appendix section A.13 (Figure A. 10).

Starting from the information provided by 12 image-based features (ADC, T_1 and T_2 relaxation times, $K_{trans}, v_e, K_{ep}, v_b, K_1, k_2, k_3, v_p$ and $MRGlu$) at the whole dataset level, a two-step methodological procedure was followed :

- **Tumor clustering:** each tumor was first partitioned into regional clusters by using unsupervised clustering procedure. Multiparametric profiles of the clusters were assessed. Also, for 2 of the 11 patients, the clustering results could be compared to histology to assess the biological relevance of our tumor partitioning.
- **Dimensionality reduction by features selection:** secondly, advanced machine learning methods were used to identify, among all the features, the most relevant that best defined the tumor supervoxels.

3.2.2.2. Identification of supervoxels by tumors clustering

A. Main concepts

Clustering consists in organizing a set of data into fewer homogeneous groups. Within each cluster, the data are grouped according to a similar characteristic, which is maximized into the cluster and minimized between the clusters (185). Data similarity is typically based on the notion of distance (norms-, correlations-, or sets-based distances). Clustering methods may be basically classified into three main categories, depending on the algorithmic process:

- Partition-based approaches (exclusive/hard or overlapping/fuzzy)
- Hierarchical-based approaches (agglomerative or divisive)
- Model-based approaches (probability distributions)

Many clustering methods are available in the scikit-learn library of Python (https://scikit-learn.org/stable/modules/clustering.html#overview-of-clustering-methods). The most widely

used method remains K-means clustering, a partition-based approach that separates samples in n distinct groups / clusters by minimizing the within-cluster-sum-of-squares (i.e. the Euclidean distance between each point and the arithmetic mean position/centroid of its cluster). Although being easy to implement, K-means clustering has many limitations, in particular the lack of cluster structure flexibility; the equal variance requirement of all the clusters; the random initialization of the centroids positioning; and the need to choose the number of clusters "a priori", although the "elbow method" based on the optimal inertia (sum of squared distances of samples to their closest cluster center) or the Gap statistic (186) may be used.

Gaussian Mixture Model (GMM) is a model-based clustering approach (187). Given the general equation of a Gaussian mixture distribution

$$p(x) = \sum_{k=1}^{K} \pi_k N(x|\mu_k, \Sigma_k) \quad (3.1)$$

Where x is the vector of voxel data points, K is the number of Gaussians to be modeled, π_k is the proportion of the voxel data points that belongs to the component k, and $N(x|\mu_k, \Sigma_k)$ is the multivariate Gaussian distribution of x, with mean vector μ_k and covariance matrix Σ_k

GMM fit the voxel data to $p(x)$ and find the posterior distribution of the responsibilities that each Gaussian has for each data point by expectation-maximization (Figure 3.12).

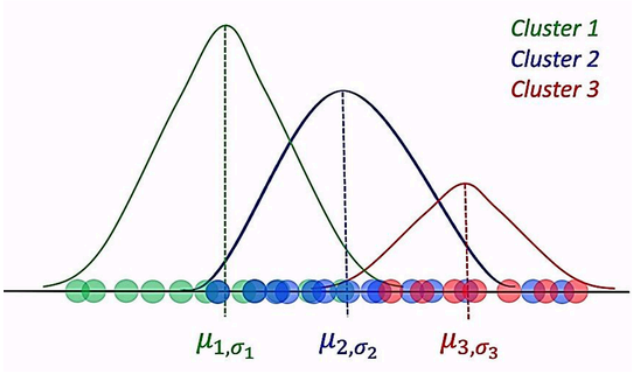

Figure 3.12: Concept of Gaussian Mixture Model clustering. All the voxels are assigned to a Gaussian $X_{i\sim}(\mu_i;\ \sigma_i)$.

B. Methods

GMM is more flexible than K-means, allowing different cluster structures (spheres or ellipses with any orientation) and variances. Two recent PET/MRI studies (188,189) with histology val-

idation (189) showed GMM to be relevant for tumor partioning into several tissue classes. Because our preliminary clustering experiments based on K-means appeared non-relevant (data not shown), we tested GMM on our dataset. Because we had no "a priori" on the optimal number of clusters to partition the tumors based on our 12 features of interest, 11 Gaussian distributions partitions (n-1 features) were tested and compared using both the Akaike Information and Bayesian Information criteria (AIC and BIC) (190,191)

$$AIC = 2k - 2log(\hat{L}) \text{ (3.2)}$$

$$BIC = log\,(n)k - 2log(\hat{L}) \text{ (3.3)}$$

Where n is the sample size, k is the number of parameters estimated by the model, $\hat{L}$ is the maximum value of the likelihood function of the model M, defined by $\hat{L} = p(x|\hat{\theta}, M)$, with x the observed data and $\hat{\theta}$ the parameter values that maximize the likelihood function.

Figure 3.13 shows the results of the GMM clustering results using k = {1, …12}.

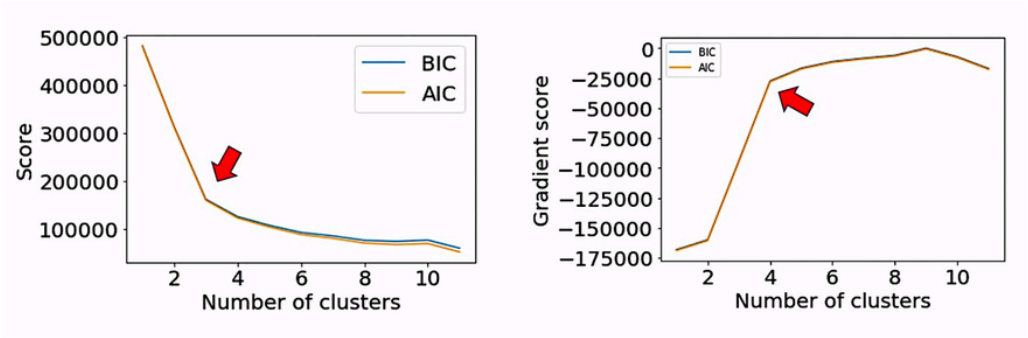

Figure 3.13: AIC and BIC scores as function of the number of clusters. The red arrows indicate, both for the AC/BIC score (left part) and their gradient versions (right part).

An optimal number k of clusters would be $3 \leq k \leq 4$. We thus compared all the cluster maps of the 11 tumors with k = 3 and k = 4 clusters. Because the differences were not relevant, we thus considered k = 3 to be the most relevant, and kept this number for the rest of the project.

C. Results

Based on the whole dataset (11 tumors, 17 316 pooled voxels), the unsupervised GMM clustering algorithm provided 3 main regional clusters that could be applied to each tumor. The

multimodal features correlations (spearman coefficient, r_s) for the 3 clusters, together with their respective number of voxels at the whole dataset level, are provided in Figures (3.14), (3.15) and (3.16). Also, a summary of the biomarker values (median, IQR) at the whole dataset level is provided in Table 3.4.

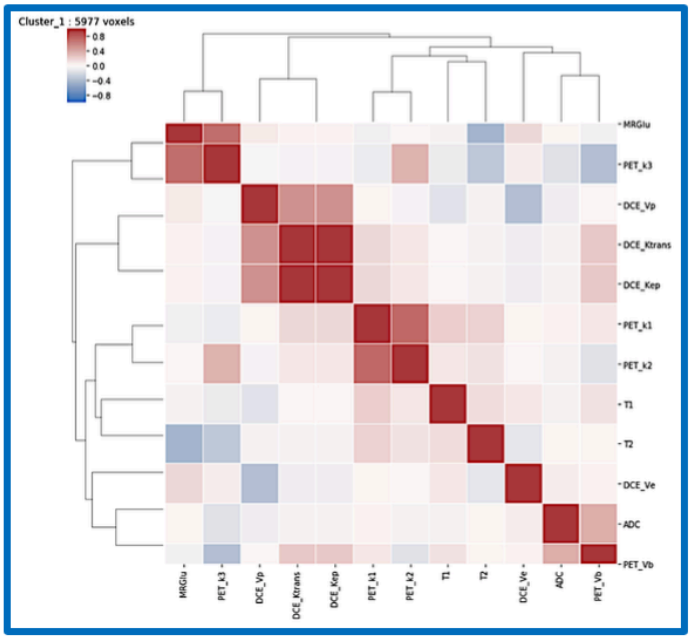

Figure 3.14: Multimodal PET/MRI features interlinks at the whole dataset level for cluster 1.

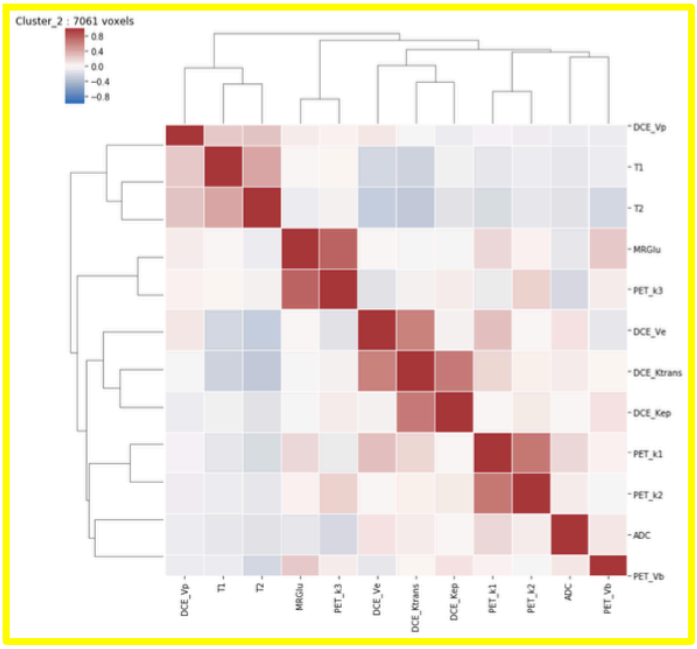

Figure 3.15: Multimodal PET/MRI features interlinks at the whole dataset level for cluster 2.

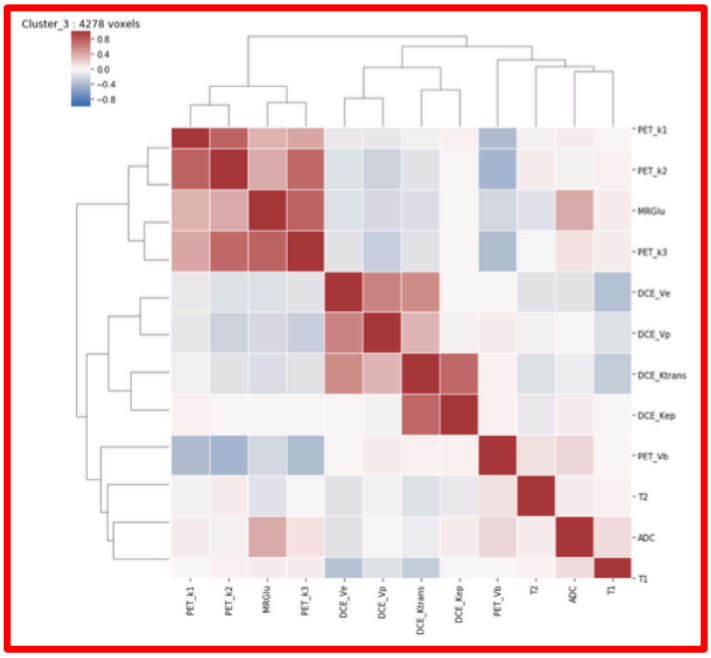

Figure 3.16: Multimodal PET/MRI features interlinks at the whole dataset level for cluster 3.

Features	Cluster 1	Cluster 2	Cluster 3
Voxels number	5977	7061	4278
ADC ($\times 10^{-3}$mm².s^{-1})	1.24 [0.6-1.7]	1.4 [0.8-1.9]	1.6 [1.2-2.2]
T1 (ms)	1523 [1386-1678]	1734 [1493-1944]	1663 [1301-1964]
T2 (ms)	80 [73-91]	92 [81-101]	92 [85-99]
K_{trans} (min^{-1})	1.07 [0.75-1.50]	0.26 [0.11-0.54]	0.37 [0.18-0.77]
v_e	1.0 [1.0-1.0]	0.35 [0.16-0.63]	0.33 [0.20-0.63]
K_{ep} (min^{-1})	1.07 [0.75-1.5]	0.70 [0.42-1.24]	1.03 [0.63-1.76]
v_p	0.29 [0.09-0.7]	0.007 [0.0-0.03]	0.06 [0.02-0.13]
K_1 (ml.min^{-1}.ml^{-1})	0.28 [0.22-0.37]	0.24 [0.17-0.31]	0.29 [0.22-0.37]
k_2 (min^{-1})	0.71 [0.51-1.0]	0.63 [0.5-0.8]	1.38 [0.76-2.05]
k_3 (min^{-1})	0.11 [0.07-0.17]	0.1 [0.07-0.16]	0.37 [0.17-0.62]
$MRGlu$ (μmol.ml^{-1}.min^{-1})	0.22 [0.16-0.27]	0.18 [0.13-0.27]	0.34 [0.24-0.46]
v_b	0.08 [0.05-0.11]	0.07 [0.04-0.1]	0.06 [0.04-0.09]

Table 3.4: Mean profile of each cluster at the whole dataset level. All the between cluster differences were statistically significant (Mann Whitney test, $p < 0.05$) except for K_{ep} between Clusters 1 and 2.

These unsupervised statistical clustering results show distinct biological behaviors among the three supervoxels:

- Cluster 1 (blue color code) appears characterized by low to moderate values of ADC reflecting higher cellularity, low T_1/T_2 relaxation times, with dominant interstitial space (v_e) and high permeability (K_{trans}), whereas the cellular metabolic activity remains low (k_3 and $MRGLU$). The associated high vascular density/perfusion (K_{trans}, v_b, v_p) may thus suggest interstitial/fibrotic areas, the former known to be interlinked with neo-angiogenesis (192–194).
- Cluster 2 (yellow color code) appears characterized by significant lower cellularity (ADC values are quite superior) compared to the cluster 1, with moderate to high interstitial component (v_e). The vascular density appears strongly lower compared to the cluster 1 (v_p), together with the perfusion (K_1, K_{trans}). Also, the glucose metabolic activity is low (k_3, $MRGLU$). This cluster may correspond to lower vascularized interstitial/fibrotic tumor area.

- Finally, Cluster 3 (red color code) appears characterized by a lower cellular density (ADC), significant higher metabolic activity (k_2 and k_3) combined with very low vascular density (v_p and v_b), well-known characteristics of tumor adaptation to hypoxia/tumor aggressivity (184,195).

D. Confrontation to histology

For 2 of the 11 patients (patients 5 and 13), Dr MR Ghigna (Department of Pathology, Hôpital Marie Lannelongue) could make a direct confrontation to histology. For this purpose, surgical specimens of lobectomy were oriented before slicing, with identification of the hilum, mediastinal side, lateral side, posterior and anterior side, by a method developed by Dr S. Mussot, at Hôpital Marie Lannelongue, Le Plessis Robinson, Université Paris-Saclay, France. The surgical specimens were then dissected starting from the apical (cranial) segment to the basal (caudal) segment, resulting in multiples slices of 8 mm thickness, as illustrated in Figure 3.17.

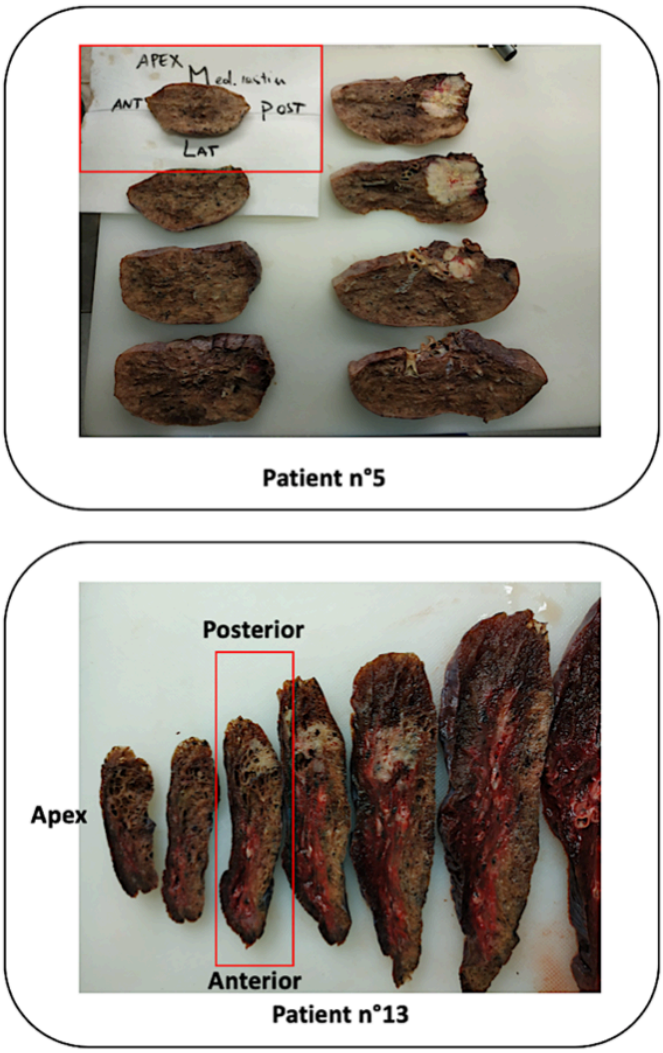

Figure 3.17: Surgical specimens with conservation of the anatomical orientation.

For each specimen, the tumor was measured and then dissected. A tissue block map was performed for each tumor. The tissue blocks were then formalin fixed and paraffine embedded; 4 µm-thick blocks sections were stained with hematoxylin-eosin (Figure 3.18).

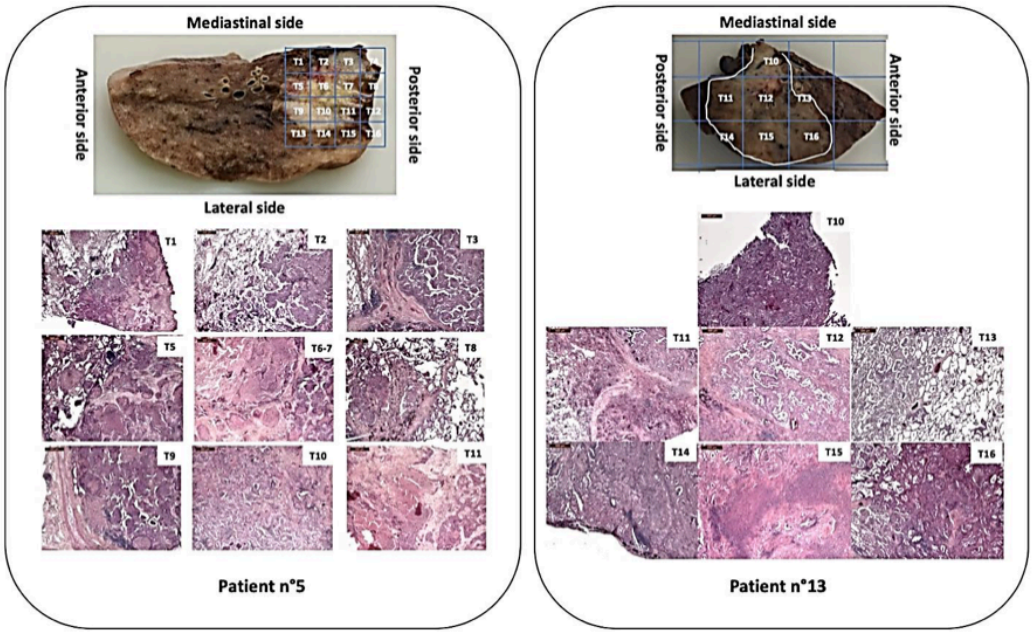

Figure 3.18: Staining with hematoxylin-eosin

The immune-staining using the antibody CD34 was performed in selected block tissues to evaluate the vessels density. Figures (3.19) and (3.20) provide direct confrontation between the PET-MR based cluster results and the main histological profiles of the tumor slices.

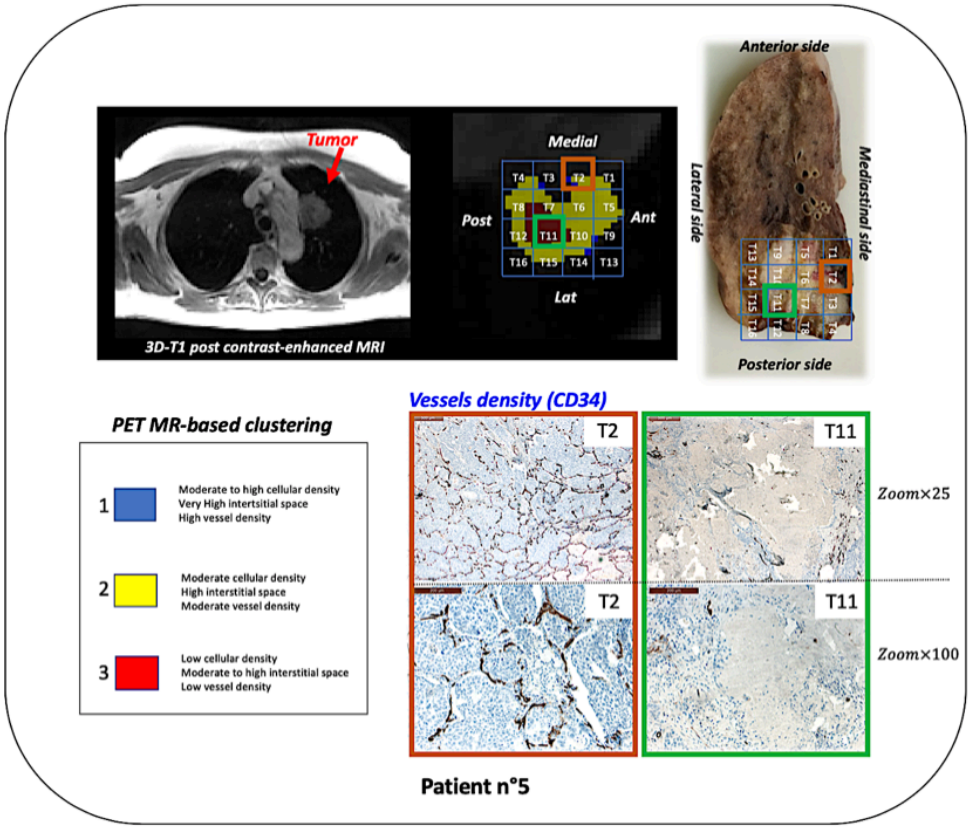

Figure 3.19: Face to face comparison between imaging and histology for the patient 5. For vessels density pictures, zoom is $\times 25$ *on the top and* $\times 100$ *on bottom.*

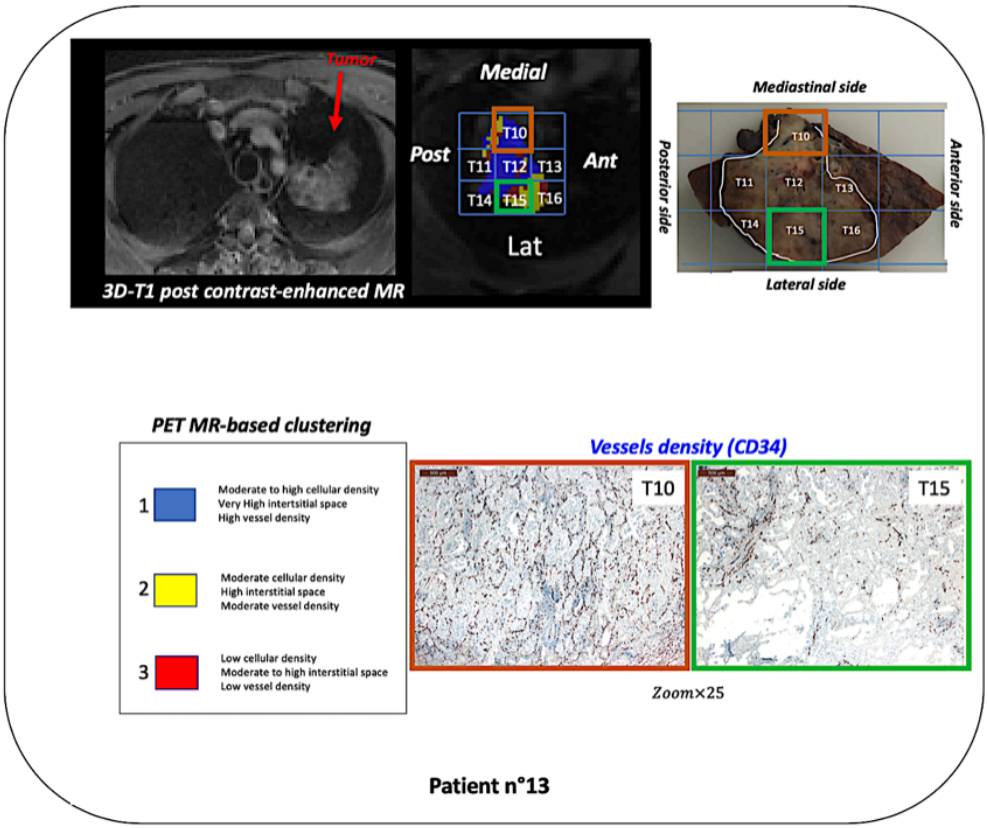

Figure 3.20 Face to face comparison between imaging and histology for the patient 13. For vessels density pictures, zoom is × 25.

Figures (3.18), (3.19), and (3.20) show overall good visual agreement between our PET-MRI based clustering approach and the histological characteristics of the specimens:

- On Figures (3.18) and (3.19) (patient 5), block T2 (cluster yellow with blue on PET-MRI images) is characterized by a moderate to high cellular density, with a relatively high vascular density revealed by CD34 immunostaining (Figure 3.19), that correspond to a mix between tumor and fibrotic tissue area. Block T11 (cluster red on PET-MRI images) shows large parts of necrosis (Figure 3.18) with low vessel density, the majority of tumors cells being grouped nearby the rare neovascular structures (Figure 3.19).
- On Figures (3.18) and (3.20) (patient 13), block T10 (blue cluster on the PET-MRI images) is also characterized by a moderate to high cellular density, with a relatively

high vascular density revealed by CD34 immunostaining (Figure 3.20). Block T15 (mix of clusters red and yellow clusters on the PET-MRI image) has also concordant histological characteristics: Figure 3.18 shows vast areas of necrosis / interstitial tissue surrounding tumor cells. On Figure 3.20, the left upper part of the block (red cluster on the PET-MRI images) shows higher concentration of tumor cells with neovessels, whereas the right part of the block (yellow cluster on the PET-MRI images) shows low vascular and cellular density.

Our one-stop-shop ^{18}F-FDG PET-MRI imaging protocol provided at least 12 ^{18}F-FDG PET/MRI imaging biomarkers of NSCLC in a 1-hour acquisition. Based on our unsupervised GMM clustering approach, these multimodal imaging biomarkers of tissue structure, perfusion/vascularization and glucose metabolism, all simultaneously combined together for the first time in NSCLC, could identify 3 general intra-tumor sub-regional profiles. We could thus respond "YES" to the first of the two questions asked at the beginning of this section.

Now remains the second one to elucidate: what are we measuring mainly in these 3 super voxels?

3.2.2.3. Supervoxel characterization by features selection

In this last part of the project, we tried to solve this particular issue by finding the most relevant combination of features that best defined our 3 clusters. For this purpose, metaheuristic procedures derived from machine learning and data mining were used (196).

A. Main concepts

Numerous statistical approaches have been proposed to select features, and may be divided into three main categories: filter, wrapper and embedded methods (Figure 3.21) (197):

- In filter methods, the relevance of features is entirely defined by their intrinsic properties via numerous univariate statistics (information gain, chi-square test, Fisher score, correlation coefficients, ANOVA and linear discriminant analyses). Consequently, the feature selection is not driven by the output task, and multicollinearity is not considered.

- Wrapper methods (backward elimination, forward selection, bidirectional elimination, recursive feature elimination) integrate the model performance into the feature selection process. Although features interactions are considered here, the model has to be trained and cross-validated for any feature subset combination, making this approach computationally expensive.
- Finally, the embedded methods (regularization for generalized linear models and decision trees) are also based on the model performance to select the most relevant features. Contrarily to wrapper methods, the features selection process is intrinsically driven by the learning process, optimizing the number of features subsets. Therefore, embedded methods are less computationally intensive and less prone to overfitting.

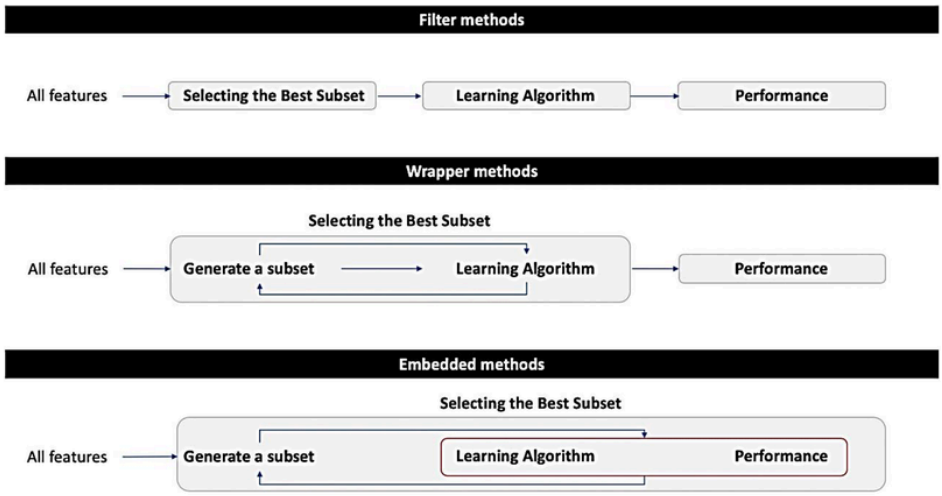

Figure 3.21: Feature selection methods.

B. Methods

Based on those considerations, embedded methods were retained to find the best combination, among the dozen of ^{18}F-FDG PET and MRI imaging biomarkers we extracted, that optimize our multiclass classification task. For this purpose, three different supervised machine learning algorithms were tested: two penalized regression procedures (Least Absolute Shrinkage and Selection Operator-LASSO and Elastic Net) and one decision tree algorithm (XGBoost).

In our supervised learning classification task, the aim was thus to predict the cluster category (1, 2 or 3) from a large dataset of input voxels, each characterized by 12 PET-MRI features.

1. *Models and parameters*

In supervised learning, given Θ the parameters to learn from the data, the objective or loss function is formalized as follow:

$$Obj(\Theta) = L(\Theta) + \Omega(\Theta) \text{ (3.4)}$$

Where the training loss L measures the goodness of fit on training data, and the regularization Ω controls the complexity / stability of the model.

The most widely used regularization methods are

$$L1\ norm\ (Lasso) : \Omega = \lambda \|\Theta\|_1 \text{(3.5)}$$

$$L2\ norm\ (Ridge) : \Omega = \lambda \|\Theta\|_2 \text{ (3.6)}$$

○ *Linear classifiers: LASSO and Elastic Net*

LASSO (*198*) and Elastic Net (199) penalized regressions consist in adding L1 (LASSO) or L1 + L2 (ElasticNet) regularizations to a linear regression model. Given n the overall training data, i the i^{th} training example, y_i the ground truth, $\hat{y}_i$ the prediction for the i^{th} training example, d the dimension of the training data, and w their corresponding weights, equations (3.4) and (3.5) yield

$$Obj_{LASSO}(y_i, \hat{y}_i) = \sum_{i=1}^{n} l(y_i, \hat{y}_i) + \lambda \sum_{j=0}^{d} |w_j| \text{ (3.7)}$$

Where $\sum_{j=0}^{p} |w_j| < t$, t being a fixed value (the upper bound for the sum of the coefficients); λ is the tuning parameter that controls the strength of the regularization, by shrinking some of the coefficients w_j to 0. Larger is λ, more the number of coefficients w_j are shrunk to 0. If λ=0, we are in the case of a non-penalized regression.

In the same way, equations (3.4) and (3.6) yield

$$Obj_{ElasticNet}(y_i, \hat{y}_i) = \sum_{i=1}^{n} l(y_i, \hat{y}_i) + \lambda_1 \sum_{j=0}^{d} |w_j| + \lambda_2 \sum_{j=0}^{d} {w_j}^2 \text{ (3.8)}$$

Where λ_1 and λ_2 are the two tuning parameters that control the regularization.

Because we are in the case of a multiclass classification task, a logistic loss was chosen, and more precisely a cross-entropy loss function defined by

$$l(y_i, \hat{y}_i) = -(y_i \log(\hat{y}_i) + (1 - y_i) \log(1 - \hat{y}_i)) \quad (3.9)$$

Finally, equations (3.7) and (3.9) yield

$$Obj_{LASSO}(y_i, \hat{y}_i) = \sum_{i=1}^{n} \left[-(y_i \log(x_{ij} w_j) + (1 - y_i) \log(1 - x_{ij} w_j)) \right] + \lambda \sum_{j=0}^{d} |w_j| \quad (3.10)$$

And equations (3.8) and (3.9) yield

$$Obj_{ElasticNet}(y_i, \hat{y}_i) = \sum_{i=1}^{n} \left[-(y_i \log(x_{ij} w_j) + (1 - y_i) \log(1 - x_{ij} w_j)) \right] + \lambda_1 \sum_{j=0}^{d} |w_j| + \lambda_2 \sum_{j=0}^{d} {w_j}^2 \quad (3.11)$$

- ***Extreme Gradient Boosting***

Decision-trees-based machine learning algorithms are graphical predictive modeling approaches widely used for regression and classification tasks. Tree-based algorithms have evolved over the years, and ensemble methods have been developed to improve their accuracy:

- Bootstrap aggregating (bagging) is an ensemble meta algorithm that combine predictions from multiple decision trees through majority voting mechanism (200).
- Random forest is a bagging-based approach where only subset of features are randomly selected to build multiple decision trees (201).
- Boosting consist in combining weak predictor models into stronger ones to improve the prediction task. Predictor models are generated, weighted, aggregated and improved iteratively on a learning set of data whose weights are corrected progressively (202).
- Gradient Boosting combines boosting meta-algorithms with gradient descent optimization function (203,204).
- Extreme Gradient Boosting (XGBoost), developed at the University of Washington, is the last generation of decision-tree-based meta algorithms (*205*). XGBoost uses optimized gradient boosting framework through systems optimization and algorithmic improvement: hardware optimization, parallelized tree building, improvement of Tree pruning computation, regularization to prevent overfitting (L1 and L2), quantile sketch algorithm for weighted datasets, cross-validation capability

For tree-boosting, equation (3.4) has to be adapted to decision-tree algorithms:

First, let consider a general tree structure defined as

$$f_t(x_i) = O_{q(x)}, O \epsilon R^T, q: R^d \rightarrow \{1, 2, \dots T\} \text{ (3.12)}$$

where x_i is the i^{th} observation of a training dataset, T the number of leaves, O the vector of output scores on leaves, and q a function assigning each data x_i to the corresponding leaf.

Second, in tree-learning, given equation (3.12), the prediction value at step t, is defined by

$$\mathcal{Y}_i(t) = \sum_{k=1}^{t} f_k(x_i) = \mathcal{Y}_i^{(t-1)} + f_t(x_i) \text{ (3.13)}$$

And third, in Gradient boosting, the aim is to find optimal O values that minimize the loss function, by gradient descent optimization. The regularization term Ω is here defined by

$$\Omega(f) = \gamma T + \frac{1}{2}\lambda \sum_{j=1}^{T} O_j^2 \text{ (3.14)}$$

Where γ is an hyperparameters that control the degree of tree pruning, and λ is a regularization parameter that prevent overfitting.

Finally, given equations (3.12), (3.13), and (3.14), equation (3.4) becomes

$$Obj_{XGBoost}(y_i, \mathcal{Y}_i)^t = \sum_{i=1}^{n} l\left((y_i, \mathcal{Y}_i{}^{(t-1)} + f_t(x_i)\right) + \sum_i^t \Omega(f_i) \text{ (3.15)}$$

As we are in the case of a classification task, loss function is again a logistic loss. A general overview of XGBoost is provided in Figure 3.22 (for more details, please refer to https://xgboost.readthedocs.io/en/latest/tutorials/model.html.

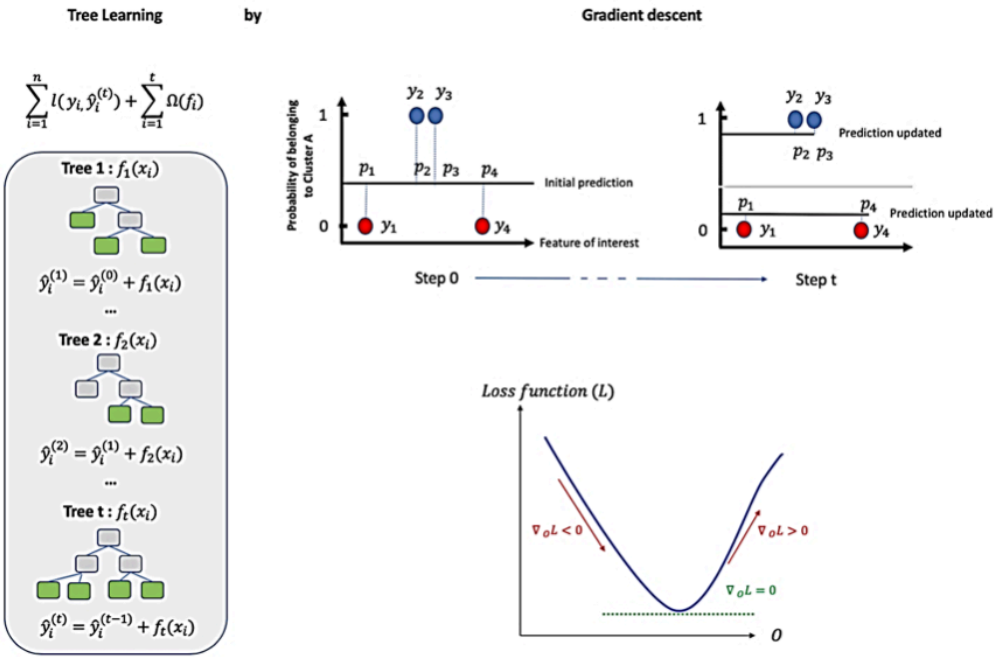

Figure 3.22: Tree Learning by gradient boosting. At each step, the values of output scores of the leaves are optimized by gradient descent, starting from the values of the previous tree. At the end, for each observation, the predictions reach the observed classifications.

2. Processing

Overall procedure (Figure 3.23) was performed off-line on a standalone personal computer (Intel Core i5, central processing units at 2.7GHz; 8 GB of RAM) using Python (library Scikit-learn (206) and XGBoost (205)), and included the following methodological steps:

- A dataframe was first generated from the multimodal dataset (11 tumors), defined by n = 17 316 rows (one row per voxel) and m = 13 columns (12 columns of ^{18}F-FDG PET and MRI features including $MRGlu, v_b, K_1, k_2, k_3, ADC, T_1, T_2, K_{trans}, v_e, K_{ep}, v_p$; and one column for the cluster label). For consistency sake, all the outliers defined by a z score > 3 SD (10% of the whole dataset) were set to 3 SD.
- ^{18}F-FDG and MRI data were defined as input variables (X) and the cluster labels (1, 2 or 3) as the predicted values (y).
- To avoid overfitting, the whole dataset was randomly splitted into training and testing sets by applying an empirical 75% / 25% ratio. Two samples of 12 987 and 4 329

voxels were generated respectively. Because regularization of linear classifiers is affected by the magnitude of the data, the features were normalized for LASSO and ElasticNet classifications tasks.

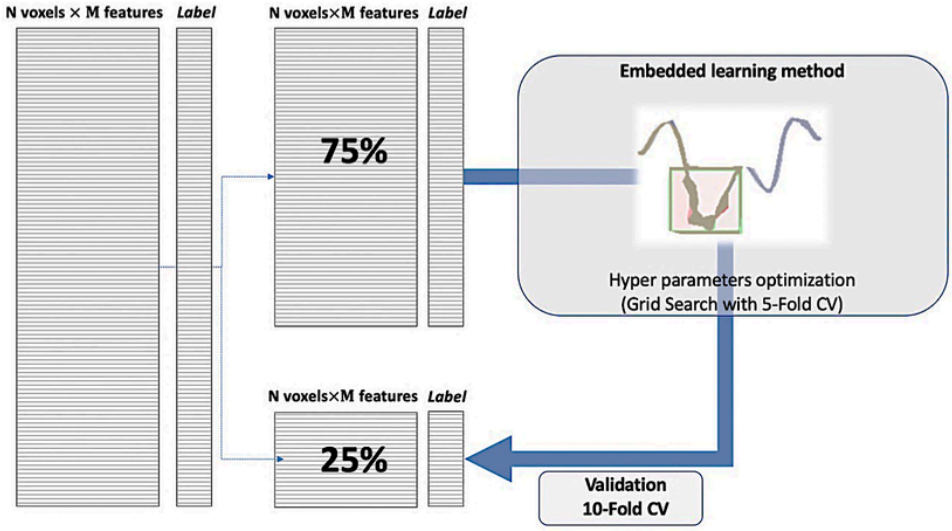

Figure 3.23: Overview of the feature selection methodology.

3. Results

○ Linear classifiers

Linear classifiers (LASSO and ElasticNet) were tested in a one-stop-shop fashion by using the Logistic Regression classifier function (equation (3.9) from the scikit learn library (*206*) (multiclass option = "multinomial", solver: "saga"). A 5-fold cross-validated grid search optimization was performed (score function: "accuracy") to find the best linear predictive classifier with optimized hyper parameters in a one-stop-shop procedure. After preliminary experiments, the following hyperparameters values were tested:

- Penalty: {L1 norm, ElasticNet}
- C for regularization strength: {0.01, 0.5, 0.8, 1, 1.2, 1.5, 2, 2.5, 5, 10, 25}
- L1 ratio for ElasticNet mixing parameter: {10^{-10}, 10^{-9}, 10^{-7}, 10^{-6}, 10^{-5}}

The grid search procedure provided the following hyperparameters:

- Penalty: L1 norm
- C for regularization strength: 0.8
- L1 ratio for ElasticNet mixing parameter: 10^{-10}

The pre-trained model with these optimized hyperparameters provided an accuracy score of 94 % (for comparison, a simple LASSO regressor without optimization provided an accuracy score of 83 %) to predict the cluster profile of a voxel. Figure 3.24 provides the overall features weighting for each of the three clusters. Importantly, the model retained all the 12 features to reach this accuracy score. When applying this pre-trained model to the validation set with a 10-Fold cross validation procedure, we finally obtained an overall mean accuracy of 94% (SD = 0.5%).

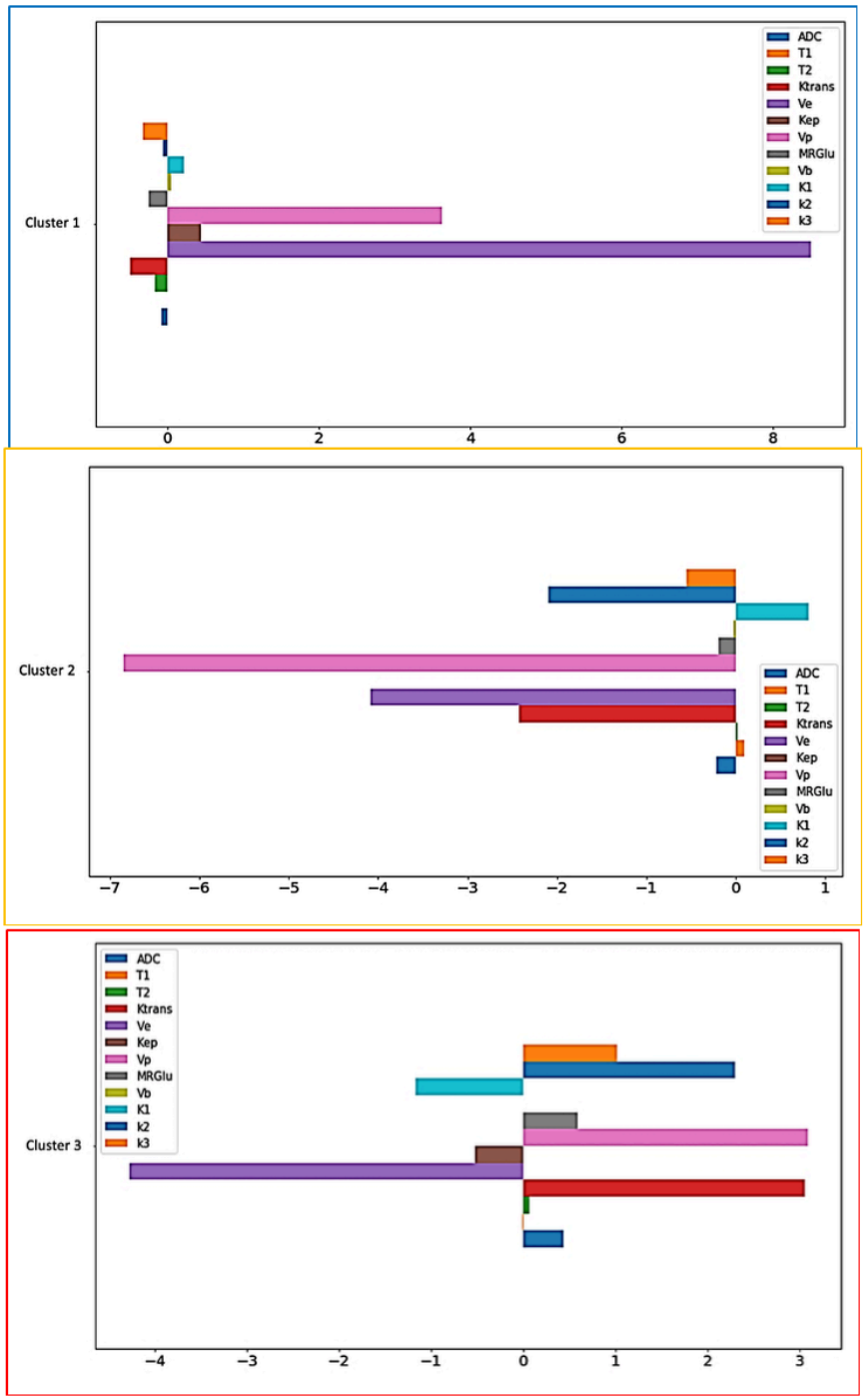

Figure 3.24: Features importance according to the magnitude of the linear regression coefficients.

- ***XGBoost***

The XGBClassifier function from xgboost library was used (205). For our multiclass task, only the main parameters were specifically defined (objective function = "multi: softprob", number of class = 3). Also, to find the best compromise between features selection and accuracy of the model, multiple feature importance thresholds were explored. Figure 3.25 provides the pre-trained model accuracy, function of the number of features selected.

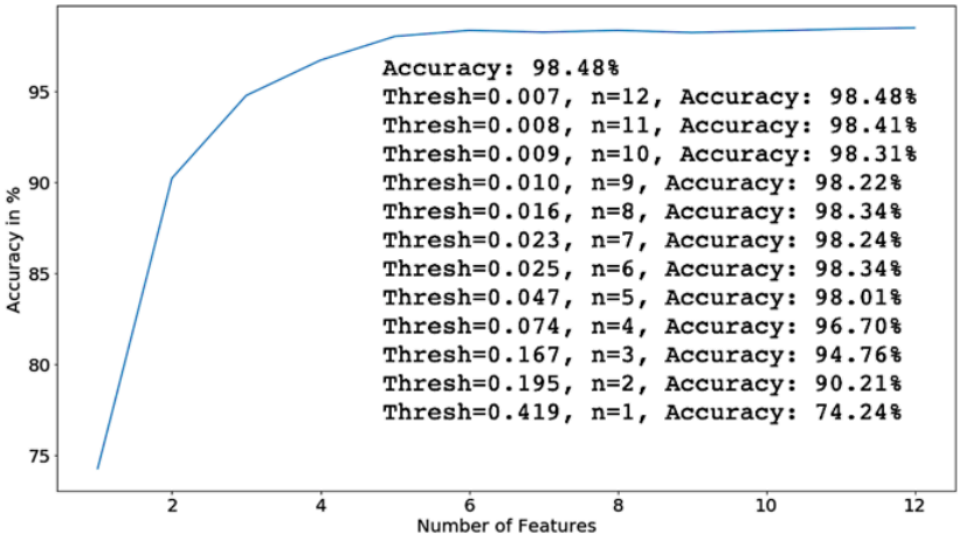

Figure 3.25: Accuracy of the XGBoost classifier function of the number of features selected. feature importance thresholds are based on the Number of times a feature is selected for splitting, weighted by the squared improvement to the model as a result of each split, and averaged over all trees (207).

The best accuracy reached 98.5% when considering 12 features. However, starting from 74.2% with one feature, accuracy exceeded 95% when considering 4 or more features.

Figure 3.26 provides the feature importance scores obtained for the 12 features.

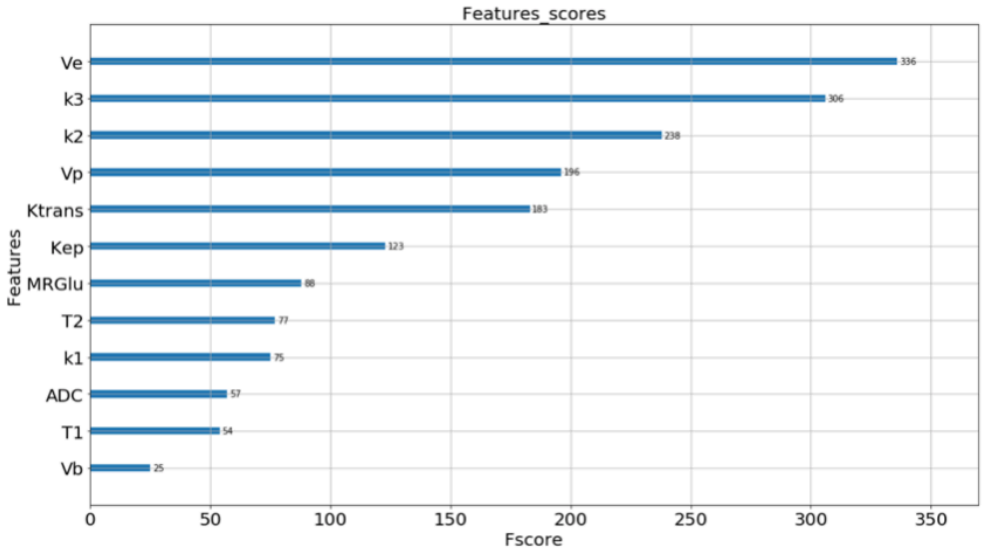

Figure 3.26: Features importance plot. F-scores (x -axis) correspond to the number of times the features (y -axis) are used to split the data across all trees. the most important features considered by the model are v_e, k_3, k_2 and v_p parameters.

Based on these results,

- A target threshold of 0.05 was set to reach an overall accuracy of 97%, by using the 4 most important ^{18}F-FDG PET and MRI features identified above
- And the classifier was restarted.

Figure 3.27 provides the feature importance scores of the dimensionality reduced model.

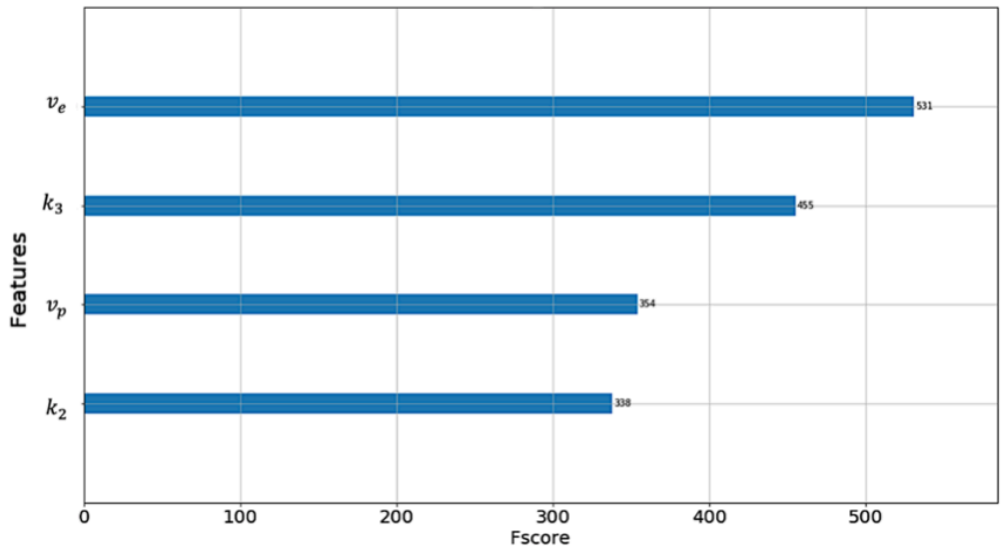

Figure 3.27: Features importance plot of the selected features. F-scores (x-axis) correspond to the number of times the features (y-axis) are used to split the data across all trees.

When applying the pre-trained XGBoost selected model to the validation set with a 10-Fold cross validation procedure, we finally obtained a mean overall accuracy of 97% (SD = 0.7).

The same clustering process as initially performed for the overall features (12 features) was then re-applied, but this time with the 4 features selected by XGBoost. Results are provided in Figure 3.28 and Table 3.5.

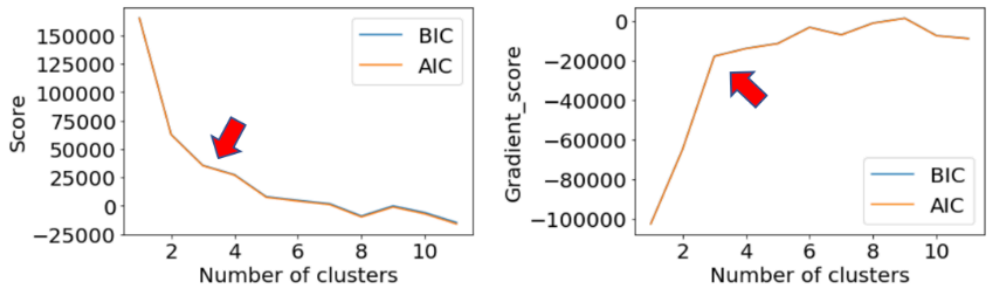

Figure 3.28: AIC and BIC scores as function of the number of clusters for the 4 selected features.

		Cluster 1	Cluster 2	Cluster 3
Number of voxels of 2mm³		**6232** *5977*	***6895*** *7061*	**4189** *4278*
MRI	v_e	1.0 [1.0-1.0] *1.0 [1.0-1.0]*	0.46 [0.23-0.71] *0.35 [0.16-0.63]*	0.22 [0.14-0.35] *0.33 [0.20-0.63]*
	v_p	0.30 [0.09-0.7] *0.29 [0.09-0.7]*	0.01 [0.0-0.05] *0.007 [0.0-0.03]*	0.02 [0.005-0.05] *0.06 [0.02-0.13]*
PET	k_2 (min^{-1})	0.73 [0.52-1.0] *0.71 [0.51-1.0]*	0.62 [0.5-0.8] *0.63 [0.5-0.8]*	1.33 [0.79-1.97] *1.39 [0.76-2.06]*
	k_3 (min^{-1})	0.11 [0.07-0.17] *0.11 [0.07-0.17]*	0.09 [0.07-0.13] *0.1 [0.07-0.16]*	0.35 [0.23-0.60] *0.38 [0.17-0.63]*

Table 3.5: Mean profile of each cluster at the whole dataset level. All the between cluster differences were statistically significant (Mann Whitney test, $p < 0.05$). Initial values (12 features) are provided in grey for comparison.

As illustrated in Figure 3.28, unsupervised GMM clustering provided the same number of clusters. Also, the biological behavior among the three supervoxels was similar (Table 3.5). Comparison of the 3D cluster maps (12 or 4 features) is provided in Appendix section A.14 (Figure A. 11).

3.2.2.4. Conclusion

Our metaheuristic approach showed that the three supervoxels we identified can be summarized by four main PET-MRI parameters: v_e, k_3, v_p, and k_2 respectively ordered by feature importance:

- DCE parameter v_e is considered an estimate of the tumor interstitial space, that may represent either conjunctive or necrotic tumor parts (208). Interestingly, previous studies showed v_e to be a significant predictor of tumor response to treatment in several malignancies (209,210) including locally advanced NSCLC (211).
- DCE parameter v_p is an estimate of the tumor microvascular density. Again, this biomarker has recently been shown to be of clinical relevance for the diagnosis of brain metastases (212) and the response assessment of stereotactic body radiation therapy in NSCLC (213).
- PET parameters k_2 and k_3 reflect the net enzymatic activity through the ratio $\frac{k_3}{(k_2+k_3)}$ (214,215). Interestingly, PET kinetic modeling also showed high relevance as surro-

gates of tumor aggressiveness or prognosis factors in a wide variety of malignancies (216–219), including NSCLC model (220).

Based on these overall results, the supervoxels we identified may thus represent 3 main PET-MRI biological "signatures":

- Interstitial space
- Vascular density
- Tumor cell aggressiveness / adaptation to hypoxic condition.

4. Conclusion & perspectives

4.1. Summary

Tumor heterogeneity is considered an important factor of progression and resistance to treatment. Non-small cell lung cancer (NSCLC), a naturally highly heterogeneous tumor model, is the leading cause of cancer death worldwide. Oncological imaging, essential for the diagnosis, pre-therapeutic staging and monitoring of NSCLC, is mainly based on morphological and / or semi quantitative metabolic criteria, which are intrinsically limited, and cannot capture the tumor biological complexity. In the era of precision medicine and the emergence of personalized therapies, the development of more "holistic" imaging biomarkers is necessary to better characterize this tumor heterogeneity. Quantitative multiparametric imaging offers unique opportunities to characterize tumor biological being at the intra-tumor regional level, and integrated PET-MRI devices could significantly improve our multimodal quantitative analysis capabilities in this field. PET-MRI applied to NSCLC is emerging, and its comprehensive multi-parametric assessment had never been performed at the intra-tumor regional level. We therefore proposed, in this highly stimulating project, to assess the feasibility of a complete dynamic simultaneous PET-MRI multi-parametric approach to characterize the intra tumor regional biological heterogeneity of NSCLC.

Due to the inherent lock-in capabilities of commercially available integrated PET-MRI systems, and the lack of advanced multimodal post-processing pipelines on professional workstations, we had to face numerous methodological challenges to reach our goal: We implemented the reference ^{18}F-FDG PET compartmental model of Sokoloff in Python programming environment to generate “home-made” PET kinetic 3D maps of glucose metabolism. For this purpose, the kinetic parameters of glucose metabolism were computed by fitting the related PET data to the state-of-the-art Sokoloff’s compartmental model on a voxel-wise basis, using “in-house” second order Runge-Kutta procedures combined with Levenberg-Marquardt non-linear least-square fitting optimization. To validate the approach, several implementation tests were performed on 2 patients, including denoising, noise-weighted or adaptive adjustment of the cost-function. We validated, on original phantom experiments, a reverse phase-encoding method to correct EPI geometric distortions related to DWI, that we could not neglect in this 3T PET-MRI multimodal imaging project applied to the Lung. We thus performed

a prospective clinical evaluation on 12 patients with Lung Cancer, and showed significant improvement in DWI-related PET-MRI image matching of our tumors, with significant impact on the regional quantitative ADC maps. We implemented and tested, on the 3T PET-MRI device, T_1/T_2 quantitative MRI applied to lung tumors. Accuracy and reliability of variable flip angle (VFA, without and with B_1 mapping) and saturation recovery (SR) T_1-mapping and multi-echo FSE T_2-mapping (MEFSE, without and with first echo discarding $\pm$ Miller's noise filtering) were assessed on phantom experiments performed twice at 1 week of delay time. We showed that SR-based T_1-mapping outperformed VFA (without and with B_1 mapping) to estimate T_1 relaxation times above 500ms, both in terms of accuracy and reliability. Also, we showed MEFSE T_2-mapping to be highly accurate and reliable for estimating T_2 relaxation times in the range 64-278ms, without the need to discard the first echo or remove the noise floor. Given these experimental results, we then clinically tested T_1/T_2 mapping on 15 patients, and generated, for the first time on integrated 3T PET-MRI, T_1/T_2 parametric maps of lung tumors. We implemented the reference DCE-MRI compartmental model (extended version) in Python programming environment to generate "home-made" DCE kinetic 3D maps of perfusion/vascularization. For this purpose, the kinetic parameters of perfusion / vascularization were computed by fitting the related DCE data to the state-of-the-art extended Tofts compartmental model on a voxel-wise basis, using "in-house" second order Runge-Kutta procedures combined with Levenberg-Marquardt non-linear least-square fitting optimization. Estimation of the relaxation time T_{10}, respiratory motion compensation, noise filtering, and DCE signal conversion into $[Gd]_{plasma}$ were considered.

Based on the validation of these methodological steps, we designed an original full dynamic PET-MRI simultaneous imaging protocol project we applied on treatment naïve NSCLC patients. All patients were recruited via two channels: a prospective clinical research protocol (IMAHTEP, ClinicalTrial.gov NCT03606070) in partnership with the Thorax committee of Gustave Roussy Institute, Paris-Saclay University; and a prospective clinical recruitment I built in partnership with the Department of Thoracic Surgery, Hôpital Marie-Lannelongue (Paris-Saclay University, Le Plessis-Robinson, France) and the Department of Respiratory and Intensive Care Medicine, Pulmonary Hypertension National Referral Center, Hôpitaux Universitaires Paris-Saclay, Assistance Publique-Hôpitaux de Paris, CHU Bicêtre, Kremlin-Bicêtre, France). Using multimodal post-processing procedures specifically designed to allow ^{18}F-FDG dynamic

PET and DWI/T-mapping/DCE-MRI multimodal analyses at the tumor voxel level, we confronted for the first time on integrated 3T PET-MRI, at the regional voxel level, the biomarkers of metabolism and perfusion / vascularization in 14 biopsy-proven and treatment naïve NSCLC. We showed high inter and intra individual heterogeneity in the regional interlinks between metabolism and vascularization, two fundamental biological hallmarks of tumor progression, and highlighted their complementarity. Also, we showed on 11 biopsy-proven and treatment naïve NSCLC, that a voxel-wise unsupervised Gaussian Mixture partitioning of the multidimensional PET-MRI data ultimately individualized 3 generic supervoxels. By using metaheuristic machine learning approaches, we identified a surrogate PET-MRI biological signature of these 3 supervoxels, which could be defined, with an accuracy of 97%, by 4 of the 12 biomarkers we studied: v_e, v_p, k_2 and k_3.

Simultaneous dynamic ^{18}F-FDG PET-MRI is clinically feasible in NSCLC, and has unique capabilities to decipher the regional interlinks between the fundamental hallmarks of cancer.

4.2. Perspectives

This multimodal methodological work demonstrated the clinical feasibility of a multidimensional ^{18}F-FDG PET-MRI protocol applied to NSCLC, and explored at the regional intra-tumor level its multiparametric functional signature, that could serve as a basis for future larger prospective studies. Anyway, several methodological limitations should be further improved to optimize such multiparametric quantitative approach. Respiratory motion corrupts the dynamic imaging data and impacts the kinetic parameters estimates. Rapid changes in PET radiotracer distribution or MRI contrast-enhancement together with no visible structures and inherent low SNR in early PET frames make motion compensation challenging in dynamic PET-MRI. Combining advanced DCE motion compensation methods (152) with PET dynamic joint motion estimation/correction frameworks (221) could be a nice way to address these multiple technical considerations into unified procedures. Also, MR relaxometry remains challenging in clinical practice due to numerous technical dependencies and lack of standardization. The T-mapping sequences we used in this project were accurate and reliable. However, because they are historically designed for cardiac imaging purpose, we could only acquire several slices for each tumor. Furthermore, our protocol required one sequence for T_1 and T_2-mapping respectively. Recently, quantitative MRI has gained renewed interest in other clinical applications with the emergence of synthetic MRI and Finger Printing (222–226). These new paradigms of data acquisition and post-processing provide multiple 3D contrast and parametric maps in one-stop-shop procedures, with fewer technical dependencies. Their implementation and optimization on integrated PET-MRI systems would be of high interest to leverage the PET-MRI multimodal quantitative capabilities. In the era of precision medicine, multiparametric PET-MRI should open the way to highly-personalized treatment evaluation. In this way, future steps could be:

- To validate this PET-MRI multimodal-based tissular characterization of tumors on larger prospective cohorts
- To use such fully integrated PET-MRI multiparametric procedure to further improve the prediction of response to innovative treatments.

APPENDIX

A.1. Influence of data sampling on our PET kinetic modelling

Considering a tumor subset of 57 voxels, we used 29 different levels of data sampling for our nonlinear least square fitting procedure (range = 20 to 2000 points) sampling were tested, by using the following empirical increment:

- From 20 to 200 points, with a 10 points regular increment,
- From 200 to 1000 points, with a 100 points regular increment,
- 1500 points
- 2000 points.

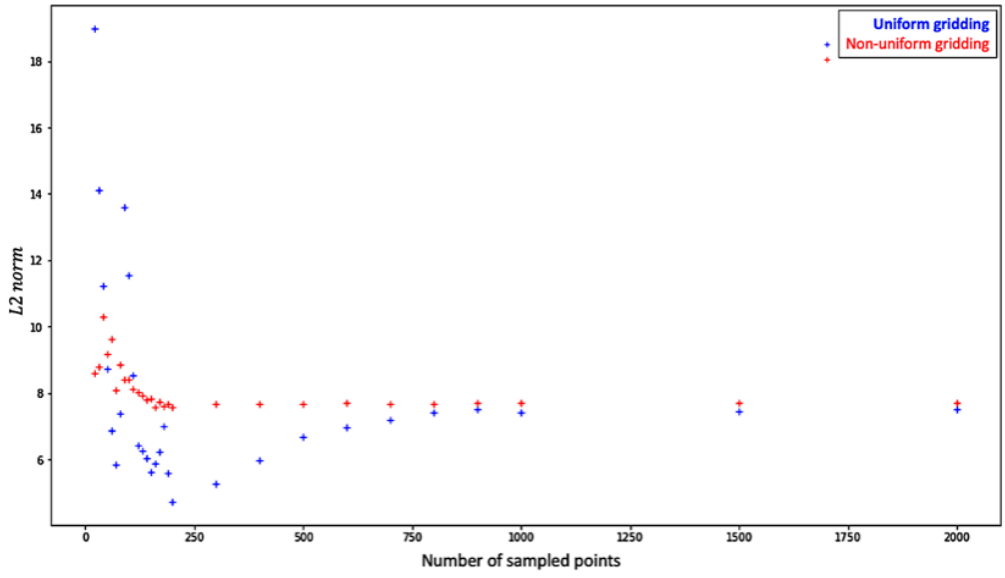

Figure A. 1 : This plot represents the number of points to be sampled (x-axis) function of the mean $L2\,norm$ *of the overall voxels (y-axis) that corresponds to* $\sqrt{N} \times RMSE$*, where N is the number of frames. We can clearly see that, on this subset of 57 tumor voxels, the algorithm provides the same performance for uniform and non-uniform gridding above 1000 points.*

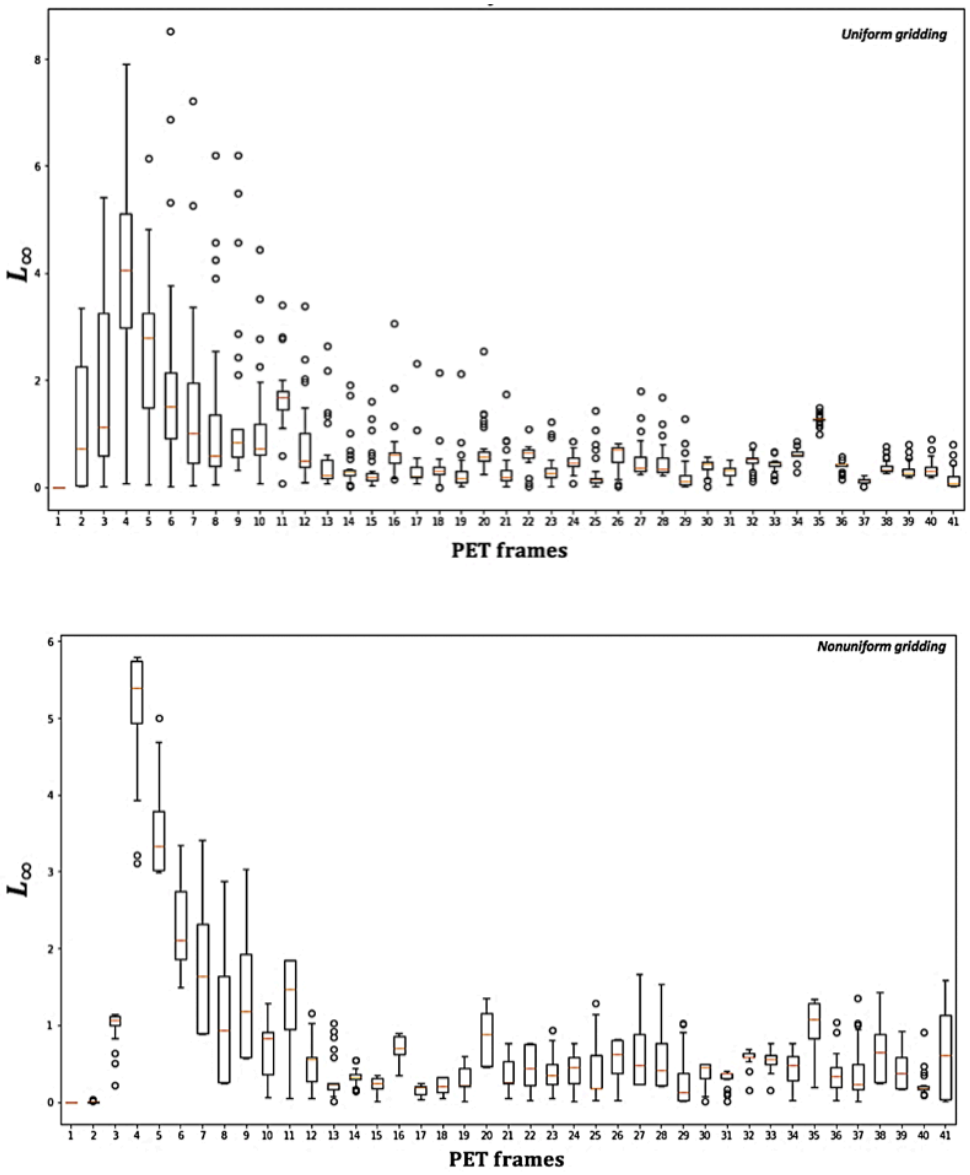

Figure A. 2 : These plots represent for each frame (x-axis) the L_∞ norms of the 29 levels of points to be sampled (boxplots). We can see that, considering all the levels of data sampling, for the first 5 frames, the nonuniform gridding had better performance compared to uniform gridding (both lower L_∞ norm values and variability). For the 5th to the 30th frame, the nonuniform gridding provided less outliers. For the 31th to the 41th frame, the uniform gridding appeared more consistent.

A.2. PET kinetic modeling accuracy without smoothing

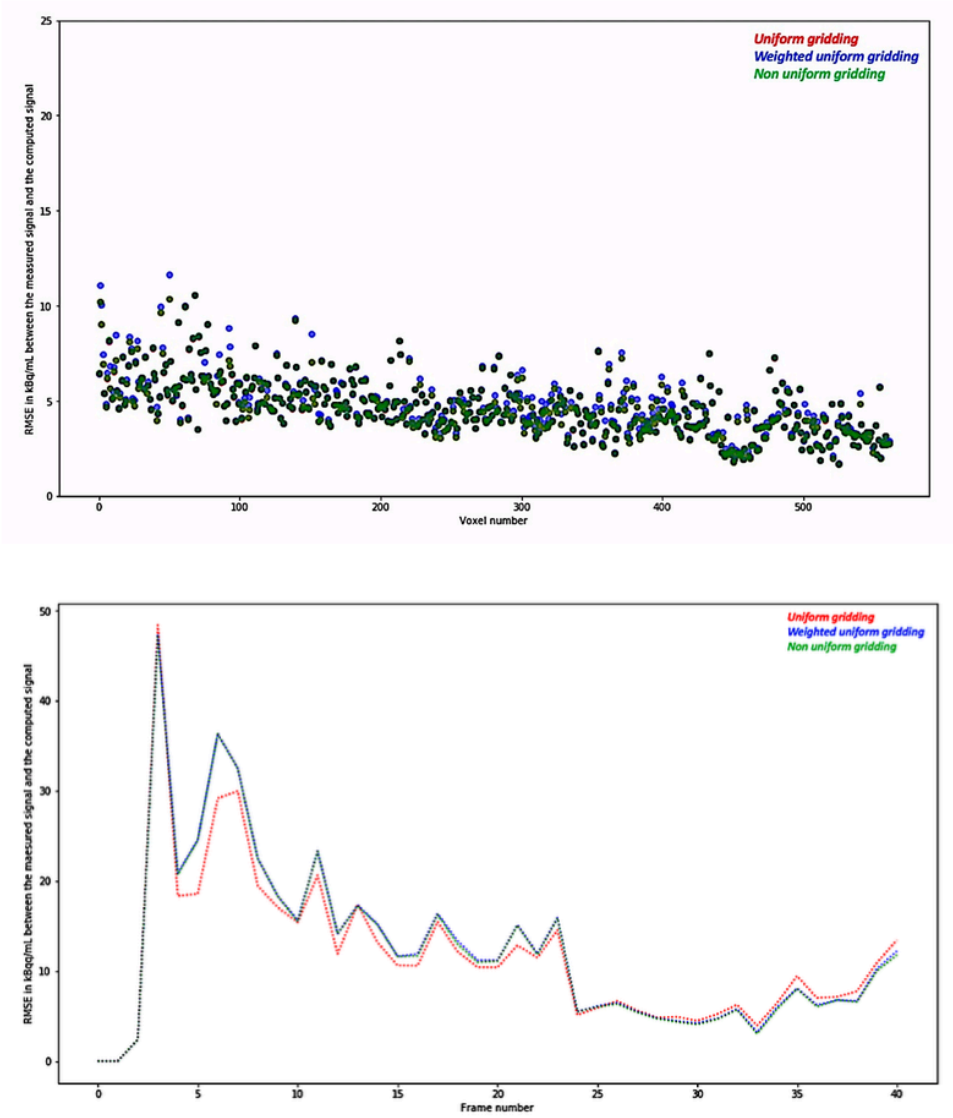

Figure A. 3: Without smoothing, the mean iteration number was increased (18.6, 28.7 and 18.2 respectively for uniform, uniform weighted and nonuniform) and for 12 voxels, the nonuniform method did not converged after the maximal 400 iterations. Also, as provided in the figures, RMSE among the frames were higher (median values were 10.6, 11.2 and 11.1 kBq/ml). In all the case, RSME between the 4th and 5th frame (40s and 50s post-injection respectively) increased together with the signal measured, corresponding to the first blood pass. Overall RMSE4 and RMSE5 were 48.4 kBq/ml and 18.3 kBq/mL; 47.4 kBq/mL and 20.9 kBq/mL; and 47.1 kBq/mL and 20.7 kBq/mL for the uniform, uniform weighted and nonuniform gridding respectively (for the smoothed PET data: 52.3 kBq/mL and 12.8 kBq/mL; 46.8 kBq/mL and 22.4 kBq/mL; and 46.8 kBq/mL and 22.4 kBq/mL for the uniform, uniform weighted and nonuniform gridding respectively).

A.3. Voxel-wise results of the PET kinetic fitting procedures.

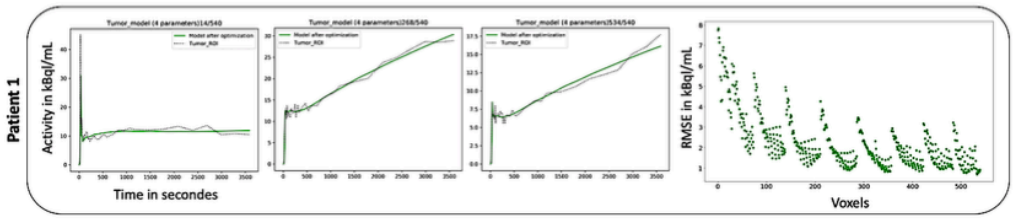

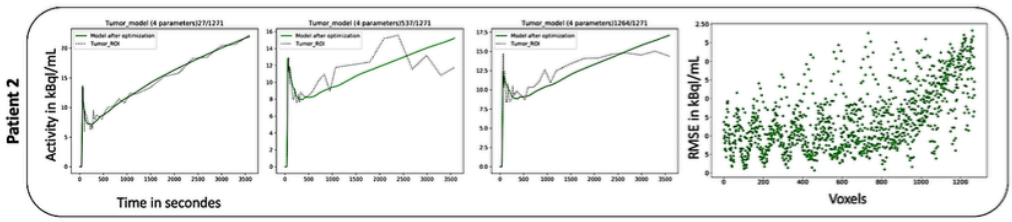

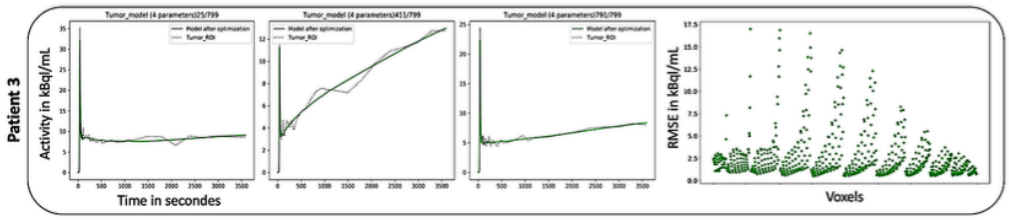

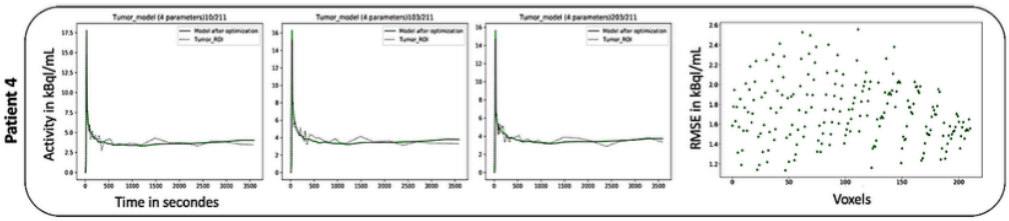

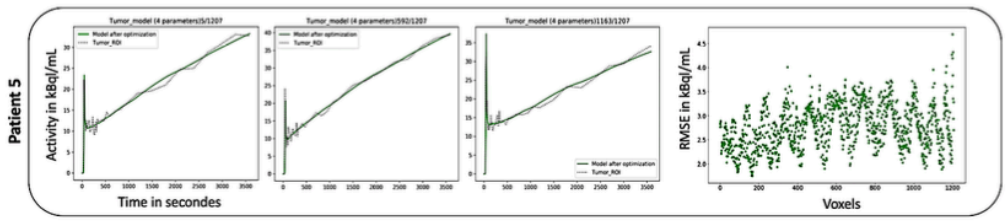

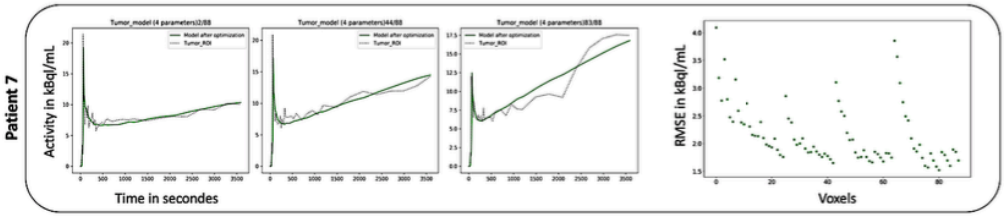
Patient 7
Activity in kBq/mL
Time in secondes
RMSE in kBq/mL
Voxels

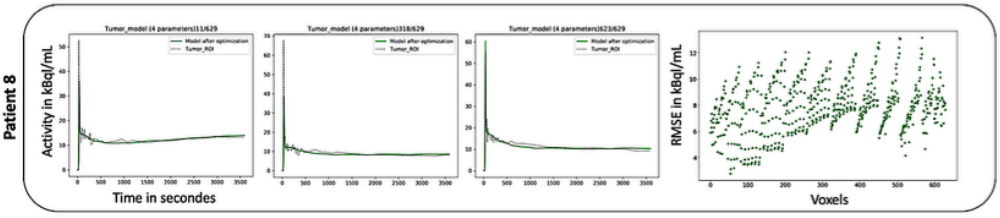
Patient 8
Activity in kBq/mL
Time in secondes
RMSE in kBq/mL
Voxels

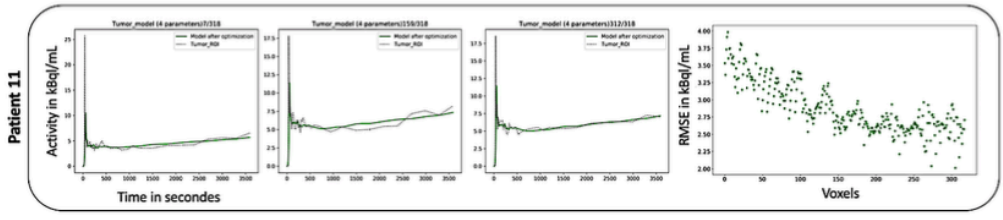
Patient 11
Activity in kBq/mL
Time in secondes
RMSE in kBq/mL
Voxels

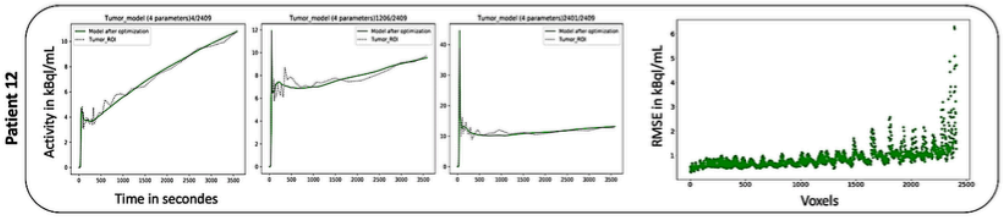
Patient 12
Activity in kBq/mL
Time in secondes
RMSE in kBq/mL
Voxels

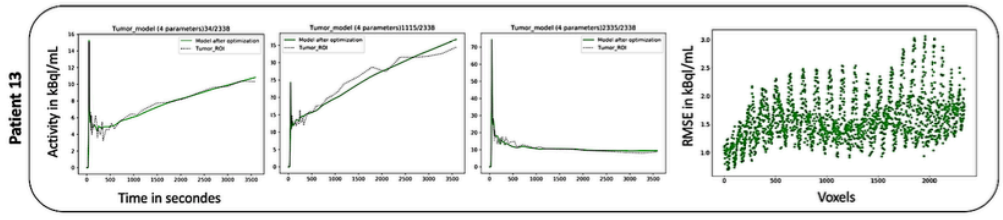
Patient 13
Activity in kBq/mL
Time in secondes
RMSE in kBq/mL
Voxels

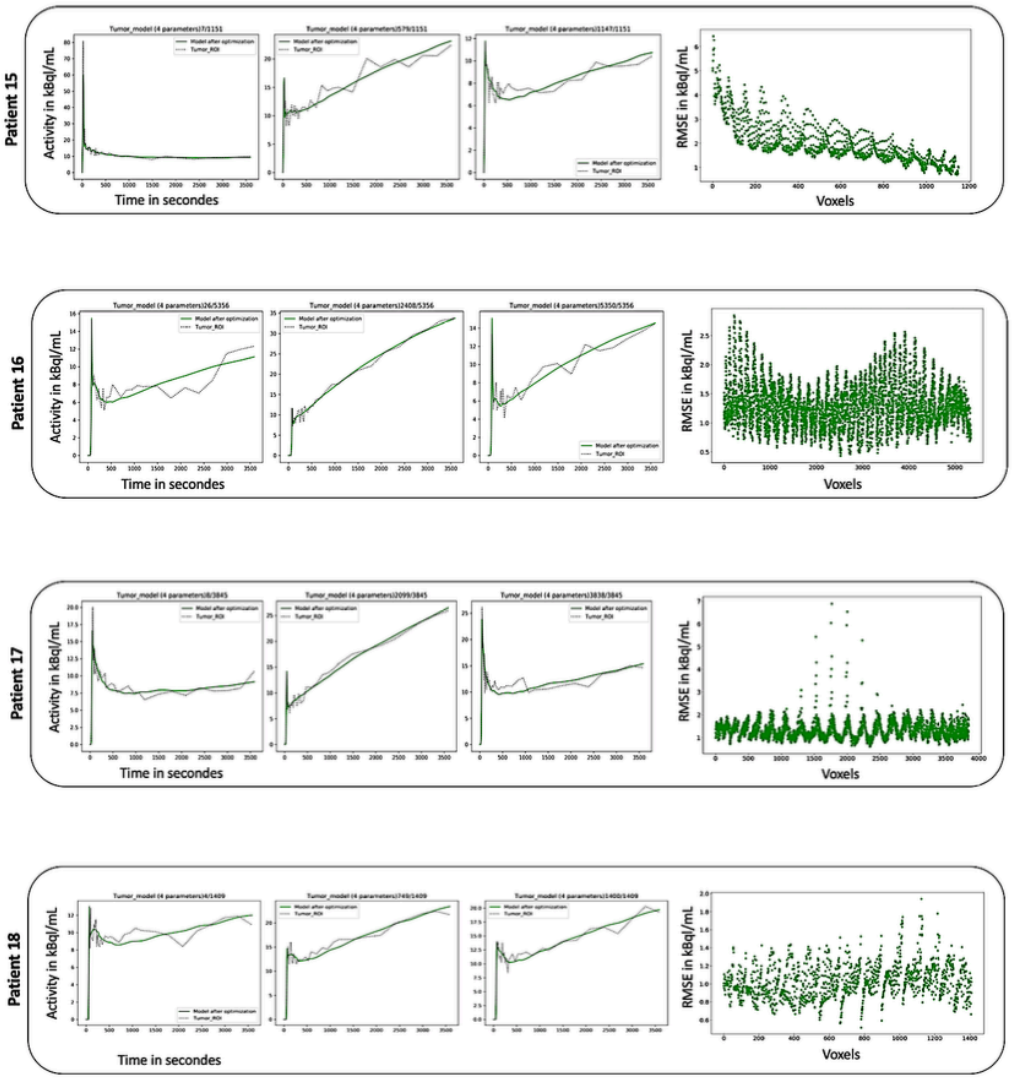

Figure A. 4 : For each patient, three illustrative voxels are presented. The black dotted line corresponds to the measured signal, and the green solid line to the estimated signal after curve fitting. Also, the overall voxel-wise RMSE is provided in the right panel (x -axis is the voxel identity number in the tumor of interest, and y -axis is the RMSE in kBq/mL).

A.4. Summary of the PET kinetic fitting procedures.

		PET	
		RMSE in kBq/mL	
Tumor	Voxels of 2mm^3	Mean (SD)	Median (IQR)
1	540	2.3 (1.3)	1.9 (1.3-2.8)
2	1271	1.2 (0.4)	1.1 (0.9-1.4)
3	799	2.5 (2.6)	1.52 (0.97-2.80)
4	211	1.7 (0.3)	1.7 (1.5-1.9)
5	1207	2.8 (0.5)	2.8 (2.4-3.1)
7	88	2.2 (0.5)	1.9 (1.8-2.4)
8	629	7.8 (1.9)	7.8 (6.6-9.0)
11	318	2.9 (0.37)	2.8 (2.6-3.2)
12	2409	0.89 (0.45)	0.80 (0.64-1.02)
13	2338	1.59 (0.41)	1.53 (1.31-1.83)
15	1151	2.0 (0.9)	1.75 (1.44-2.31)
16	5356	1.3 (0.38)	1.26 (1.03 -1.51)
17	3845	1.31 (0.40)	1.23 (1.05-1.5)
18	1409	1.03 (0.18)	1.02 (0.9-1.14)

Table A. 1 : Summary of the voxel-wise RMSE of the PET kinetic modeling for the 14 patients. RMSE (in kBq/mL) are provided as mean (SD) and median (IQR).

A.5. Phantom experiments: quality of the fits for ADC map computation.

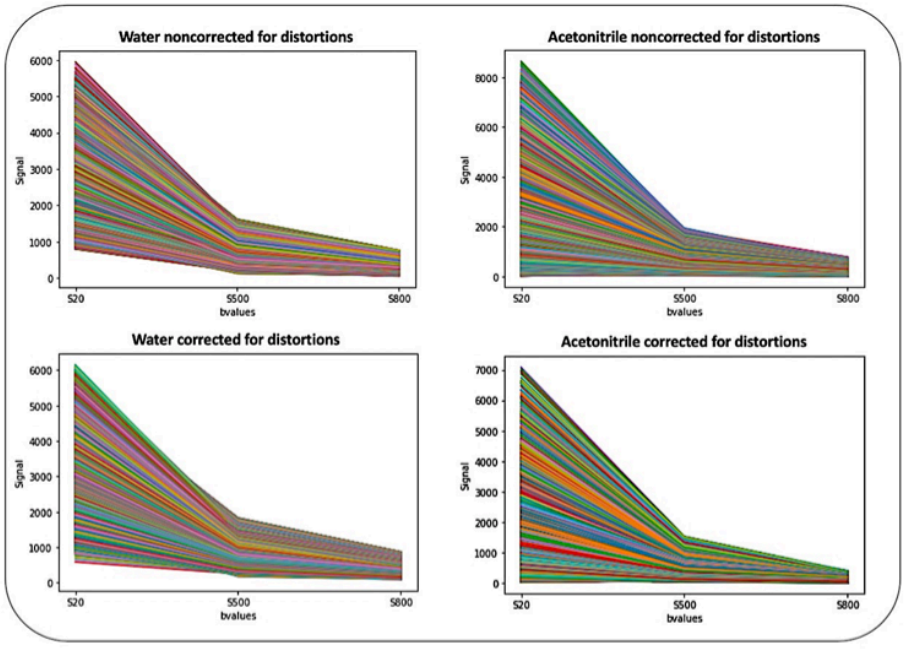

Figure A. 5: For the two tubes (water and acetonitrile), DWI signal intensities (session 1) are provided in a voxel-wise fashion for each of the 3 b values. Top: the data noncorrected for distortions are provided; bottom: the data corrected for distortions are provided.

ADC maps computation : quality of the fits

			No correction		Correction	
	Tube		Water	Acetonitrile	Water	Acetonitrile
	Voxels		144 617	180 304	144 617	180 304
Session 1	RMSE	Mean (SD)	0.04 (0.05)	0.10 (0.11)	0.04 (0.05)	0.11 (0.11)
		Median (IQR)	0.03 (0.02-0.05)	0.07 (0.03-0.13)	0.03 (0.02-0.05)	0.08 (0.04-0.15)
Session 2	RMSE	Mean (SD)	0.05 (0.06)	0.11 (0.10)	0.05 (0.06)	0.12 (0.1)
		Median (IQR)	0.03 (0.02-0.05)	0.08 (0.04-0.2)	0.03 (0.02-0.06)	0.09 (0.04-0.2)
Session 3	RMSE	Mean (SD)	0.05 (0.06)	0.09 (0.09)	0.04 (0.05)	0.1 (0.09)
		Median (IQR)	0.03 (0.02-0.05)	0.06 (0.03-0.1)	0.03 (0.02-0.05)	(0.08 (0.04-0.1)

Table A. 2 : Quality of the curve fitting procedures after loglinear fitting of the signal intensities. RMSE, expressed as $\mathrm{Log}(Signal\ intensity)$*, are provided before and after correction of the distortion.*

A.6. Phantom experiments: results of the curve fitting procedures for T_1-mapping

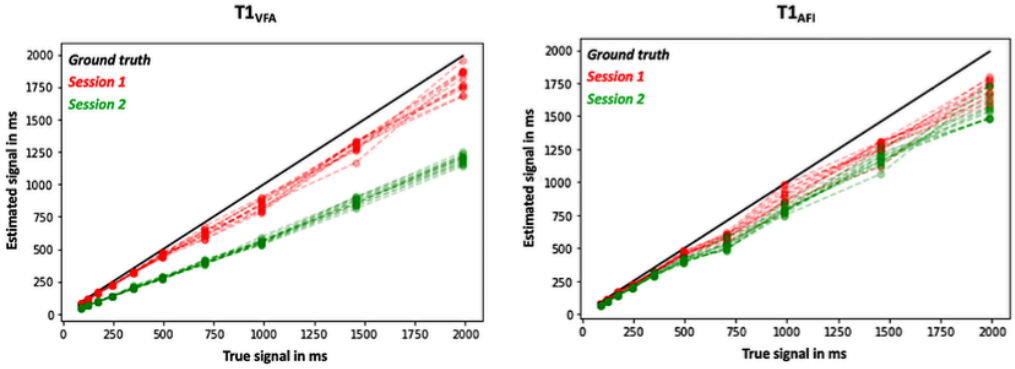

Figure A. 6 : Results of the two T_1-mapping phantom sessions. VFA and VFA plus AFI correction are plotted. In both cases, the true signal (x-axis) is plotted against the measured signal (y-axis).

$T1_{VFA}$		Session 1		Session 2	
Sphere	Voxels	$RMSE_{mean}$(SD)	$RMSE_{median}$(IQR)	$RMSE_{mean}$(SD)	$RMSE_{median}$(IQR)
1	12	4.4 (0.4)	4.5 (4.3-4.7)	3.9 (0.6)	3.9 (3.7-4.2)
2		4.1 (0.6)	4.2 (3.8-4.5)	3.7 (0.6)	3.6 (3.3-4.2)
3		3 (0.4)	3 (2.7-3.2)	2.9 (0.4)	2.8 (2.6-3.2)
4		3.5 (0.6)	3.5 (3.2-3.9)	4.0 (0.6)	4.2 (3.6-4.6)
5		5.0 (0.3)	5.1 (4.7-5.2)	5.5 (0.5)	5.5 (5.1-5.8)
6		5.5 (0.6)	5.4 (5.0-5.9)	8.8 (0.7)	8.8 (8.3-9.3)
7		6.5 (0.7)	6.6 (5.8-6.8)	12.9 (0.5)	12.9 (12.7-13.3)
8		8.5 (0.6)	8.7 (8.0-9.0)	17.6 (2.0)	18.2 (15.9-19.2)
9		12.6 (1.4)	12.8 (12.0-13.3)	27 (2.2)	26.8 (25.6-28.6)
10		19.5 (2.4)	19.4 (17.9-21.9)	46.6 (5.1)	46.1 (41.4-50.7)

Table A. 3: Results of the curve fitting procedures for T_1-mapping (VFA). RMSE are expressed in $\frac{Sn}{\sin a_n}$ (a.u).

$T1_{AFI}$		Session 1		Session 2	
Sphere	Voxels	$RMSE_{mean}$(SD)	$RMSE_{median}$(IQR)	$RMSE_{mean}$(SD)	$RMSE_{median}$(IQR)
1	12	4.5 (0.4)	4.6 (4.3-4.8)	3.5 (0.6)	3.5 (3.2-3.7)
2		4.1 (0.6)	4.2 (3.8-4.5)	3.3 (0.6)	3.2 (3.0-3.7)
3		2.9 (0.4)	2.9 (2.6-3.2)	2.5 (0.3)	2.5 (2.2-2.8)
4		3.6 (0.7)	3.6 (3.3-3.9)	3.7 (0.6)	3.9 (3.3-4.0)
5		5.0 (0.3)	5.1 (4.7-5.2)	4.8 (0.4)	4.8 (4.5-5.1)
6		5.5 (0.6)	5.5 (5.0-5.9)	7.6 (0.6)	7.6 (7.2-7.9)
7		6.5 (0.7)	6.6 (5.8-6.8)	11.1 (0.5)	11.0 (10.9-11.4)
8		8.5 (0.6)	8.6 (8.0-9.0)	15.1 (1.6)	15.5 (13.6-16.4)
9		12.6 (1.4)	12.8 (11.9-13.3)	23.0 (1.8)	22.9 (21.9-24.3)
10		19.4 (2.4)	19.3 (17.8-21.8)	40.0 (4.2)	39.7 (35.8-43.2)

Table A. 4 : Results of the curve fitting procedures for T_1-mapping (AFI). RMSE are expressed in $\frac{Sn}{\sin \alpha_n}$ (a.u).

A.7. Phantom experiments: Results of the curve fitting procedures for T_2-mapping

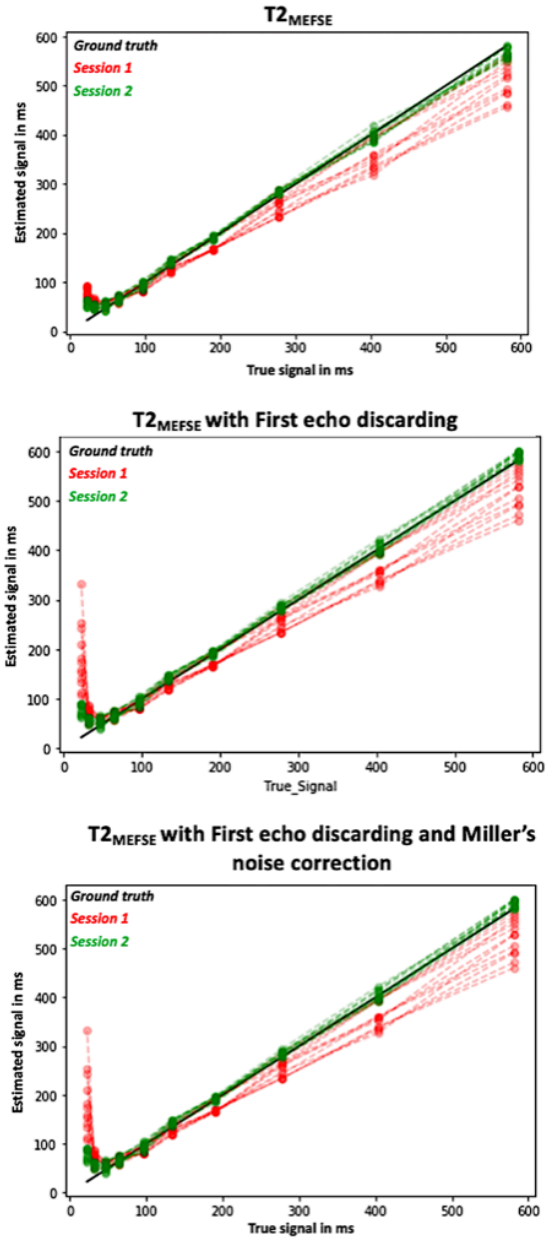

Figure A. 7 : MEFSE, MEFSE with First echo discarding, and MEFSE plus First echo discarding plus Miller's noise correction results for the two T_2-mapping phantom sessions. In all cases, the true signal (x-axis) is plotted against the measured signal (y-axis).

$T2_{MEFSE}$		Session 1		Session 2	
Sphere	Voxels	$RMSE_{mean}$(SD)	$RMSE_{median}$(IQR)	$RMSE_{mean}$(SD)	$RMSE_{median}$(IQR)
1	12	0.006 (0.001)	0.005 (0.005-0.006)	0.01 (0.002)	0.01 (0.008-0.01)
2		0.008 (0.002)	0.007 (0.007-0.009)	0.007 (0.002)	0.007 (0.006-0.008)
3		0.007 (0.002)	0.006 (0.006-0.008)	0.008 (0.002)	0.009 (0.007-0.009)
4		0.01 (0.004)	0.01 (0.09-0.01)	0.01 (0.002)	0.009 (0.009-0.01)
5		0.009 (0.002)	0.009 (0.008-0.01)	0.01 (0.003)	0.01 (0.009-0.01)
6		0.03 (0.01)	0.03 (0.02-0.03)	0.03 (0.007)	0.03 (0.02-0.03)
7		0.05 (0.02)	0.06 (0.04-0.06)	0.04 (0.01)	0.04 (0.03-0.05)
8		0.2 (0.02)	0.2 (0.18-0.22)	0.14 (0.03)	0.14 (0.12-0.17)
9		0.5 (0.06)	0.5 (0.46-0.51)	0.43 (0.16)	0.35 (0.34-0.44)
10		0.9 (0.2)	0.9 (0.7-1.01)	0.65 (0.04)	0.65 (0.62-0.67)

Table A. 5 : Results of the curve fitting procedures for T2MEFSE. RMSE are expressed in $Log(Signal\ intensity)$ *(a.u).*

$T2_{MEFSE}$ First echo		Session 1		Session 2	
Sphere	Voxels	$RMSE_{mean}$(SD)	$RMSE_{median}$(IQR)	$RMSE_{mean}$(SD)	$RMSE_{median}$(IQR)
1	12	0.005 (0.001)	0.005 (0.004-0.005)	0.007 (0.002)	0.007 (0.005-0.008)
2		0.007 (0.001)	0.007 (0.006-0.008)	0.005 (0.002)	0.006 (0.004-0.006)
3		0.007 (0.002)	0.006 (0.006-0.009)	0.008 (0.002)	0.008 (0.007-0.01)
4		0.01 (0.005)	0.01 (0.008-0.01)	0.009 (0.001)	0.009 (0.008-0.009)
5		0.009 (0.002)	0.009 (0.008-0.01)	0.008 (0.004)	0.007 (0.006-0.01)
6		0.03 (0.01)	0.03 (0.02-0.03)	0.02 (0.007)	0.03 (0.02-0.03)
7		0.05 (0.02)	0.05 (0.04-0.06)	0.04 (0.01)	0.04 (0.03-0.05)
8		0.2 (0.03)	0.2 (0.17-0.21)	0.14 (0.03)	0.13 (0.12-0.15)
9		0.4 (0.06)	0.41 (0.40-0.43)	0.4 (0.2)	0.3 (0.28-0.41)
10		0.6 (0.16)	0.6 (0.5-0.8)	0.5 (0.05)	0.5 (0.4-0.5)

Table A. 6 : Results of the curve fitting procedures for T2MEFSE with First echo discarding. RMSE are expressed in $Log(Signal\ intensity)$ *(a.u).*

$T2_{MEFSE}$ First echo & Noise corr		Session 1		Session 2	
Sphere	Voxels	$RMSE_{mean}$(SD)	$RMSE_{median}$(IQR)	$RMSE_{mean}$(SD)	$RMSE_{median}$(IQR)
1	12	0.009 (0.002)	0.009 (0.008-0.01)	0.01 (0.004)	0.01 (0.009-0.02)
2		0.01 (0.002)	0.01 (0.01-0.02)	0.01 (0.003)	0.01 (0.008-0.013)
3		0.014 (0.005)	0.01 (0.01-0.02)	0.017 (0.005)	0.017 (0.014-0.019)
4		0.02 (0.009)	0.02 (0.016-0.03)	0.02 (0.002)	0.02 (0.016-0.019)
5		0.02 (0.004)	0.02 (0.015-0.022)	0.016 (0.007)	0.014 (0.011-0.02)
6		0.06 (0.02)	0.05 (0.04-0.06)	0.05 (0.014)	0.05 (0.04-0.054)
7		0.1 (0.03)	0.1 (0.07-0.12)	0.08 (0.03)	0.08 (0.06-0.1)
8		0.4 (0.05)	0.4 (0.3-0.4)	0.28 (0.06)	0.26 (0.24-0.30)
9		0.9 (0.12)	0.82 (0.80-0.86)	0.76 (0.34)	0.59 (0.56-0.82)
10		1.3 (0.3)	1.24 (1.0-1.5)	0.91 (0.10)	0.90 (0.83-0.96)

Table A. 7 : Results of the curve fitting procedures for T2MEFSE with First echo discarding and Miller's noise correction. RMSE are expressed in $Log(Signal\ intensity)$ *(a.u).*

A.8. Voxel-wise results of the DCE kinetic fitting procedures.

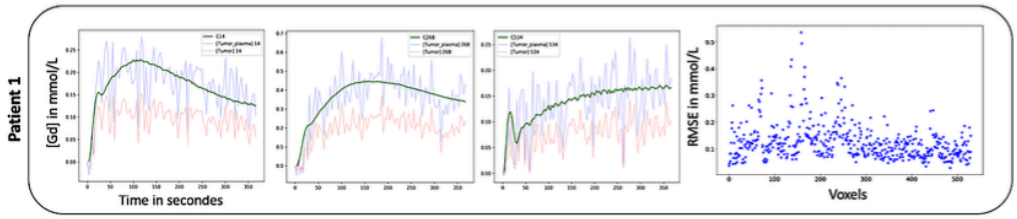

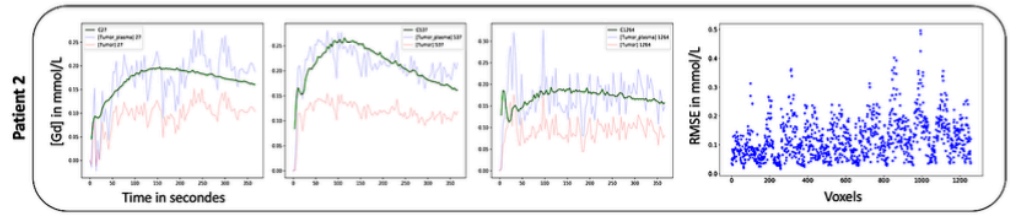

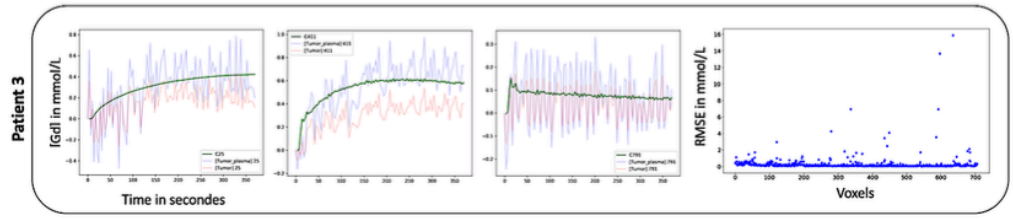

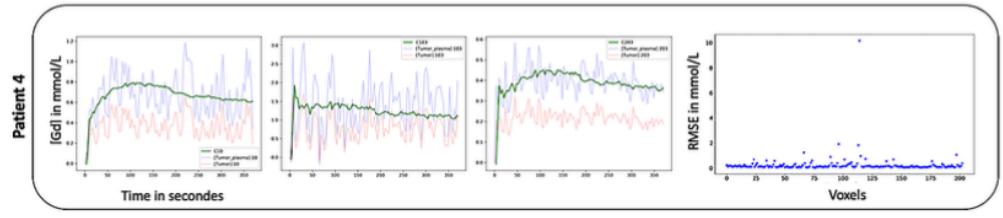

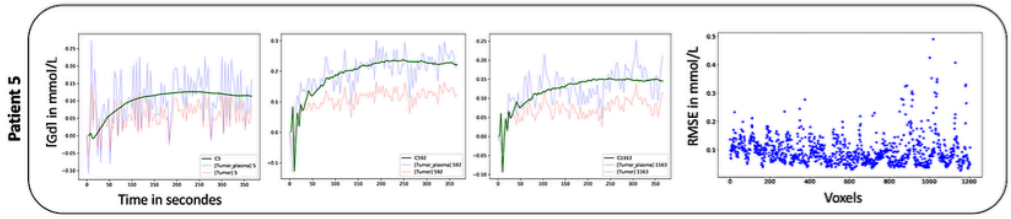

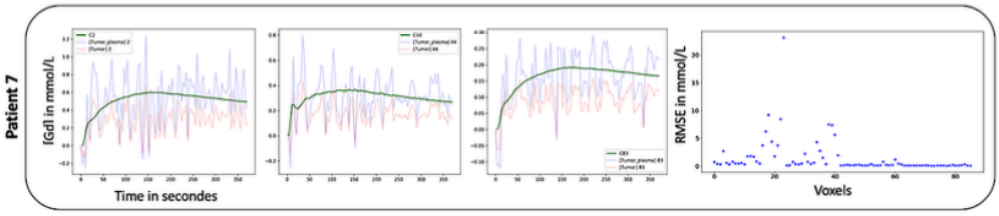
Patient 7
[Gd] in mmol/L
Time in secondes
RMSE in mmol/L
Voxels

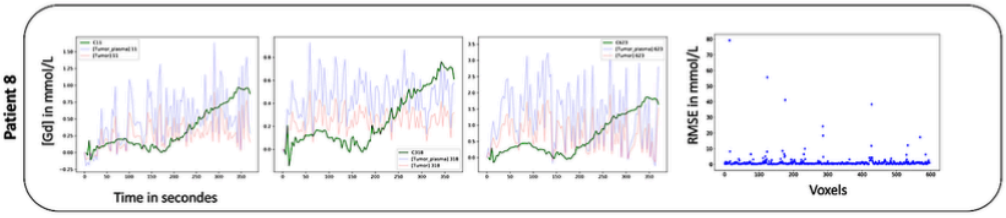
Patient 8
[Gd] in mmol/L
Time in secondes
RMSE in mmol/L
Voxels

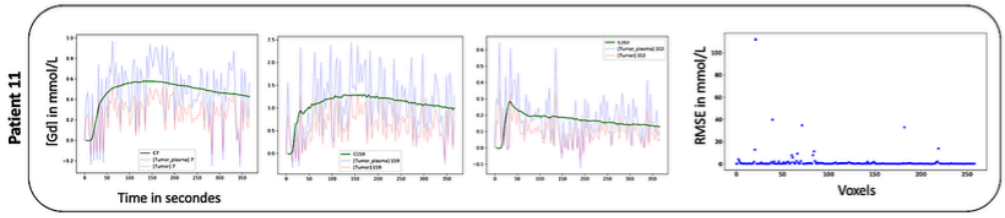
Patient 11
[Gd] in mmol/L
Time in secondes
RMSE in mmol/L
Voxels

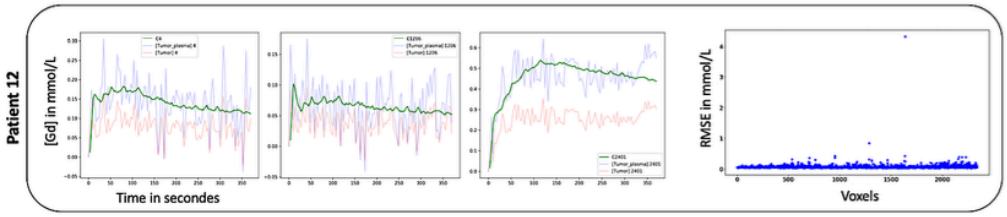
Patient 12
[Gd] in mmol/L
Time in secondes
RMSE in mmol/L
Voxels

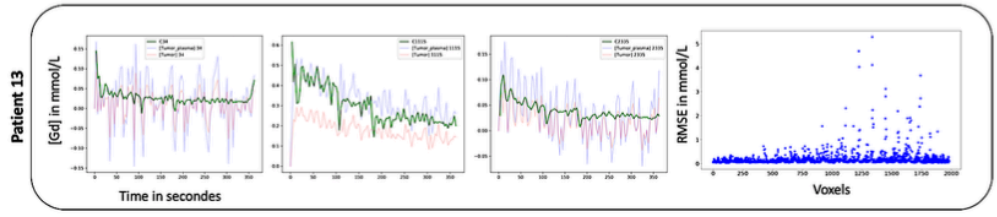
Patient 13
[Gd] in mmol/L
Time in secondes
RMSE in mmol/L
Voxels

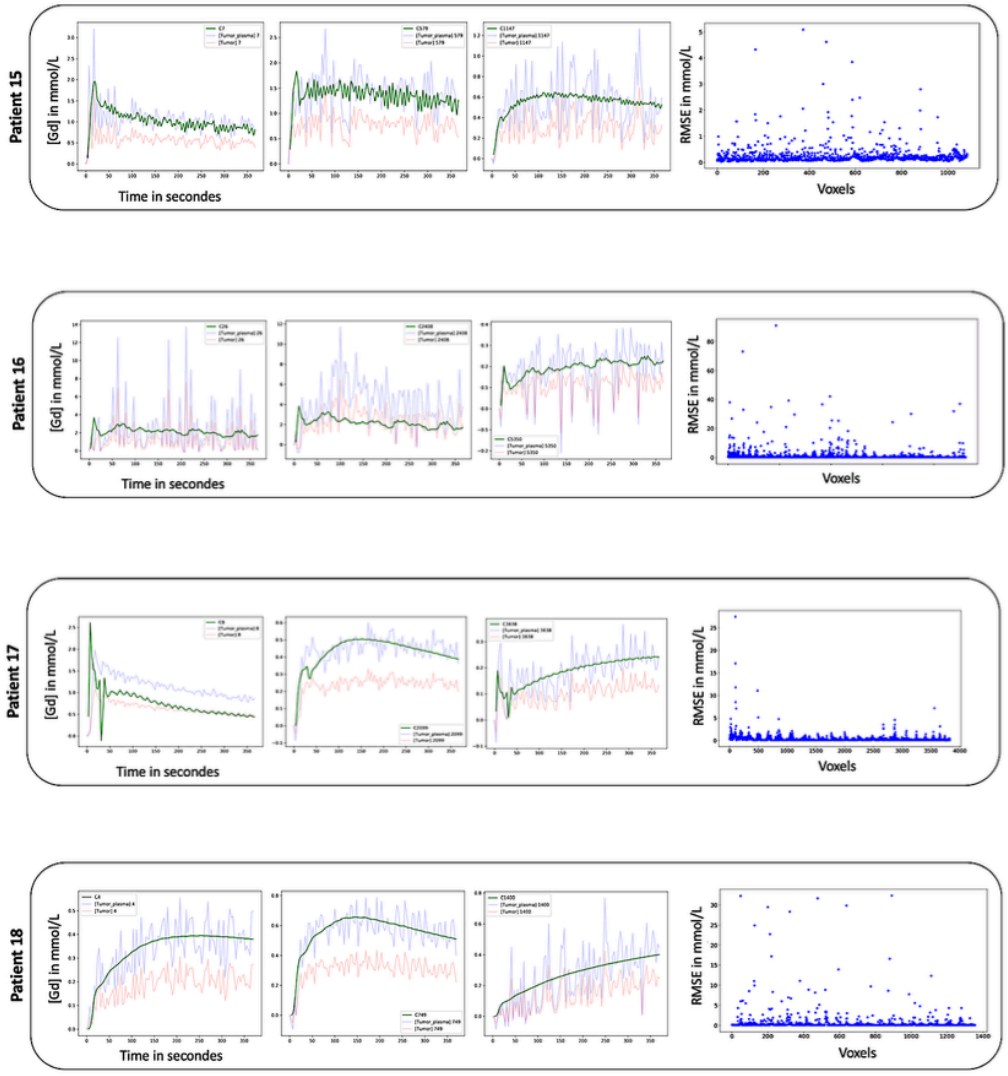

Figure A. 8 : For each patient, the same three illustrative voxels shown in Figure A. 4 are presented. The red line corresponds to the blood concentration of gadolinium, the blue line to the plasma concentration of gadolinium, and the green line to the estimated signal after curve fitting of the plasma concentration of gadolinium. Also, the overall voxel-wise RMSE is provided in the right panel (x-axis is the voxel identity number in the tumor of interest, and y-axis is the RMSE in mmol/L).

A.9. Summary of the DCE kinetic fitting procedures.

		DCE	
		RMSE in mmol/L	
Tumor	Voxels of $2mm^3$	Mean (SD)	Median (IQR)
1	540	0.13 (0.07)	0.11 (0.08-0.15)
2	1271	0.12 (0.07)	0.11 (0.07-0.16)
3	799	0.27 (0.9)	0.09 (0.05-0.2)
4	211	0.25 (0.7)	0.12 (0.09-0.20)
5	1207	0.1 (0.05)	0.09 (0.06-0.12)
7	88	1.39 (3.1)	0.29 (0.1-0.8)
8	629	1.30 (4.9)	0.50 (0.3-1.0)
11	318	1.50 (8.0)	0.24 (0.14-0.6)
12	2409	0.07 (0.1)	0.06 (0.05-0.07)
13	2338	0.19 (0.32)	0.11 (0.07-0.2)
15	1151	0.25 (0.39)	0.16 (0.1-0.3)
16	5356	0.6 (2.8)	0.15 (0.09-0.31)
17	3845	0.30 (0.72)	0.13 (0.08-0.33)
18	1409	0.63 (2.6)	0.13 (0.08-0.25)

Table A. 8 : Summary of the voxel-wise RMSE of the DCE kinetic modeling for the 14 patients. RMSE (in kBq/mL) are provided as mean (SD) and median (IQR).

A.10.Clinical trial: the IMAHTEP study

GE Healthcare

ATTESTATION

Paris, le 18 Avril 2017

A qui de droit,

Nous, Louise DELEVOYE, attestons par la présente, donner l'autorisation à l'Institut Gustave Roussy, d'utiliser les documents suivants dans le cadre de l'étude clinique IMAHTEP menée avec le système SIGNA™ PET/MR :

· Manuel de l'opérateur du système SIGNA™ PET/MR (Rév. 2, janvier 2015) ;
· Certificat de marquage CE ;
· Déclaration CE de conformité SIGNA™ PET/MR.

Cordialement,

Louise DELEVOYE
Counsel Research
GE Healthcare

GE MEDICAL SYSTEMS
Société en Commandite Simple
283, RUE DE LA MINIERE
78530 BUC - FRANCE
RCS VERSAILLES B 315 013 359
Tél. +33 (0)1 30 70 40 40

GE Medical Systems Société en Commandite Simple
Au capital de 88.846.785 euros
Siège social : 283, rue de la Minière
78530 Buc
France
T +33 (0)1 30 70 40 40
RCS Versailles B 315 013 359

FICHE D'APPROBATION DU CONTRAT

UPSUD N° P ….. 0

Nature du Contrat : Recherche clinique (Complément)

Objet de l'Etude : Imagerie multiparamétrique TEP-IRM du cancer pulmonaire
Ajout de 13 patients à l'effectif d'un contrat déjà finalisé par ailleurs.

Partenaires : GE - IGR

Durée du contrat – Date de début et date de fin : 30 mois

Montant du Financement alloué au Laboratoire : 34 684 euros HT

A
Le
Vu, Le Directeur du Laboratoire
Mr. BARRANGER Luc

A Paris
Le 26/07/2017
Vu, Le Responsable Scientifique
M. Emmanuel Durand

Pr Emmanuel DURAND
Biophysique et Médecine Nucléaire
Hôpitaux Universitaires Paris Sud - site de Bicêtre
78, rue du Général Leclerc
94275 Le Kremlin - Bicêtre cedex
Tél. : 01 45 21 25 07 / 01 45 21 35 60
RPPS 10001274496

A Orsay
Le
Vu, Pour le DARI d'UPSud
Madame Soizic LEFEUVRE

FICHE D'EVALUATION DES COUTS D'UN CONTRAT (non europeen)

Nom du Laboratoire UPSud :
Nom des (du) partenaires extérieurs :

		Nbre chercheurs (Hommes par jour)	Coût pour la durée du contrat
Evaluation			**€ HT**
1) COUT GLOBAL DU PERSONNEL TITULAIRE AFFECTE AU CONTRAT			
CR2 ou MC2	583,75 € HT/jour		0,00
CR1 ou MC1	647,90 € HT/jour		0,00
DR2 ou PR2	715,85 € HT/jour (coûts *environnés*)		0,00
DR1 ou PR1	805,26 € HT/jour		0,00
DR0 ou PR0	855,87 € HT/jour		0,00
2) DEPENSES SUPPLEMENTAIRES NECESSAIRES A L'EXECUTION DU CONTRAT			
Rémunérations des personnels			0,00
Fonctionnement, consommables			34 684,00
Equipement			
Frais de missions			
Heures de calcul			
Autres services extérieurs			
Utilisation de "Très Grands Equipements"			
Autres dépenses			
TOTAL DES DEPENSES EVALUEES incluant 14% de frais généraux		**A**	40 330,23

Participation de l'Industriel : **montant du contrat de recherche**

dans le cas d'une prestation de service (A=B) :

dans le cas d'une collaboration de recherche : **B** **34 684,00**

Taux de participation : **86** % (*)

Montant affecté à l'Etude (hors frais généraux) ***29 828,24***

Justification du "taux de participation de l'industriel" (*) et autres observations :

Directeur du Laboratoire

NOM : DARRASSE
Prénom : Luc
Date :
Signature :

Responsable Scientifique

NOM : BESSON/DURAND
Prénom : Florent/Emmanuel
Date : 27/07/2017
Signature :

à renseigner

27/07/2017

DE LA RECHERCHE À L'INDUSTRIE

cea

www.cea.fr

GE HEALTHCARE
283, rue de la Minière
78533 BUC, FRANCE

A l'attention de M. SOUCHAY

Orsay, le 24 mars 2017

Objet : Offre de prix dans le cadre d'une collaboration sur le protocole de recherche IMATEP
Réf : DRF/JOLIOT/GAF/2017-022

Monsieur,

Dans le cadre de la collaboration que vous envisagez avec l'IR4M sur le projet IMATEP au Service Hospitalier Frédéric Joliot à Orsay, nous vous proposons l'offre de prix suivante :

Pour un examen TEP-IRM avec [^{16}F]FDG : 1334 € HT, soit 1601 € TTC (TVA 20%)
Pour 26 examens TEP-IRM avec [^{18}F]FDG : 34 684 € HT, soit 41 621 € TTC (TVA 20%)

Validation du devis : 3 mois, une convention de recherche biomédicale devra être signée
Condition de facturation :
- annuellement en fonction du nombre d'examens réalisés
- payable à 30 jours fin de mois date d'émission de facture

Nous vous prions d'agréer, Monsieur, nos salutations distinguées.

Vincent Lebon

Copie (mail) :
DRF/JOLIOT/SHFJ : V.Lebon
DRF/JOLIOT/Dir : S.Pietri - M.Roux - E. Cousin
Université Paris-Sud / IR4M : F.Besson

Commissariat à l'énergie atomique et aux énergies alternatives
Centre de Saclay | 91191 Gif-sur-Yvette Cedex
PC 141 - ORSAY
T +33 (0)1 69 08 78 06 | F +33 (0)1 69 08 75 08
magali.roux@cea.fr
Etablissement public à caractère industriel et commercial | RCS Paris B 775 685 019

Direction de la Recherche Fondamentale
Institut des Sciences du Vivant Frédéric Joliot

DIRECTION DE LA RECHERCHE CLINIQUE
Directeur : Professeur Gilles VASSAL

Jérôme Ducrocq
01 42 11 60 31
jerome.ducrocq@gustaveroussy.fr

COMPTE RENDU

BOARD GUSTAVE ROUSSY PROMOTEUR

VENDREDI 15 JANVIER 2016
Salle de réunion de la DRC +1

Le Board Gustave Roussy Promoteur analyse, très tôt dans leur développement, les projets de recherche biomédicale que leur investigateur principal propose à la promotion par Gustave Roussy.
Les comptes rendus sont envoyés aux porteurs de projet ainsi qu'au responsable du comité.

Membres présents : M. DI PALMA, J. DUCROCQ, E. LANOY, G. VASSAL, D. VUILLIER

Membres excusés : E. BENHAMOU, A. LE CESNE, J. MURET

Copie : A. EGGERMONT, E. SOLARY, M. DUCREUX

Projet n°2016-002: de **C. CARAMELLA** (**F. BESSON**) : « *Intégration multiparamétrique TEP-IRM pour une nouvelle approche de l'hétérogénéité tumorale dans le cancer bronchique non à petites cellules (CBNPC)* »

Projet sur une nouvelle approche de l'hétérogénéité tumorale dans les cancers bronchiques NPC suite à l'émergence de la TEP-IRM permettant de combiner les deux techniques avec un même appareil. Il s'agit d'une étude exploratoire/observationnelle qui vise à réaliser des examens TEP-IRM avant et après traitement en plus des examens classiques avec un double objectif : étudier la complémentarité TEP-IRM et la prédiction à la résistance au traitement. 30 patients seraient inclus.

AVIS DU BGRP : AVIS FAVORABLE

Commentaires :

- **S'assurer de l'homogénéité des traitements reçus par les patients participant à l'étude**
- **Affiner la partie statistique et trouver un statisticien Gustave Roussy. Qui réalise l'analyse des données ? Qui héberge la base de données ?**
- **Voir Delphine Vuillier pour le budget.**

Statisticien(ne) : A définir

** INBOUND NOTIFICATION : FAX RECEIVED SUCCESSFULLY **

TIME RECEIVED	REMOTE CSID	DURATION	PAGES	STATUS
June 15, 2017 1:03:37 PM GMT+02:00	+33155874290	38	1	Received

Fax émis par : +33155874298 ANSM/DMDIAG 15-06-17 12:55 Pg: 1/1

ansm
Agence nationale de sécurité du médicament et des produits de santé

RÉPUBLIQUE FRANÇAISE

Direction des dispositifs médicaux de diagnostic et des plateaux techniques
Equipe produits des dispositifs médicaux Radiogènes, d'injection,
d'Aide patient et Logiciels
Dossier suivi par Myriam MALOTAUX
Tél. : +33 (0)1 55 87 36 96
Fax : +33 (0)1 55 87 37 42
E-mail : ec.dm-cos@ansm.sante.fr

Saint-Denis, le 15 JUIN 2017

Objet : Intégration Multiparamétrique TEP-IRM pour une nouvelle Approche de l'Hétérogénéité Tumorale dans le cancer bronchique non à petites cellules (CBNPC) : Etude Pilote

N° d'enregistrement : DMDPT-RIAL/MM/2016-A02074-47

Madame,

Par courriel daté du 24/04/2017, vous avez adressé à l'Agence nationale de sécurité du médicament et des produits de santé (ANSM) une demande d'autorisation de recherche portant sur un dispositif médical/dispositif médical de diagnostic *in vitro* pour la recherche citée en objet.

Au vu du dossier fourni (version 1.0 du 19/04/2017 du protocole), j'autorise cette recherche en France.

En vertu de l'article L. 1121-4 du code de la santé publique, je vous précise toutefois que cette recherche doit bénéficier d'un avis favorable d'un comité de protection des personnes (CPP) pour pouvoir être mise en place en France.

Je vous rappelle notamment que, pendant le déroulement de la recherche et pour ce qui concerne l'ANSM, toute modification substantielle du dossier initialement soumis doit faire l'objet d'une demande d'autorisation en vertu de l'article L. 1123-9 du code de la santé publique et des dispositions réglementaires prises pour son application. Les effets/évènements indésirables graves ainsi que les faits nouveaux susceptibles de porter atteinte à la sécurité des personnes sont à déclarer en vertu de l'article L. 1123-10 du code de la santé publique. La fin de l'essai est également à déclarer en vertu de l'article L. 1123-11 du code de la santé publique.

Je vous prie d'agréer, Madame, Monsieur, l'expression de mes salutations distinguées.

Le chef de produits des dispositifs médicaux radiogènes, d'injection, d'aide patient et des logiciels
Direction des dispositifs médicaux de diagnostic et des plateaux techniques

Hélène BRUYERE

INSTITUT GUSTAVE ROUSSY
114 rue Edouard Vaillant
94805 VILLEJUIF CEDEX

A l'attention de Madame Valérie Johnson
Télécopie : 01.42.11.62.90

Copie : CPP "Est-III"

COMITÉ de PROTECTION des PERSONNES EST-III

Hôpital de Brabois. Rue du Morvan - 54511 VANDŒUVRE-LES-NANCY Cedex

Téléphone : 03 83 15 43 24 - **Télécopie** : 03.59.62.06.02 - **Courriel** : cppest.3@chru-nancy.fr

Nancy, le vendredi 7 juillet 2017

Mme Valérie JOHNSON
Chargée d'affaires réglementaires
Et assurance qualité
Institut Gustave ROUSSY
114 rue Edouard Vaillant
94805 VILLEJUIF cedex

Projet de recherche enregistré
Sous les références
N°ID RCB: 2016-A02074-47
N° CPP: 17.06.02

Madame,

Je vous prie de bien vouloir trouver ci-joint l'avis du Comité concernant les modifications apportées au protocole intitulé :

« Intégration Multiparamétrique TEP-IRM pour une nouvelle approche de l'hétérogénéité tumorale dans le cancer bronchique non à petites cellules (CBNPC) : étude pilote ».

Veuillez agréer, Madame, l'assurance de ma sincère considération.

Le Président

Docteur P. PETON

COMITÉ de PROTECTION des PERSONNES EST-III

Hôpital de Brabois. Rue du Morvan - 54511 VANDŒUVRE-LES-NANCY Cedex

Téléphone : 03 83 15 43 24 - **Télécopie** : 03.59.62.06.02 - **Courriel** : cppest.3@chru-nancy.fr

Projet de recherche enregistré
Sous les références
N°ID RCB: 2016-A02074-47
N° CPP: 17.06.02

Le Comité a été saisi le 22 juin 2017 par Mme Valérie JOHNSON, Chargée d'affaires réglementaires et assurance qualité, représentant l'Institut Gustave Roussy, promoteur, pour l'examen des modifications apportées au protocole intitulé :

« Intégration Multiparamétrique TEP-IRM pour une nouvelle approche de l'hétérogénéité tumorale dans le cancer bronchique non à petites cellules (CBNPC) : étude pilote ».

Dont l'investigateur est Mme le Dr Caroline CARAMELLA – Service Radiodiagnostique – Institut Gustave Roussy.

Le Comité a examiné ces modifications lors de sa séance du **4 juillet 2017**. Ont participé aux délibérations :

- les membres du Collège n° 1 :
Catégorie 1 : Mr Peton (Titulaire), Mme Luporsi (Titulaire), Mr Perrin (Titulaire), Mr Beau (Titulaire)
Catégorie 2 : Mr Groscolas (Suppléant),
Catégorie 3 : Mr Bureau (Titulaire), Melle Raffy (Suppléante),
Catégorie 4 : Mr Pfeiffer (Titulaire), Mme Hertz (Suppléante),
- les membres du Collège n° 2 :
Catégorie 5 : Mr Martinet (Suppléant),
Catégorie 6 : Mme Torchia (Titulaire),
Catégorie 8 : Mme Toussaint (Titulaire), Mme Dumas Lavenac (Suppléante),
Catégorie 9 : Mr Vidal (Titulaire), Mme Boutet (Suppléante), Mme Sommelet (Suppléante), Mr Gris (Suppléant).

Le Comité a adopté la délibération suivante : **AVIS FAVORABLE pour :**

- Le courrier de demande d'avis daté du 24.04.2017
- Formulaire de demande d'avis daté du 24.04.2017
- Document additionnel daté et signé du 24.04.2017
- Attestation d'assurance datée du 27.04.2017
- Le mail de la société SHAM France en date du 16.06.2017
- Protocole version n°1.0 du 19.04.2017
- Le résumé du protocole : version n°1.0 du 19.04.2017
- Le manuel opérateur du système SIGNA PET/MR Rév.2 (01/2015)
- L'autorisation délivrée par le tiers propriétaire des données (GE Healthcare) au promoteur pour l'utilisation des données relatives au dispositif
- La note d'information et le formulaire de consentement : version 1.1 du 22.06.2017
- La liste investigateurs : version 1.0 du 28.03.2017
- CV des investigateurs principaux.
-

NB : il convient de corriger la lettre d'information. 7 patients sont mentionnés au lieu de 20.

vendredi 7 juillet 2017

Le Président

Docteur P. PETON

NOTE D'INFORMATION & FORMULAIRE DE CONSENTEMENT

" INTEGRATION MULTIPARAMETRIQUE TEP-IRM POUR UNE NOUVELLE APPROCHE DE L'HETEROGENEITE TUMORALE DANS LE CANCER BRONCHIQUE NON A PETITES CELLULES (CBNPC) : ETUDE PILOTE "

"IMAHTEP"

N°CSET 2016/2499
N° d'enregistrement 2016-A02074-47

(Original pour le médecin-investigateur,
copie à remettre au patient)

Investigateur Coordonnateur : Dr CARAMELLA
Promoteur : Gustave Roussy

Gustave Roussy promoteur

GUSTAVE ROUSSY
CANCER CAMPUS
GRAND PARIS

Madame, Monsieur,

Votre médecin vous propose de participer à une étude clinique. Cette recherche biomédicale est à l'initiative de Gustave Roussy qui est promoteur de cette étude. Le médecin qui vous suivra pendant l'étude est appelé médecin-investigateur.

Avant que vous ne décidiez de participer à cette étude (et de dater et signer le formulaire de consentement), il vous est demandé de lire attentivement ces pages. Elles vous apporteront les informations nécessaires concernant les différents aspects de l'étude, les éventuels bénéfices, risques et gênes qu'elle pourrait vous occasionner. N'hésitez pas à poser des questions au médecin-investigateur car il est là pour y répondre. Vous pouvez prendre le temps nécessaire pour vous décider à participer ou non à cette étude clinique. Et si vous le souhaitez, vous pouvez en discuter avec votre entourage ou votre médecin traitant avant de prendre votre décision.

/// LES OBJECTIFS DE LA RECHERCHE

Les outils d'imagerie actuels essentiels dans la prise en charge de votre cancer, permettent difficilement d'évaluer à un stade très précoce (c'est à dire peu de temps après le début du traitement), les effets de la radio-chimiothérapie sur le cancer. Pour cette raison un suivi régulier après traitement est réalisé, de manière à suivre les changements du cancer dans le temps, et ainsi pouvoir évaluer les effets du traitement.
Une nouvelle méthode d'imagerie appelée TEP-IRM, combinant des informations plus sophistiquées, est disponible depuis moins d'un an en France. L'objectif de cette recherche est d'explorer les informations fournies par cette nouvelle méthode d'imagerie TEP-IRM sur votre cancer, car elle pourrait permettre d'évaluer, plus rapidement que les outils d'imagerie actuels, les effets du traitement par radio-chimiothérapie sur votre cancer.

/// LA METHODOLOGIE

Cette **recherche ne retardera ni ne modifiera d'aucune manière la prise en charge habituelle de votre cancer**. Vous réaliserez, **en plus de votre bilan classique**, deux examens d'imagerie supplémentaires dénommés TEP-IRM :

- Le premier examen TEP-IRM sera réalisé juste avant le début du traitement ;
- Le deuxième examen TEP-IRM sera réalisé environ 2 mois et demi après le début du traitement.

/// LE DEROULEMENT DE L'ETUDE

Vous réaliserez vos deux examens sur la même machine TEP-IRM, au sein du Service Hospitalier Fréderic Joliot situé à Orsay, en Ile de France. Le premier examen sera réalisé dans les jours précédant le début de votre traitement. Le deuxième examen, également réalisé au sein du Service Hospitalier Fréderic Joliot, aura lieu environ deux mois et demi après le premier examen.

Pour chacun des deux examens TEP-IRM que vous réaliserez, il faudra compter environ 1h30 dans le service (installation dans la machine d'une durée de 20 minutes, et réalisation des images dans la machine pendant 1h00).

Université Paris-Saclay
Espace Technologique / Immeuble Discovery
Route de l'Orme aux Merisiers RD 128 / 91190 Saint-Aubin, France

Pour chacun des deux examens TEP-IRM :

- Vous devrez être à jeun dans les 6h précédant l'examen ;
- Le médecin responsable de l'étude vous réexpliquera les procédures de l'examen, s'assurera de votre consentement à la réalisation de l'examen, vérifiera l'absence de contre-indications à la réalisation de l'examen (claustrophobie, insuffisance rénale sévère, diabète non équilibré, prothèses métalliques et pacemaker) et recueillera sur un petit carnet les informations nécessaires pour l'examen (votre poids, votre taille, la date de début de votre traitement le cas échéant) ;
- Une manipulatrice en radiologie
    - Mettra en place un petit cathéter veineux sur votre bras droit
    - Vérifiera votre taux de sucre dans le sang avec un petit appareil adapté qui prélèvera une goutte de sang au bout de votre doigt ;
- Vous serez ensuite allongés sur le dos dans la machine TEP-IRM (qui ressemble à une IRM), pour une durée totale d'une heure ;
- Pour votre confort, un oreiller et des reposes jambes vous seront proposés ;
- Vous aurez également des bouchons d'oreilles et un casque car la machine peut faire un peu de bruit ;
- Un électrocardiogramme et une ceinture abdominale adaptée permettront de suivre votre pouls et votre respiration tout au long de l'examen ;
- Vous disposerez d'une alarme dans la main de votre choix, vous permettant de signaler, à n'importe quel moment de l'examen, toute gêne ou problème ;
- Les images débuteront juste après l'administration, par le petit cathéter de votre bras, d'un premier produit (^{18}F-FDG) permettant de réaliser les images TEP ;
- Environ 5 minutes avant la fin de l'examen, un deuxième produit (Gadolinium) vous sera administré par le même cathéter, permettant de réaliser certaines images IRM.

Au décours de l'examen, la manipulatrice en radiologie vous enlèvera votre petit cathéter et le médecin responsable s'assurera, avant de vous libérer, que tout va bien pour vous. Une petite collation vous sera également proposée. Vous pourrez ensuite retourner chez vous normalement, sans aucune précaution particulière.

Dans le cadre de cette étude, aucune visite particulière ne sera effectuée en dehors de l'entretien réalisé par le médecin responsable au moment de chaque examen TEP-IRM.
Vous serez suivi par votre médecin oncologue-radiothérapeute, dans le cadre de votre maladie, de manière tout à fait standard.

/// NOMBRE DE PARTICIPANTS ET DUREE DE L'ETUDE

Cette étude est la première de ce type et chacun des vingt participants ne réalisera que deux examens TEP-IRM. Ces deux examens n'auront aucune influence sur la prise en charge habituelle de votre cancer.

/// LES BENEFICES ATTENDUS

Cette étude pourrait concourir à mieux comprendre les effets du traitement sur votre cancer, et évaluer les modifications plus précocement que les méthodes d'imagerie actuellement utilisées.
Les examens réalisés n'auront aucune influence sur la prise en charge habituelle de votre cancer.

Université Paris-Saclay
Espace Technologique / Immeuble Discovery
Route de l'Orme aux Merisiers RD 128 / 91190 Saint-Aubin, France

/// LES RISQUES

Associés à la machine TEP-IRM :
De manière générale, le risque inhérent à la réalisation d'un examen TEP-IRM doit être considéré comme négligeable. Quelques effets indésirables mineurs, strictement identiques aux examens TEP et IRM que vous aurez déjà passé de manière séparée lors du bilan standard de votre cancer, peuvent être mentionnés :

a) Les risques liés à la machine TEP : Aucun risque répertorié.
b) Les risques liés à la machine IRM :
   - Sensation de fourmillement / échauffement : les champs magnétiques permettant de réaliser les images peuvent parfois induire une sensation de fourmillement et ou échauffement. Ces effets sont transitoires et sans danger pour votre santé.
   - Le bruit : d'une manière générale, le bruit excessif lors de la réalisation des images peut rendre inconfortable l'examen, et, en l'absence de précautions, provoquer une diminution de l'audition. Pour ces raisons, la mise en place de bouchons dans les oreilles et d'un casque anti-bruit est le moyen le plus facile et le plus efficace pour prévenir tous les désagréments dus au bruit.

Associés à l'administration des produits par voie intraveineuse :

- Comme pour toute pose de cathéter, il existe un risque de petit hématome (un "bleu"), de douleur ou d'infection au site de prélèvement (à l'endroit où a été effectué la piqûre), et de malaise.
- Le premier produit injecté (^{18}F-FDG permettant de réaliser les images TEP) ne présente strictement aucun effet secondaire, notamment toxique ou allergique.
- Le deuxième produit injecté (Gadolinium permettant de réaliser certaines images IRM) peut potentiellement, en cas d'insuffisance rénale chronique, induire une fibrose des reins. Par conséquent, cette étude n'inclura donc pas de patients à risque, et seuls des produits de catégorie 2, c'est à dire à risque minime ou inexistant de fibrose, seront utilisés. Comme pour tout produit de contraste, des réactions d'hypersensibilité peuvent être observées, et ce notamment en cas de terrain à risque : antécédents d'allergie, sensibilité aux produits de contraste, asthme. Pour éviter ce type d'effet indésirable, cette étude n'inclura donc pas de patients présentant des antécédents de réaction allergique ou d'asthme.

/// LES ALTERNATIVES THERAPEUTIQUES

Le médecin-investigateur pourra vous donner davantage d'informations à propos des risques et bénéfices liés à votre participation à cette étude clinique. N'hésitez pas à lui poser la question avant de prendre votre décision. Dans tous les cas, vous bénéficierez d'une prise en charge appropriée.

/// PARTICIPATION VOLONTAIRE / INTERRUPTION DE PARTICIPATION

Votre participation à cette étude est entièrement libre et volontaire. Vous devez être affilié(e) à un régime de sécurité sociale ou bénéficiaire d'un tel régime (y compris la CMU) pour pouvoir y participer. Vous ne pouvez pas participer simultanément à une autre étude.

Vous pouvez décider de refuser de participer ou de sortir de l'étude à tout moment, sans avoir à vous justifier et sans que cela n'ait de conséquence sur votre suivi médical ni sur la qualité de vos soins ultérieurs.

Si vous retirez votre consentement, les informations recueillies dans le cadre de cette étude seront conservées et analysées, sauf si vous exprimez votre refus auprès du médecin investigateur. Dans ce cas, les données de l'étude vous concernant seront détruites.

/// NOUVELLES INFORMATIONS SUR L'ETUDE

Vous serez informé(e) en temps opportun de toute nouvelle information concernant votre sante ou donnée nouvelle qui pourrait influencer votre volonté de poursuivre votre participation à cette étude. Si de nouvelles informations venaient à modifier celles qui vous sont présentées dans ce document, un nouveau document vous serait remis afin que vous en soyez informé(e) et afin que vous confirmiez, ou non, votre souhait de poursuivre cette étude.

/// COÛTS POTENTIELS / REMUNERATION ET INDEMNISATION

Vous ne serez pas payé(e) pour votre participation à cette étude. Néanmoins le coût de votre transport sera pris en compte.
Vous bénéficierez gratuitement de tous les examens exclusivement requis pour cette étude, et qui ne font pas partie de vos soins médicaux réguliers.

/// ASSURANCE

Le promoteur de cet essai qui en assure la gestion et la responsabilité est Gustave Roussy – 114 rue Edouard Vaillant – 94 805 VILLEJUIF - France.
Gustave Roussy a souscrit une assurance (n° de contrat 124895) auprès de la Société SHAM France) dans les conditions prévues à l'article L. 1121-10 du code de la santé publique, garantissant sa responsabilité civile et celle de tout intervenant en cas de conséquences dommageables de la recherche pour la personne qui s'y prête ou pour ses ayants droit. Si vous estimez avoir subi un préjudice du fait de votre participation à cette étude, vous devrez en informer votre médecin-investigateur.

/// PROTECTION DES PATIENTS / CONFIDENTIALITE DES DONNEES

Conformément à la Loi 2004-806 du 9 août 2004 sur les recherches biomédicales (Code de la santé publique) et les Bonnes Pratiques Cliniques, ce protocole a été autorisé par l'Agence Nationale de Sécurité du Médicament et des produits de santé (ANSM) le 15/06/2017 et il a reçu l'avis favorable d'un Comité de Protection des Personnes (CPP EST 3) le 07/07/2017.

Conformément aux recommandations du Plan Cancer, ce document a été soumis pour relecture, avis et conseil au comité de patients de la Ligue nationale contre le cancer.

Tous les fichiers et les dossiers dans lesquels apparaîtra votre identité seront gardés par le médecin-investigateur et resteront strictement confidentiels. Votre dossier médical restera confidentiel et ne pourra être consulté que par les autorités de santé et par des personnes dûment mandatées par le promoteur de l'essai et soumises au secret professionnel, sous la responsabilité de votre médecin. Conformément à la loi n°2002-303 du 4 mars 2002 relative aux droits des malades et à la qualité du système de santé vous avez un droit d'accès à votre dossier médical.

Dans le cadre de cette recherche, un traitement de vos données personnelles va être mis en œuvre pour permettre d'analyser les résultats de l'étude. L'utilisation ultérieure des données collectées dans le cadre de futures recherches scientifiques, en dehors de cette étude, est également possible.

Le traitement se fera de manière anonyme et confidentielle : les données seront identifiées par un numéro de code et/ou vos initiales ou les trois premières lettres de votre nom/prénom.

Ces données seront, dans des conditions assurant leur confidentialité, transmises au promoteur de la recherche, et pourront également être transmises à des personnes ou sociétés agissant pour son compte, à des personnes ou sociétés partenaires ou, le cas échéant, à des autorités de santé françaises ou étrangères. Dans ce cadre, les données pourront être transférées en dehors de la

France, y compris vers des pays non-européen. Les destinataires peuvent éventuellement être situés dans un pays ne bénéficiant pas d'un niveau de protection des données équivalent à celui en vigueur au sein de l'Union Européenne. Cependant, le promoteur prendra toutes les mesures nécessaires à fin d'assurer la protection et la confidentialité des données, comme de garantir votre anonymat.

Le traitement des données est soumis à la loi n° 78-17 du 6 janvier 1978 modifiée, relative à l'informatique, aux fichiers et aux libertés Il est conforme aux requis imposés par la méthodologie de référence, éditée par la CNIL, « MR-001 ». Il a fait l'objet d'une procédure d'autorisation auprès de la CNIL.
Conformément aux dispositions de la loi relative à l'informatique, aux fichiers et aux libertés, précitée, vous disposez d'un droit d'accès et de rectification. Vous disposez également d'un droit d'opposition à la transmission des données couvertes par le secret professionnel susceptibles d'être traitées. Vous pouvez exercer votre droit à tout moment en vous adressant au médecin-investigateur.

Le médecin investigateur sera amené à communiquer des informations sur votre état de santé après la fin de votre participation à l'étude (par exemple votre statut vital ou l'évolution de votre maladie).

Les résultats de l'étude pourront être communiqués à la communauté scientifique lors de séminaires, de congrès ou publiés dans la presse scientifique, en garantissant la confidentialité absolue des données vous concernant, ainsi que votre anonymat.
Selon les dispositions de l'article L 1122-1 du Code de la Santé Publique, les patients ayant participé à l'étude seront informés, à leur demande, par les médecins-investigateurs des résultats globaux de cette recherche à son terme.

Enfin, nous vous informons que votre médecin traitant sera informé de votre participation à l'étude, sauf si vous exprimez votre refus auprès du médecin investigateur.

/// CONTACTS POUR INFORMATIONS COMPLEMENTAIRES OU EN CAS D'URGENCE

Si vous souhaitez obtenir des informations complémentaires ou si vous rencontrez un problème quelconque au cours de votre participation, veuillez contacter le médecin-investigateur, ou un membre de son équipe :

Nom : .....
Téléphone : .....

Ou tampon

Vous pouvez également contacter le coordonateur de l'étude, le Dr CARAMELLA, au numéro suivant : 01 42 11 43 99 (Gustave Roussy)

FORMULAIRE DE CONSENTEMENT -- IMAHTEP N°CSET 2016/2499 -- IDRCB N°2016-A02074-47

Nom du patient : ..... **Prénom :** .....

Il m'est proposé(e) de participer à une étude clinique organisée par Gustave Roussy, et intitulée ***« Intégration Multiparamétrique TEP-IRM pour une nouvelle Approche de l'Hétérogénéité Tumorale dans le cancer bronchique non à petites cellules (CBNPC) : Etude Pilote ».***

En application des dispositions du Code de la Santé Publique, j'ai pris connaissance de la note d'information (**page 1 à 6**). Il m'a été laissé le temps de poser toutes les questions que je souhaitais et toutes les questions posées ont reçu une réponse satisfaisante.

J'ai bien noté que je suis libre d'accepter ou de refuser de participer à l'étude et libre d'interrompre ma participation à tout moment, sans avoir à me justifier ni sans que cela n'ait de conséquence sur la suite et la qualité de mon suivi médical.

Je déclare être affilié(e) à un régime de sécurité sociale ou bénéficiaire d'un tel régime.

Les données médicales ainsi que le dossier médical me concernant resteront strictement confidentiels. Je n'autorise leur consultation que par Gustave Roussy, ses partenaires ou prestataires dûment habilités ainsi que par les autorités de santé. Je comprends que mon nom ne sera jamais mentionné dans les rapports consacrés à cette étude et que mon identité ne sera pas communiquée.

J'accepte le recueil de mes données personnelles ainsi que leur traitement informatique par le promoteur ou par des personnes ou sociétés agissant pour son compte. J'accepte que mes données rendues anonymes soient éventuellement transmises en dehors de France, voire dans un pays ne bénéficiant pas d'un niveau de protection des données équivalent à celui en vigueur au sein de l'Union Européenne (sous la responsabilité du Promoteur). Je suis informé(e) que je dispose d'un droit d'opposition à la transmission des données. Je peux exercer ce droit à tout moment et sous toutes formes, par l'intermédiaire du médecin investigateur qui contactera Gustave Roussy.

J'ai été informé(e)

- Qu'une assurance a été souscrite par Gustave Roussy permettant de couvrir les dommages liés à l'étude conformément à l'art. L1121-10 du Code de la Santé Publique.
- Que cette étude sera conduite conformément à la législation française en vigueur et qu'elle a reçu l'autorisation de l'Agence Nationale de Sécurité du Médicament et des produits de santé et l'avis favorable du Comité de Protection des Personnes (CPP EST 3).

J'accepte librement et volontairement de participer à l'étude proposée ***(CSET 2016/2499, N° IDRCB 2016-A02074-47)***

Cocher les cases appropriées en fonction de votre volonté (OUI/NON)	OUI	NON
Sauf refus exprimé par écrit, j'accepte librement et volontairement que les données collectées pourront être utilisées dans le cadre de futures recherches scientifiques en dehors de ce protocole de recherche clinique.	☐	☐

Partie à remplir par le patient	Partie à remplir par le médecin investigateur
Nom et prénom :	Nom et prénom :
Signature :	Signature :
Date :	Date :

(Original pour le médecin-investigateur, copie à remettre au patient)

Université Paris-Saclay
Espace Technologique / Immeuble Discovery
Route de l'Orme aux Merisiers RD 128 / 91190 Saint-Aubin, France

GUSTAVE ROUSSY
CANCER CAMPUS
GRAND PARIS

/ DIRECTION DE LA RECHERCHE CLINIQUE
SERVICE PROMOTION DES ETUDES CLINIQUES

114, rue Edouard-Vaillant
94805 Villejuif Cedex - France

www.gustaveroussy.fr

Gustave Roussy promoteur

« la DRC est labellisée
Délégation à la Recherche
Clinique et à l'Innovation
par le Ministère de la Santé »

GUSTAVE ROUSSY
CANCER CAMPUS GRAND PARIS

Code Promoteur de l'essai : CSET 2016/2499

N° ID-RCB : 2016-A02074-47

Intégration Multiparamétrique TEP-IRM pour une nouvelle Approche de l'Hétérogénéité Tumorale dans le cancer bronchique non à petites cellules (CBNPC) : Etude Pilote

Titre abrégé du protocole / Acronyme : IMAHTEP

Version finale n° 1.0 du 19/04/2017

INVESTIGATEUR COORDONNATEUR	**Nom : CARAMELLA Caroline** Adresse : 114 Rue Edouard Vaillant, 94800 Villejuif Tél. : 01 42 11 43 99 Fax : 01 42 11 54 95 Email : Caroline.CARAMELLA@gustaveroussy.fr

PROMOTEUR GUSTAVE ROUSSY CANCER CAMPUS GRAND PARIS	**Gustave Roussy** **114 rue Edouard Vaillant** **94 805 Villejuif** **France**	Signature du Directeur de la Direction de la Recherche Clinique: Date : 19/04/2017

PAGE DE SIGNATURE DU PROTOCOLE

« Intégration Multiparamétrique TEP-IRM pour une nouvelle Approche de l'Hétérogénéité Tumorale dans le cancer bronchique non à petites cellules (CBNPC) : Etude Pilote »
« IMAHTEP »

N°ID-RCB: 2016-A02074-47

N° CSET : 2016/2499

Version n°1.0 du 19/04/2017

Centre investigateur :

Service :

Nom et adresse de l'établissement :

Je soussigné, , reconnais avoir pris connaissance de l'ensemble du protocole intitulé « **« Intégration Multiparamétrique TEP-IRM pour une nouvelle Approche de l'Hétérogénéité Tumorale dans le cancer bronchique non à petites cellules (CBNPC) : Etude Pilote** », et je m'engage à conduire ce protocole conformément aux Bonnes Pratiques Cliniques, aux dispositions législatives et réglementaires en vigueur et tel qu'il est décrit dans ce document.

Date : ___ / ___ / 20

Signature :

Université Paris-Saclay
Espace Technologique / Immeuble Discovery
Route de l'Orme aux Merisiers RD 128 / 91190 Saint-Aubin, France

CONTACTS DE L'ETUDE

	Nom et Adresse	Numéro Téléphone / Numéro Fax
Promoteur	**Gustave Roussy** 114 Rue Edouard Vaillant 94805 Villejuif Cedex	Tel : 01 42 11 42 11
Investigateur Principal	Dr CARAMELLA Caroline Gustave Roussy	Tel : 01 42 11 43 99 caroline.caramella@gustaveroussy.fr
Statisticien	Adrien ALLORANT Gustave Roussy DRC - SBE	Adrien.ALLORANT@gustaveroussy.fr
Data manager	Dr Florent BESSON CHU Bicêtre, AP-HP Investigateur associé, doctorant du projet IMATHEP, UMR 8081 Paris-Sud)	Tel : 01 45 21 46 93 Fax : 01 45 21 21 12 florent.besson@aphp.fr
Pharmacovigilance	Dr Salim Laghouati Gustave Roussy DRC - UFPV	Tel: 01 42 11 61 00 Fax: 01 42 11 61 50 phv@gustaveroussy.fr
ARC promoteur	Thibault RAOULT Gustave Roussy SPEC	Tel: 01 42 11 38 92 Fax: 01 42 11 62 90 Thibault.RAOULT@gustaveroussy.fr

SYNOPSIS – PROTOCOLE CSET N°2016/2499

N°ID-RCB	**2016-A02074-47**		**Version et Date**		V1.0	19/04/2017	
Titre de l'Essai	**Intégration Multiparamétrique TEP-IRM pour une nouvelle Approche de l'Hétérogénéité Tumorale dans le Cancer Bronchique Non à Petites Cellules (CBNPC) : Etude Pilote**						
Titre abrégé ou Acronyme	**IMAHTEP**		**Phase de l'essai**		Faisabilité		
Promoteur	Gustave Roussy 114 rue Edouard Vaillant 94805 Villejuif Cedex France						
Investigateur Coordonnateur	**Dr CARAMELLA Caroline**						
Nombre de centres	**Total**	**2**	**France**	**2**	**International**		**0**
Objectif Principal	Estimer la reproductibilité intra et inter-opérateur d'une cartographie régionale multiparamétrique TEP-IRM dans le cancer bronchique non à petites cellules (CBNPC) localement avancé.						
Objectif(s) secondaire(s)	Déterminer l'amplitude des modifications régionales des paramètres TEP-IRM du CBNPC sous traitement. Corrélation des paramètres d'imagerie à la survie des patients						
Plan de l'étude	Etude pilote de faisabilité prospective monocentrique						
Critères d'inclusion	1. CBNPC localement avancé (stades IIB, IIIA ou IIIB de la classification TNM 7ème édition) 2. Prise en charge thérapeutique exclusive par radio-chimiothérapie concomitante administrée conformément aux recommandations internationales (bithérapie par sels de platine) 3. Consentement signé 4. Patients affiliés au régime de la sécurité sociale ou bénéficiaire d'un régime similaire.						
Critères d'exclusion	1. Mineur 2. Femme enceinte/allaitante 3. Personne privée de liberté par décision judiciaire ou administrative, personnes majeures faisant l'objet d'une mesure de protection légale ou hors d'état d'exprimer leur consentement 4. ATCD de Cancer dans les 2 années précédant l'enregistrement 5. ATCD de radiothérapie / chirurgie thoracique 6. Patients sous traitement expérimental ou pour lequel l'administration d'un traitement expérimental est prévue 7. Patients claustrophobes 8. Insuffisance rénale sévère (Clairance MDRD Cockroft < 30ml/min) 9. Diabète non contrôlé, hyperglycémie > 1,8g/L 10. Patient porteur d'implants métalliques non compatibles avec l'IRM ou de tout matériel médical électronique implanté de manière inamovible (e.g pacemaker, neurostimulateur, implants cochléaires, etc.)						

Université Paris-Saclay
Espace Technologique / Immeuble Discovery
Route de l'Orme aux Merisiers RD 128 / 91190 Saint-Aubin, France

<table>
<tr><td>Traitements étudiés</td><td colspan="3">Caractérisation de l'hétérogénéité tumorale par une cartographie régionale multiparamétrique TEP-IRM.
Les patients réaliseront :
- un examen TEP-IRM réalisé avant le traitement par radio-chimiothérapie (TEP-IRM$_0$ dite baseline)
- un examen TEP-IRM réalisé à mi-parcours du traitement (TEP-IRM$_1$ sous traitement), soit après avoir reçu 33±4 Gy (environ 2,5mois après la première TEP-IRM).</td></tr>
<tr><td>Critère d'évaluation principal</td><td colspan="3">Mesure de la reproductibilité intra et inter-opérateur des cartographies régionales multiparamétriques TEP-IRM réalisées avant et sous traitement.</td></tr>
<tr><td>Critères d'évaluation secondaire(s)</td><td colspan="3">Analyse de la variance (ANOVA) des paramètres d'imagerie obtenus avant et après traitement (TEP-IRM$_0$ et TEP-IRM$_1$).
Analyse descriptive de la survie (globale et sans progression) afin d'explorer ses liens avec les paramètres d'imagerie.</td></tr>
<tr><td>Nombre de patients</td><td colspan="3">Aucune étude dans le monde n'a réalisé ce type d'évaluation TEP-IRM combinée du CBNPC sous traitement sur une population homogène (stade tumoral, traitement) avec critères de sélections pré-établis.
Ce projet pilote étant par conséquent une étude de faisabilité princeps, il n'est pas possible à ce stade de prédire l'effectif de patients nécessaires à la mise en évidence des changements des paramètres d'imagerie sous traitement. Par conséquent un nombre arbitraire de patients est choisi : 20 patients évaluables.</td></tr>
<tr><td></td><td>Total de patients évaluables</td><td>France : 20</td><td>Gustave Roussy : 20</td></tr>
<tr><td rowspan="4">Durée de l'essai</td><td colspan="2">Durée d'inclusion</td><td>12 mois</td></tr>
<tr><td colspan="2">Durée maximale de participation du patient</td><td>Jusqu'à réalisation du second TEP-IRM (Environ 2,5 mois)</td></tr>
<tr><td colspan="2">Durée de suivi du patient</td><td>15 mois</td></tr>
<tr><td colspan="2">Durée globale de l'essai</td><td>30 mois</td></tr>
</table>

Université Paris-Saclay
Espace Technologique / Immeuble Discovery
Route de l'Orme aux Merisiers RD 128 / 91190 Saint-Aubin, France

Tableau récapitulatif des investigations

		$TEP\text{-}IRM_0$	$TEP\text{-}IRM_1$
Investigations (paramètres d'imagerie)	**TEP**	SUV et dérivés	SUV et dérivés
		Textures	Textures
		MRGlu (dynamique)	MRGlu (dynamique)
	IRM	Morphologie	Morphologie
		Diffusion	Diffusion
		Cartographie ADC	Cartographie ADC
		Correction d'atténuation et du mouvement	Correction d'atténuation et du mouvement
		Perfusion (dynamique)	Perfusion (dynamique)
		T1 et T2 mapping	T1 et T2 mapping

TABLE DES MATIERES

1 INTRODUCTION ET RATIONNEL DE L'ESSAI

1.1 Synthèse des résultats antérieurs

L'hétérogénéité tumorale est un facteur majeur de progression et de survie tumorale[1,2]. Le cancer bronchique non à petites cellules (CBNPC) est la première cause de mortalité oncologique dans le monde avec une espérance de vie de moins de 10% à 5 ans pour les stades avancés. Le traitement de référence du CBNPC localement avancé inopérable (stade III) est la radio-chimiothérapie concomitante, mais la grande hétérogénéité du CBNPC favorise l'émergence fréquente de résistances, notamment locorégionales, aux traitements[3]. De plus, l'évaluation précoce est souvent difficile après radio-chimiothérapie, parce que les critères d'imagerie standard (RECIST 1.1) ne permettent pas de discriminer de façon fiable les effets post-thérapeutiques précoces (inflammation, radionécrose) d'éventuelles récidives locales[4,5]. C'est pourquoi l'imagerie oncologique multiparamétrique émerge. Les biomarqueurs ciblant le métabolisme (TEP)[6,7] et la vascularisation tumorale (IRM)[8-10] ont montré des résultats prometteurs en oncologie. Les quelques études multiparamétriques TEP et IRM fusionnées déjà réalisées dans le CBNPC restent néanmoins peu nombreuses (une dizaine en 15 ans), de méthodologies hétérogènes, et enfin ne font pas d'analyse fine de l'hétérogénéité régionale intra tumorale. Une meilleure caractérisation de cette hétérogénéité par une approche multiparamétrique TEP-IRM combinée fine pourrait favoriser l'identification précoce de zones de résistance après traitement, et permettre ainsi une adaptation thérapeutique beaucoup plus précoce.

Parce que l'imagerie hybride TEP-IRM permet de confronter de façon unique les informations multiparamétriques TEP et IRM (alignement parfait des images TEP et IRM, acquisitions de manière simultanée), cette modalité d'imagerie pourrait, dans les années à venir, tenir une place de choix dans l'évaluation oncologique du CBNPC.

1.2 Données du/des traitement(s) à évaluer

Les machines hybrides TEP-IRM combinées sont commercialisées dans le monde depuis 2011. Il existe actuellement en France trois machines TEP-IRM, opérationnelles depuis l'an dernier (SHFJ d'Orsay, sur laquelle sera réalisé ce projet, Pitié-Salpêtrière et CERMEP de Lyon). Compte tenu du caractère extrêmement récent de ce type de machine, aucune donnée n'existe actuellement sur l'apport des machines hybrides TEP-IRM dans l'évaluation thérapeutique du CBNPC localement avancé. Partant du constat que chacune des 2 modalités (TEP et IRM de perfusion) ont montré d'une part leur intérêt indéniable dans l'évaluation précoce sous traitement et le pronostic des patients oncologiques, et compte tenu de la mise en exergue de l'approche combinée TEP-IRM dans l'évaluation initiale du cancer bronchique illustrée par de récentes études[11-15], nous pensons que la combinaison des informations TEP et IRM à l'échelle du voxel, uniquement réalisable sur ce type de machine (recalage parfait et simultanéité de l'acquisition des images TEP et IRM) permettrait une analyse plus fine de l'hétérogénéité tumorale du CBNPC et donc une évaluation sous traitement plus performante que chacune des deux modalités prises indépendamment l'une de l'autre. La robustesse de ce type d'approche nécessite néanmoins d'être évaluée et validée.

1.3 Evaluation du Bénéfice / Risque

Un dispositif TEP-IRM combine une machine TEP et une machine IRM en un seul appareil. Concernant la TEP, l'injection d'une quantité infime (dose dite « traceuse ») d'un produit radiopharmaceutique émetteur de rayonnements ionisants à demi vie très courte (en l'occurrence le ^{18}Fluoro-deoxy-glucose, analogue du glucose radiomarqué au ^{18}Fluor, demi vie = 110minutes) nécessaire à la réalisation des images n'est pourvoyeuse d'aucun effet secondaire. D'autre part, l'irradiation résultante globale est inférieure à 5-7 micro sieverts, soit deux fois moins que l'irradiation d'une TDM thoraco-abdominale de radiologie standard (10-14 micro sieverts).

Concernant l'IRM, l'obtention des images est basée sur l'utilisation de champs magnétiques et d'ondes de radiofréquences, dont l'utilisation en routine clinique n'a montré aucun effet délétère pour la santé. La présence de bruit durant l'examen peut néanmoins rendre inconfortable l'examen, raison pour laquelle l'utilisation de bouchons dans les oreilles et d'un casque protecteur est systématique et limite tous les

désagréments sonores. L'administration de chélates de gadolinium nécessaire aux séquences de perfusion peut potentiellement, chez les patients insuffisants rénaux chroniques, induire une fibrose néphrogénique systémique, dont la physiopathologie reste à ce jour inconnue. Par conséquent nous ne réaliserons nos examens que chez des patients présentant une fonction rénale satisfaisante, en utilisant un produit de contraste de catégorie 2 (Dotarem®), c'est à dire à risque minime ou inexistant de fibrose néphrogénique systémique. Ainsi le risque inhérent à la réalisation d'un examen TEP-IRM est considéré comme négligeable.
Les examens TEP-IRM seront réalisés **en plus et de manière concomitante au bilan diagnostique standard des patients, n'induisant par conséquent aucune perte de chance pour les participants de l'étude.**

2 OBJECTIFS DE L'ESSAI

2.1 Objectif principal

Estimer la reproductibilité intra et inter-opérateur d'une cartographie régionale multiparamétrique TEP-IRM dans le cancer bronchique non à petites cellules (CBNPC) localement avancé.

2.2 Objectifs secondaires

- Déterminer l'amplitude des modifications régionales des paramètres TEP-IRM du CBNPC sous traitement.
- Corrélation des paramètres d'imagerie à la survie des patients

3 METHODOLOGIE

Cette étude pilote de faisabilité est une étude exploratoire, prospective, multicentrique.
Un échantillon de 20 patients présentant un CBNPC localement avancé (stade IIB-IIIA-IIIB de la classification TNM 7ème édition) bénéficiera, **en plus et de manière concomitante à la prise en charge diagnostique et thérapeutique standard**, de deux examens d'imagerie TEP-IRM, réalisés sur le même dispositif installé au Service Hospitalier Frédéric Joliot d'Orsay (CEA - Service Hospitalier Frédéric Joliot , 4 place du Général Leclerc, 91401 Orsay Cedex) :

- Un examen TEP-IRM réalisé juste avant traitement (TEP-IRM$_0$ dite baseline)
- Un examen TEP-IRM réalisé à mi-parcours du traitement (TEP-IRM$_1$ sous traitement), soit après avoir reçu 33±4 Gy (environ 2,5 mois après la première TEP-IRM).

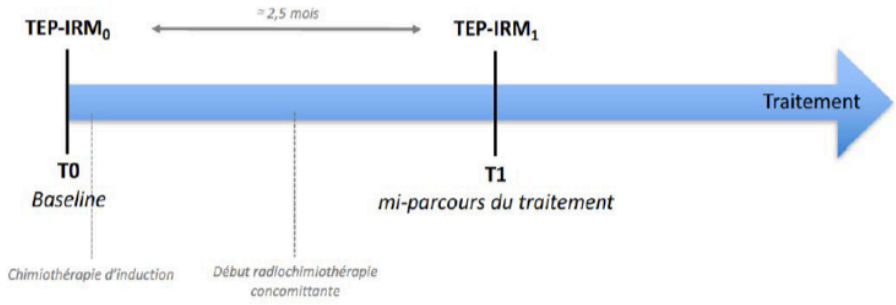

Université Paris-Saclay
Espace Technologique / Immeuble Discovery
Route de l'Orme aux Merisiers RD 128 / 91190 Saint-Aubin, France

Protocole d'imagerie :

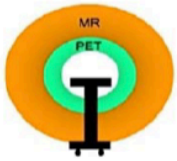

PET-MR

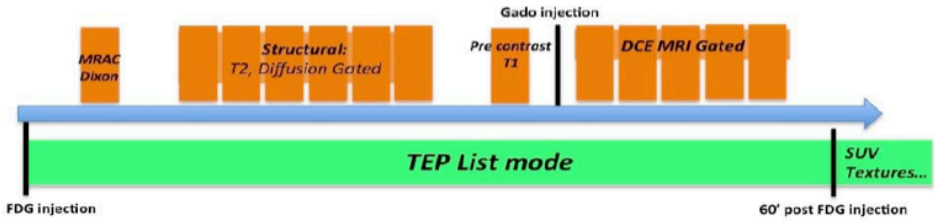

Toutes les acquisitions TEP-IRM de l'étude seront standardisées (protocole identique) et centrées sur le thorax,

Modalités pratiques :

Patient allongé en décubitus dorsal pendant toute la durée de l'examen
Antenne surfacique sur le thorax
Cal-mousse au niveau des jambes, et oreiller au niveau de la tête pour plus de confort.
Bouchons d'oreille + casque d'insonorisation pour IRM.
Poire d'appel d'urgence dans la main pour signaler tout problème éventuel.

Champ de vue :

Thorax incluant la masse tumorale et les principaux axes vasculaires médiastinaux (nécessaires au calcul de la fonction d'entrée artérielle pour les séquences d'IRM de perfusion).

Acquisitions TEP :

L'acquisition des images TEP débutera immédiatement après l'injection intra-veineuse du radiotraceur (^{18}F-FDG), en mode liste (c'est à dire enregistrement continu), pendant une durée totale de 60 minutes.
L'enregistrement continu du mode liste permettra d'extraire les paramètres dynamiques du métabolisme glucidique (MRGlu, cf infra).
Selon les recommandations internationales, les paramètres statiques (cf infra) seront extraits 1h post-injection, justifiant les 60 minutes de protocole d'acquisition.

Acquisitions IRM (± asservissement respiratoire / cardiaque standards par ceinture pneumatique positionnée au niveau de l'abdomen / monitoring ECG) :

Pendant l'acquisition des images TEP (soit 1 heure d'examen), différentes séquences IRM seront successivement réalisées, comprenant notamment :

- Une séquence Dixon standard en apnée (< 20 secondes) qui permettra la correction d'atténuation ultérieure des images TEP.
- Une séquence ZTE pour suivre le mouvement respiratoire.
- Des séquences structurelles en pondération T2 (respiration libre avec asservissement respiratoire/cardiaque), qui permettront l'analyse morphologique de la masse tumorale.
- Des séquences de T1 et T2 mapping pour l'analyse quantitative tissulaire.
- Des séquences de diffusion (respiration libre avec asservissement respiratoire/cardiaque) qui permettront l'étude de la densité cellulaire et le calcul du coefficient de diffusion apparent, permettant de quantifier le degré de cellularité au sein de la masse tumorale.
- Une séquence standard d'IRM dynamique de perfusion d'une durée de 5 minutes (respiration libre avec asservissement respiratoire/cardiaque), après l'injection intra-veineuse de gadolinium, selon les recommandations internationales (QIBA version 1.0, 2012), qui permettra d'évaluer la perfusion tumorale.

Ainsi, pour chaque TEP-IRM, l'ensemble du protocole durera au total 60 minutes et :

- Comportera l'injection intra-veineuse de deux produits (^{18}F FDG pour les images TEP et Gadolinium pour l'IRM de perfusion)
- Le patient allongé et au repos dans la machine pendant l'examen pourra, à tout moment, signaler toute gêne/inconfort et / ou faire stopper le protocole.

Extraction et post-processing des données d'imagerie :

Université Paris-Saclay
Espace Technologique / Immeuble Discovery
Route de l'Orme aux Merisiers RD 128 / 91190 Saint-Aubin, France

1)

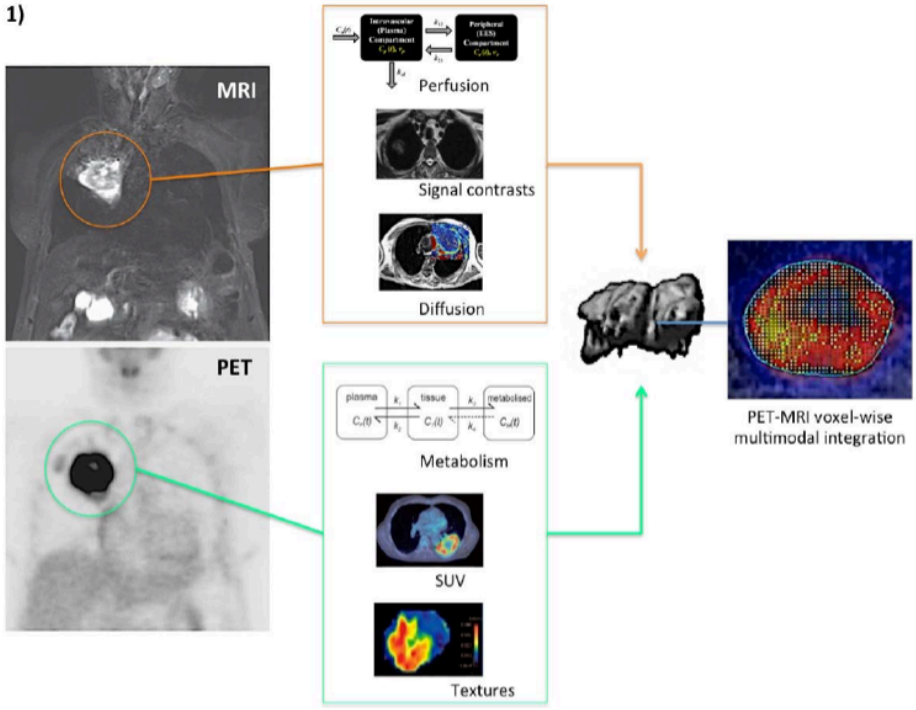

Les paramètres TEP et IRM seront extraits à partir de volumes tumoraux d'intérêt. Des masses tumorales supérieurs à 33,5cm3 (3 x FWHM) seront nécessaires pour limiter les effets de volume partiel pouvant influer sur le calcul des paramètres d'imagerie et la régionalisation tumorale[16,17].

Paramètres TEP :

a) Statiques :
Les paramètres TEP statiques comprendront le SUV et ses dérivés (SUVmax, SUVmean, SULmax, SULmean), ainsi que des indices texturaux[18].

b) Dynamiques :
Les paramètres dynamiques ayant montré leur plus-value dans l'évaluation thérapeutique en Oncologie[19-21], des données métaboliques dynamiques (MRGlu) seront également extraites.

Paramètres IRM :

Les paramètres IRM comprendront

a) Des indices dynamiques de perfusion standards (QIBA version 1.0, 2012),

b) Des paramètres de densité cellulaire (valeurs d'ADC calculées à partir des séquences de diffusion).

c) Des paramètres de quantification tissulaire (T1 et T2 mapping)

Analyses :

Pour chaque tumeur, les données d'imagerie seront analysées à l'échelle du voxel / groupes de voxels (clusters). Les cartes d'activités régionales intra-tumorales ainsi générées seront finalement combinées en paramètre composites d'activité biologique régionale (régionalisation paramétrique)[17].

Finalement les données TEP-IRM avant et sous traitement seront confrontées d'un point de vue régional, afin d'évaluer les modifications tumorales régionales sous traitement.

4 SELECTION DES PATIENTS

4.1 Critères d'inclusion

1. CBNPC localement avancé (stade IIB, IIIA ou IIIB de la classification TNM 7ème édition)
2. Prise en charge thérapeutique exclusive par radio-chimiothérapie concomitante administrée conformément aux recommandations internationales (bithérapie par sels de platine)
3. Consentement signé
4. Patients affiliés au régime de la sécurité sociale ou bénéficiaire d'un régime similaire

4.2 Critères de non inclusion

1. Mineur
2. Femme enceinte / allaitante
3. Personne privée de liberté par décision judiciaire ou administrative, personnes majeures faisant l'objet d'une mesure de protection légale ou hors d'état d'exprimer leur consentement
4. ATCD de Cancer dans les 2 années précédant l'enregistrement
5. ATCD de radiothérapie / chirurgie thoracique
6. Patients sous traitement expérimental ou pour lequel l'administration d'un traitement expérimental est prévue
7. Patients claustrophobes
8. Insuffisance rénale sévère (Clairance MDRD Cockroft < 30ml/min)
9. Diabète non contrôlé, Hyperglycémie > 1,8g/L
10. Patient porteur d'implants métalliques non compatibles avec l'IRM ou de tout matériel médical électronique implanté de manière inamovible (e.g pacemaker, neurostimulateur, implants cochléaires, etc.)

5 ENREGISTREMENT DES PATIENTS

Les patients seront identifiés lors des réunions de concertation multidisciplinaires et seront recrutés à Gustave Roussy. Les patients éligibles et ayant signé le formulaire de consentement seront enregistrés à Gustave Roussy.

6 DEROULEMENT DE L'ESSAI - TRAITEMENTS

Le patient aura un examen médical préalablement à la recherche. Ce bilan initial consistera en une évaluation du stade de la maladie, une mesure du poids et de la taille et une évaluation de la clairance à la créatinine et du taux de glucose sanguin afin de confirmer que le patient est éligible à la recherche.
Les examens réalisés dans les 3 mois avant l'enregistrement du patient à l'essai ne nécessitent pas d'être répétés.

Après leur inclusion, les patients réaliseront :

- un examen TEP-IRM réalisé avant le traitement (TEP-IRM$_0$ dite baseline)
- un examen TEP-IRM réalisé à mi-parcours du traitement (TEP-IRM$_1$ sous traitement), soit après avoir reçu 33±4 Gy (environ 2,5mois après la première TEP-IRM).
-

Avant chaque TEP-IRM, un contrôle de la glycémie sanguine sera réalisé par glycémie capillaire.

Les recommandations d'usage applicables lors des IRM devront être respectées (*e.g* piercing, tatouage, etc.).

En parallèle de cet essai clinique, les patients inclus seront traités par association Radiothérapie-Chimiothérapie (bithérapie à base de sels de platine) conformément aux recommandations internationales.
La chimiothérapie devra débuter dans les 3 semaines suivant l'inclusion dans l'étude.
La radiothérapie débutera à J42 du début du traitement, mais pourra éventuellement être débutée à J63. Elle sera administrée à la dose de 66 Gy en 33 séances de 2 Gy.

Les données d'évolution de la maladie seront recueillies depuis les examens réalisés lors de la prise en charge standard du patient.

7 CRITERES D'EVALUATION

7.1 Critère principal

Mesure de la reproductibilité intra et inter-opérateur des cartographies régionales multiparamétriques TEP-IRM réalisées avant et sous traitement.

7.2 Critères secondaires

Analyse de la variance (ANOVA) des paramètres d'imagerie obtenus avant et après traitement (TEP-IRM0 et TEP-IRM1).
Analyse descriptive de la survie (globale et sans progression) afin d'explorer ses liens avec les paramètres d'imagerie.

8 DETERMINATION DU NOMBRE DE PATIENTS ET ANALYSE STATISTIQUE

8.1 Nombre de sujets nécessaires

Aucune étude dans le monde n'a réalisé ce type d'évaluation TEP-IRM combinée du CBNPC sous traitement sur une population homogène (stade tumoral, traitement) avec critères de sélections préétablis.
Ce projet pilote étant par conséquent une étude de faisabilité princeps, il n'est pas possible à ce stade de prédire l'effectif de patients nécessaires à la mise en évidence des changements des paramètres d'imagerie sous traitement. Par conséquent un nombre arbitraire de 20 patients évaluables est choisi.

8.2 Analyse statistique

a) Reproductibilité intra et inter-opérateur d'une cartographie régionale multiparamétrique TEP-IRM

Chaque observateur (au moins deux, Dr Caroline CARAMELLA et Dr Florent BESSON) effectuera deux traitements de l'image d'une lésion donnée, avec un intervalle de temps suffisamment long pour éviter le biais de mémoire. La reproductibilité intra sera évaluée à partir de la stabilité des deux cartographies régionales établies par le même observateur sur la même image. La reproductibilité inter observateur sera mesurée à partir de la similitude des deux découpages en clusters réalisés par les deux observateurs, à partir du traitement d'une même image.

b) Amplitude des modifications régionales des paramètres TEP-IRM du CBNPC sous traitement.
On procédera à une analyse de la variance (ANOVA) des paramètres d'imagerie obtenus avant et après traitement ($TEP\text{-}IRM_0$ et $TEP\text{-}IRM_1$). L'effet du traitement sera évalué dans le cadre d'une ANOVA multivariée par un test du rapport de vraisemblance.

c) Analyse à la survie des patients

On procédera à une analyse descriptive de la survie, afin d'explorer ses liens avec les paramètres d'imagerie.

8.3 Sujets analysés

Patients ayant effectué les deux examens TEP-IRM.

8.4 Analyses intermédiaires

Non applicable

8.5 Fin de l'essai

La fin de l'essai correspond à la date de recueil du décès du dernier patient ou à 15 mois après la dernière TEP-IRM réalisée sous traitement (TEP-IRM$_1$) par le dernier des 20 patients évaluable, la date la plus précoce étant retenue.

9 EVENEMENTS INDESIRABLES GRAVES

Dans cette étude de faisabilité, la probabilité d'évènements indésirables graves est faible.
Les seuls effets indésirables attendus liés à la recherche sont ceux liés à la réalisation de la TEP-IRM à savoir une allergie au gadolinium.

9.1 Définition Générale

Est considéré comme un évènement indésirable grave (EIG) tout évènement :

- Entraînant le décès,
- Mettant en jeu le pronostic vital,
- Entraînant une hospitalisation ou une prolongation d'hospitalisation,
- Provoquant une invalidité permanente ou une incapacité temporaire grave,
- Provoquant une anomalie congénitale, une malformation fœtale ou un avortement,
- Médicalement significatif.

Les termes invalidité et incapacité correspondent à tout handicap physique ou psychique temporaire ou permanent, cliniquement significatif et retentissant sur l'activité physique et/ou la qualité de vie du patient.

Est considéré comme médicalement significatif tout événement clinique ou résultat de laboratoire considéré comme grave par l'investigateur et ne correspondant pas aux critères de gravité définis ci-dessus. Ils peuvent faire courir un risque au patient et nécessitent une intervention médicale pour prévenir une issue correspondant à l'un des critères de gravité mentionné précédemment (exemples : les transmissions d'un agent infectieux, les surdosages, les seconds cancers et les grossesses et faits nouveaux peuvent être considérés comme médicalement significatifs).

N'est pas considéré comme un événement indésirable grave (EIG) :

- Une hospitalisation < à 24 heures,
- Une hospitalisation programmée préalablement au début de l'essai et/ou prévue par le protocole (biopsie, chimiothérapie..).

9.2 Critère d'intensité

Le critère d'intensité ne doit pas être confondu avec le critère de gravité qui sert de guide pour définir les obligations de déclaration.

L'intensité des événements sera estimée selon l'extrait de la classification NCI-CTCAE version 4.0 (cf annexe I). L'intensité des évènements indésirables non listés dans cette classification sera appréciée selon les qualificatifs suivants :

Université Paris-Saclay
Espace Technologique / Immeuble Discovery
Route de l'Orme aux Merisiers RD 128 / 91190 Saint-Aubin, France

Légère (grade 1) : n'affecte pas l'activité quotidienne habituelle du patient
Modérée (grade 2) : perturbe l'activité quotidienne habituelle du patient
Sévère (grade 3) : empêche l'activité quotidienne habituelle du patient
Très Sévère (grade 4) : impose des mesures de réanimation/ menace le pronostic vital
Décès (grade 5)

9.3 Conduite à tenir en cas d'événement indésirable grave

L'investigateur informe l'Unité Fonctionnelle de Pharmacovigilance (UFPV) de tous les **Evènements Indésirables Graves Attendus (EIG-A) et inattendus (EIG-I),** qu'ils soient imputables ou non à la recherche, qui se produisent durant l'étude ou dans les 30 jours suivant la dernière TEP-IRM.

Tous les Événements Indésirables Graves retardés (survenant après cette période de 30 jours) considérés comme raisonnablement liés à la recherche doivent être déclarés sans limitation de délai.

La déclaration des EIGs se fait en envoyant par fax, dans les **24 heures** ouvrées suivant leur constatation, **le formulaire de notification d'un EIG.**

Coordonnées de l'Unité Fonctionnelle de PharmacoVigilance :
Adresse : Gustave Roussy, Direction de la Recherche Clinique, Unité Fonctionnelle de PharmacoVigilance, 114 rue Edouard Vaillant 94805 Villejuif Cedex
Tél : 01 42 11 61 00 (9H00 – 18h00 du lundi au vendredi, sauf jours fériés)
Fax : 01 42 11 61 50 **E-mail** : phv@gustaveroussy.fr

L'investigateur notera pour chaque évènement :

- Sa description aussi clairement que possible selon la terminologie médicale,
- L'intensité,
- La date de début et de fin de l'événement,
- Les mesures entreprises et la nécessité ou non d'un traitement correcteur,
- Son évolution. En cas d'évènement non fatal, l'évolution devra être suivie jusqu'à la guérison ou le retour à l'état antérieur ou à la stabilisation d'éventuelles séquelles,
- La relation de causalité avec la TEP/IRM la pathologie traitée, une autre pathologie ou un autre traitement. L'investigateur doit également joindre au rapport d'évènement indésirable grave, à chaque fois que possible :
  - Une copie du compte-rendu d'hospitalisation ou de prolongation d'hospitalisation,
  - Une copie du rapport d'autopsie (le cas échéant)
  - Une copie de tous les résultats d'examens complémentaires pertinents réalisés, y compris les résultats négatifs pertinents en y joignant les valeurs normales du laboratoire,
  - Tout autre document qu'il juge utile et pertinent.

Tous ces documents doivent être anonymisés.

Des compléments d'informations pourront être demandés (par fax, par téléphone ou lors d'une visite) par le moniteur et/ou l'UFPV.

9.4 Suivi des EIG et envoi des follow-up

L'investigateur est responsable du suivi médical approprié des patients jusqu'à la résolution ou la stabilisation de l'effet ou jusqu'au décès du patient. Cela peut impliquer parfois que ce suivi se prolonge après la sortie du patient de l'essai.

Il transmet les informations complémentaires à l'UFPV à l'aide d'un formulaire de déclaration des EIGs (en cochant la case Suivi n° X pour préciser qu'il s'agit d'un follow-up et non d'un rapport initial) dans les

24 heures suivant leur obtention. Il transmet également le dernier suivi à la résolution ou à la stabilisation de l'EIG.

Il conserve les documents concernant l'effet indésirable présumé afin de permettre, en cas de nécessité de compléter les informations précédemment transmises.
Il répond aux demandes d'informations complémentaires de l'UFPV afin de documenter l'observation initiale et met en œuvre les décisions de la DRC en rapports avec les EIGs.

9.5 Information des investigateurs, du CPP et de l'ANSM

L'UFPV adressera à tous les investigateurs de l'étude une copie de tout effet indésirable grave et inattendu lié à la recherche.

L'UFPV avisera également les investigateurs, le CPP et l'ANSM de toutes les informations à sa disposition jugées pertinentes quand à la sécurité des patients et pouvant conduire à une réévaluation, dans le sens défavorable, du rapport bénéfice/risque de la recherche, provenant d'autres études menées sur les mêmes produits ou selon la même méthodologie ou provenant de publication, de notification spontanée ou d'une autre autorité réglementaire.

L'UFPV adressera également au CPP et l'ANSM un rapport annuel de sécurité conformément aux exigences réglementaires.

10 CRITERES D'ARRET DE L'ESSAI

L'essai peut être suspendu ou arrêté par le promoteur en concertation avec le coordonnateur et en accord avec les autorités compétentes pour les raisons suivantes :

- un recrutement insuffisant de patients.

11 ASPECTS ETHIQUES ET REGLEMENTAIRES

11.1 Réglementation

L'essai clinique est conduit conformément à :

- La déclaration d'Helsinki 1964, amendée à Fortaleza en 2013 ;
- La Directive 95/46/CE relative au traitement des données à caractère personnel ;
- Et à la réglementation locale en vigueur notamment
    - la loi de Santé Publique du 9 août 2004 ;
    - l'ordonnance n°2016-800 du 16 Juin 2016 relative aux recherches impliquant la personne humaine ;
    - la loi n°2016-41 du 26 Janvier 2004 relative à la modernisation du système de santé ;
    - la loi Informatique et Libertés du 6 janvier 1978 modifiée par la loi du 6 août 2004 relative à la protection des personnes physiques à l'égard des traitements de données à caractère personnel ;
    - la loi n°2002-203 du 4 mars 2002 relative aux droits des malades et à la qualité du système de santé.

11.2 Comité de Protection des Personnes – Autorité compétente

Ce protocole a été soumis au Comité de Protection des Personnes EST 3 qui a donné un avis favorable le 07/07/2017 et à l'Agence Nationale de sécurité du médicament et des produits de santé (ANSM) qui a donné son approbation le 15/06/2017.

Toute modification substantielle du protocole fera l'objet d'une demande d'amendement auprès de ce CPP et/ou de l'ANSM.

Gustave Roussy a souscrit une assurance de responsabilité civile auprès de la société SHAM France (Lyon) (contrat N°124895).

Gustave Roussy déclarera le début et la fin de l'essai au CPP et à l'ANSM.

Un rapport final de l'essai sera rédigé au plus tard 1 an après la fin de l'essai dont le résumé sera adressé à l'ANSM et au CPP.

Gustave Roussy assurera l'archivage des documents essentiels de l'essai dans le classeur promoteur pour une durée minimale de 15 ans après la fin de la recherche.

11.3 Information et Consentement des participants

Préalablement à la réalisation de toute procédure liée à la recherche biomédicale, toute personne se prêtant à la recherche exprime son consentement libre, éclairé et écrit. Ce consentement est recueilli après que le participant ait été informé par l'investigateur lors d'une consultation et après un délai de réflexion suffisant.
Après avoir pris connaissance de la notice d'information, le patient, s'il accepte de participer, devra dater et signer le formulaire de consentement. Ce consentement doit également être signé par l'investigateur. L'original doit être archivé par l'investigateur et une copie remise au participant à la recherche.

11.4 Responsabilités des investigateurs

L'investigateur principal de chaque établissement concerné s'engage à conduire l'essai clinique conformément au protocole qui a été approuvé par le CPP et l'autorité compétente.

L'investigateur ne doit apporter aucune modification au protocole sans l'autorisation écrite du promoteur et sans que le CPP et l'autorité compétente ait donné leur autorisation sur les modifications proposées.

Il est de la responsabilité de l'investigateur principal :

- de fournir au promoteur son curriculum vitae ainsi que ceux des co-investigateurs,

- d'identifier les membres de son équipe qui participent à l'essai et de définir leurs responsabilités,

- d'assurer le recrutement des patients après autorisation du promoteur,

Il est de la responsabilité de chaque investigateur :

- de recueillir le consentement éclairé daté et signé personnellement par le participant à la recherche avant toute procédure de sélection spécifique à l'essai,

- de compléter régulièrement les cahiers d'observation (case report form (CRF)) pour chacun des patients inclus dans l'essai et de laisser à l'Assistant de Recherche Clinique (ARC) mandaté par le Promoteur un accès direct aux documents-source afin que ce dernier puisse valider les données du CRF,

- de dater, corriger et de signer les corrections des CRF pour chacun des patients inclus dans l'essai,

- d'accepter les visites régulières de l'ARC et éventuellement celles des auditeurs mandatés par le promoteur ou des inspecteurs des autorités compétentes.

Toute la documentation relative à l'essai (protocole, consentements, cahiers d'observation, dossier investigateur, etc…), ainsi que les documents originaux (résultats de laboratoire, radiologies, comptes-rendus de consultations, rapports d'examens cliniques, etc.) est considérée comme confidentielle et doit être détenue dans un lieu sûr. L'investigateur Principal devra conserver les données ainsi qu'une liste d'identification des patients pendant une durée minimale de 15 ans après la fin de l'étude.

12 RECUEIL DES DONNEES

Les données seront colligées sur un cahier d'observation / fiches standardisées et incluront :
- Les caractéristiques des patients au moment de l'examen (âge, poids, taille, glycémie, stade de la tumeur, créatininémie)
- les données d'imagerie extraites pour l'étude (cf section 3).

La base de données sera hébergée au CHU Bicêtre.

13 ASSURANCE QUALITE - MONITORING

Afin de garantir l'authenticité et la crédibilité des données, le centre de coordination a mis en place un système d'assurance qualité qui comprend :

- la gestion de l'essai selon les procédures de Gustave Roussy,
- le contrôle qualité des formulaires de consentement par l'ARC promoteur.

13.1 Monitoring

Le contrôle qualité sur site sera effectué par l'ARC promoteur qui doit vérifier l'obtention du consentement pour chaque participant.

14 PROPRIETES DES DONNEES / REGLES DE PUBLICATIONS

Les investigateurs s'engagent, pour eux-mêmes et pour toutes les personnes amenées à suivre le déroulement de l'essai, à garantir la confidentialité de toutes les informations fournies par Gustave Roussy jusqu'à la publication des résultats de l'étude.

Toutes communications, manuscrits ou présentations doivent comporter une rubrique qui mentionne le promoteur, les investigateurs / institutions qui ont participé à l'essai, les groupes coopérateurs, les sociétés savantes qui ont contribué à sa réalisation et les organismes qui ont supporté financièrement la recherche.

15 REFERENCES BIBLIOGRAPHIQUES

1. Gerlinger M, Rowan AJ, Horswell S, et al. Intratumor heterogeneity and branched evolution revealed by multiregion sequencing. *N Engl J Med.* 2012;366(10):883-892.

2. Easwaran H, et al. Cancer epigenetics: tumor heterogeneity, plasticity of stem-like states, and drug resistance. Mol Cell. 2014;54(5): 716-727.

3. Chen Z, et al. Non-small-cell lung cancers: a heterogeneous set of diseases. Nat Rev Cancer 2014; 14(8): 535-46.

4. Tirkes T, Hollar MA, Tann M, Kohli MD, Akisik F, Sandrasegaran K. Response criteria in oncologic imaging: review of traditional and new criteria. *Radiographics.* 2013;33(5):1323-1341.

5. Hoink AJ, Heindel W, Buerke B. Radiological Evaluation of the Therapeutic Response of Malignant Diseases: Status Quo, Innovative Developments and Requirements for Radiology. *Rofo.* 2014;186(10):927-936.

6. Garber K. Energy boost: the Warburg effect returns in a new theory of cancer. *J Natl Cancer Inst.* 2004;96(24):1805-1806.

7. Boellaard R, Delgado-Bolton R, Oyen WJ, Giammarile F, Tatsch K, Eschner W, Verzijlbergen FJ, Barrington SF, Pike LC, Weber WA, Stroobants S, Delbeke D, Donohoe KJ, Holbrook S, Graham MM, Testanera G, Hoekstra OS, Zijlstra J, Visser E, Hoekstra CJ, Pruim J, Willemsen A, Arends B, Kotzerke J, Bockisch A, Beyer T, Chiti A, Krause BJ; European Association of Nuclear Medicine (EANM). FDG PET/CT: EANM procedure guidelines for tumour imaging: version 2.0. Eur J Nucl Med Mol Imaging. 2015;42(2):328-54.

8. Folkman J. Tumor angiogenesis: therapeutic implications. *N Engl J Med.* 1971;285(21):1182-1186.

9. Yang X, Knopp MV. Quantifying tumor vascular heterogeneity with dynamic contrast-enhanced magnetic resonance imaging: a review. *J Biomed Biotechnol.* 2011;2011:732848.

10.Yabuuchi H, Hatakenaka M, Takayama K, et al. Non-small cell lung cancer: detection of early response to chemotherapy by using contrast-enhanced dynamic and diffusion-weighted MR imaging. *Radiology.* 2011;261(2):598-604.

11. Schwenzer NF, Schraml C, Muller M, et al. Pulmonary lesion assessment: comparison of whole-body hybrid MR/PET and PET/CT imaging--pilot study. *Radiology.* 2012;264(2):551-558.

12. Rauscher I, Eiber M, Furst S, et al. PET/MR imaging in the detection and characterization of pulmonary lesions: technical and diagnostic evaluation in comparison to PET/CT. *J Nucl Med.* 2014;55(5):724-729.

13. Heusch P, et al. Thoracic staging in lung cancer: prospective comparison of 18F-FDG PET/MR imaging and 18F-FDG PET/CT. J Nucl Med. 2014; 55(3): 373-378.

14. Fraioli F, Screaton NJ, Janes SM, et al. Non-small-cell lung cancer resectability: diagnostic value of PET/MR. *Eur J Nucl Med Mol Imaging.* 2015;42(1):49-55.

15. Schaarschmidt BM, et al. Correlation of the apparent diffusion coefficient (ADC) with the standardized uptake value (SUV) in lymph node metastases of non-small cell lung cancer (NSCLC) patients using hybrid 18F-FDG PET/MRI. PLoS One. 2015;10(1):e0116277.

16. Orlhac F, Soussan M, Maisonobe JA, Garcia CA, Vanderlinden B, Buvat I. Tumor texture analysis in 18F-FDG PET: relationships between texture parameters, histogram indices, standardized uptake values, metabolic volumes, and total lesion glycolysis. *J Nucl Med.* 2014;55(3):414-422.

17. Metz S, et al. Multiparametric MR and PET Imaging of Intratumoral Biological Heterogeneity in Patients with Metastatic Lung Cancer Using Voxel-by-Voxel Analysis. Plos One. 2015; 10(7): e0132386.

18. Orlhac F, Soussan M, Chouahnia K, Martinod E, Buvat I.18F-FDG PET-Derived Textural Indices Reflect Tissue-Specific Uptake Pattern in Non-Small Cell Lung Cancer. PLoS One. 2015 Dec 15;10(12):e0145063. doi: 10.1371/journal.pone.0145063. eCollection 2015.

19. Dimitrakopoulou-Strauss A, Strauss LG, Schwarzbach M, Burger C, Heichel T, Willeke F, Mechtersheimer G, Lehnert T. J Nucl Med. 2001 May;42(5):713-20

20. Dimitrakopoulou-Strauss A[1], Strauss LG, Egerer G, Vasamiliette J, Schmitt T, Haberkorn U, Kasper B. Prediction of chemotherapy outcome in patients with metastatic soft tissue sarcomas based on dynamic FDG PET (dPET) and a multiparameter analysis. Eur J Nucl Med Mol Imaging. 2010;37(8):1481-9

21. Dimitrakopoulou-Strauss A, Strauss LG, Egerer G, Vasamiliette J, Mechtersheimer G, Schmitt T, Lehner B, Haberkorn U, Stroebel P, Kasper B. Impact of dynamic 18F-FDG PET on the early prediction of therapy outcome in patients with high-risk soft-tissue sarcomas after neoadjuvant chemotherapy: a feasibility study. J Nucl Med. 2010;51(4):551-8.

Annexe 1 – Critères de toxicité (CTCAE)

Se référer à l'échelle d'évaluation de la toxicité CTCAE qui est joint séparément et que l'on peut télécharger sur le site du NCI

http://ctep.cancer.gov/protocolDevelopment/electronic_applications/ctc.htm#ctc_40

NATIONAL CANCER INSTITUTE
Cancer Therapy Evaluation Program

http://ctep.cancer.gov/

Common Terminology Criteria for Adverse Events v4.0 (NCI-CTCAE)

A.11.PET and DCE kinetics parameters of the 14 tumors

Tumors	Voxels	PET parameters					DCE parameters			
	($2mm^3$)	k_1 ($ml\ g^{-1}min^{-1}$)	k_2 (min^{-1})	k_3 (min^{-1})	MRGlu ($\mu mol\ g^{-1}min^{-1}$)	v_b (a.u)	K_{trans} (min^{-1})	v_e (a.u)	K_{ep} (min^{-1})	v_p (a.u)
1	540	0.22 (0.18-0.26)	0.71 (0.54-0.81)	0.13 (0.1-0.14)	0.15 (0.12-0.17)	0.05 (0.03-0.07)	0.26 (0.13-0.52)	0.68 (0.42-1.0)	0.53 (0.25-1.0)	$7.8.10^{-3}$ (0-0.045)
2	1271	0.26 (0.22-0.32)	0.68 (0.45-1.03)	0.15 (0.10-0.20)	0.24 (0.19-0.26)	0.05 (0.03-0.06)	0.74 (0.59-1.03)	1.0 (1.0-1.0)	0.74 (0.59-1.04)	0.4 (0.2-0.7)
3	799	0.08 (0.06-0.11)	0.31 (0.22-0.44)	0.09 (0.05-0.14)	0.09 (0.07-0.10)	0.13 (0.09-0.18)	0.15 (0.06-0.60)	0.33 (0.08-1.0)	0.49 (0.24-29.2)	0.03 (0-0.12)
4	211	0.15 (0.12-0.18)	1.09 (0.85-1.40)	0.033 (0.029-0.036)	0.026 (0.022-0.032)	0.084 (0.076-0.093)	0.65 (0.22-1.19)	0.63 (0.33-1.0)	1.06 (0.51-2.37)	0.15 (0.04-0.36)
5	1207	0.19 (0.15-0.24)	0.57 (0.46-0.77)	0.19 (0.15-0.24)	0.35 (0.30-0.38)	0.09 (0.08-0.10)	0.06 (0.04-0.11)	0.17 (0.13-0.21)	0.41 (0.26-0.65)	0.016 (0.009-0.024)
7	88	0.38 (0.34-0.42)	1.30 (1.14-1.47)	0.089 (0.068-0.109)	0.11 (0.09-0.14)	0.066 (0.057-0.077)	0.73 (0.31-1.54)	1.0 (0.47-1.0)	1.14 (0.58-1.97)	0.05 (0-1.00)
8	629	0.14 (0.12-0.16)	0.41 (0.35-0.5)	0.028 (0.022-0.034)	0.053 (0.048-0.06)	0.109 (0.084-0.13)	0.056 (0.03-0.12)	0.95 (0.32-1.0)	0.11 (0.06-0.2)	0.008 (0.004-0.017)
11	318	0.11 (0.07-0.13)	0.66 (0.44-0.72)	0.08 (0.05-0.1)	0.063 (0.045-0.084)	0.18 (0.16-0.19)	0.45 (0.13-0.94)	0.19 (0.03-0.63)	1.67 (1.05-3.31)	3.1×10^{-9} (0-0.076)
12	2409	0.22 (0.17-0.26)	0.55 (0.47-0.61)	0.071 (0.059-0.088)	0.14 (0.11-0.19)	0.05 (0.03-0.07)	0.28 (0.15-0.46)	0.52 (0.29-0.77)	0.55 (0.39-0.81)	0.034 (0-0.09)
13	2338	0.26 (0.20-0.32)	0.63 (0.45-0.83)	0.08 (0.05-0.14)	0.22 (0.14-0.34)	0.11 (0.09-0.14)	0.93 (0.57-1.29)	1.0 (0.38-1.0)	1.1 (0.8-2.36)	0.25 (0.0003-0.81)
15	1151	0.15 (0.13-0.18)	0.48 (0.34-0.65)	0.11 (0.09-0.14)	0.16 (0.13-0.19)	0.09 (0.06-0.13)	0.71 (0.29-1.12)	0.74 (0.33-1.0)	1.08 (0.79-1.45)	0.08 (0.000073-0.27)
16	5356	0.29 (0.22-0.36)	1.29 (0.80-1.96)	0.32 (0.19-0.57)	0.33 (0.22-0.43)	0.05 (0.03-0.08)	0.28 (0.1-0.67)	0.29 (0.15-0.64)	0.88 (0.47-1.48)	0.04 (0.001-0.11)
17	3845	0.33 (0.23-0.44)	0.77 (0.55-1.04)	0.1 (0.06-0.14)	0.21 (0.15-0.25)	0.097 (0.077-0.14)	0.89 (0.55-1.26)	1.0 (0.85-1.0)	1.023 (0.68-1.38)	0.05 (0-0.22)
18	1409	0.31 (0.27-0.35)	0.68 (0.57-0.77)	0.07 (0.05-0.08)	0.14 (0.11-0.17)	0.052 (0.032-0.072)	0.23 (0.12-0.5)	0.53 (0.36-1.0)	0.53 (0.31-0.70)	0.0083 (0-0.034
All	21 571	0.25 (0.17-0.33)	0.68 (0.48-1.02)	0.11 (0.07-0.2)	0.20 (0.13-0.29)	0.08 (0.05-0.10)	0.44 (0.14-0.92)	0.64 (0.24-1.0)	0.79 (0.44-1.3)	0.04 (0.0007-0.19)

Table A. 9 : PET and DCE kinetic parameters. For each tumor, data are provided as mean (IQR).

A.12.Illustrations of the ^{18}F-FDG dynamic PET and DCE kinetics 3D maps of the 14 tumors.

Tumor #1

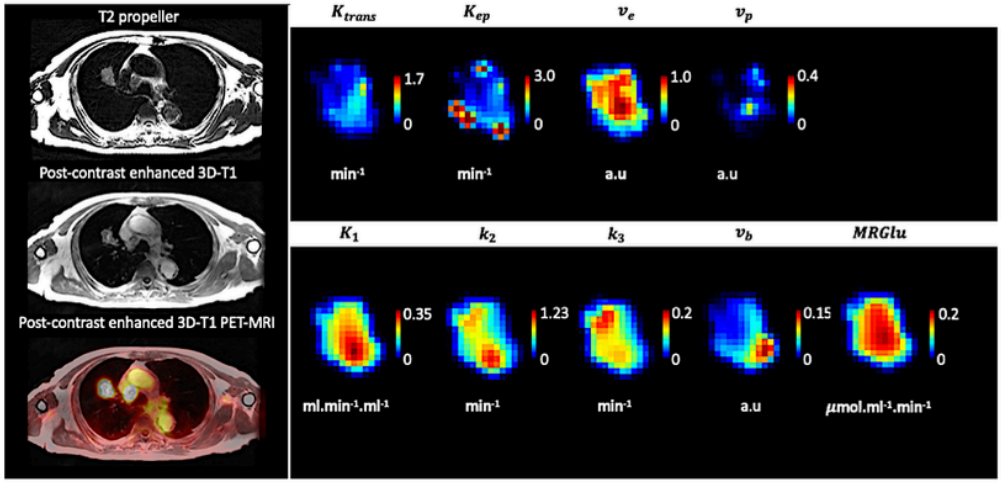

Tumor #2

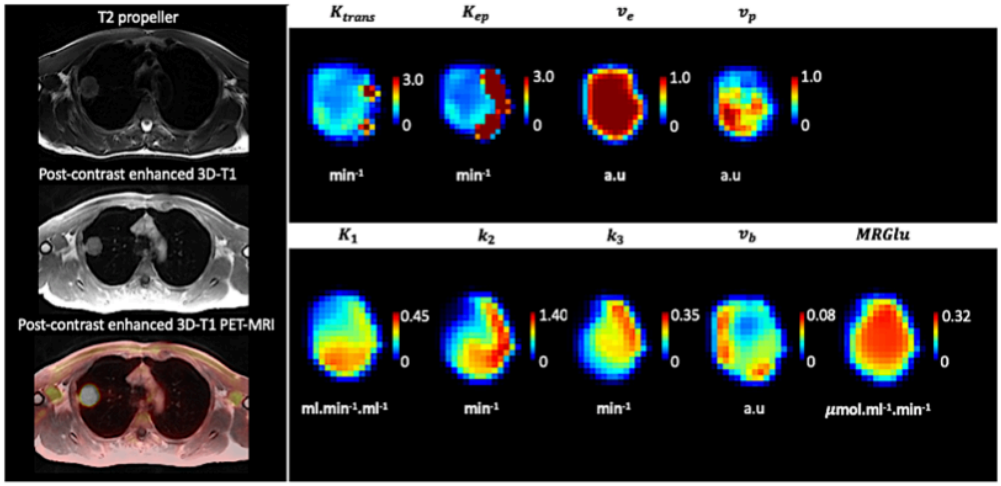

Tumor #3

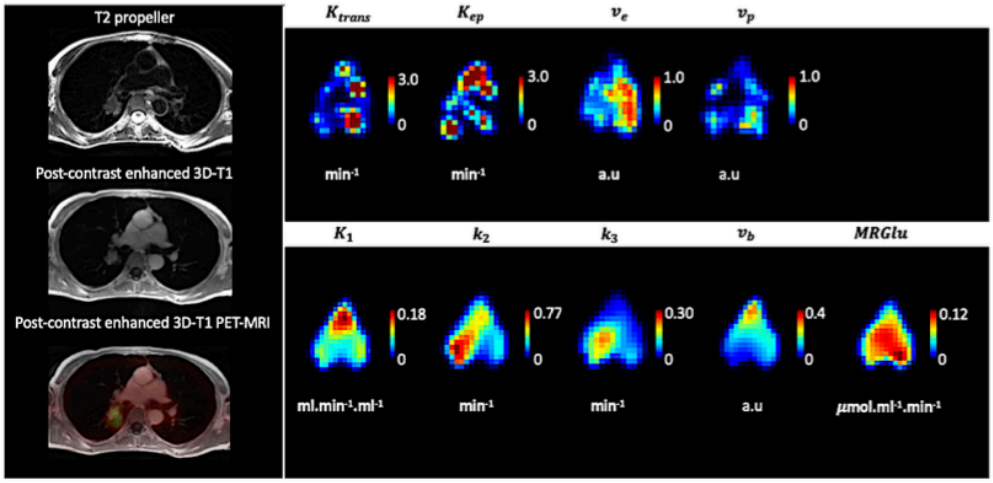

Tumor #4

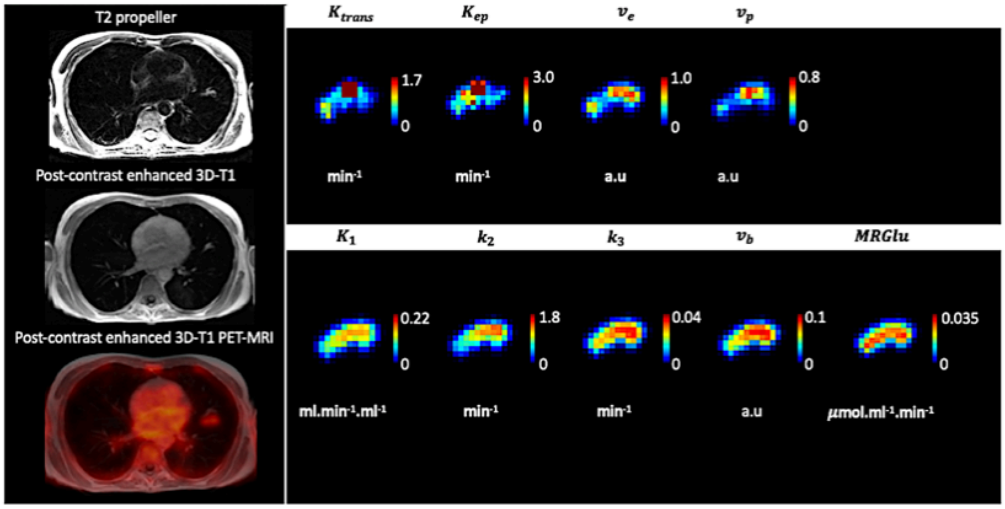

Tumor #5

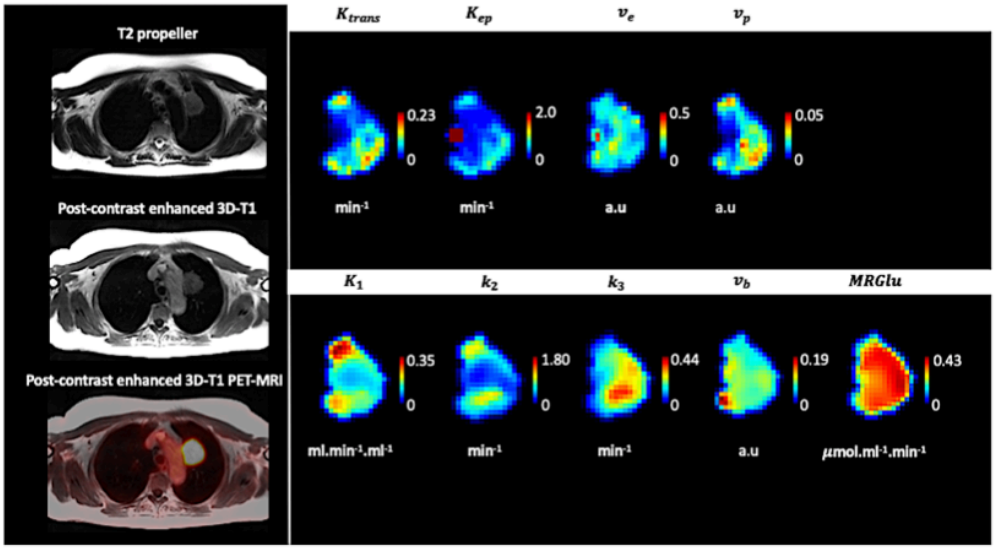

Tumor #7

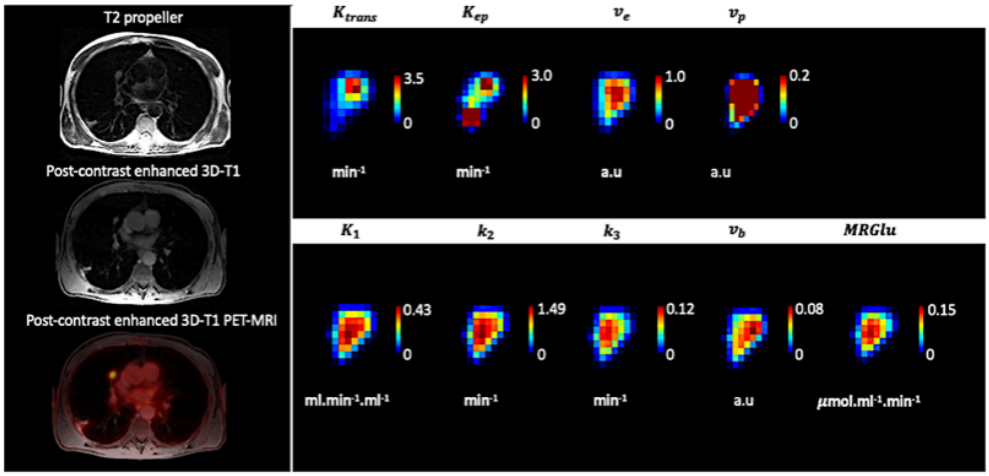

Tumor #8

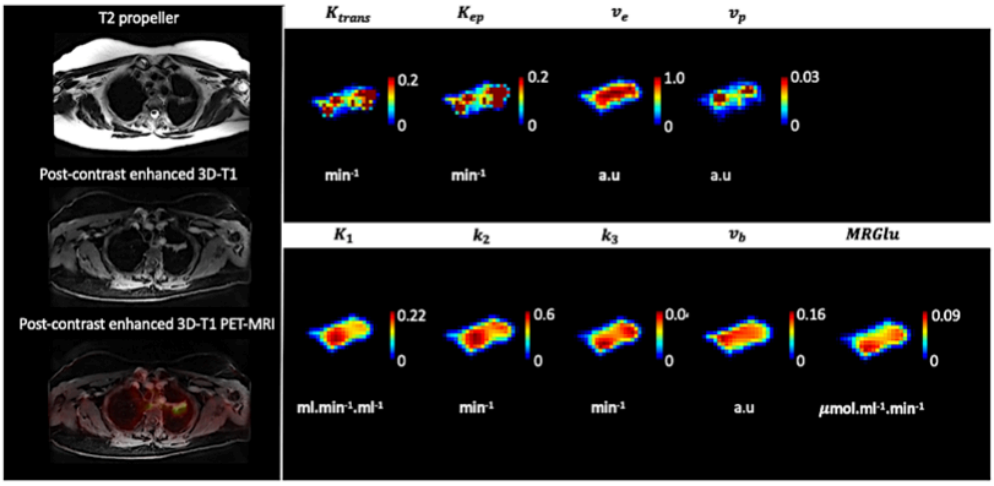

Tumor #11

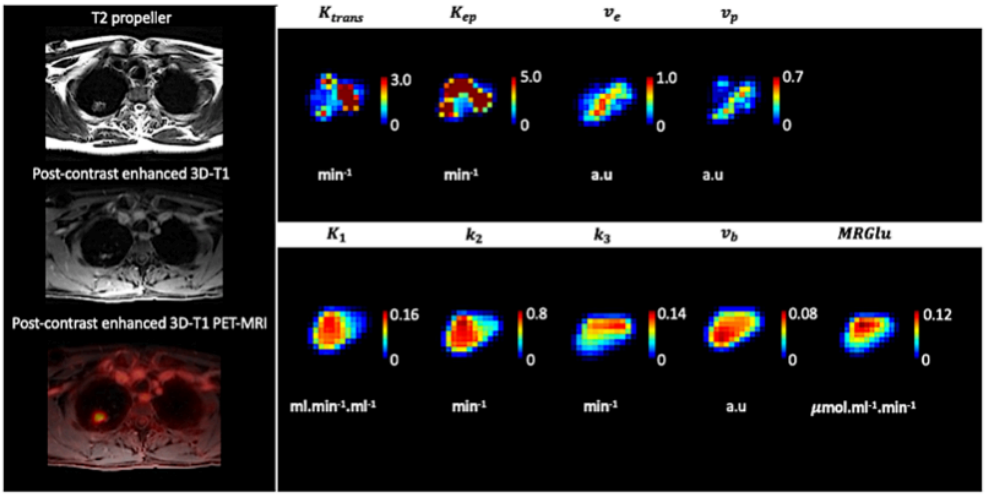

Tumor #12

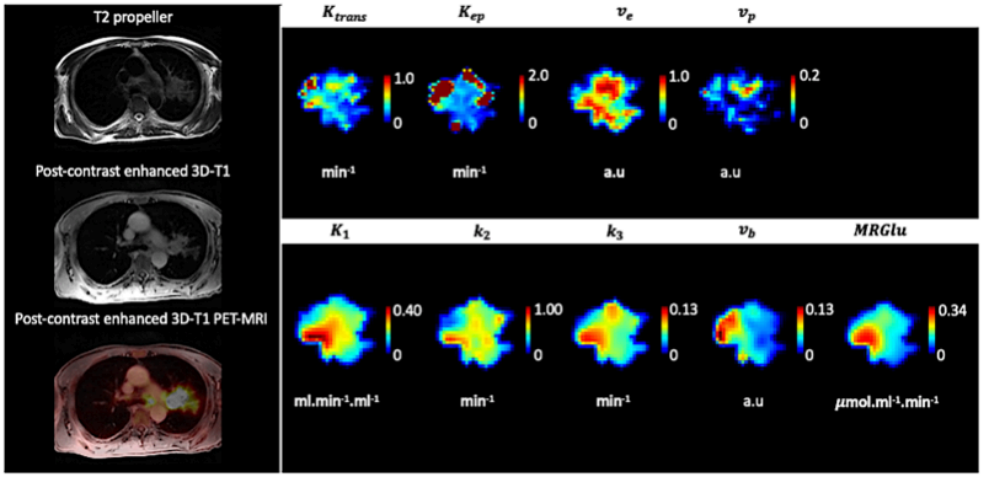

Tumor #13

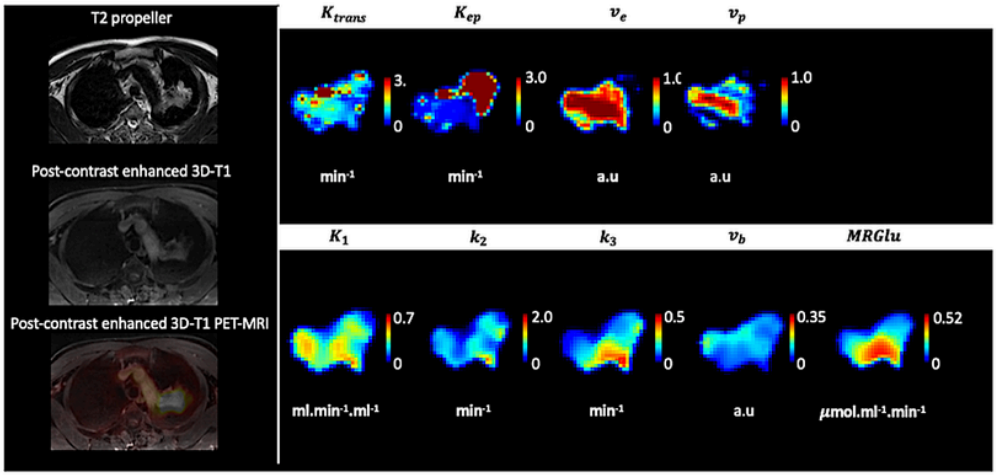

Tumor #15

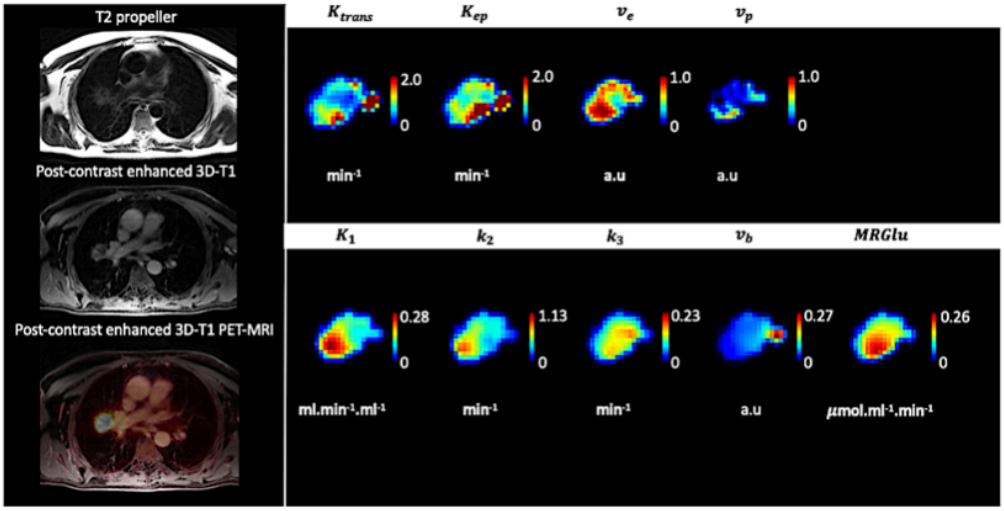

Tumor #16

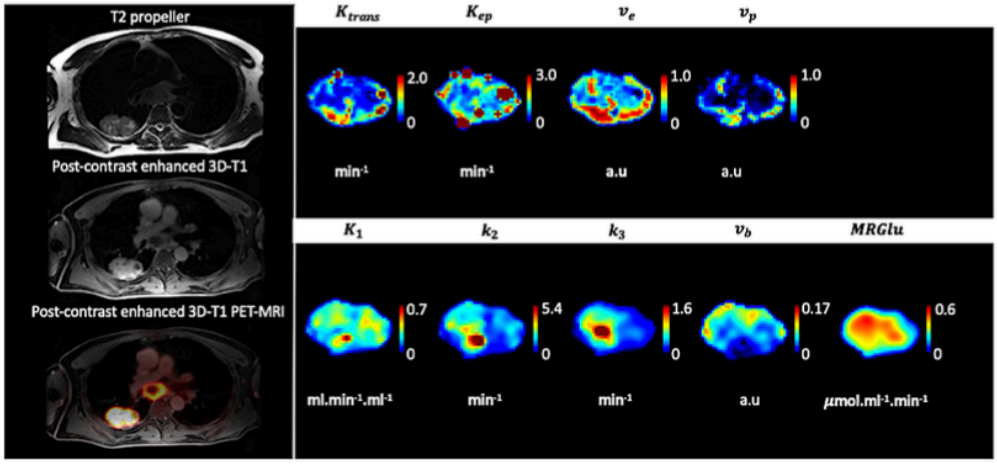

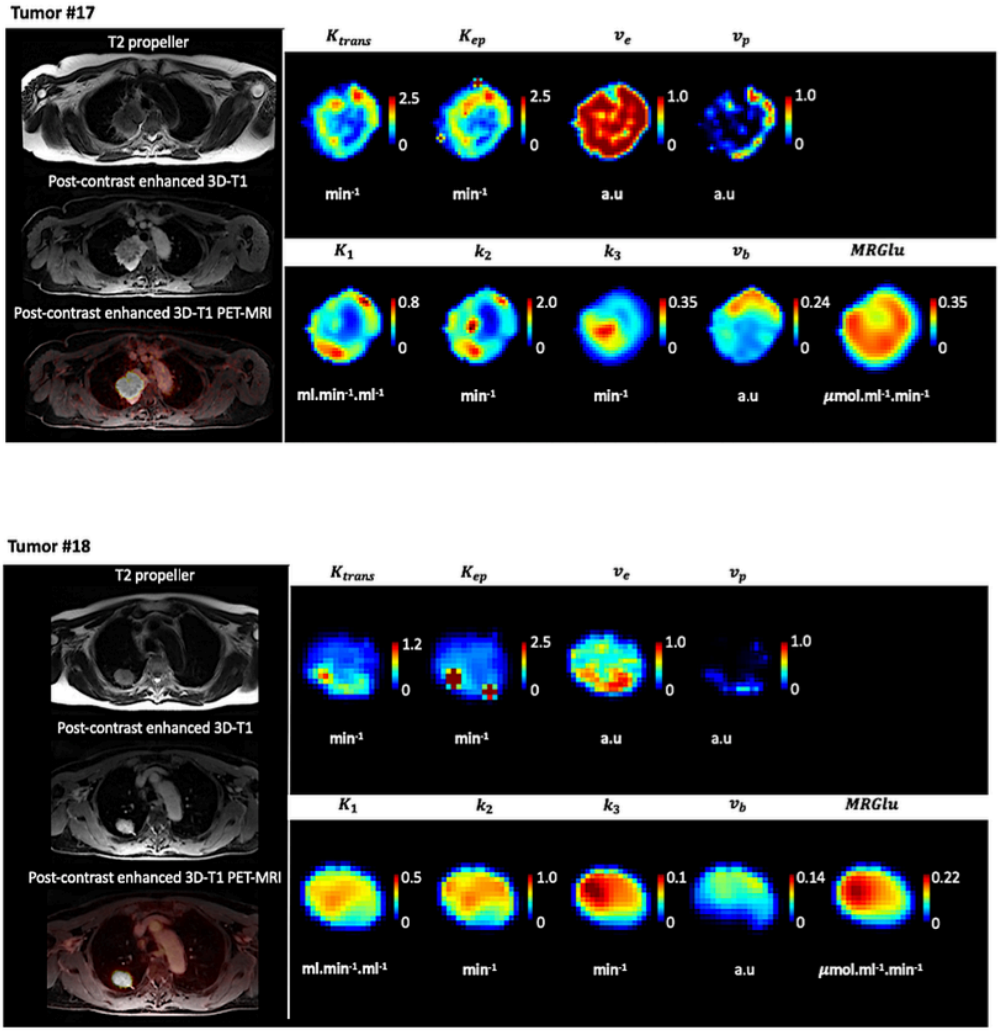

Figure A. 9 : PET and DCE kinetic parametric maps of the 14 tumors. For display, all the maps were smoothed with a 3mm Gaussian filter.

A.13. Illustrations of the ^{18}F-FDG and MRI whole multimodal 3D maps of the 11 tumors.

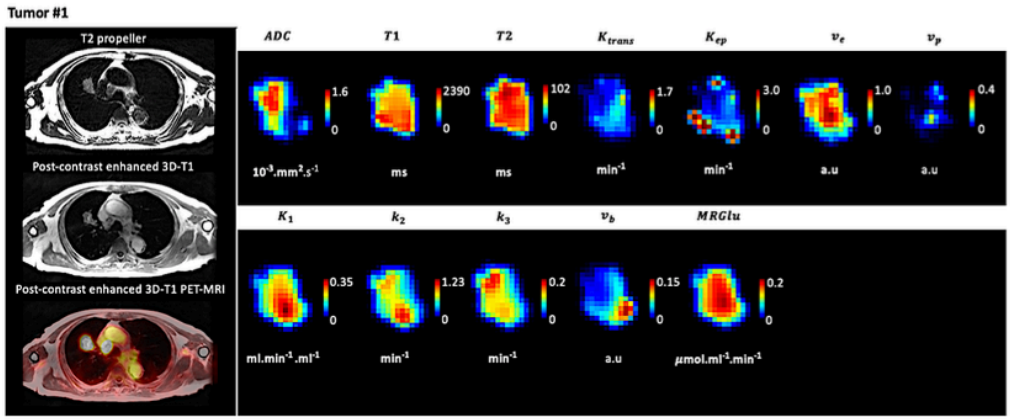

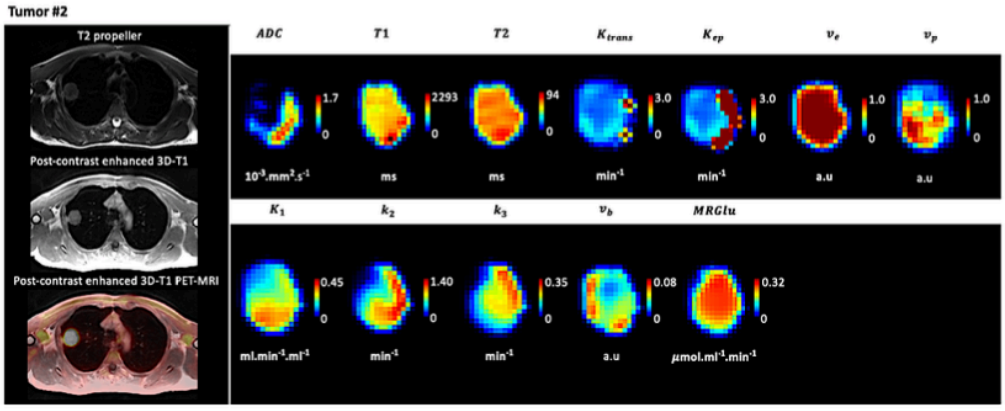

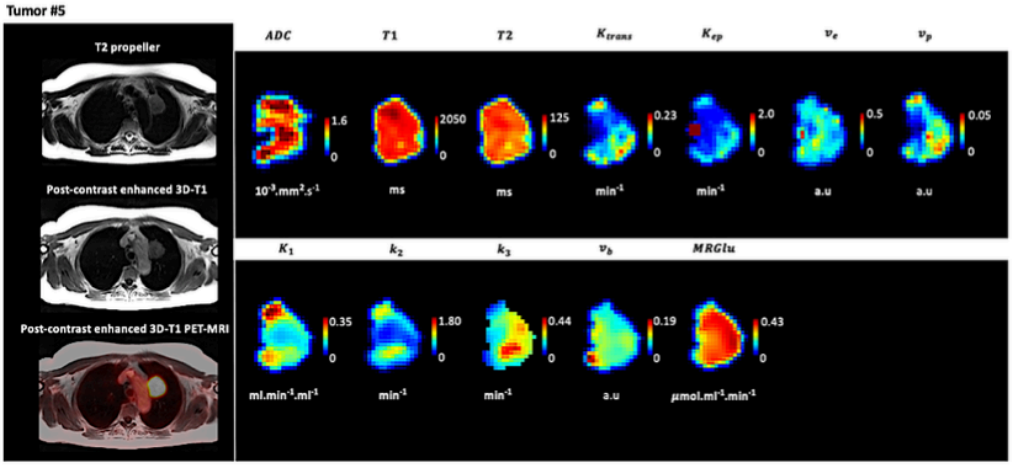
Tumor #5
T2 propeller
Post-contrast enhanced 3D-T1
Post-contrast enhanced 3D-T1 PET-MRI
ADC
T1
T2
K_{trans}
K_{ep}
v_e
v_p
1.6
0
2050
0
125
0
0.23
0
2.0
0
0.5
0
0.05
0
$10^{-3}.mm^2.s^{-1}$
ms
ms
min^{-1}
min^{-1}
a.u
a.u
K_1
k_2
k_3
v_b
MRGlu
0.35
0
1.80
0
0.44
0
0.19
0
0.43
0
$ml.min^{-1}.ml^{-1}$
min^{-1}
min^{-1}
a.u
$\mu mol.ml^{-1}.min^{-1}$

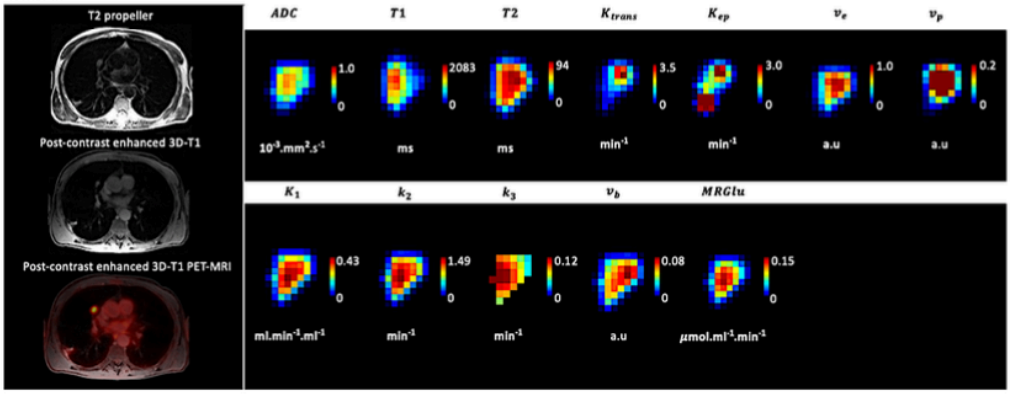
Tumor #7
T2 propeller
Post-contrast enhanced 3D-T1
Post-contrast enhanced 3D-T1 PET-MRI
ADC
T1
T2
K_{trans}
K_{ep}
v_e
v_p
1.0
0
2083
0
94
0
3.5
0
3.0
0
1.0
0
0.2
0
$10^{-3}.mm^2.s^{-1}$
ms
ms
min^{-1}
min^{-1}
a.u
a.u
K_1
k_2
k_3
v_b
MRGlu
0.43
0
1.49
0
0.12
0
0.08
0
0.15
0
$ml.min^{-1}.ml^{-1}$
min^{-1}
min^{-1}
a.u
$\mu mol.ml^{-1}.min^{-1}$

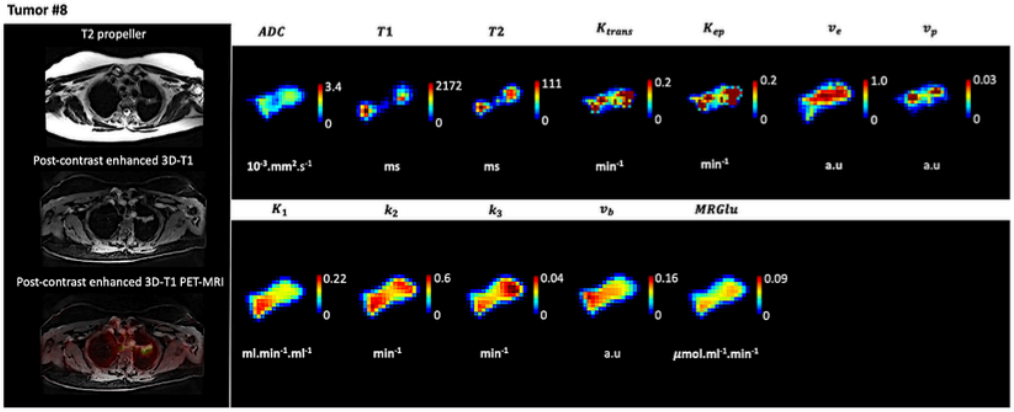
Tumor #8
T2 propeller
Post-contrast enhanced 3D-T1
Post-contrast enhanced 3D-T1 PET-MRI
ADC
T1
T2
K_{trans}
K_{ep}
v_e
v_p
3.4
0
2172
0
111
0
0.2
0
0.2
0
1.0
0
0.03
0
$10^{-3}.mm^2.s^{-1}$
ms
ms
min^{-1}
min^{-1}
a.u
a.u
K_1
k_2
k_3
v_b
MRGlu
0.22
0
0.6
0
0.04
0
0.16
0
0.09
0
$ml.min^{-1}.ml^{-1}$
min^{-1}
min^{-1}
a.u
$\mu mol.ml^{-1}.min^{-1}$

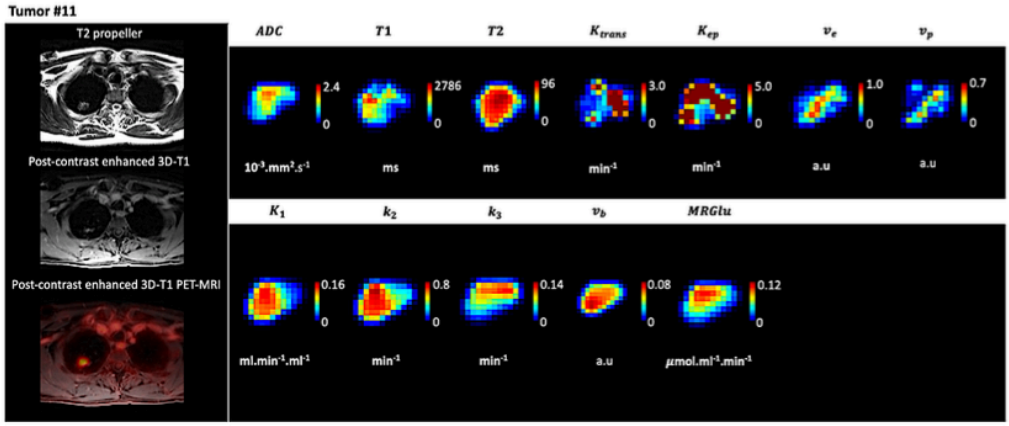
Tumor #11
T2 propeller
Post-contrast enhanced 3D-T1
Post-contrast enhanced 3D-T1 PET-MRI
ADC
T1
T2
K_{trans}
K_{ep}
v_e
v_p
2.4
0
2786
0
96
0
3.0
0
5.0
0
1.0
0
0.7
0
$10^{-3}.mm^2.s^{-1}$
ms
ms
min^{-1}
min^{-1}
a.u
a.u
K_1
k_2
k_3
v_b
MRGlu
0.16
0
0.8
0
0.14
0
0.08
0
0.12
0
$ml.min^{-1}.ml^{-1}$
min^{-1}
min^{-1}
a.u
$\mu mol.ml^{-1}.min^{-1}$

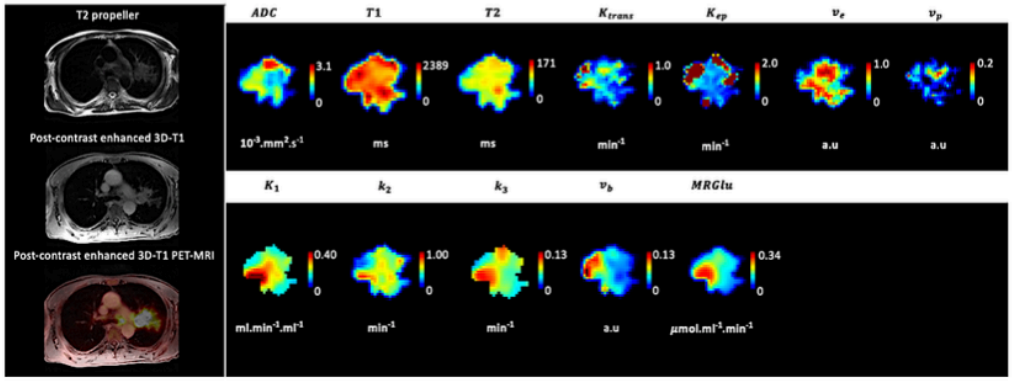
Tumor #12
T2 propeller
Post-contrast enhanced 3D-T1
Post-contrast enhanced 3D-T1 PET-MRI
ADC
T1
T2
K_{trans}
K_{ep}
v_e
v_p
3.1
0
2389
0
171
0
1.0
0
2.0
0
1.0
0
0.2
0
$10^{-3}.mm^2.s^{-1}$
ms
ms
min^{-1}
min^{-1}
a.u
a.u
K_1
k_2
k_3
v_b
MRGlu
0.40
0
1.00
0
0.13
0
0.13
0
0.34
0
$ml.min^{-1}.ml^{-1}$
min^{-1}
min^{-1}
a.u
$\mu mol.ml^{-1}.min^{-1}$

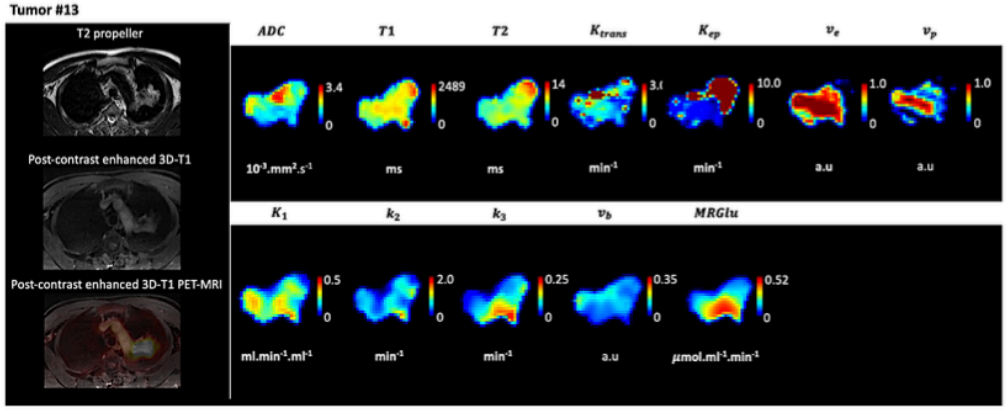
Tumor #13
T2 propeller
Post-contrast enhanced 3D-T1
Post-contrast enhanced 3D-T1 PET-MRI
ADC
T1
T2
K_{trans}
K_{ep}
v_e
v_p
3.4
0
2489
0
14
0
3.(
0
10.0
0
1.0
0
1.0
0
$10^{-3}.mm^2.s^{-1}$
ms
ms
min^{-1}
min^{-1}
a.u
a.u
K_1
k_2
k_3
v_b
MRGlu
0.5
0
2.0
0
0.25
0
0.35
0
0.52
0
$ml.min^{-1}.ml^{-1}$
min^{-1}
min^{-1}
a.u
$\mu mol.ml^{-1}.min^{-1}$

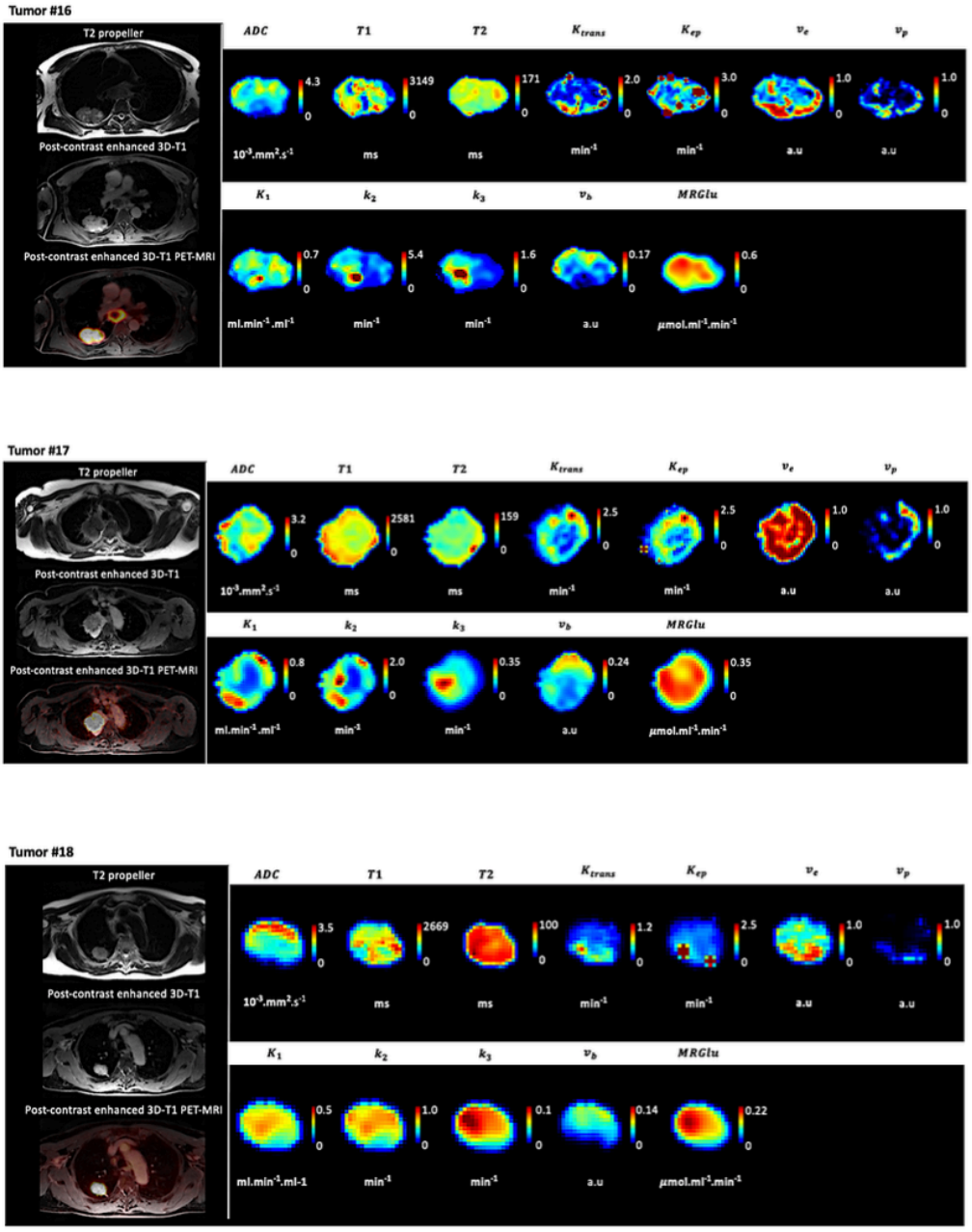

Figure A. 10: Full multiparametric maps of the 11 tumors. For display, all the maps were smoothed with a 3mm Gaussian filter.

A.14. Illustration of the 3D cluster maps after dimensionality reduction.

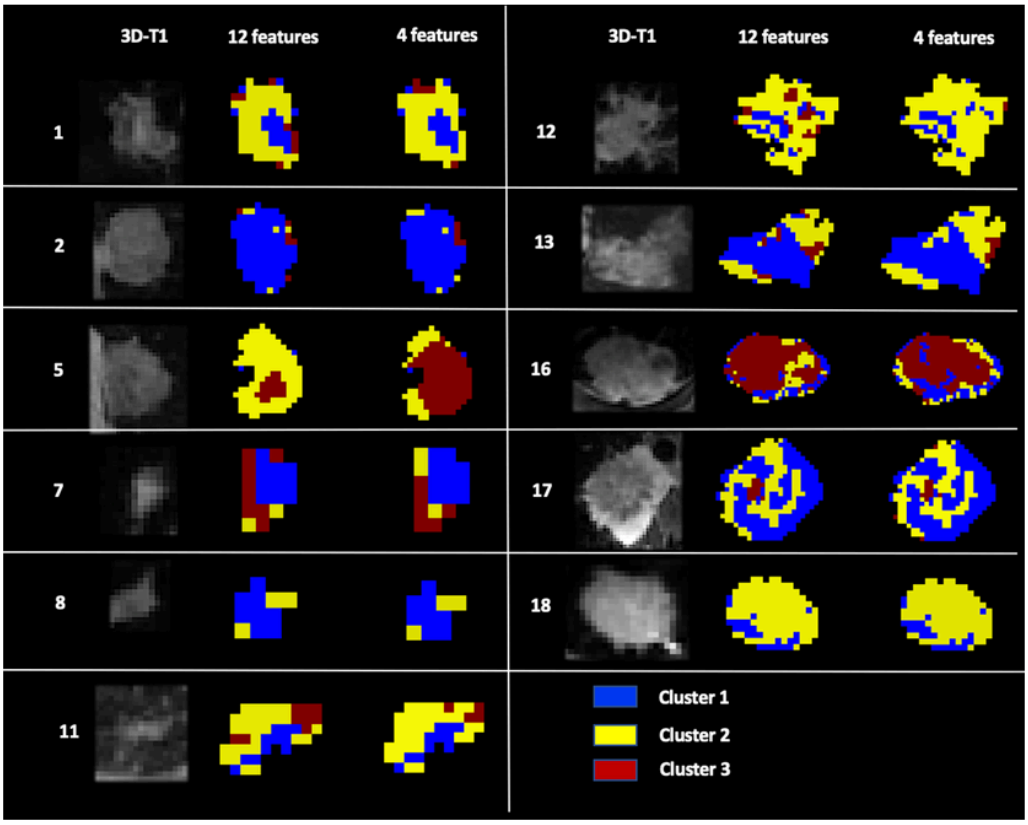

Figure A. 11 : The first column corresponds to the 3D-T1 images of the tumors; the second columns to the clustering based on 11 features; and the last column to the same clustering based on the 4 selected features.

LIST OF FIGURES

LIST OF TABLES

BIBLIOGRAPHY

1. Christensen NL, Hammer BE, Heil BG, Fetterly K. Positron emission tomography within a magnetic field using photomultiplier tubes and lightguides. *Phys Med Biol*. 1995;40:691-697.

2. Shao Y, Cherry SR, Farahani K, et al. Simultaneous PET and MR imaging. *Phys Med Biol*. 1997;42:1965-1970.

3. Townsend DW, Carney JPJ, Yap JT, Hall NC. PET/CT today and tomorrow. *J Nucl Med*. 2004;45 Suppl 1:4S-14S.

4. Vandenberghe S, Marsden PK. PET-MRI: a review of challenges and solutions in the development of integrated multimodality imaging. *Phys Med Biol*. 2015;60:R115-R154.

5. Zaidi H, Ojha N, Morich M, et al. Design and performance evaluation of a whole-body Ingenuity TF PET–MRI system. *Phys Med Biol*. 2011;56:3091-3106.

6. Delso G, Furst S, Jakoby B, et al. Performance Measurements of the Siemens mMR Integrated Whole-Body PET/MR Scanner. *Journal of Nuclear Medicine*. 2011;52:1914-1922.

7. Vrachimis A, Burg MC, Wenning C, et al. [18F]FDG PET/CT outperforms [18F]FDG PET/MRI in differentiated thyroid cancer. *Eur J Nucl Med Mol Imaging*. 2016;43:212-220.

8. Kirchner J, Sawicki LM, Nensa F, et al. Prospective comparison of 18F-FDG PET/MRI and 18F-FDG PET/CT for thoracic staging of non-small cell lung cancer. *Eur J Nucl Med Mol Imaging*. 2019;46:437-445.

9. Schwartz M, Gavane SC, Bou-Ayache J, et al. Feasibility and diagnostic performance of hybrid PET/MRI compared with PET/CT for gynecological malignancies: a prospective pilot study. *Abdom Radiol*. 2018;43:3462-3467.

10. Schaarschmidt BM, Heusch P, Buchbender C, et al. Locoregional tumour evaluation of squamous cell carcinoma in the head and neck area: a comparison between MRI, PET/CT and integrated PET/MRI. *Eur J Nucl Med Mol Imaging*. 2016;43:92-102.

11. Grueneisen J, Schaarschmidt BM, Heubner M, et al. Implementation of FAST-PET/MRI for whole-body staging of female patients with recurrent pelvic malignancies: A comparison to PET/CT. *European Journal of Radiology*. 2015;84:2097-2102.

12. Besson FL, Lebon V, Durand E. What are we expecting from PET/MRI? *Médecine Nucléaire*. 2016;40:31-40.

13. Czernin J, Ta L, Herrmann K. Does PET/MR Imaging Improve Cancer Assessments? Literature Evidence from More Than 900 Patients. *Journal of Nuclear Medicine*. 2014;55:59S-62S.

14. Gerlinger M, Swanton C. How Darwinian models inform therapeutic failure initiated by clonal heterogeneity in cancer medicine. *Br J Cancer*. 2010;103:1139-1143.

15. Gerlinger M, Rowan AJ, Horswell S, et al. Intratumor Heterogeneity and Branched Evolution Revealed by Multiregion Sequencing. *N Engl J Med*. 2012;366:883-892.

16. Easwaran H, Tsai H-C, Baylin SB. Cancer Epigenetics: Tumor Heterogeneity, Plasticity of Stem-like States, and Drug Resistance. *Molecular Cell*. 2014;54:716-727.

17. Postmus PE, Kerr KM, Oudkerk M, et al. Early and locally advanced non-small-cell lung cancer (NSCLC): ESMO Clinical Practice Guidelines for diagnosis, treatment and follow-up†. *Annals of Oncology*. 2017;28:iv1-iv21.

18. Nishino M. Tumor Response Assessment for Precision Cancer Therapy: Response Evaluation Criteria in Solid Tumors and Beyond. *American Society of Clinical Oncology Educational Book*. 2018:1019-1029.

19. Aide N, Hicks RJ, Le Tourneau C, Lheureux S, Fanti S, Lopci E. FDG PET/CT for assessing tumour response to immunotherapy: Report on the EANM symposium on immune modulation and recent review of the literature. *Eur J Nucl Med Mol Imaging*. 2019;46:238-250.

20. Heusch P, Buchbender C, Kohler J, et al. Thoracic Staging in Lung Cancer: Prospective Comparison of 18F-FDG PET/MR Imaging and 18F-FDG PET/CT. *Journal of Nuclear Medicine*. 2014;55:373-378.

21. Schaarschmidt B, Buchbender C, Gomez B, et al. Thoracic staging of non-small-cell lung cancer using integrated 18F-FDG PET/MR imaging: diagnostic value of different MR sequences. *Eur J Nucl Med Mol Imaging*. 2015;42:1257-1267.

22. Schaarschmidt BM, Buchbender C, Nensa F, et al. Correlation of the Apparent Diffusion Coefficient (ADC) with the Standardized Uptake Value (SUV) in Lymph Node Metastases

of Non-Small Cell Lung Cancer (NSCLC) Patients Using Hybrid 18F-FDG PET/MRI. Byrnes KR, ed. *PLOS ONE*. 2015;10:e0116277.

23. Schaarschmidt BM, Grueneisen J, Metzenmacher M, et al. Thoracic staging with 18F-FDG PET/MR in non-small cell lung cancer – does it change therapeutic decisions in comparison to 18F-FDG PET/CT? *Eur Radiol*. 2017;27:681-688.

24. Sokoloff L, Reivich M, Kennedy C, et al. THE [^{14} C]DEOXYGLUCOSE METHOD FOR THE MEASUREMENT OF LOCAL CEREBRAL GLUCOSE UTILIZATION: THEORY, PROCEDURE, AND NORMAL VALUES IN THE CONSCIOUS AND ANESTHETIZED ALBINO RAT. *J Neurochem*. 1977;28:897-916.

25. Morris ED, Endres CJ, Schmidt KC, Christian BT, Muzic RF, Fisher RE. Kinetic Modeling in Positron Emission Tomography. In: Emission Tomography. Elsevier; 2004:499-540.

26. Hawkins RA, Phelps ME, Huang SC. Effects of temporal sampling, glucose metabolic rates, and disruptions of the blood-brain barrier on the FDG model with and without a vascular compartment: studies in human brain tumors with PET. *J Cereb Blood Flow Metab*. 1986;6:170-183.

27. Herrero P, Sharp TL, Dence C, Haraden BM, Gropler RJ. Comparison of 1-(11)C-glucose and (18)F-FDG for quantifying myocardial glucose use with PET. *J Nucl Med*. 2002;43:1530-1541.

28. Chang H, Fitzpatrick JM. A technique for accurate magnetic resonance imaging in the presence of field inhomogeneities. *IEEE Transactions on Medical Imaging*. 1992;11:319-329.

29. Holland D, Kuperman JM, Dale AM. Efficient correction of inhomogeneous static magnetic field-induced distortion in Echo Planar Imaging. *NeuroImage*. 2010;50:175-183.

30. Simonetti OP, Finn JP, White RD, Laub G, Henry DA. "Black blood" T2-weighted inversion-recovery MR imaging of the heart. *Radiology*. 1996;199:49-57.

31. Roujol S, Weingärtner S, Foppa M, et al. Accuracy, Precision, and Reproducibility of Four T1 Mapping Sequences: A Head-to-Head Comparison of MOLLI, ShMOLLI, SASHA, and SAPPHIRE. *Radiology*. 2014;272:683-689.

32. Kim H. Variability in Quantitative DCE-MRI: Sources and Solutions. *J Nat Sci*. 2018;4.

33. Phelps ME, Hoffman EJ, Mullani NA, Ter-Pogossian MM. Application of annihilation coincidence detection to transaxial reconstruction tomography. *J Nucl Med*. 1975;16:210-224.

34. Ter-Pogossian MM, Phelps ME, Hoffman EJ, Mullani NA. A positron-emission transaxial tomograph for nuclear imaging (PETT). *Radiology*. 1975;114:89-98.

35. Hoffman EJ, Phelps ME. An analysis of some of the physical aspects of positron transaxial tomography. *Comput Biol Med*. 1976;6:345-360.

36. Hudson HM, Larkin RS. Accelerated image reconstruction using ordered subsets of projection data. *IEEE Trans Med Imaging*. 1994;13:601-609.

37. Henkin RE, ed. Nuclear medicine. 2nd ed. Philadelphia: Mosby Elsevier; 2006.

38. Budinger TF. PET instrumentation: What are the limits? *Seminars in Nuclear Medicine*. 1998;28:247-267.

39. Schaart DR, Seifert S, Vinke R, et al. LaBr(3):Ce and SiPMs for time-of-flight PET: achieving 100 ps coincidence resolving time. *Phys Med Biol*. 2010;55:N179-189.

40. Queiroz MA, Delso G, Wollenweber S, et al. Dose Optimization in TOF-PET/MR Compared to TOF-PET/CT. Chen K, ed. *PLoS ONE*. 2015;10:e0128842.

41. Samarin A, Burger C, Wollenweber SD, et al. PET/MR imaging of bone lesions – implications for PET quantification from imperfect attenuation correction. *Eur J Nucl Med Mol Imaging*. 2012;39:1154-1160.

42. Wagenknecht G, Kaiser H-J, Mottaghy FM, Herzog H. MRI for attenuation correction in PET: methods and challenges. *Magn Reson Mater Phy*. 2013;26:99-113.

43. Keereman V, Mollet P, Berker Y, Schulz V, Vandenberghe S. Challenges and current methods for attenuation correction in PET/MR. *Magn Reson Mater Phy*. 2013;26:81-98.

44. Levin CS, Maramraju SH, Khalighi MM, Deller TW, Delso G, Jansen F. Design Features and Mutual Compatibility Studies of the Time-of-Flight PET Capable GE SIGNA PET/MR System. *IEEE Trans Med Imaging*. 2016;35:1907-1914.

45. Boellaard R. Standards for PET image acquisition and quantitative data analysis. *J Nucl Med*. 2009;50 Suppl 1:11S-20S.

46. Woodard HQ, Bigler RE, Freed B. Letter: Expression of tissue isotope distribution. *J Nucl Med*. 1975;16:958-959.

47. Sugawara Y, Zasadny KR, Neuhoff AW, Wahl RL. Reevaluation of the Standardized Uptake Value for FDG: Variations with Body Weight and Methods for Correction. *Radiology*. 1999;213:521-525.

48. Kim CK, Gupta NC, Chandramouli B, Alavi A. Standardized uptake values of FDG: body surface area correction is preferable to body weight correction. *J Nucl Med*. 1994;35:164-167.

49. Boellaard R, Delgado-Bolton R, Oyen WJG, et al. FDG PET/CT: EANM procedure guidelines for tumour imaging: version 2.0. *European Journal of Nuclear Medicine and Molecular Imaging*. 2015;42:328-354.

50. Cochet A, Pigeonnat S, Khoury B, et al. Evaluation of Breast Tumor Blood Flow with Dynamic First-Pass 18F-FDG PET/CT: Comparison with Angiogenesis Markers and Prognostic Factors. *Journal of Nuclear Medicine*. 2012;53:512-520.

51. Humbert O, Riedinger J-M, Vrigneaud J-M, et al. 18F-FDG PET-Derived Tumor Blood Flow Changes After 1 Cycle of Neoadjuvant Chemotherapy Predicts Outcome in Triple-Negative Breast Cancer. *J Nucl Med*. 2016;57:1707-1712.

52. Durand E, Besson F. How is the standard uptake value (SUV) linked to the influx constant in Sokoloff's model for 18F-FDG? *Médecine Nucléaire*. 2015;39:11-17.

53. Spence AM, Muzi M, Graham MM, et al. Glucose metabolism in human malignant gliomas measured quantitatively with PET, 1-[C-11]glucose and FDG: analysis of the FDG lumped constant. *J Nucl Med*. 1998;39:440-448.

54. Ng CK, Soufer R, McNulty PH. Effect of hyperinsulinemia on myocardial fluorine-18-FDG uptake. *J Nucl Med*. 1998;39:379-383.

55. Wiggers H, Bøttcher M, Nielsen TT, Gjedde A, Bøtker HE. Measurement of myocardial glucose uptake in patients with ischemic cardiomyopathy: application of a new quantitative method using regional tracer kinetic information. *J Nucl Med*. 1999;40:1292-1300.

56. Peltoniemi P, Lönnroth P, Laine H, et al. Lumped constant for [^{18} F]fluorodeoxyglucose in skeletal muscles of obese and nonobese humans. *American Journal of Physiology-Endocrinology and Metabolism*. 2000;279:E1122-E1130.

57. Virtanen KA, Peltoniemi P, Marjamäki P, et al. Human adipose tissue glucose uptake determined using [18 F]-fluoro-deoxy-glucose ([18 F]FDG) and PET in combination with microdialysis. *Diabetologia*. 2001;44:2171-2179.

58. Wu H. Measurement of the Global Lumped Constant for 2-Deoxy-2-[18F]Fluoro-D-Glucose in Normal Human Brain Using [15O]Water and 2-Deoxy-2-[18F]Fluoro-D-Glucose Positron Emission Tomography Imaging A Method with Validation Based on Multiple Methodologies. *Molecular Imaging & Biology*. 2003;5:32-41.

59. Iozzo P, Jarvisalo MJ, Kiss J, et al. Quantification of Liver Glucose Metabolism by Positron Emission Tomography: Validation Study in Pigs. *Gastroenterology*. 2007;132:531-542.

60. Young H, Baum R, Cremerius U, et al. Measurement of clinical and subclinical tumour response using [18F]-fluorodeoxyglucose and positron emission tomography: review and 1999 EORTC recommendations. *European Journal of Cancer*. 1999;35:1773-1782.

61. Gambhir SS, Schwaiger M, Huang SC, et al. Simple noninvasive quantification method for measuring myocardial glucose utilization in humans employing positron emission tomography and fluorine-18 deoxyglucose. *J Nucl Med*. 1989;30:359-366.

62. Muzi M, Vesselle H, Grierson JR, et al. Kinetic analysis of 3'-deoxy-3'-fluorothymidine PET studies: validation studies in patients with lung cancer. *J Nucl Med*. 2005;46:274-282.

63. de Geus-Oei L-F, Visser EP, Krabbe PFM, et al. Comparison of image-derived and arterial input functions for estimating the rate of glucose metabolism in therapy-monitoring 18F-FDG PET studies. *J Nucl Med*. 2006;47:945-949.

64. Tsutsui Y, Awamoto S, Himuro K, Umezu Y, Baba S, Sasaki M. Characteristics of Smoothing Filters to Achieve the Guideline Recommended Positron Emission Tomography Image without Harmonization. *Asia Ocean J Nucl Med Biol*. 2018;6:15-23.

65. Vriens D, Visser EP, de Geus-Oei L-F, Oyen WJG. Methodological considerations in quantification of oncological FDG PET studies. *Eur J Nucl Med Mol Imaging*. 2010;37:1408-1425.

66. Abramowitz M, Stegun IA, eds. Handbook of mathematical functions: with formulas, graphs, and mathematical tables. 9. Dover print.; [Nachdr. der Ausg. von 1972]. New York, NY: Dover Publ; 2013.

67. Besson FL, Henry T, Meyer C, et al. Rapid Contour-based Segmentation for ^{18} F-FDG PET Imaging of Lung Tumors by Using ITK-SNAP: Comparison to Expert-based Segmentation. *Radiology*. 2018;288:277-284.

68. Hoult DI, Richards RE. The signal-to-noise ratio of the nuclear magnetic resonance experiment. 1976. *J Magn Reson*. 2011;213:329-343.

69. Bloch F. Nuclear Induction. *Phys Rev*. 1946;70:460-474.

70. Stanisz GJ, Odrobina EE, Pun J, et al. T1, T2 relaxation and magnetization transfer in tissue at 3T. *Magn Reson Med*. 2005;54:507-512.

71. Bojorquez JZ, Bricq S, Acquitter C, Brunotte F, Walker PM, Lalande A. What are normal relaxation times of tissues at 3 T? *Magnetic Resonance Imaging*. 2017;35:69-80.

72. Brown MA, Semelka RC. MR Imaging Abbreviations, Definitions, and Descriptions: A Review. *Radiology*. 1999;213:647-662.

73. Paschal CB, Morris HD. K-space in the clinic. *J Magn Reson Imaging*. 2004;19:145-159.

74. Brigham EO. The fast Fourier transform and its applications. Englewood Cliffs, N.J: Prentice Hall; 1988.

75. Hennig J. K-space sampling strategies. *European Radiology*. 1999;9:1020-1031.

76. Hahn EL. Spin Echoes. *Phys Rev*. 1950;80:580-594.

77. Stejskal EO, Tanner JE. Spin Diffusion Measurements: Spin Echoes in the Presence of a Time-Dependent Field Gradient. *The Journal of Chemical Physics*. 1965;42:288-292.

78. Park MY, Byun JY. Understanding the Mathematics Involved in Calculating Apparent Diffusion Coefficient Maps. *American Journal of Roentgenology*. 2012;199:W784-W784.

79. Le Bihan D, Breton E, Lallemand D, Grenier P, Cabanis E, Laval-Jeantet M. MR imaging of intravoxel incoherent motions: application to diffusion and perfusion in neurologic disorders. *Radiology*. 1986;161:401-407.

80. Mansfield P. Multi-planar image formation using NMR spin echoes. *Journal of Physics C: Solid State Physics*. 1977;10:L55-L58.

81. Olin A, Krogager L, Rasmussen JH, et al. Preparing data for multiparametric PET/MR imaging: Influence of PET point spread function modelling and EPI distortion correction on the spatial correlation of [18F]FDG-PET and diffusion-weighted MRI in head and neck cancer. *Physica Medica*. 2019;61:1-7.

82. Zeilinger MG, Lell M, Baltzer PAT, Dörfler A, Uder M, Dietzel M. Impact of post-processing methods on apparent diffusion coefficient values. *Eur Radiol*. 2017;27:946-955.

83. Saritas EU, Cunningham CH, Lee JH, Han ET, Nishimura DG. DWI of the spinal cord with reduced FOV single-shot EPI. *Magn Reson Med*. 2008;60:468-473.

84. Korn N, Kurhanewicz J, Banerjee S, Starobinets O, Saritas E, Noworolski S. Reduced-FOV excitation decreases susceptibility artifact in diffusion-weighted MRI with endorectal coil for prostate cancer detection. *Magnetic Resonance Imaging*. 2015;33:56-62.

85. Miller KL, Pauly JM. Nonlinear phase correction for navigated diffusion imaging. *Magn Reson Med*. 2003;50:343-353.

86. Jezzard P, Balaban RS. Correction for geometric distortion in echo planar images from B0 field variations. *Magn Reson Med*. 1995;34:65-73.

87. Reber PJ, Wong EC, Buxton RB, Frank LR. Correction of off resonance-related distortion in echo-planar imaging using EPI-based field maps. *Magn Reson Med*. 1998;39:328-330.

88. Andersson JLR, Skare S, Ashburner J. How to correct susceptibility distortions in spin-echo echo-planar images: application to diffusion tensor imaging. *NeuroImage*. 2003;20:870-888.

89. Ruthotto L, Kugel H, Olesch J, et al. Diffeomorphic susceptibility artifact correction of diffusion-weighted magnetic resonance images. *Physics in Medicine and Biology*. 2012;57:5715-5731.

90. Yushkevich PA, Piven J, Hazlett HC, et al. User-guided 3D active contour segmentation of anatomical structures: significantly improved efficiency and reliability. *Neuroimage*. 2006;31:1116-1128.

91. Avants BB, Tustison NJ, Stauffer M, Song G, Wu B, Gee JC. The Insight ToolKit image registration framework. *Frontiers in Neuroinformatics*. 2014;8.

92. Kosiński W, Michalak P, Gut P. Robust Image Registration Based on Mutual Information Measure. *Journal of Signal and Information Processing*. 2012;03:175-178.

93. Besson FL, Fernandez B, Faure S, et al. Diffusion-weighted Imaging Voxelwise-matched Analyses of Lung Cancer at 3.0-T PET/MRI: Reverse Phase Encoding Approach for Echo-planar Imaging Distortion Correction. *Radiology*. March 2020:192013.

94. Damadian R, Zaner K, Hor D, DiMaio T. Human Tumors Detected by Nuclear Magnetic Resonance. *Proceedings of the National Academy of Sciences*. 1974;71:1471-1473.

95. Ross RJ, Thompson JS, Kim K, Bailey RA. Nuclear magnetic resonance imaging and evaluation of human breast tissue: preliminary clinical trials. *Radiology*. 1982;143:195-205.

96. McSweeney MB, Small WC, Cerny V, Sewell W, Powell RW, Goldstein JH. Magnetic resonance imaging in the diagnosis of breast disease: use of transverse relaxation times. *Radiology*. 1984;153:741-744.

97. Andersson T, Ericsson A, Eriksson B, et al. Relative proton density and relaxation times in liver metastases during interferon treatment. *BJR*. 1989;62:433-437.

98. Krasin MJ, Xiong X, Reddick WE, et al. A model for quantitative changes in the magnetic resonance parameters of muscle in children after therapeutic irradiation. *Magnetic Resonance Imaging*. 2006;24:1319-1324.

99. Roebuck JR, Haker SJ, Mitsouras D, Rybicki FJ, Tempany CM, Mulkern RV. Carr-Purcell-Meiboom-Gill imaging of prostate cancer: quantitative T2 values for cancer discrimination. *Magnetic Resonance Imaging*. 2009;27:497-502.

100. Drain LE. A Direct Method of Measuring Nuclear Spin-Lattice Relaxation Times. *Proc Phys Soc A*. 1949;62:301-306.

101. Hahn EL. An Accurate Nuclear Magnetic Resonance Method for Measuring Spin-Lattice Relaxation Times. *Phys Rev*. 1949;76:145-146.

102. Look DC, Locker DR. Time Saving in Measurement of NMR and EPR Relaxation Times. *Review of Scientific Instruments*. 1970;41:250-251.

103. Brix G, Schad LR, Deimling M, Lorenz WJ. Fast and precise T1 imaging using a TOMROP sequence. *Magnetic Resonance Imaging*. 1990;8:351-356.

104. Messroghli DR, Radjenovic A, Kozerke S, Higgins DM, Sivananthan MU, Ridgway JP. Modified Look-Locker inversion recovery (MOLLI) for high-resolutionT1 mapping of the heart. *Magn Reson Med*. 2004;52:141-146.

105. Chow K, Yang Y, Shaw P, Kramer CM, Salerno M. Robust free-breathing SASHA T1 mapping with high-contrast image registration. *J Cardiovasc Magn Reson*. 2016;18:47.

106. Gupta RK. A new look at the method of variable nutation angle for the measurement of spin-lattice relaxation times using fourier transform NMR. *Journal of Magnetic Resonance (1969)*. 1977;25:231-235.

107. Blüml S, Schad LR, Stepanow B, Lorenz WJ. Spin-lattice relaxation time measurement by means of a TurboFLASH technique. *Magn Reson Med*. 1993;30:289-295.

108. Insko EK, Bolinger L. Mapping of the Radiofrequency Field. *Journal of Magnetic Resonance, Series A*. 1993;103:82-85.

109. Cunningham CH, Pauly JM, Nayak KS. Saturated double-angle method for rapidB1+ mapping. *Magn Reson Med*. 2006;55:1326-1333.

110. Akoka S, Franconi F, Seguin F, Le Pape A. Radiofrequency map of an NMR coil by imaging. *Magnetic Resonance Imaging*. 1993;11:437-441.

111. Jiru F, Klose U. Fast 3D radiofrequency field mapping using echo-planar imaging. *Magn Reson Med*. 2006;56:1375-1379.

112. Yarnykh VL. Actual flip-angle imaging in the pulsed steady state: A method for rapid three-dimensional mapping of the transmitted radiofrequency field. *Magn Reson Med*. 2007;57:192-200.

113. Klose U. Mapping of the radio frequency magnetic field with a MR snapshot FLASH technique: Technical Reprt: Mapping of the radio frequency magnetic field. *Med Phys*. 1992;19:1099-1104.

114. Brunner DO, Pruessmann KP. B_1^+ interferometry for the calibration of RF transmitter arrays. *Magn Reson Med*. 2009;61:1480-1488.

115. Chung S, Kim D, Breton E, Axel L. Rapid B1+ mapping using a preconditioning RF pulse with TurboFLASH readout. *Magn Reson Med*. 2010:n/a-n/a.

116. Nehrke K, Börnert P. DREAM-a novel approach for robust, ultrafast, multislice B_1 mapping: DREAM B_1 Mapping. *Magn Reson Med*. 2012;68:1517-1526.

117. Oh CH, Hilal SK, Cho ZH, Mun IK. Radio frequency field intensity mapping using a composite spin-echo sequence. *Magnetic Resonance Imaging*. 1990;8:21-25.

118. Chang YV. Rapid B1 mapping using orthogonal, equal-amplitude radio-frequency pulses. *Magn Reson Med*. 2012;67:718-723.

119. Sacolick LI, Wiesinger F, Hancu I, Vogel MW. B1 mapping by Bloch-Siegert shift. *Magn Reson Med*. 2010;63:1315-1322.

120. Carr HY, Purcell EM. Effects of Diffusion on Free Precession in Nuclear Magnetic Resonance Experiments. *Phys Rev*. 1954;94:630-638.

121. Meiboom S, Gill D. Modified Spin-Echo Method for Measuring Nuclear Relaxation Times. *Review of Scientific Instruments*. 1958;29:688-691.

122. Hennig J. Multiecho imaging sequences with low refocusing flip angles. *Journal of Magnetic Resonance (1969)*. 1988;78:397-407.

123. Pell GS, Briellmann RS, Waites AB, Abbott DF, Lewis DP, Jackson GD. Optimized clinical T2 relaxometry with a standard CPMG sequence. *J Magn Reson Imaging*. 2006;23:248-252.

124. Miller AJ, Joseph PM. The use of power images to perform quantitative analysis on low SNR MR images. *Magnetic Resonance Imaging*. 1993;11:1051-1056.

125. Feng Y, He T, Gatehouse PD, et al. Improved MRI R_2* relaxometry of iron-loaded liver with noise correction: Improved MRI R_2* for Liver Iron Quantification. *Magn Reson Med*. 2013;70:1765-1774.

126. Milford D, Rosbach N, Bendszus M, Heiland S. Mono-Exponential Fitting in T2-Relaxometry: Relevance of Offset and First Echo. Fan X, ed. *PLoS ONE*. 2015;10:e0145255.

127. Slavin GS, Stainsby JA. True T1 mapping with SMART1Map (saturation method using adaptive recovery times for cardiac T1 mapping): a comparison with MOLLI. *J Cardiovasc Magn Reson*. 2013;15:P3, 1532-429X-15-S1-P3.

128. Mosher TJ, Dardzinski BJ, Smith MB. Human Articular Cartilage: Influence of Aging and Early Symptomatic Degeneration on the Spatial Variation of T2—Preliminary Findings at 3 T. *Radiology*. 2000;214:259-266.

129. Le Roux P. Non-CPMG Fast Spin Echo with Full Signal. *Journal of Magnetic Resonance*. 2002;155:278-292.

130. Maier CF, Tan SG, Hariharan H, Potter HG. T2 quantitation of articular cartilage at 1.5 T. *J Magn Reson Imaging*. 2003;17:358-364.

131. Smith HE, Mosher TJ, Dardzinski BJ, et al. Spatial variation in cartilage T2 of the knee. *J Magn Reson Imaging*. 2001;14:50-55.

132. Nöth U, Shrestha M, Schüre J-R, Deichmann R. Quantitative in vivo T2 mapping using fast spin echo techniques – A linear correction procedure. *NeuroImage*. 2017;157:476-485.

133. Koo TK, Li MY. A Guideline of Selecting and Reporting Intraclass Correlation Coefficients for Reliability Research. *Journal of Chiropractic Medicine*. 2016;15:155-163.

134. Yarnykh VL. Optimal radiofrequency and gradient spoiling for improved accuracy of T1 and B1 measurements using fast steady-state techniques. *Magn Reson Med*. 2010;63:1610-1626.

135. Balezeau F, Eliat P-A, Cayamo AB, Saint-Jalmes H. Mapping of low flip angles in magnetic resonance. *Phys Med Biol*. 2011;56:6635-6647.

136. Hurley SA, Yarnykh VL, Johnson KM, Field AS, Alexander AL, Samsonov AA. Simultaneous variable flip angle-actual flip angle imaging method for improved accuracy and precision of three-dimensional T1 and B1 measurements. *Magn Reson Med*. 2012;68:54-64.

137. Cuenod CA, Balvay D. Perfusion and vascular permeability: Basic concepts and measurement in DCE-CT and DCE-MRI. *Diagnostic and Interventional Imaging*. 2013;94:1187-1204.

138. Padhani AR, Husband JE. Dynamic Contrast-enhanced MRI Studies in Oncology with an Emphasis on Quantification, Validation and Human Studies. *Clinical Radiology*. 2001;56:607-620.

139. Choyke PL, Dwyer AJ, Knopp MV. Functional tumor imaging with dynamic contrast-enhanced magnetic resonance imaging. *J Magn Reson Imaging*. 2003;17:509-520.

140. Khalifa F, Soliman A, El-Baz A, et al. Models and methods for analyzing DCE-MRI: A review: Models and methods for analyzing DCE-MRI. *Med Phys*. 2014;41:124301.

141. Yang X, Knopp MV. Quantifying Tumor Vascular Heterogeneity with Dynamic Contrast-Enhanced Magnetic Resonance Imaging: A Review. *Journal of Biomedicine and Biotechnology*. 2011;2011:1-12.

142. Tofts PS, Kermode AG. Measurement of the blood-brain barrier permeability and leakage space using dynamic MR imaging. 1. Fundamental concepts. *Magn Reson Med*. 1991;17:357-367.

143. Tofts PS. Modeling tracer kinetics in dynamic Gd-DTPA MR imaging. *J Magn Reson Imaging*. 1997;7:91-101.

144. Hunter GJ, Hamberg LM, Choi N, Jain RK, McCloud T, Fischman AJ. Dynamic T1-weighted magnetic resonance imaging and positron emission tomography in patients with lung cancer: correlating vascular physiology with glucose metabolism. *Clin Cancer Res*. 1998;4:949-955.

145. Naish JH, Kershaw LE, Buckley DL, Jackson A, Waterton JC, Parker GJM. Modeling of contrast agent kinetics in the lung using T1-weighted dynamic contrast-enhanced MRI. *Magn Reson Med*. 2009;61:1507-1514.

146. Chang Y-C, Yu C-J, Chen C-M, et al. Dynamic contrast-enhanced MRI in advanced nonsmall-cell lung cancer patients treated with first-line bevacizumab, gemcitabine, and cisplatin. *J Magn Reson Imaging*. 2012;36:387-396.

147. Xu J, Mei L, Liu L, Wang K, Zhou Z, Zheng J. Early assessment of response to chemotherapy in lung cancer using dynamic contrast-enhanced MRI: a proof-of-concept study. *Clinical Radiology*. 2018;73:625-631.

148. Torheim G, Amundsen T, Rinck PA, Haraldseth O, Sebastiani G. Analysis of contrast-enhanced dynamic MR images of the lung. *J Magn Reson Imaging*. 2001;13:577-587.

149. Huang H, Shen L, Ford J, Gao L, Pearlman J. Early lung cancer detection based on registered perfusion MRI. *Oncol Rep*. April 2006.

150. Xue H, Guehring J, Srinivasan L, et al. Evaluation of Rigid and Non-rigid Motion Compensation of Cardiac Perfusion MRI. In: Metaxas D, Axel L, Fichtinger G, Székely G, eds. Medi-

cal Image Computing and Computer-Assisted Intervention – MICCAI 2008. Vol 5242. Lecture Notes in Computer Science. Berlin, Heidelberg: Springer Berlin Heidelberg; 2008:35-43.

151. Kachenoura N, Cluzel P, Frouin F, et al. Evaluation of an edge-based registration method: application to magnetic resonance first-pass myocardial perfusion data. *Magnetic Resonance Imaging*. 2011;29:853-860.

152. Filipovic M, Vuissoz P-A, Codreanu A, Claudon M, Felblinger J. Motion compensated generalized reconstruction for free-breathing dynamic contrast-enhanced MRI. *Magn Reson Med*. 2011;65:812-822.

153. Feng Q, Zhou Y, Li X, et al. Liver DCE-MRI Registration in Manifold Space Based on Robust Principal Component Analysis. *Sci Rep*. 2016;6:34461.

154. Nowak RD. Wavelet-based Rician noise removal for magnetic resonance imaging. *IEEE Trans Image Process*. 1999;8:1408-1419.

155. Manjon J, Carbonellcaballero J, Lull J, Garciamarti G, Martibonmati L, Robles M. MRI denoising using Non-Local Means. *Medical Image Analysis*. 2008;12:514-523.

156. Krissian K, Aja-Fernandez S. Noise-Driven Anisotropic Diffusion Filtering of MRI. *IEEE Trans on Image Process*. 2009;18:2265-2274.

157. Manjón JV, Coupé P, Martí-Bonmatí L, Collins DL, Robles M. Adaptive non-local means denoising of MR images with spatially varying noise levels: Spatially Adaptive Nonlocal Denoising. *J Magn Reson Imaging*. 2010;31:192-203.

158. Shen Y, Goerner FL, Snyder C, et al. T1 Relaxivities of Gadolinium-Based Magnetic Resonance Contrast Agents in Human Whole Blood at 1.5, 3, and 7 T: *Investigative Radiology*. 2015;50:330-338.

159. Billett HH. Hemoglobin and Hematocrit. In: Walker HK, Hall WD, Hurst JW, eds. Clinical Methods: The History, Physical, and Laboratory Examinations. 3rd ed. Boston: Butterworths; 1990.

160. Tofts PS, Brix G, Buckley DL, et al. Estimating kinetic parameters from dynamic contrast-enhanced T(1)-weighted MRI of a diffusable tracer: standardized quantities and symbols. *J Magn Reson Imaging*. 1999;10:223-232.

161. Li X, Morgan PS, Ashburner J, Smith J, Rorden C. The first step for neuroimaging data analysis: DICOM to NIfTI conversion. *Journal of Neuroscience Methods*. 2016;264:47-56.

162. Foster B, Bagci U, Mansoor A, Xu Z, Mollura DJ. A review on segmentation of positron emission tomography images. *Computers in Biology and Medicine*. 2014;50:76-96.

163. van Dalen JA, Hoffmann AL, Dicken V, et al. A novel iterative method for lesion delineation and volumetric quantification with FDG PET: *Nuclear Medicine Communications*. 2007;28:485-493.

164. Hofheinz F, Dittrich S, Pötzsch C, Hoff J van den. Effects of cold sphere walls in PET phantom measurements on the volume reproducing threshold. *Phys Med Biol*. 2010;55:1099-1113.

165. Ohno Y, Koyama H, Yoshikawa T, et al. Three-way Comparison of Whole-Body MR, Coregistered Whole-Body FDG PET/MR, and Integrated Whole-Body FDG PET/CT Imaging: TNM and Stage Assessment Capability for Non–Small Cell Lung Cancer Patients. *Radiology*. 2015;275:849-861.

166. Regier M, Derlin T, Schwarz D, et al. Diffusion weighted MRI and 18F-FDG PET/CT in non-small cell lung cancer (NSCLC): Does the apparent diffusion coefficient (ADC) correlate with tracer uptake (SUV)? *European Journal of Radiology*. 2012;81:2913-2918.

167. Heusch P, Köhler J, Wittsack H-J, et al. Hybrid [18F]-FDG PET/MRI including non-Gaussian diffusion-weighted imaging (DWI): Preliminary results in non-small cell lung cancer (NSCLC). *European Journal of Radiology*. 2013;82:2055-2060.

168. Schaarschmidt BM, Buchbender C, Nensa F, et al. Correlation of the Apparent Diffusion Coefficient (ADC) with the Standardized Uptake Value (SUV) in Lymph Node Metastases of Non-Small Cell Lung Cancer (NSCLC) Patients Using Hybrid 18F-FDG PET/MRI. Byrnes KR, ed. *PLoS ONE*. 2015;10:e0116277.

169. Metz S, Ganter C, Lorenzen S, et al. Multiparametric MR and PET Imaging of Intratumoral Biological Heterogeneity in Patients with Metastatic Lung Cancer Using Voxel-by-Voxel Analysis. Muñoz-Barrutia A, ed. *PLOS ONE*. 2015;10:e0132386.

170. Iizuka Y, Matsuo Y, Umeoka S, et al. Prediction of clinical outcome after stereotactic body radiotherapy for non-small cell lung cancer using diffusion-weighted MRI and 18F-FDG PET. *European Journal of Radiology*. 2014;83:2087-2092.

171. Fouad YA, Aanei C. Revisiting the hallmarks of cancer. *Am J Cancer Res*. 2017;7:1016-1036.

172. Tateishi U, Nishihara H, Tsukamoto E, Morikawa T, Tamaki N, Miyasaka K. Lung tumors evaluated with FDG-PET and dynamic CT: the relationship between vascular density and glucose metabolism. *J Comput Assist Tomogr*. 2002;26:185-190.

173. Hoekstra CJ, Stroobants SG, Hoekstra OS, Smit EF, Vansteenkiste JF, Lammertsma AA. Measurement of perfusion in stage IIIA-N2 non-small cell lung cancer using H(2)(15)O and positron emission tomography. *Clin Cancer Res*. 2002;8:2109-2115.

174. Miles KA, Griffiths MR, Keith CJ. Blood flow-metabolic relationships are dependent on tumour size in non-small cell lung cancer: a study using quantitative contrast-enhanced computer tomography and positron emission tomography. *Eur J Nucl Med Mol Imaging*. 2006;33:22-28.

175. Zhang J, Chen L, Chen Y, et al. Tumor Vascularity and Glucose Metabolism Correlated in Adenocarcinoma, but Not in Squamous Cell Carcinoma of the Lung. Zhang Z, ed. *PLoS ONE*. 2014;9:e91649.

176. Ushijima C, Tsukamoto S, Yamazaki K, Yoshino I, Sugio K, Sugimachi K. High vascularity in the peripheral region of non-small cell lung cancer tissue is associated with tumor progression. *Lung Cancer*. 2001;34:233-241.

177. Birau A, Ceausu RA, Cimpean AM, Gaje P, Raica M, Olariu T. Assessement of angiogenesis reveals blood vessel heterogeneity in lung carcinoma. *Oncol Lett*. 2012;4:1183-1186.

178. Schober P, Boer C, Schwarte LA. Correlation Coefficients: Appropriate Use and Interpretation. *Anesth Analg*. 2018;126:1763-1768.

179. Simoncic U, Leibfarth S, Welz S, et al. Comparison of DCE-MRI kinetic parameters and FMISO-PET uptake parameters in head and neck cancer patients. *Med Phys*. 2017;44:2358-2368.

180. Lee KH, Kang SK, Goo JM, et al. Relationship Between Ktrans and K1 with Simultaneous Versus Separate MR/PET in Rabbits with VX2 Tumors. *Anticancer Res*. 2017;37:1139-1148.

181. Mullani NA, Herbst RS, O'Neil RG, Gould KL, Barron BJ, Abbruzzese JL. Tumor blood flow measured by PET dynamic imaging of first-pass 18F-FDG uptake: a comparison with 15O-labeled water-measured blood flow. *J Nucl Med*. 2008;49:517-523.

182. Sourbron SP, Buckley DL. On the scope and interpretation of the Tofts models for DCE-MRI. *Magn Reson Med*. 2011;66:735-745.

183. Shukla-Dave A, Obuchowski NA, Chenevert TL, et al. Quantitative imaging biomarkers alliance (QIBA) recommendations for improved precision of DWI and DCE-MRI derived biomarkers in multicenter oncology trials: QIBA Recommendations. *Journal of Magnetic Resonance Imaging*. November 2018.

184. Miles KA. Warburg revisited: imaging tumour blood flow and metabolism. *Cancer Imaging*. 2008;8:81-86.

185. Ming-Syan Chen, Jiawei Han, Yu PS. Data mining: an overview from a database perspective. *IEEE Trans Knowl Data Eng*. 1996;8:866-883.

186. Tibshirani R, Walther G, Hastie T. Estimating the number of clusters in a data set via the gap statistic. *J Royal Statistical Soc B*. 2001;63:411-423.

187. McLachlan GJ, Peel D. Finite mixture models. New York: Wiley; 2000.

188. Schmitz J, Schwab J, Schwenck J, et al. Decoding Intratumoral Heterogeneity of Breast Cancer by Multiparametric *In Vivo* Imaging: A Translational Study. *Cancer Res*. 2016;76:5512-5522.

189. Divine MR, Katiyar P, Kohlhofer U, Quintanilla-Martinez L, Pichler BJ, Disselhorst JA. A Population-Based Gaussian Mixture Model Incorporating 18F-FDG PET and Diffusion-Weighted MRI Quantifies Tumor Tissue Classes. *J Nucl Med*. 2016;57:473-479.

190. Schwarz G. Estimating the Dimension of a Model. *Ann Statist*. 1978;6:461-464.

191. Akaike H. Information Theory and an Extension of the Maximum Likelihood Principle. In: Parzen E, Tanabe K, Kitagawa G, eds. Selected Papers of Hirotugu Akaike. Springer Series in Statistics. New York, NY: Springer New York; 1998:199-213.

192. Turner-Warwick M. Precapillary Systemic-pulmonary Anastomoses. *Thorax*. 1963;18:225-237.

193. Keane MP. Angiogenesis and Pulmonary Fibrosis: Feast or Famine? *Am J Respir Crit Care Med*. 2004;170:207-209.

194. Eldridge L, Wagner EM. Angiogenesis in the lung. *J Physiol (Lond)*. 2019;597:1023-1032.

195. Semenza GL. HIF-1 and tumor progression: pathophysiology and therapeutics. *Trends in Molecular Medicine*. 2002;8:S62-S67.

196. Bianchi L, Dorigo M, Gambardella LM, Gutjahr WJ. A survey on metaheuristics for stochastic combinatorial optimization. *Nat Comput*. 2009;8:239-287.

197. Saeys Y, Inza I, Larranaga P. A review of feature selection techniques in bioinformatics. *Bioinformatics*. 2007;23:2507-2517.

198. Tibshirani R. Regression Shrinkage and Selection Via the Lasso. *Journal of the Royal Statistical Society: Series B (Methodological)*. 1996;58:267-288.

199. Zou H, Hastie T. Regularization and variable selection via the elastic net. *J Royal Statistical Soc B*. 2005;67:301-320.

200. Breiman L. Bagging predictors. *Mach Learn*. 1996;24:123-140.

201. Tin Kam Ho. The random subspace method for constructing decision forests. *IEEE Trans Pattern Anal Machine Intell*. 1998;20:832-844.

202. Schapire RE. The strength of weak learnability. *Mach Learn*. 1990;5:197-227.

203. Mason L, Baxter J, Bartlett P, Frean M. Boosting Algorithms as Gradient Descent. In: Advances in Neural Information Processing Systems 12: Proceedings of the 1999 Conference.

204. Friedman JH. machine. *Ann Statist*. 2001;29:1189-1232.

205. Chen T, Guestrin C. XGBoost: A Scalable Tree Boosting System. In: Proceedings of the 22nd ACM SIGKDD International Conference on Knowledge Discovery and Data Mining - KDD '16. San Francisco, California, USA: ACM Press; 2016:785-794.

206. Pedregosa F, Varoquaux G, Gramfort A, et al. Scikit-learn: Machine Learning in Python. *arXiv:12010490 [cs]*. June 2018.

207. Elith J, Leathwick JR, Hastie T. A working guide to boosted regression trees. *J Anim Ecology*. 2008;77:802-813.

208. Ellingsen C, Egeland TAM, Galappathi K, Rofstad EK. Dynamic contrast-enhanced magnetic resonance imaging of human cervical carcinoma xenografts: Pharmacokinetic analysis and correlation to tumor histomorphology. *Radiotherapy and Oncology*. 2010;97:217-224.

209. Kim J-H, Kim CK, Park BK, Park SY, Huh SJ, Kim B. Dynamic contrast-enhanced 3-T MR imaging in cervical cancer before and after concurrent chemoradiotherapy. *Eur Radiol*. 2012;22:2533-2539.

210. Cheng JC-H, Yuan A, Chen J-H, et al. Early Detection of Lewis Lung Carcinoma Tumor Control by Irradiation Using Diffusion-Weighted and Dynamic Contrast-Enhanced MRI. Lin C-P, ed. *PLoS ONE*. 2013;8:e62762.

211. Tao X, Wang L, Hui Z, et al. DCE-MRI Perfusion and Permeability Parameters as predictors of tumor response to CCRT in Patients with locally advanced NSCLC. *Sci Rep*. 2016;6:35569.

212. Hatzoglou V, Tisnado J, Mehta A, et al. Dynamic contrast-enhanced MRI perfusion for differentiating between melanoma and lung cancer brain metastases. *Cancer Med*. 2017;6:761-767.

213. Huang Y-S, Chen JL-Y, Hsu F-M, et al. Response assessment of stereotactic body radiation therapy using dynamic contrast-enhanced integrated MR-PET in non-small cell lung cancer patients: Response Assessment of SBRT Using MR-PET. *J Magn Reson Imaging*. 2018;47:191-199.

214. Furler SM, Jenkins AB, Storlien LH, Kraegen EW. In vivo location of the rate-limiting step of hexose uptake in muscle and brain tissue of rats. *American Journal of Physiology-Endocrinology and Metabolism*. 1991;261:E337-E347.

215. Tseng J, Dunnwald LK, Schubert EK, et al. 18F-FDG kinetics in locally advanced breast cancer: correlation with tumor blood flow and changes in response to neoadjuvant chemotherapy. *J Nucl Med*. 2004;45:1829-1837.

216. Dimitrakopoulou-Strauss A, Strauss LG, Burger C, et al. Prognostic aspects of 18F-FDG PET kinetics in patients with metastatic colorectal carcinoma receiving FOLFOX chemotherapy. *J Nucl Med*. 2004;45:1480-1487.

217. Strauss LG, Klippel S, Pan L, Schönleben K, Haberkorn U, Dimitrakopoulou-Strauss A. Assessment of quantitative FDG PET data in primary colorectal tumours: which parameters are important with respect to tumour detection? *Eur J Nucl Med Mol Imaging*. 2007;34:868-877.

218. Dimitrakopoulou-Strauss A, Strauss LG, Egerer G, et al. Prediction of chemotherapy outcome in patients with metastatic soft tissue sarcomas based on dynamic FDG PET (dPET) and a multiparameter analysis. *Eur J Nucl Med Mol Imaging*. 2010;37:1481-1489.

219. Epelbaum R, Frenkel A, Haddad R, et al. Tumor Aggressiveness and Patient Outcome in Cancer of the Pancreas Assessed by Dynamic 18F-FDG PET/CT. *Journal of Nuclear Medicine*. 2013;54:12-18.

220. Yang Z, Zan Y, Zheng X, et al. Dynamic FDG-PET Imaging to Differentiate Malignancies from Inflammation in Subcutaneous and In Situ Mouse Model for Non-Small Cell Lung Carcinoma (NSCLC). Tagliabue E, ed. *PLoS ONE*. 2015;10:e0139089.

221. Jiao J, Bousse A, Thielemans K, et al. Direct Parametric Reconstruction With Joint Motion Estimation/Correction for Dynamic Brain PET Data. *IEEE Trans Med Imaging*. 2017;36:203-213.

222. Gulani V, Schmitt P, Griswold MA, Webb AG, Jakob PM. Towards a Single-Sequence Neurologic Magnetic Resonance Imaging Examination: Multiple-Contrast Images From an IR TrueFISP Experiment: *Investigative Radiology*. 2004;39:767-774.

223. Warntjes JBM, Leinhard OD, West J, Lundberg P. Rapid magnetic resonance quantification on the brain: Optimization for clinical usage. *Magn Reson Med*. 2008;60:320-329.

224. Ma D, Gulani V, Seiberlich N, et al. Magnetic resonance fingerprinting. *Nature*. 2013;495:187-192.

225. Chen Y, Panda A, Pahwa S, et al. Three-dimensional MR Fingerprinting for Quantitative Breast Imaging. *Radiology*. 2019;290:33-40.

226. Leroi L, Coste A, de Rochefort L, et al. Simultaneous multi-parametric mapping of total sodium concentration, T1, T2 and ADC at 7 T using a multi-contrast unbalanced SSFP. *Magnetic Resonance Imaging*. 2018;53:156-163.

PUBLICATION LIST

Journal Articles

[18]F-FDG PET and DCE kinetic modeling and their correlations in primary NSCLC: First voxel-wise correlative analysis of human simultaneous [18F]FDG PET-MRI data.

Besson FL, Fernandez B, Faure S, Mercier O, Seferian A, Mignard X, Mussot S, Le Pechoux C, Caramella C, Botticella A, Levy A, Parent F, Bulifon S, Montani D, Mitilian D, Fadel E, Planchard D, Besse B, Ghigna-Bellinzoni MR, Comtat C, Lebon V, Durand E. (**Submitted, under review**).

Diffusion-weighted Imaging Voxelwise-matched Analyses of Lung Cancer at 3.0-T PET/MRI: Reverse Phase Encoding Approach for Echo-planar Imaging Distortion Correction.

Besson FL, Fernandez B, Faure S, Mercier O, Seferian A, Blanchet É, Mignard X, Chetouani A, Bulifon S, Mussot S, Parent F, Bouderraoui F, Montani D, Mitilian D, Fadel E, Ghigna-Bellinzoni MR, Cherkaoui H, Comtat C, Lebon V, Durand E. **Radiology**. **2020** Mar 24:192013. doi: 10.1148/radiol.2020192013. Online ahead of print. PMID: 32208099

Rapid Contour-based Segmentation for 18F-FDG PET Imaging of Lung Tumors by Using ITK-SNAP: Comparison to Expert-based Segmentation.

Besson FL, Henry T, Meyer C, Chevance V, Roblot V, Blanchet E, Arnould V, Grimon G, Chekroun M, Mabille L, Parent F, Seferian A, Bulifon S, Montani D, Humbert M, Chaumet-Riffaud P, Lebon V, Durand E. **Radiology. 2018** Jul;288(1):277-284. doi: 10.1148/radiol.2018171756. Epub 2018 Apr 3. PMID: 29613842

What are we expecting from PET/MRI ?

Besson FL, Lebon V, Durand E. **Journal Français de Médecine Nucléaire 2016** February ;40(1) : 31-40. doi : 10.1016/j.mednuc.2016.01.002.

Conference proceedings

- **European Association of Nuclear Medicine and Molecular Imaging (EANM), Barcelona, Spain, October 12-16 2019.**

EPI distorsion correction for Lung PET-MRI oncology.
Besson FL, Fernandez B, Faure S, Seferian A, Mercier O, Mignard X, Parent F, Bulifon S, Montani, Mussot S, Fadel E, Mitilian D, Blanchet E, Chetouani A, Bouderraoui F, Cherkaoui H, Planchard, Naltet C, Le Pechoux C, Caramella C, Besse B, Comtat C, Gervais P, Lebon V, Durand E. (**E-poster**)

Quantitative T1 and T2-mapping for multimodal PET-MRI Lung oncology purpose.
Besson FL, Fernandez B, Faure S, Guillot G, A. Vignaud, Mercier O, Seferian A, Mussot S, Blanchet E, Mitilian D, Chetouani A, Bulifon S, Bouderraoui F, Mignard X, Le Pechoux C, Montani D, de Montpreville V, Levy A, Fadel E, Planchard D, Besse B, Gervais P, Comtat C, Lebon V, Durand E. (**E-poster**)

One-stop-shop fully integrated dynamic PET-MRI for the characterization of lung lesions: a feasibility study.
Besson FL, Fernandez B, Faure S, Seferian A, Mercier O, Mignard X, Blanchet E, Mussot S, Bulifon S, Mitilian D, Chetouani A, Bouderraoui F, Mabille L, Cherkaoui H, Botticella A, Caramella C, Pradere P, Le Pechoux C, Fadel E, Planchard D, Besse B, Comtat C, Gervais P, Lebon V*, Durand E. (**Oral presentation**).

- **Radiological Society of north America (RSNA), Chicago, United States of America, November 26 to December 1th 2017.**

Active Contour-Based Segmentation for 18F-FDG PET Thoracic Oncology: A Powerful Alternative to the Clinical State-of-the-Art Expert-based Segmentation.
Besson FL, Henry T, Myer C, Chevance V, Roblot V, Blanchet E, Arnoud V, Grimon G, Chekroun M, Mabille L, Parent F, Seferian A, Bulifon A, Montani D, Humbert M, Chaumet-Riffaud P, Lebon V, Durand E. (**Oral presentation**).

université PARIS-SACLAY

ÉCOLE DOCTORALE
Physique et ingénierie : Electrons, Photons, Sciences du vivant (EOBE)

Titre : Intégration dynamique TEP-IRM pour une nouvelle approche multiparamétrique de l'hétérogénéité tumorale dans le cancer bronchique non à petites cellules (CBNPC).

Mots clés : Tomographie par émission de positrons; imagerie par résonance magnétique; imagerie multimodale TEP-IRM; cancer bronchique non à petites cellules (CBNPC).

Résumé : L'hétérogénéité tumorale est un facteur important de progression et de résistance au traitement. L'imagerie multiparamétrique TEP-IRM offre des opportunités uniques de caractérisation biologique cellulaire, mais n'a jamais été évalué à l'échelle régionale intra-tumorale dans le cancer du poumon non à petites cellules (CBNPC), première cause de décès oncologique. Une approche multiparamétrique dynamique simultanée TEP-IRM au ^{18}F-FDG a été développée en ce sens. Cette approche a nécessité l'implémentation « maison » de la méthode de référence de quantification TEP du métabolisme glucidique (modèle tri-compartimental de Sokoloff); le développement d'une méthode de correction inédite des distorsions géométriques en imagerie de diffusion, validée sur fantôme et testée cliniquement ; la validation sur fantôme de méthodes d'IRM quantitative (relaxométrie T1/T2), également testées cliniquement; et l'implémentation « maison » du modèle compartimental de Tofts (version étendue) pour l'évaluation de la vascularisation tumorale en IRM dynamique de perfusion. Les résultats de nos travaux expérimentaux effectués à l'échelle intra-tumorale régionale illustrent l'hétérogénéité des rapports entre métabolisme glucidique et vascularisation dans le CBNPC, deux caractéristiques biologiques fondamentales de progression tumorale, et montrent qu'un partitionnement tumoral non supervisé par modèle de mélange gaussien, intégrant l'ensemble des biomarqueurs TEP-IRM de ce projet, individualise 3 types de supervoxels, dont la signature biologique peut être prédite avec une exactitude de 97% par 4 biomarqueurs TEP-IRM dominants, révélés par méthodes métaheuristiques d'apprentissage machine.

Title: Integrating PET-MR data for a multiparametric approach of tumour heterogeneity in non-small-cell lung cancer (NSCLC)

Keywords: positron emission tomography; magnetic resonance imaging; PET-MRI multimodal imaging; non-small cell lung cancer

Abstract: Tumor heterogeneity is an important factor of progression and resistance to treatment. Multiparametric PET-MRI imaging offers unique opportunities to characterize biological cellular processes, but has never been evaluated at the regional level in Non-Small Cell Lung Cancer (NSCLC), the leading cause of oncological death. A simultaneous dynamic multiparametric ^{18}F-FDG PET-MRI approach has been developed to this end. This approach required the "in-house" implementation of the reference absolute PET quantitative method of glucose metabolism (Sokoloff's tri-compartmental model); the development of a method for correcting geometric distortions in diffusion weighted imaging, validated on phantom and clinically tested; the phantom validation of quantitative MRI methods (T1/T2 relaxometry), also clinically tested; and the "in-house" implementation of the Tofts compartmental model (extended version) for the evaluation of tumor vascularization by dynamic perfusion MRI. The results of our work, performed at the regional intra-tumor level, illustrate the heterogeneity of the regional interlinks between glucose metabolism and vascularization in NSCLC, two fundamental biological hallmarks of tumor progression, and show that an unsupervised tumor partitioning by Gaussian mixture model, integrating all the PET-MRI biomarkers of this project, individualizes 3 types of supervoxels, whose biological signature can be predicted with 97% accuracy by 4 dominant PET-MRI biomarkers, revealed by metaheuristic machine learning methods.

Université Paris-Saclay
Espace Technologique / Immeuble Discovery
Route de l'Orme aux Merisiers RD 128 / 91190 Saint-Aubin, France